

CHARACTERISING GALACTIC FEEDBACK
THROUGH MULTIWAVELENGTH OBSERVATIONS
ACROSS COSMIC TIME

Stephen Molyneux

A thesis submitted in partial fulfillment of the requirements of
Liverpool John Moores University
for the degree of Doctor of Philosophy

June 29, 2023

Declaration

The work presented in this thesis was carried out at the Astrophysics Research Institute, Liverpool John Moores University and at the European Southern Observatory (ESO). Unless otherwise stated, it is the original work of the author. While registered as a candidate for the degree of Doctor of Philosophy, for which submission is now made, the author has not been registered as a candidate for any other award. This thesis has not been submitted in whole, or in part, for any other degree.

Stephen Molyneux
Astrophysics Research Institute
Liverpool John Moores University
IC2, Liverpool Science Park
146 Brownlow Hill
Liverpool L3 5RF
UK

Abstract

Understanding how and when galaxies form as well as how they evolve across cosmic time is a fundamental question in our studies of the Universe. From our current understanding galaxies form some time in the first few hundred million years after the big bang. These first galaxies and the stars within them release high energy photons that ionise their surroundings, changing the state of the Universe from being neutral to ionised. The period of the Universe in which these first galaxies form is therefore known as the epoch of reionisation and lasts until roughly one billion years after the big bang, at around a redshift of 6.

During the lifetime of galaxies from formation to the present day they can evolve via several processes. There are external processes such as the environment of the galaxy, as well as merging with other galaxies which are crucial to building up from masses of several thousand solar masses to billions of solar masses. There are also internal processes within galaxies that can impact upon galaxy evolution. One of the vital internal processes to understand is the relation between galaxies and their central supermassive black holes. In particular, the case of growing supermassive black holes (known active galactic nuclei). These active galactic nuclei can release large amounts of energy into their host galaxy which can impact upon the galaxies ability to form stars and change how galaxies evolve.

Here I present work covering the general topic of galaxy evolution from galaxies in the epoch of reionisation to those in the local universe which are known to host active galactic nuclei. I begin with the spectroscopic redshift confirmation of a galaxy in the very early Universe, as well as some basic analysis of some of the properties of this galaxy including the kinematics of the gas

and comparisons to galaxies in the local Universe. Studies of these early galaxies are important to give insights into the first galaxies that form and the environment of the early Universe. These galaxies are also the building blocks that go on to shape the galaxy population we see today, and so are crucial to understand the processes of galaxy formation and evolution.

I will then present a series of multi-wavelength observations performed to analyse the relationship between active galactic nuclei and their host galaxies. In particular, feedback from active galactic nuclei in the form of radio jets and how this impacts upon the prevalence of ionised outflows and the excitation of molecular gas in their host galaxies. These studies provide insights into the connection between central supermassive black holes and their host galaxies which is plays a vital contribution in galaxy evolution.

The questions that will be addressed in this thesis are: 1) What are the properties of galaxies in the epoch of reionisation, and 2) How do AGN and quasars impact upon the multi-phase interstellar medium of their host galaxies, including the mechanism by which AGN feedback takes place.

Publications

Within this thesis, the work within Chapters has been presented in the following jointly authored publications:

1. *Spectroscopic confirmation of a gravitationally lensed Lyman-break galaxy at $z_{[CII]} = 6.827$ using NOEMA*,
Molyneux S. J., Smit, R., Schaerer, D., Bouwens, R. J., Bradley, L., Hodge, J. A., Longmore, S. N., Schouws, S., van der Werf, P., Zitrin, A., Phillips, S., 2022, MNRAS, 512, 535.
2. *Extreme ionised outflows are more common when the radio emission is compact in AGN host galaxies*,
Molyneux S. J., Harrison, C. M., Jarvis, M. E., 2019, A&A 631, A132.
3. *The Quasar Feedback Survey: characterising CO excitation in quasar host galaxies*,
Molyneux S. J., Calistro Rivera, G., De Breuck, C., Harrison, C. M., Mainieri, V., Lundgren, A., Kakkad, D., Circosta, C., Girdhar, A., Costa, T., Mullaney, J. R., Kharb, P., Arrigoni Battaia, F., Farina, E. P., Alexander, D. M., Ward, S. R., Silpa S., Smit, R., 2023, accepted for publication in MNRAS.

Publication 1 forms the basis of Chapter 2. All the analysis carried out was performed by S. J. Molyneux with major scientific contributions from R. Smit. Calibrated NOEMA data were provided by R. Smit and further reduced, imaged and analysed by S. J. Molyneux.

Publication 2 forms the basis of Chapter 3. All the analysis carried out was performed by S. J. Molyneux with major scientific contributions from C. M. Harrison and M. E. Jarvis. M. E. Jarvis provided work on the resolved radio structures for a subsample of the total sample studied in this work. The majority of this work was completed before S. J. Molyneux started the PhD, however is included in this thesis as it has not been used for any other qualification and is also very relevant to the work performed during the PhD. The sample analysed in this work is the parent sample for the work presented in Chapter 4.

Publication 3 forms the basis of Chapter 4. All analysis carried out was performed by S. J. Molyneux with major scientific contributions from G. Calistro Rivera, C. De. Breuck and C. M. Harrison.

Whilst writing this thesis, S. J. Molyneux has also contributed to the following publications, which are focused on topics related to the thesis work:

4. *Quasar feedback survey: multiphase outflows, turbulence, and evidence for feedback caused by low power radio jets inclined into the galaxy disc*,
Girdhar, A., Harrison, C. M., Mainieri, V., Bittner, A., Costa, T., Kharb, P., Mukherjee, D., Arrigoni Battaia, F., Alexander, D. M., Calistro Rivera, G., Circosta, C., De Breuck, C., Edge, A. C., Farina, E. P., Kakkad, D., Lansbury, G. B., **Molyneux, S. J.**, Mullaney, J. R., Silpa, S., Thomson, A. P., Ward, S. R., 2022, MNRAS, 512, 1608.
5. *The quasar feedback survey: discovering hidden Radio-AGN and their connection to the host galaxy ionized gas*,
Jarvis, M. E., Harrison, C. M., Mainieri, V., Alexander, D. M., Arrigoni Battaia, F., Calistro Rivera, G., Circosta, C., Costa, T., De Breuck, C., Edge, A. C., Girdhar, A., Kakkad, D., Kharb, P., Lansbury, G. B., **Molyneux, S. J.**, Mukherjee, D., Mullaney, J. R., Farina, E. P., Silpa, S., Thomson, A. P., Ward, S. R., 2021, MNRAS, 503, 1780.
6. *Prevalence of radio jets associated with galactic outflows and feedback from quasars*,
Jarvis, M. E., Harrison, C. M., Thomson, A. P., Circosta, C., Mainieri, V., Alexander, D. M., Edge, A. C., Lansbury, G. B., **Molyneux, S. J.**, Mullaney, J. R., 2019, MNRAS, 485, 2710.

S. J. Molyneux also contributed to the following conference proceedings:

7. *Establishing the impact of powerful AGN on their host galaxies,*

Harrison, C. M., **Molyneux, S. J.**, Scholtz, J., Jarvis, M. E., 2021, *Galaxy Evolution and Feedback across Different Environments*. Proceedings of the International Astronomical Union, Volume 359, pp. 203.

Acknowledgements

There are a lot of people who have supported, guided and inspired me throughout this PhD journey, and helped me to grow as a person as well as a researcher. I am incredibly grateful to all who have been there throughout this journey.

Firstly I'd like to thank my supervisors, whom without none of the work in this thesis would have been possible. I want to start with Chris, you were not an official supervisor during my PhD but working with you before the PhD cemented my decision to take this path and so without you I would not be where I am today. Thank you for taking me on to work with you at ESO and for all your continued support and supervision since then. It has truly been a pleasure and I have learnt so much from you, not only scientifically but also how you support the people around you and create a welcoming and nurturing working environment. You have been a big inspiration and an example for how academia should be.

Renske, thank you for being so supportive throughout these past 3.5 years. With a global pandemic, two maternity leaves and me spending 2 years in a different country it was certainly eventful but you have always made time to help and guide me through this PhD. Both working closely in Liverpool and virtually as well as supporting my studentship at ESO. You have helped me to grow as a researcher and I have learnt so much from you. Thank you for everything!

Gaby, you have been a wonderful supervisor and have always been there for support and guidance throughout everything, both scientifically and personal. I really can't thank you enough for all that you have done during this time and I will always cherish this period of my academic career working with you. You have also been a huge inspiration and a great role model.

Carlos, thank you for playing a huge role in one of the major highlights of my PhD, the visit to APEX and Paranal. Since I was first at ESO back in 2018 it has been something I wanted to tick off my bucket list and so thank you for your support and help in making this happen. Thank you also for sharing your *extensive* knowledge of sub-mm observations (particularly APEX), even if not all of it was retained by me it was always interesting and inspiring to see someone speak with such passion. Of course I will also always remember the Belgian fries at the APEX base camp. Thank you for being a great supervisor at ESO and always making time for meetings and discussions.

Also to Meghan, my masters supervisor at the University of Nottingham who also helped support my PhD applications. Thank you for your support and it has always been great to see you/catch up at various points during my PhD.

Moving on from supervisors, to Clive Tadhunter and Ivan Baldry, thank you for taking the time to examine this thesis, and for your great insights and ideas during and beyond the viva examination.

To Mariya thank you for encouraging and supporting my application to the ESO research internship, which I see as the starting point to my academic life and without which I would not be here today writing this thesis. Calum, you helped make that 6 months science communication internship a joy, even though it definitely descended into insanity at times. Thanks for all your support during my PhD as well, and always being there to turn to with anything. Much obliged!

To Kateryna, Dan and Barna, you were the first students I met at ESO (we don't talk about Starkbierfest), but you made me see that a PhD maybe wasn't so bad and motivated me to do so! Also to Serban and Benoit, since the early days of Freetime in Garching you have always been around and it's been a genuine pleasure to spend time with you, (especially your incredible tiramisu Benoit!). I've enjoyed so many laughs with you all since then!

To Miranda, you also acted like a supervisor during my internship working with Chris and yourself. I am very thankful to you for that, and I have lost count of the times I've gone back to your papers to see how you did something and/or checking targets in QFeedS! To Meghan and Silvia thank you for encouraging me to apply to Liverpool for the PhD, it was an excellent suggestion and of course played a big part of my PhD!

My time both in Liverpool and ESO wouldn't have been the same without the Liverpool/ESO gang! So to Tutku and Gemma, you have been amazing friends throughout this PhD and I'm so glad we have shared the journey together. A special mention to three incredible science communicators, Juliet, Anita and Rebecca, not only are you all an inspiration, but you are amazing friends who were always there to turn to and I've enjoyed so many laughs with you all. Elena, we had a short (too short) overlap at ESO but it was a pleasure and I'm so grateful for your friendship during and since. I'm so glad we have seen each other again at various conferences, ESO trips and of course Max Pezzali (look at one of the inspirational quotes haha)! I'm looking forward to seeing you at no doubt many more AGN conferences and in Florence. Simon, I still remember your first day at ESO, it seems both such a long time ago but also only yesterday! Thank you for your friendship and of course your amazing cooking which made many ESO events that little bit better!

Tom, Anna and Justin, the online Beer Friday gang, thank you for making those Friday evenings so entertaining! It was genuinely something I looked forward to every week and something which I won't ever forget! Samuel, of course part of the AGN/QFeedS gang. Thank you for your friendship throughout the time at ESO and beyond. Thanks also for the incredibly organised

hikes which provided much needed relaxation/exercise over the weekends, and especially for taking careful consideration and making sure they were planned so my knees would survive the descent.

Joshiwa, all those table football matches got me through a lot of days, whether just to take a break from work or release some stress it was always great fun! Camila you have been an amazing friend throughout this PhD and watching your talks/presentations have always inspired me. I can't wait to see the amazing astronomer that I doubt you will become! There you were always, and still are, such a huge inspiration with everything you do! No doubt you will be a science superstar and I won't even be surprised when you do so. Avinash, it was always great to chat as you passed by my office and you always seemed to be around, sometimes even weekends and holidays, but as a result you were able to capture the pictures for my favourite .gif! Chi Yan, of course still office mates for life! Chiara thank you for being a wonderful friend through everything and for introducing me to Max Pezzali who's songs and lyrics were an essential part to my PhD (also please read one of the inspirational quotes!). To Dominika, Ivanna, Alonso, Keegan, Luca, Roman and Alessandra thank you for so many great memories! I'm so glad our paths crossed and it wouldn't have been half as fun without you all.

I now need to group more people together otherwise this will get far too long... To Aaron, Aashish, Adrian, Aleksandra, Alice, Alvaro x2, Andrew, Amanda, Chiara, Dani, Divya, Dominique, Elena x2 (too many Elena's to thank!), Ellie, Irene, Jess, Jianhang, Justyn, Karina, Katja, Khashi, Laura, Marie, Mari-Liis, Naomi, Pierrick, Roland, Rory, Sabrina, Sami, Sara x2, Sebastian, Tommy, Yessica, Veena, Victor, Vishaal and everyone in the ESO Science Communication department, your kindness and friendship before and throughout the PhD is something I will always treasure.

To everyone else at ESO and the ARI, thank you for all your support, friendship and interesting conversations which have enriched my PhD. Thanks to my family for their support throughout my PhD. I hope the summary at the end will translate what I have been doing for the last 3.5 years or so!

Finally, to all who made contributions to the context free quotes, thank you for still giving me endless laughs throughout my PhD when reading through the list. A selection make an appearance in between chapters so do take a look and see if you recognise any!

“Started making it, had a breakdown... bon appetit!”

James Acaster

“Nessun rimpianto, nessun rimorso”

Max Pezzali

Contents

Declaration	ii
Abstract	iii
Publications	v
Acknowledgements	viii
List of Figures	xv
List of Tables	xvii
1 Introduction	1
1.1 From the first galaxies to the present day	1
1.1.1 The first galaxies	3
1.1.2 The Epoch of Reionisation	5
1.1.3 Observing the first galaxies and the epoch of reionisation	6
1.1.4 “Cosmic Noon”	12
1.1.5 The present day galaxy population	14
1.2 The interstellar medium	15
1.2.1 The warm ionised phase	15
1.2.2 The molecular phase	16
1.3 Line Emission Processes	17
1.3.1 Atomic energy levels	18
1.3.2 Molecular energy levels	19
1.4 AGN and quasars	21
1.4.1 What makes an AGN?	22
1.4.2 AGN feedback	25
1.4.3 The role of radio jets in AGN and their effect on the interstellar medium	28
1.5 Sub-mm observatories	32
1.5.1 APEX	33
1.5.2 ALMA	34
1.5.3 NOEMA	35
1.6 Summary and thesis outline	37

2	Spec-z confirmation of Abell 1703-zD1 using NOEMA	39
2.1	Introduction	39
2.2	Sample selection and observations	41
2.2.1	Target selection and properties	42
2.2.2	NOEMA observations and data reduction	43
2.3	Line scans	47
2.3.1	A1703-zD1	48
2.3.2	Serendipitous source neighbouring A1703-zD1	50
2.3.3	EGS-5711 & EGS-1952	51
2.3.4	EGS-5711 tentative detection	52
2.3.5	Empty scans	54
2.4	Source properties	54
2.4.1	$L_{\text{[CII]}}$ vs SFR relation	55
2.4.2	L_{IR} and SFR_{IR} constraints	57
2.4.3	Velocity Structure of A1703-zD1	58
2.5	Summary and conclusions	60
3	Galactic ionised outflows are more common when the radio emission is compact in AGN host galaxies	63
3.1	Introduction	64
3.2	The Sample, Catalogues and Radio Data	66
3.2.1	Catalogues and sample selection	67
3.2.2	Follow-up radio observations	69
3.3	Analyses	70
3.3.1	Characterising the emission-line profiles	70
3.3.2	Compact and extended radio emission	72
3.3.3	Basic radio size measurements	73
3.3.4	Morphological classification	74
3.3.5	Final classification into compact and extended radio sources	75
3.4	Results and Discussion	76
3.4.1	Trends between ionised gas velocities and radio sizes	79
3.4.2	Outflows are more prevalent with compact radio emission	79
3.4.3	Implications of this result	83
3.5	Conclusions	84
4	Characterising CO excitation in quasar host galaxies	88
4.1	Introduction	89
4.2	Sample selection	93
4.3	Observations and data reduction	96
4.3.1	CO(1-0) observations	96
4.3.2	CO(2-1) Observations	99
4.3.3	CO(3-2) Observations	101
4.3.4	CO(6-5) and CO(7-6) Observations	101
4.3.5	Ancillary Multiwavelength Data	102

4.4	Analysis and results	103
4.4.1	Comparison samples	103
4.4.2	Spectral properties	105
4.4.3	Molecular gas masses	110
4.4.4	CO excitation	112
4.4.5	Gas temperature and density	120
4.4.6	Comparing CO and ionised gas line profiles	123
4.5	Discussion	126
4.5.1	No observed impact on total CO excitation	128
4.5.2	A localised impact on CO?	132
4.5.3	Comparing CO and ionised gas line profiles	135
4.6	Conclusions	136
4.7	Spectra and data tables	137
5	Summary and Outlook	155
5.1	Summary of conclusions	155
5.2	Where future observatories will take us	157
5.3	Avenues of future work	159
6	A short summary for a general audience	163
6.1	What are galaxies and how do we study them?	163
6.2	Investigating the first galaxies in the Universe	166
6.3	Supermassive black holes at the centre of galaxies	167
6.4	Identifying a link between active galactic nuclei and the velocity of gas in the galaxy	169
6.5	A study of total molecular gas content in quasar host galaxies	171
	Bibliography	174

List of Figures

1.1	Timeline of the Universe	6
1.2	Example of Lyman Break	7
1.3	Neutral Hydrogen fraction and how quick is the process of reionisation	9
1.4	Example of [CII] detections at $z > 6$	11
1.5	Example of a gravitational lens	12
1.6	Cosmic star formation rate history	13
1.7	Diagram of the structure of AGN	23
1.8	BPT diagram	24
1.9	Necessity for stellar and AGN feedback in models to reproduce galaxy populations	25
1.10	Co-evolution of AGN and their host galaxies	26
1.11	Relation between radio luminosity and prevalence of ionised outflows	30
1.12	Enhanced CO excitation around radio jets	31
1.13	Atmospheric transmission across mm and sub-mm wavelengths	33
1.14	Atacama Pathfinder EXperiment telescope (APEX)	34
1.15	ALMA observatory	35
1.16	The NOEMA interferometer	36
2.1	A1703-zD1 SED and redshift probability distribution	44
2.2	EGS-5711 SED and redshift probability distribution	45
2.3	EGS-1952 SED and redshift probability distribution	45
2.4	NOEMA imaging of A1703-zD1	49
2.5	NOEMA [CII] spectra of A1703-zD1	49
2.6	Serendipitous line detection in A1703-zD1	50
2.7	Imaging of serendipitous line detection in A1703-zD1	51
2.8	Tentative detection of EGS-5711	53
2.9	Spectra for tentative detection of EGS-5711	53
2.10	Empty scans of EGS-5711	54
2.11	Empty scans of EGS-1952	54
2.12	[CII] line luminosity vs star formation rate	56
2.13	Velocity structure of A1703-zD1	59
3.1	Radio luminosity versus [OIII] luminosity for AGN in Molyneux et al. (2019)	68
3.2	Examples of radio classifications of compact and extended emission	71
3.3	Fits for single component and two components [OIII] emission	72
3.4	[OIII] emission line width versus radio size	80

3.5	Cumulative fractions of [OIII] FWHM across the sample	81
4.1	Sample selection for Molyneux+23	94
4.2	Curves of growth for CO(1-0) data in QFeedS	98
4.3	Example spectra of J1100+0846	109
4.4	Stellar mass versus the gas fraction	113
4.5	Low J_{CO} CO SLED	115
4.6	High J_{CO} CO SLED	116
4.7	Histograms and violin plots of line ratios in QFeedS	121
4.8	Line ratios versus bolometric luminosity	123
4.9	r_{21} vs r_{32} as a measure of temperature and density	124
4.10	Comparing line profiles of CO and OIII	126
4.11	W_{80} of SDSS and W_{80} of MUSE at 3 arcsec	127
4.12	W_{80} of SDSS and W_{80} of MUSE at 30 arcsec	127
4.13	J0909+1052 spectra	138
4.14	J0945+1737 spectra	138
4.15	J0958+1439 spectra	139
4.16	J1000+1242 spectra	139
4.17	J1010+0612 spectra	140
4.18	J1010+1413 spectra	140
4.19	J1016+0028 spectra	141
4.20	J1055+1102 spectra	141
4.21	J1100+0846 spectra	142
4.22	J1108+0659 spectra	142
4.23	J1114+1939 spectra	143
4.24	J1116+2200 spectra	143
4.25	J1222-0007 spectra	144
4.26	J1316+1753 spectra	144
4.27	J1356+1026 spectra	145
4.28	J1430+1339 spectra	145
4.29	J1518+1403 spectra	146
4.30	Contour plots of CO(1-0)	147
5.1	Artist's impression of ESO's Extremely Large Telescope	158
6.1	Examples of different types of galaxies	164
6.2	Examples of galaxies nearby and distant	165
6.3	Observations from NOEMA and the Hubble space telescope of A1703-zD1	167
6.4	Event Horizon Telescope imaging of M87	168
6.5	Schematic of radio jets and their influence on gas in the galaxy	170
6.6	Schematic of gas excitation in galaxies	172

List of Tables

2.1	Table of source properties in Molyneux et al. (2022)	47
2.2	Galaxy properties from Molyneux et al. (2022)	55
3.1	Statistics of [OIII] emission line profiles for compact and extended radio emission	78
4.1	Table of sources properties for Molyneux+23	95
4.2	Table of molecular gas mass properties	114
4.3	Table of CO line ratios in QFeedS	119
4.4	Table of median line ratios and comparisons to the literature	122
4.5	Details of the CO observations	149
4.6	CO(1-0) line properties	150
4.7	CO(2-1) line properties	151
4.8	CO(3-2) line properties	152
4.9	CO(6-5) line properties	153
4.10	CO(7-6) line properties	153
4.11	[OIII] line properties	153

Context free quotes

“I just want to ride the big swans”

“You can love Sir Killalot and Grommit”

“I try to stop by every day and give you a few”

“Welcome to the ELT. Here’s your walnuts. You’ll need ‘em ”

“What an Englishman can do to a sausage is enough to make a proud Greek man cry”

“You have to juggle round fruit, but only round fruit, juggling bananas would be crazy!”

[on the subject of Pingu] “I think that’s where I learned empathy”

“I’m like the Master Video Archive — I’ve got nothing left”

“A meeting point for forever alone people”

“You can have a lot of fun with foil”

“We have a camel in our midst”

Introduction

In this introduction I will give a brief overview of our current understanding of galaxy formation and evolution as well as of active galactic nuclei (AGN) and how they impact on galaxy evolution. This will help provide context for the work presented in this thesis as well as motivate and highlight the importance of this research.

I will first present an overview of galaxy formation and evolution from the first galaxies up to the present day galaxy population in Section 1.1. Following this, in Section 1.2 I will introduce the interstellar medium and the different phases of gas present in galaxies that are relevant for this research. In Section 1.4 I will then introduce active galactic nuclei and highlight their importance as a mechanism which regulates galaxy evolution in the observed co-evolution between galaxies and their central supermassive black holes. In Section 1.5, I introduce the sub-mm telescopes and observatories that have been essential for the work presented in this thesis. Finally, in Section 1.6 I will summarise the introduction and introduce the chapters of this thesis.

1.1 From the first galaxies to the present day

Galaxies are gravitationally bound systems which contain stars, gas, dark matter and in their centres a supermassive black hole. These “components” of galaxies all play a role in both the

formation and evolution of galaxies, and so studying each of them is of critical importance for a full understanding of how galaxies form and evolve.

These studies are important as galaxies can have very different properties, and to understand the reasons behind this we need to understand how and why galaxies evolve over time. Galaxies come in different sizes, ranging from few kpc to 100s of kpc with masses $\sim 10^7 - 10^{12} M_{\odot}$ (solar masses). When comparing distant galaxies to those observed much closer, distant galaxies have been found to be more compact [Daddi et al. \(2005\)](#); [Buitrago et al. \(2008\)](#); [Williams et al. \(2014\)](#), suggesting that they build mass over time. Current models suggest that galaxies grow via merging with other galaxies and also via accretion (e.g. [White & Rees, 1978](#); [Cole et al., 2000](#); [Conselice, 2014](#)). There is also evidence that these mergers can promote activity of AGN and quasars ([Ellison et al., 2019](#); [Pierce et al., 2023](#)). See more about AGN and quasars in [Section 1.4](#).

The environment that galaxies live in can also vary, sometimes being part of a larger cluster of galaxies or alternatively being more isolated with a few smaller companions ([Press & Schechter, 1974](#); [Springel et al., 2005](#)). Further, galaxies come in a diversity of shapes and can typically be classified as elliptical, spiral or irregular ([Hubble, 1927](#); [van den Bergh, 1960](#); [Sandage, 1961](#); [van den Bergh, 1976](#)). They can also contain different structures within them, such as bars, disks and bulges ([Gadotti, 2009](#)). A link between galaxy morphology and star formation activity has also been identified ([Lee et al., 2013](#); [Conselice, 2014](#); [Bait et al., 2017](#)). Spiral galaxies are observed to be more active in forming stars, whereas ellipticals are often quenched as star formation has stopped (galaxies with little or no star formation are known as passive galaxies).

Further, this correlates with the colour of galaxies. They display a bimodal distribution which consist of blue star-forming spirals and red passive ellipticals ([Baldry et al., 2004](#); [Schawinski et al., 2014](#); [Bremer et al., 2018](#)). In between these two populations is a seemingly transitional “green valley” ([Salim et al., 2007](#); [Wyder et al., 2007](#); [Gonçalves et al., 2012](#)), whereby galaxies are becoming quenched, all of which points to a close relationship between galaxy morphology/colour and star formation activity.

From this evidence, it is clear that galaxies can evolve throughout their life cycle, both in colour, morphology and internal structures (e.g. [de Sá-Freitas et al., 2022, 2023](#)). There is a plethora of

observed galaxies in the Universe and the properties of these galaxies also change over time as galaxies evolve. How we get such a variety and to study how/why galaxies evolve is therefore a fundamental question of astronomy.

One option for gaining this understanding is to try to study an individual galaxy and make observations to determine how it formed and evolved over time. For our own galaxy, the Milky Way, the formation/merger history has been well mapped (Eggen et al., 1962; Searle & Zinn, 1978; Ibata et al., 1994; Mackereth et al., 2019; Kruijssen et al., 2019; Horta et al., 2021). With observations of stellar populations, their ages and metallicities as well as bulk motions, allow for an analysis and prediction of this merger history. This gives us an idea of the history and evolution of the Milky Way. However, mapping the Milky Way like this is only possible due to our ability to resolve these stellar populations and study them in such detail. Therefore, expanding this work to extragalactic sources becomes technologically very challenging if not impossible. Further, as mentioned above, galaxies can be diverse and so to really understand galaxy evolution and why these differences are present, we need to observe as much of the galaxy population as possible to achieve this understanding.

Since it is also not possible to observe a single galaxy across these different evolutionary moments due to the sheer timescales involved, we are required to study galaxy samples across cosmic time to understand the changes that take place in the galaxy population as a whole.

In the following sections I provide a brief overview of some of the key observations that have led to our current understanding of galaxy evolution. In order to achieve this understanding of how we get to the vast array of observed galaxy properties, and the changes that occur over cosmic time, we start by investigating the formation and the properties of the very first galaxies.

1.1.1 The first galaxies

The first galaxies that form in the Universe are the seeds that grow into the present day galaxy population. Therefore, understanding how these first galaxies form, their properties and their environment is crucial to understanding their evolution across cosmic time. However, given the technological challenges of observing such distant galaxies, there is still much to learn about the very early period of the Universe when these galaxies form, and only recently have these

observations been possible. In the coming years no doubt there will be huge advancements in this area due to the James Webb Space Telescope (JWST). Indeed, since its launch JWST has already been pushing the boundaries and providing crucial observations of the most distant galaxies studied to date (Curtis-Lake et al., 2023).

Our current model of how the Universe formed is that of the Lambda-CDM (Λ CDM) Big Bang cosmology model. In this picture, roughly 370,000 years after the Big Bang, the Universe cooled such that neutral hydrogen could form, becoming transparent for the first time and thus providing us with the first snapshot of the Universe known as the Cosmic Microwave Background at $z = 1100$ (Bennett et al., 1996; Schlegel et al., 1998; Spergel et al., 2003).

At this stage of the Universe there were no stars or galaxies to produce light and as a result, the Universe entered a period known as the “Dark Ages”. Until that point the only source of photons was neutral hydrogen and occasionally the 21-cm hydrogen line (caused by a change of spin state of an electron in neutral hydrogen). Neutral hydrogen also has the ability to absorb high energy photons (i.e. light from stars and galaxies).

The first galaxies are believed to have formed some time in the first 500 million years after the Big Bang but much is still unknown about the properties of these galaxies. JWST is currently providing incredible insights into this period of the Universe, stretching our understanding and current theories about how and when these first galaxies form. From recent observations with JWST, galaxies have been identified at $z > 10$ (e.g. Arrabal Haro et al., 2023), with the most distant galaxy (at time of writing) being identified spectroscopically at a redshift (z) of 13.2, named GS-z13-0 (Curtis-Lake et al., 2023). If there is a larger abundance of galaxies at $z > 10$ than is currently predicted, it may well provide the need for an update to cosmological models (e.g. Somerville & Davé, 2015; Pillepich et al., 2018) and predictions as to how galaxies can form and build up their mass so quickly.

The motivates observations of this galaxy population and shows the importance of studying this period of the Universe where much is still unknown. The discoveries made with JWST, further pushing the boundaries in this field, makefor an exciting time in this research area.

Following the formation of the first stars and galaxies, the Universe entered into a period known as the epoch of reionisation, a stage of the Universe when these first stars and galaxies were able

to ionise their surroundings.

1.1.2 The Epoch of Reionisation

The first stars and galaxies, as well as accreting supermassive black holes, radiated high energy photons, some of which were able to ionise the surrounding neutral hydrogen, forming bubbles of ionised hydrogen through which light could travel and starting the epoch of reionisation (EoR). This process could have started as early as a few hundred million years ($z \approx 15$) after the Big Bang and continued until the entire Universe was ionised by $z \approx 6$, corresponding to roughly one billion years after the Big Bang. This was confirmed through observations of quasars at $z \approx 6$ which showed the presence of the Gunn-Peterson trough (Becker et al., 2001). This Gunn-Peterson trough is a feature of a galaxy's spectrum whereby there is a reduction in flux to effectively zero, due to absorption by neutral hydrogen, first predicted in 1965 (Gunn & Peterson, 1965). This therefore showed the change in hydrogen in the Universe from neutral to ionised. This is an important phase of the Universe because it marks a transition as galaxies affected the Universe around them. The evolution of this ionisation is key to understanding the sources of ionising photons, namely the first stars and galaxies.

Galaxies that form in the EoR are therefore interesting for two reasons. Firstly, they are possible sources of the reionisation of the Universe and so can give us insights into this process and the time frame in which it occurred. Secondly, these are some of the first galaxies to form in the Universe and therefore inform us about the earliest phase of galaxy formation and evolution. Figure 1.1 shows an illustration of our current understanding as to how the timeline of the Universe looks, showing the previously mentioned dark ages and the period over which the EoR is expected to take place.

The past decade has seen hundreds of galaxies identified in the epoch of reionisation, selected from their rest-frame UV light, using Hubble Space Telescope (*HST*) and ground-based optical/NIR observatories (see Stark, 2016, for a review and references therein). However, the number which also have spectroscopic redshift determinations is only a fraction of the total and we have a limited understanding of the physical properties of these first galaxies. Accurate measurements of the redshifts of galaxies are critical to allow for targeted follow up observations and to accurately map the properties of the first galaxy population.

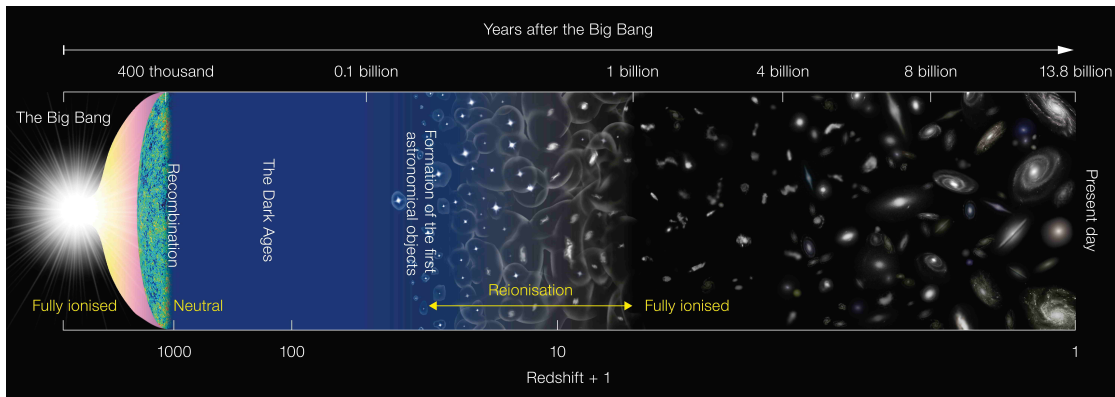


Figure 1.1: Illustration to show the key stages in the history of the Universe. Highlighted are the Cosmic Microwave Background (at Recombination), the Dark Ages, where the Universe is neutral, followed by the period of reionisation which shows growing bubbles of ionisation until $z \approx 6$ where the Universe becomes fully ionised. From there we observe the growth and evolution of galaxies until the present day. Credit: NAOJ.

1.1.3 Observing the first galaxies and the epoch of reionisation

Observations that probe this early period in the Universe are very useful, and notable previous surveys include those from the Hubble Space Telescope such as the Hubble Ultra Deep Field (Beckwith et al., 2006), the CANDELS Survey (Grogin et al., 2011) and the BUFFALO HST Survey (which takes advantage of gravitational lensing; Steinhardt et al., 2020), as well as surveys and follow up observations from Spitzer, the Very Large Telescope, Keck and others. With those surveys we can obtain an estimates of the photometric redshifts for thousands of galaxies. However, before they can be probed in further detail, a spectroscopic redshift needs to be obtained to allow accurate and targeted follow up observations – which are more reliable.

Here I will highlight some of the different methods for detecting these first galaxies and, of particular relevance to this thesis, highlighting the advancement that has arisen due to sub-mm observations from ALMA.

Lyman Break Technique

The imprint of hydrogen absorption in the UV spectrum of a galaxy can be used to determine an estimate for the redshift, with the spectra showing a sharp cut off that corresponds to the Lyman limit (912 angstroms at $z = 0$). As we observe galaxies at higher redshifts, this break in the spectra will occur at longer wavelengths. Therefore, by using multiple filters to observe at different wavelengths, we can search for a dimming of the galaxy or even for it to disappear in a

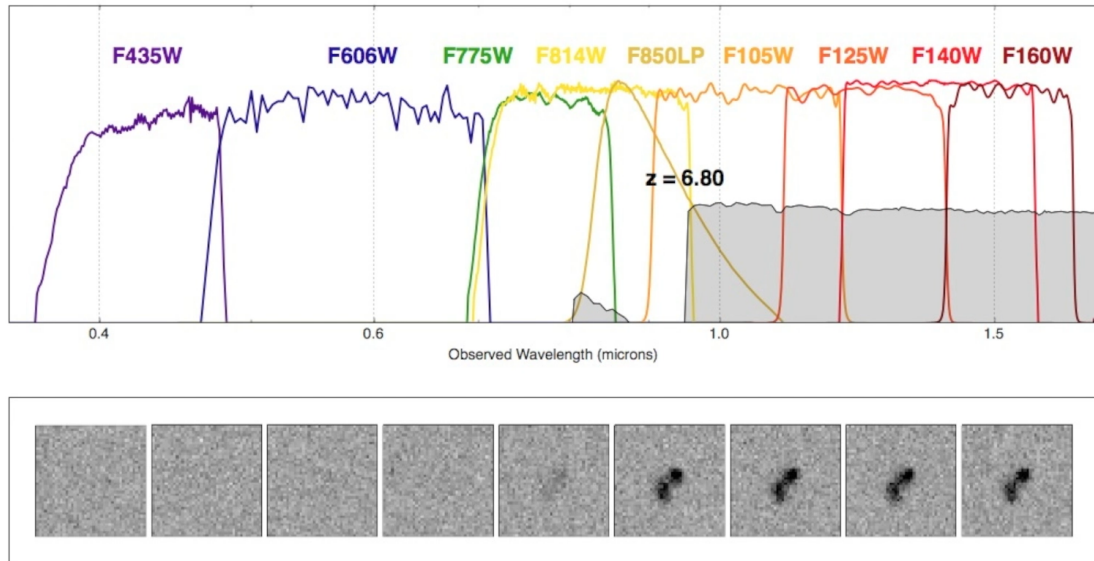


Figure 1.2: Example of the UV spectrum of a galaxy at $z = 6.80$ shown in the top panel in black, and shaded underneath in grey. Separating the above panel are coloured regions denoting different Hubble filters and the greyscale images in the panels below show how a galaxy at $z = 6.80$ would look in each of these filters. Using multiple filters to observe a galaxy and observing a “drop out” at a certain wavelength, as shown here, can be used to estimate the redshift of a galaxy. Credit: D. Magee, G. Illingworth, R. Bouwens & P. Oesch.

given filter completely. This allows us to estimate a redshift for the galaxy in question and those identified in this way are known as Lyman Break Galaxies (LBGs, e.g. [Szalay et al., 1999](#); [Bouwens et al., 2011](#)). To illustrate this method of detection and the effect itself, an example spectra for a galaxy at $z = 6.80$ is presented in Figure 1.2.

In [Oesch et al. \(2016\)](#) they present the spectroscopic confirmation of a $z = 11$ galaxy, GN-z11, when the Universe was only around 400 million years old. This is one of the most distant galaxies known to date and used Hubble WFC3/IR slitless grism spectra, with the target initially being identified from CANDELS/GOODS-N observations. Spectroscopic redshifts obtained from this Lyman break are, however, observationally expensive, and only possible for the brightest sources. There are therefore only a handful more spectroscopic redshift confirmations using this technique (e.g. [Watson et al., 2015](#); [Hoag et al., 2018](#)). We therefore need alternatives to provide more spectroscopic redshifts for galaxies in the early Universe, which can be achieved from $\text{Ly}\alpha$ and more recently, [C II] observations.

Lyman alpha

As mentioned above, a small fraction of galaxies have spectroscopic redshifts at $z > 6$. One reason for this is that the strong lines in the rest-frame optical spectrum of galaxies is redshifted

out of the optical and near-infrared atmospheric windows, while the Ly α line - the strongest line in the rest-frame UV spectrum - is difficult to observe due to its absorption by neutral hydrogen in the intergalactic and interstellar medium.

However, it is still possible to observe Ly α from galaxies in this epoch, in particular bright Ly α emission from galaxies known as Ly α emitters (LAEs). A strong Ly α signal can provide us with a spectroscopic redshift for a galaxy, by measuring the difference between the observed and laboratory rest-frame wavelength. Identifying Ly α from galaxies is normally a straight-forward task, however Ly α can be absorbed by surrounding neutral hydrogen (in the galaxy itself or the intergalactic medium; IGM) which can reduce, or completely stop, any Ly α emission being detected. Therefore, observations at $z > 6$ (where large parts of the Universe are yet to be ionised) can be challenging. Despite this, there are still detections that have been made (e.g., [Matthee et al., 2015](#); [Stark et al., 2017](#)), most likely as a result of galaxies being in ionised bubbles through which the Ly α signal can permeate (e.g. [Jung et al., 2020](#); [Endsley et al., 2021](#)).

Using this technique there has been success out to the EoR. ([Zitrin et al., 2015](#)) presents the spectroscopic confirmation of a LAE at $z = 8.68$ using the Keck Observatory. There are further such examples of LAEs at $z > 6$ (e.g. [Malhotra & Rhoads, 2004](#); [Matthee et al., 2015](#); [Ouchi et al., 2018](#)), however, these successes only show a small part of the whole picture and also represent some of the brightest and most highly star forming galaxies.

LAEs at lower redshift have been observed to have high ionisation lines, such as [O III], while the same has been inferred through broadband photometry with Spitzer (e.g. [Labbé et al., 2013](#); [Smit et al., 2014, 2015](#)) which is evidence for the ability of these galaxies to produce enough high energy photons to ionise the interstellar medium (ISM [Nakajima & Ouchi, 2014](#)). The presence, or lack of Ly α and [O III] can therefore give indications about the ionisation of the ISM and further, the IGM. For example, a lack of Ly α but strong [O III] (inferred from photometry), would indicate that the surrounding IGM is not yet ionised.

Tracing the Ly α content can therefore be very useful, because these observations also allow us to determine the amount of neutral hydrogen present in the IGM and at different redshifts, from which we can calculate how quickly reionisation occurred. [Figure 1.3](#) illustrates current work being done in the community to establish how quickly, and over what time period the process of reionising the Universe took place, by calculating the fraction of neutral hydrogen present

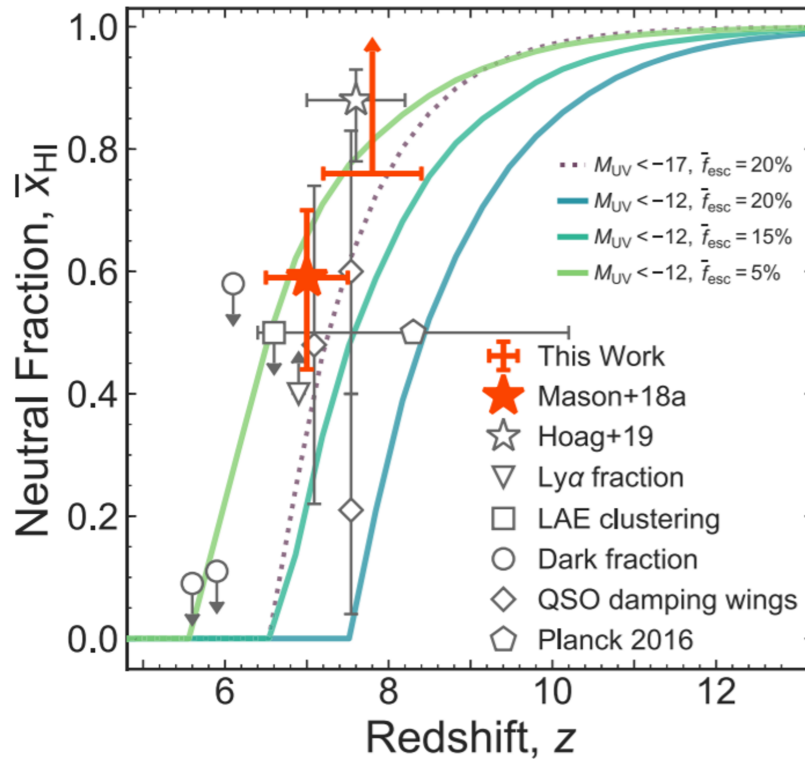


Figure 1.3: A compilation of models and observations to show the neutral hydrogen fraction as a function of redshift. This illustrates the range of scenarios for the process of reionisation in the Universe, and the time it takes for this process to take place. Credit: [Mason et al. \(2019\)](#).

in the IGM. To match the observations and models, estimates now seem to favour a slower and more gradual reionisation process (e.g., [Mason et al., 2018, 2019](#); [Hoag et al., 2019](#); [Naidu et al., 2020](#)).

Observing [C II] and the transformation made with ALMA

The fine-structure transition from singly ionised carbon, [C II]158 μm , is the most commonly used tracer of the star forming ISM in high redshift galaxies. Its brightness allows us to make observations of the first galaxies in the EoR, where this line is shifted into the sub-millimetre window of our atmosphere.

Until recently, only the brightest, most extreme and highly star forming galaxies and quasars could be studied at $z > 6$ with sub-mm observations. Most notably there were several attempts with the Plateau de Bure Interferometer (PdBI) before it was upgraded to the NOEMA Interferometer, but with limited success. These also include targeting A1703-zD1 (the main target presented in Chapter 2) in which the observations were unsuccessful in detecting [C II] ([Schaerer](#)

et al., 2015). In González-López et al. (2014) they were also unsuccessful with the PdBI in detecting [C II] in three galaxies at $z > 6.5$. With these limited observations, and only the brightest star forming galaxies, we had a very limited understanding of the broader galaxy population of more representative, “normal” galaxies.

However, observing [C II] has been transformed in the past decade by the Atacama Large Millimeter/submillimeter Array (ALMA) which, due to its sensitivity, has now opened the door to sub-mm observations of more representative galaxies in this epoch, providing spectroscopic confirmations and details of the dust and gas within.

ALMA now regularly confirms the redshifts of galaxies out to redshift $z = 9$ (e.g., Smit et al., 2018; Hashimoto et al., 2018; Tamura et al., 2019; Hodge & da Cunha, 2020; Bouwens et al., 2021) and provides a view of their dust obscured star-formation (e.g., Watson et al., 2015; Laporte et al., 2017; Bowler et al., 2018; Schouws et al., 2021), the kinematics of these sources (e.g., Smit et al., 2018; Hashimoto et al., 2019; Fujimoto, 2019; Ginolfi et al., 2020a), the cool gas traced by [C II] and highly ionised gas traced by [O III] (e.g., Maiolino et al., 2015; Inoue et al., 2016; Carniani et al., 2017; Laporte et al., 2017; Hashimoto et al., 2019; Tamura et al., 2019; Harikane et al., 2019; Bakx et al., 2020). It is therefore crucial to uncover the physical properties of these early systems to understand the evolution of the first generation of galaxies and their role in cosmic reionisation.

ALMA has demonstrated its ability to detect [C II] in UV bright galaxies which are intrinsically bright ($\sim 2 - 3 \times L^*$ at $z = 7$) at $z \gtrsim 5$ (Capak et al., 2015; Willott et al., 2015; Smit et al., 2018; Matthee et al., 2019; Béthermin et al., 2020; Bouwens et al., 2021). A specific example of the success of ALMA can be seen in Figure 1.4, in which two galaxies have spectroscopic redshift confirmations via the detection of [C II] emission (Smit et al., 2018).

Despite the capability of ALMA to probe galaxies in the EoR, it has limited sky coverage in the Northern Hemisphere and so interesting targets in this region of the sky might be left unexplored. PdBI has been upgraded in recent years and renamed the Northern Extended Millimeter Array (NOEMA) and is now the most sensitive submillimetre interferometer in the Northern Hemisphere. While less sensitive than ALMA still, efforts have been made to observe these distant galaxies with NOEMA to help fill the part of the sky that ALMA is not capable of observing (e.g. Walter et al., 2012; González-López et al., 2014; Schaerer et al., 2015). However,

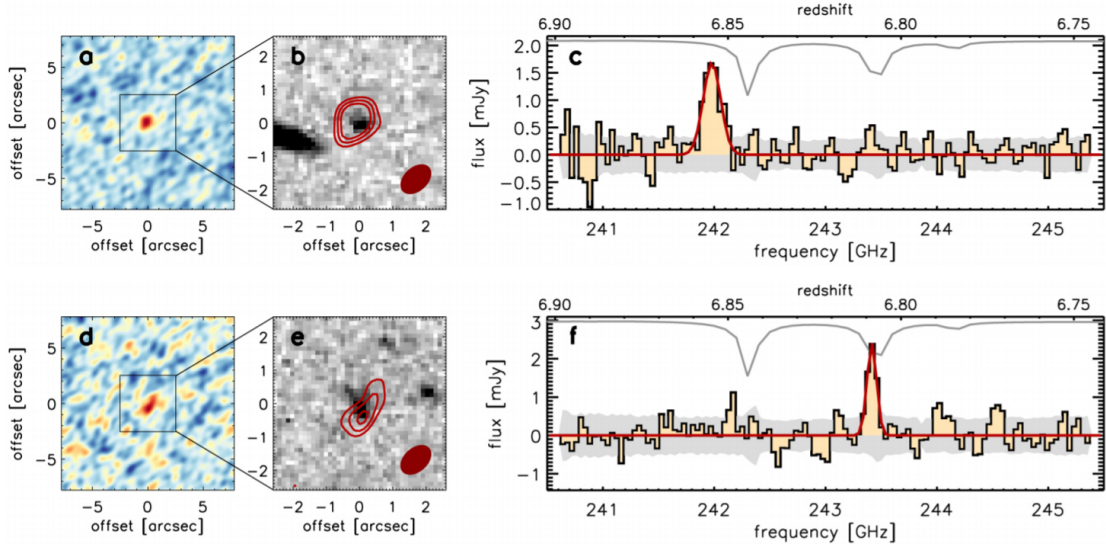


Figure 1.4: Data for two galaxies at $z > 6$, namely COS-3018555981 (upper panel) and COS-2987030247 (bottom panel). **Left panel:** ALMA narrowband images, collapsing the channels of the datacube around the line detection. **Middle panel:** HST greyscale imaging with red contours corresponding to 3, 4 and 5 σ levels from the ALMA data. **Right panel:** Spectra of the [C II] line with a gaussian fit (shown in red) to characterise the line profile and calculate redshifts of $z_{[CII]} = 6.8540 \pm 0.0003$ and $z_{[CII]} = 6.8076 \pm 0.0002$ for COS-3018555981 and COS-2987030247 respectively. Credit: [Smit et al. \(2018\)](#).

these efforts were, until recently, unsuccessful. In Chapter 2 I will present the first successful detection of [C II] emission in a normal star forming galaxy at $z > 6$ using NOEMA.

Despite the success of ALMA, observations are still lacking of galaxies at these high redshifts which are more representative of the galaxy population as a whole ($L \leq L_{z=7}^*$). One tool that we can use to assist in these observations, and to reach lower luminosity targets, are gravitational lenses.

Gravitational lenses as a tool to study high-z galaxies

One issue with studying these very distant galaxies is that, even with ALMA, it can be challenging to observe the fainter population of galaxies. Our best insights with sub-mm observatories into this fainter population are rare, apparently bright sources, which have been gravitationally lensed ([Knudsen et al., 2016](#); [Bradač et al., 2017](#); [Fujimoto et al., 2021](#); [Laporte et al., 2021](#)). Gravitational lensing will occur when a massive object (such as a galaxy cluster) bends and magnifies the light from objects behind, making them easier to observe than they otherwise would be ([Schneider et al., 1992](#)). With this, we can therefore study much fainter objects with the same technologies and telescopes that are currently available and provide more insights into these early galaxies. An example of such a gravitational lens can be seen in Figure 1.5, showing the

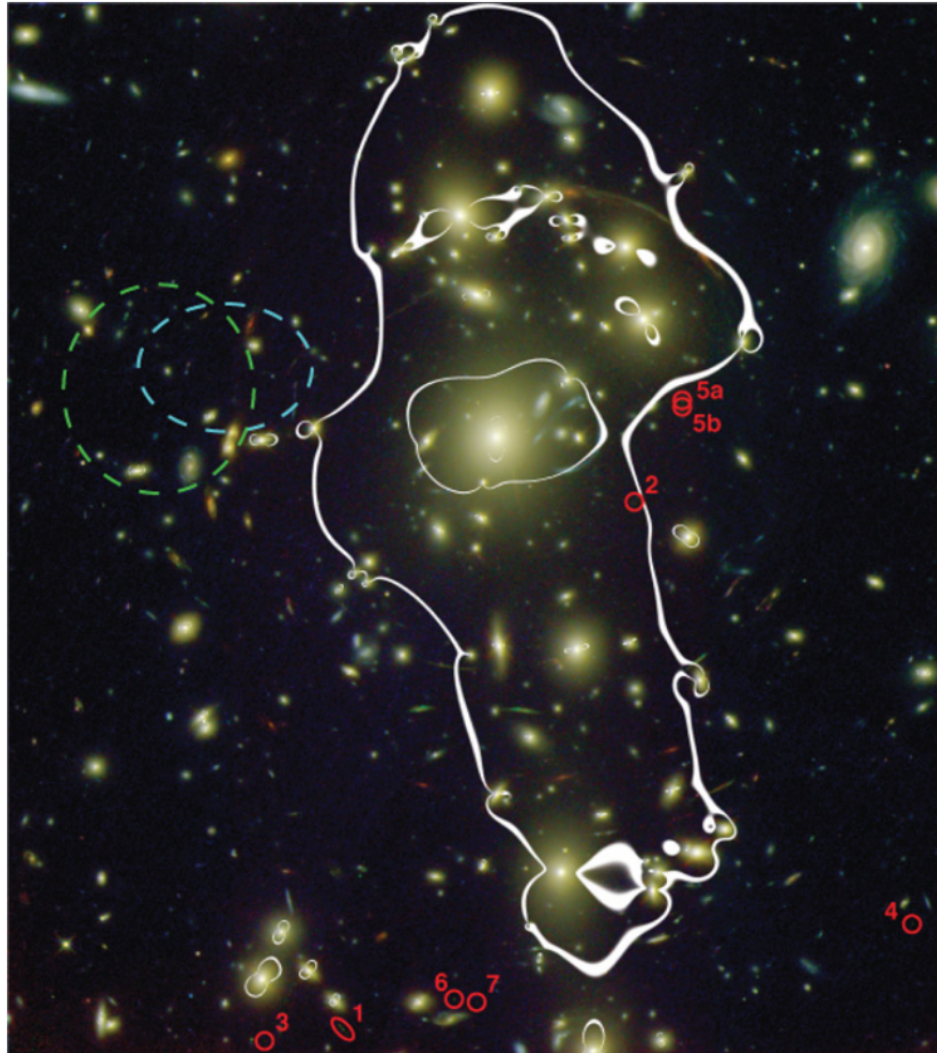


Figure 1.5: Example of a gravitational lens, the galaxy cluster Abell 1703 (at $z = 0.28$), taken from (Bradley et al., 2012). Circled in red are various lensed galaxies, where label 1 highlights the target presented in Chapter 2. The white contour indicates the critical curve for galaxies at redshift $z = 7$, where the magnification reaches > 100 . Credit: Bradley et al. (2012).

galaxy cluster Abell 1703, taken from Bradley et al. (2012). Highlighted in this figure, circled in red and labelled “1” is the galaxy Abell 1703-zD1. A study into this galaxy is presented in Chapter 2.

1.1.4 “Cosmic Noon”

From the formation of the first galaxies until around 3.5 billion years after the Big Bang, there was an increase in the cosmic star formation rate density (ρ_{SFR} , defined as the mass of stars that form per unit time in a given volume), reaching its peak at $z \approx 2$. This peak of star formation

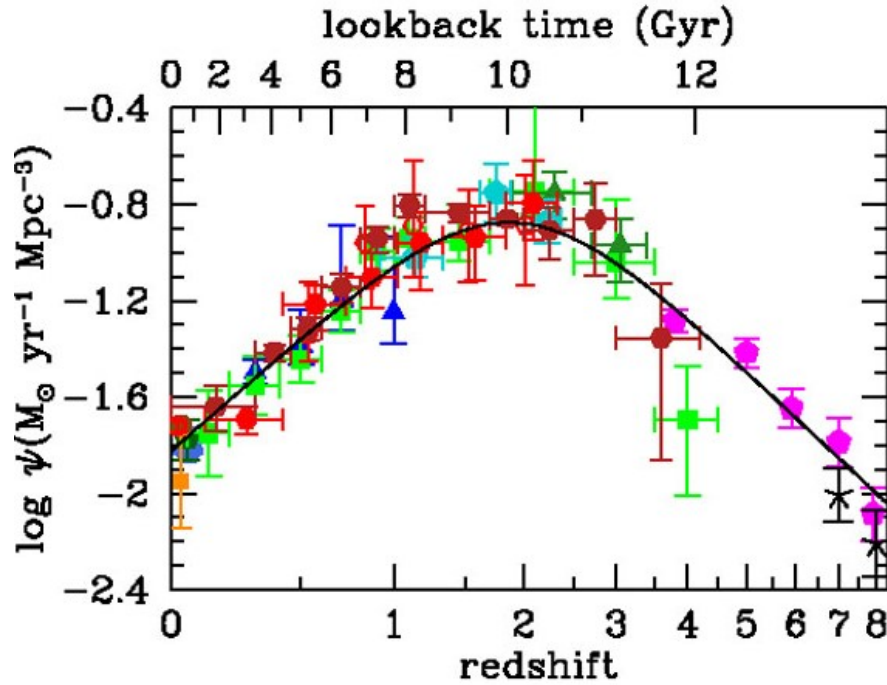


Figure 1.6: Figure to show the star formation history across cosmic time. The x-axis denotes the redshift as well as corresponding lookback time shown above the plot. The data presented is compilation from the literature and can be found in [Madau & Dickinson \(2014\)](#). There is a clear trend of increasing star formation rate density until $z \approx 2$, which then decreases until the present day at $z = 0$. Credit: [Madau & Dickinson \(2014\)](#). Different coloured symbols denote different studies at the various redshifts covered in this plot.

history is known as “Cosmic Noon” and typically refers to the redshift range $z = 1 - 3$. This increase in star formation rate density can be seen in [Figure 1.6 \(Madau & Dickinson, 2014\)](#). As a result, half of all stellar mass in the Universe formed by $z = 1$, corresponding to ~ 5 billion years after Big Bang ([Bundy et al., 2005](#); [Mortlock et al., 2011](#)). After this peak, the star formation rate density decreased until the present day. For these reasons galaxies at $z = 1 - 3$ are an exciting sample to study and they mark a useful turning point in galaxy evolution in the Universe, for comparison to both the first galaxies and the present day galaxy population.

These observations have led to a model of galaxy growth whereby stellar mass is governed by accretion, star formation and outflows, up to stellar masses of $\sim 10^{12} M_{\odot}$, where star formation quenches and galaxies become quiescent ([Dekel et al., 2009](#); [Peng et al., 2010](#); [Lilly et al., 2013](#)).

However, there are examples of local galaxies that are similar to their high- z counterparts, making these objects incredibly useful to study, as described in [Section 1.1.5](#).

1.1.5 The present day galaxy population

Galaxies at $z \approx 0$ are observed to have different properties to their high- z counterparts, and only by $z < 0.3$ do galaxies look similar to the present day population containing disks and ellipticals (Conselice, 2014). There are galaxies that look like classic ellipticals and spirals up to $z = 1$, but these are much rarer.

However, there are cases of local analogues which have similar properties to their high redshift counterparts, sharing properties such as high specific star formation rates (sSFRs) and compact galaxy sizes (Bian et al., 2016). There are green pea galaxies with similar ISM conditions and features such as strong broad [O III] lines (Cardamone et al., 2009; Steidel et al., 2014). Further, properties of Lyman break galaxies (see Section 1.1.3) are seen in some galaxies in the local Universe, matching in size, SFR, surface brightness, mass, metallicity, kinematics, dust, UV-optical color and prevalence of outflows (Overzier et al., 2008, 2009; Gonçalves et al., 2010; Heckman et al., 2011; Fisher et al., 2014). However, it has been noted that these similar properties do not necessarily replicate the ISM conditions of high redshift galaxies, (Shirazi et al., 2014), nonetheless, these similarities/differences are important to understand.

Thanks to their proximity, these galaxies are interesting to observe as they can be studied in greater detail and resolution, and therefore provide clues about the high- z galaxy population, but with a greater ease in observing them. Galaxies that are more local are naturally easier to study due to their proximity and therefore can be studied in much more detail. Resolved studies can be performed that are simply not possible for high- z galaxies, and so they can provide essential insights for the understanding of the inner workings of galaxies, from the star formation (e.g. star forming molecular clouds), and other structures within such as outflows and filaments.

This understanding of the physical processes can then be used to help understand and interpret the results of galaxies at higher redshift, where such detailed observations may not be possible. One particular component of galaxies which is vitally important for understanding the evolution of galaxies is the interstellar medium.

1.2 The interstellar medium

The interstellar medium (ISM) is the space between stars in galaxies, composed mainly of dust and gas. The gas in the ISM is comprised of different phases, namely hot ionised, warm ionised, warm neutral, cold neutral medium and molecular medium (McKee & Ostriker, 1977; Cox, 2005). Here I will introduce the warm ionised and molecular phase, as they are the most important for understanding the work presented in this thesis.

1.2.1 The warm ionised phase

The warm ionised phase of the ISM is gas that can trace the various feedback processes within a galaxy, i.e processes which produce the energy needed to ionise the gas. The feedback processes in galaxies come in several different forms ranging from active galactic nuclei, which can produce shocks and winds (e.g. Harrison et al., 2015) to stellar activity from massive OB stars (e.g. Heckman et al., 1990; Kewley et al., 2001; Ramachandran et al., 2019) and supernovae (McKee & Ostriker, 1977; Chevalier & Fransson, 1994). As it can trace these different feedback processes, it is vitally important to study the warm ionised phase of the ISM, providing insights into these fundamental processes that contribute to the evolution of galaxies.

Some of these feedback processes are also thought to be responsible for the reionisation of the Universe, such as from massive stars and AGN activity (e.g. Meiksin & Madau, 1993; Barkana, 2006; Ricotti & Shull, 2000). Understanding these ionisation processes are therefore critical to understanding the early period of the Universe and there are current efforts aiming to assess the relative importance of each process in the reionisation of the Universe up to $z \approx 6$ (see Section 1.1.2).

In addition, the warm ionised phase can produce bright lines that are observable at high- z . As mentioned in Section 1.1.3, [C II] is a bright line observable at high redshift, important for obtaining redshifts of high- z galaxies (e.g. Smit et al., 2018; Bakx et al., 2020; Fudamoto et al., 2022; Posses et al., 2023; Hygate et al., 2023). Observations of [O III] at these high redshifts are also incredibly useful for studying the prevalence of AGN activity in the early Universe (e.g. Inoue et al., 2016; Carniani et al., 2017; Hashimoto et al., 2019). This is because it can map high

velocity warm ionised gas (traced by broad ionised [O III] emission) which can be indicative of ionised outflows, making it an important line to study across cosmic time. Kinematic studies are therefore crucial to trace the impact of AGN on their host galaxy, for example, investigating how efficiently outflows can remove gas from the galaxy compared to the rate of star formation, known as the mass loading factor. Ionised outflows and AGN feedback are discussed further in Section 1.4.

In addition to studying the warm ionised phase, which is most common for studying AGN feedback processes, another way is to observe the cold phase of the gas. This area of research has been opened up by ALMA, and is important as this phase of the gas is the fuel for star formation and galaxy growth. In particular, here I will introduce the molecular gas content.

1.2.2 The molecular phase

The molecular gas is a critical component in galaxy evolution as this gas is redistributed to both promote star-formation activity and fuel BH growth (e.g. [McKee & Ostriker, 2007](#); [Kennicutt & Evans, 2012](#); [Bolatto et al., 2013](#); [Carilli & Walter, 2013](#); [Vito et al., 2014](#); [Tacconi et al., 2020](#)). It is therefore essential to analyse and characterise the properties of the molecular ISM in order to better understand galaxy formation and evolution.

Estimates of the cosmic molecular gas density suggest that the molecular gas fraction (the ratio between molecular gas mass and galaxy stellar mass) peaks at redshifts of $z = 1-3$ (see [Péroux & Howk, 2020](#), for a review), roughly mirroring the cosmic star formation rate density (see Section 1.1.4, Figure 1.6 and [Madau & Dickinson, 2014](#)) and black hole accretion density (e.g., [Aird et al., 2015](#)). This highlights the link between the cold gas and BH and galaxy growth.

H₂ is the most abundant state of molecular gas, and so would be the best tracer of the molecular gas. However, it is not observable due to a long decay time and weak emission. Therefore, the most common alternative is to observe low transitions of carbon monoxide (CO) as a tracer of H₂. Its low energy and ease to excite makes it a relatively easy way to observe the molecular gas phase of the ISM.

Knowledge of the ground state CO(1-0) line is a crucial reference that is often used to trace the total molecular gas content in galaxies. However, currently there is discussion in the community about how reliable the ground state is to accurately trace the total molecular gas content in different objects (e.g. star forming galaxies (SFGs) or (ultra) luminous infrared galaxies (U)LIRGs, see [Leroy et al., 2022a](#); [Montoya Arroyave et al., 2023](#)).

Observing CO can also open up the opportunity to study the excitation of molecular gas by mapping the CO Spectral Line Energy Distribution (CO SLED). Studies have investigated the driving mechanism for the excitation of the molecular gas (e.g. [Daddi et al., 2015](#); [Pozzi et al., 2017](#); [Mingozi et al., 2018](#); [Leroy et al., 2022b](#); [Esposito et al., 2022](#)), suggesting photodissociation regions (PDRs) and X-ray dominated regions (XDRs), of diverse temperature and gas densities, are the key physical components driving CO excitation.

Again, different samples of galaxies have shown different excitation levels. All this therefore increases the importance in characterising multiple transitions of CO across different samples to accurately determine the total molecular gas content as well as its excitation. In doing so we are also able to understand the impact of feedback processes such as stellar winds or AGN activity, where energy is transferred from these processes into the ISM (more in [Section 1.4.3](#)).

However, due to the expensive observations required to detect multiple emission lines for individual sources, most of our knowledge on molecular gas excitation is based on inhomogeneous coverage of few transitions, and limited to for the most luminous galaxies (e.g. [Kakkad et al., 2017](#); [Saintonge et al., 2017](#); [Lamperti et al., 2020](#); [Circosta et al., 2021](#); [Boogaard et al., 2021](#); [Valentino et al., 2021](#); [Harrington et al., 2021](#); [Leroy et al., 2022a](#)).

1.3 Line Emission Processes

As noted in [Section 1.2](#), it is useful to observe the ISM in different frequencies and to study different phases of the gas to gain a full understanding of ongoing processes in the galaxy. The emission lines that we observe and their properties (e.g. flux, velocity and location within the galaxy) give us an indication of the physical processes ongoing in the galaxy and these properties are dependant on the physics at the atomic and quantum level.

During this thesis the main emission lines discussed are [O III], [C II] and CO. Here I will present the background physics of the physical effects that give rise to these lines, that will aid in the interpretation of the results presented throughout this thesis.

1.3.1 Atomic energy levels

Atoms contain a nucleus in their centre which comprises of protons and neutrons, and surrounding this is a cloud of electrons. These electrons can reside in different, discrete energy levels, and which level they reside in is dependent on how much energy they have (or how “excited” they are).

However, these electrons don’t stay fixed in one energy level. An electron can be excited into a higher energy level via a transfer of energy during collisions with photons or another atom. Electrons can also move down energy levels via decay which usually occurs naturally over time. As they do so, energy is released in the form of a photon corresponding to the difference between the energy level it started at and the level it fell to. Decay can also occur during collisions where energy is taken away from the electron.

Most of the aforementioned natural decays happen relatively quickly and the emission released via these processes are known as permitted lines. However, some electrons decay with a very low probability and so only do so after a long period of time. In high density environments, where random collisions are common, there is a higher probability of decaying via collisions than decaying naturally. Therefore, in normal/high density environments these lines are not observed and are subsequently known as forbidden lines and are denoted by their square brackets (e.g. [O III] and [C II]). However, in low density environments, that can be found in the ISM, collisions are rarer, giving the electron more time to decay spontaneously, which is why there are circumstances in which we do observe these emission lines [Eddington \(1927\)](#).

The expected wavelength/frequency of line emission from a decaying electron is a single value. However, due to the uncertainty principle the lines we measure are broadened slightly. Forbidden lines are narrower than permitted lines as a result of the long time periods over which they decay, making their energy more certain. Knowing the expected energy (and therefore corresponding frequency/wavelength) is a vital tool in extragalactic astronomy. Due to the fact that

the Universe is expanding, when we measure these emission lines from extragalactic sources, we can accurately measure the distance to them based on how much the light has been shifted (stretched) from its rest frame wavelength as the source travels away from us. This therefore provides a useful tool for analysing the first galaxies to form in the Universe and to accurately take follow up observations.

In addition to the quantum level effect, other external factors can also increase the level of emission line broadening. Kinematics plays an important role in this, and analysing the line profiles in detail can be an incredibly useful tool. Due to the rotation of a galaxy, parts of the galaxy are moving towards us, and other parts moving away from us (Dalcanton et al., 1997). This leads to an increased range of velocities (and therefore also frequency) that are measured across the galaxy. Therefore, as we take a spectra of the whole galaxy we would see a broader emission line and the broader the lines, the largest the velocities at play. Therefore, if the gas is rotating very quickly, e.g. at the centre of a galaxy around a black hole, the emission lines measured can have very broad lines (Peterson & Wandel, 1999; Kauffmann et al., 2003). One such example is [O III] λ 5007, a doubly-ionised oxygen atom, meaning that it has had two electrons knocked out of the atom. Removing two electrons from the atom requires a significant amount of energy, and therefore is an indication of ongoing, high energy processes such as AGN activity (more in Section 1.4.1). [O III] is also a forbidden line, and so also suggests that low density environments are also present in AGN. Further, observations have shown very broad emission lines as well as outflows (e.g. Mullaney et al., 2013; Harrison et al., 2014; Villar-Martín et al., 2017; Ciccone et al., 2021, also see Chapter 3).

1.3.2 Molecular energy levels

In molecules (such as CO) there are energy levels referring to processes on the quantum level, specifically the vibrational or rotational energy levels. The vibrational energy is the frequency at which the molecule oscillates whereas the rotational energy levels depend on the geometry of the molecule. Those with non-linear geometry can have rotational energy which are a function of three principal moments of inertia around three axes a, b and c, which are perpendicular to each other and their origin lies at the centre of mass of the molecule (Schulz, 1973).

Of particular relevance to this thesis is the carbon monoxide molecule (CO), a molecule consisting of one carbon atom and one oxygen atom. Due to the possible rotational energies of CO, we measure CO lines at incremental frequencies of $\sim 115.3\text{GHz}$. For example, we measure CO(1-0) (corresponding to the first CO line with a quantum number $J = 1$) at $\sim 115.3\text{GHz}$. Following this we have CO(2-1) at $\sim 230.5\text{GHz}$ corresponding $J = 2$ and so on.

A higher quantum number means that the number of principal electronic shells is greater, causing a larger distance between the farthest electron and the nucleus and therefore a higher excitation. If we observe a larger amount of higher CO lines (with a higher quantum number) relative to the lower J_{CO} lines, it means that the gas as a whole is more excited. A method of measuring the excitation of the gas is to observe the line ratios (the ratio of brightness temperature between the CO lines, see for example: [Greve et al., 2014](#); [Saintonge et al., 2017](#); [Valentino et al., 2021](#); [Leroy et al., 2022a](#); [Montoya Arroyave et al., 2023](#)). Higher excitation levels occur when the temperature and density of the environment are higher. An excitation level known as “thermalised” only occurs when the temperature or density is high enough to reduce the quantum effects to effectively zero.

These emission line ratios can also be affected by optical depth effects, referring to the level of transparency. CO is generally optically thick, which would produce r_{21} line ratios of $0.5 - 1.0$ with the value reflecting the temperature and density of the gas ([Leroy et al., 2009](#)). However it can be optically thinner in regions of turbulence, for example in winds or outflows ([Zschaechner et al., 2018](#)). This may be particularly relevant in the case of studying AGN/quasars. As a general rule, $r_{21} > 1$ indicates warm, optically thin gas. Changes in temperature and density and/or the presence of multiple gas components can change the observed line ratios, but within the expected typical ranges, the assumption is that $r_{21} \approx 1$ ([Eckart et al., 1990](#); [Leroy et al., 2009](#)).

Like with the ionised gas, the same broadening and shifting of lines due to velocity also applies to the molecular lines we observe (as mentioned in Section 1.3.1). These analysis techniques are again used in Chapter 4 to investigate the properties of CO in a sample of quasars.

1.4 AGN and quasars

The centres of all massive galaxies are thought to host supermassive black holes. Various works in the early 1900s had started to target the nuclei of galaxies, and identified strange emission lines as well as a radio jet in M87 (e.g. [Fath, 1909](#); [Curtis, 1918](#)). Later, studies by Carl Seyfert connected the bright nuclei in galaxies to be the sources of the unusually broad emission lines ([Seyfert, 1943](#)). These objects then became known as Seyfert galaxies following this pioneering work.

Further studies showed that most, if not all, galaxies hosted massive black holes in their centre ([Lynden-Bell, 1969](#)), and that accretion onto the black hole did indeed provide the power for the broad emission lines seen in nearby Seyfert galaxies. Not long after came the discovery of a radio source in centre of Milky Way, showing evidence of black hole at the heart of our own galaxy ([Lynden-Bell & Rees, 1971](#)). The black hole in the centre of the Milky Way, known as Sagittarius A*, had much weaker radio and X-ray emission than had previously been observed, showing there was also a range of luminosity and activity level in galactic nuclei.

In recent years there has been more direct evidence (as direct as can be with black holes). Analysis of the orbits of stars around the Galactic centre of Milky Way showed the necessity for a very massive, but invisible, compact object around which the stars were orbiting ([Schödel et al., 2002](#); [Ghez et al., 2008](#); [Gillessen et al., 2017](#); [GRAVITY Collaboration et al., 2018](#)). Finally, the most direct evidence to date has been the observations with the Event Horizon Telescope (EHT) of both the galactic centre of the Milky Way and M87, providing observations of the supermassive black hole “shadow”, and a ring of light which is bent by the powerful gravity of the black hole (e.g. [Event Horizon Telescope Collaboration et al., 2019, 2022](#)). These also match the theoretical predictions of general relativity for such an object.

Therefore, with the presence of these supermassive black holes at the hearts of galaxies, this raises questions about their influence and role in the evolution of galaxies. In particular, the case of active galactic nuclei is a crucial phenomenon to study.

1.4.1 What makes an AGN?

As mentioned above, supermassive black holes lie at the centres of massive galaxies, but some of these black holes are growing by accreting material from an accretion disk see Figure 1.7. The sites of growing supermassive black holes are observationally identified as “active galactic nuclei”, or AGN, due to the large amounts of energy they release across the electromagnetic spectrum, which can easily outshine the stellar emission of the entire galaxy, despite arising from very compact scales. As a result, they can be luminous in most of the electromagnetic spectrum, but sometimes across the entire electromagnetic spectrum. The most powerful and highly accreting of these AGN are known as quasars.

There are several classifications of AGN, which are usually determined by how they were first identified. For example, radio AGN are bright in the radio (typically split into radio-loud and radio-quiet). There are also Seyfert galaxies which are spiral galaxies that have a strong nuclear emission, as well as blazars which are bright gamma ray sources. The activity of these sources can vary across the electromagnetic spectrum, but the important point is that they are luminous due to the activity of the AGN.

Despite these different classifications and nomenclature, there is a unified model of AGN, the structure of which can be seen in Figure 1.7. In the centre lies the supermassive black hole which is surrounded by an accretion disk, an optically thick region of dust and gas, closely orbiting around the black hole, and from which the black hole feeds and grows (Shakura & Sunyaev, 1973). Further out from the centre is an obscuring torus of dust and gas (Krolik & Begelman, 1988). Also labelled in Figure 1.7 are the narrow and broad line regions, corresponding to regions where narrow and broad spectral lines are observed respectively. Radio jets can also be present in these systems (which are of particular relevance to this thesis, see Section 1.4.3) but are not universal in AGN.

From this model it is clear that depending on the angle at which you are observing the AGN, you might observe different regions. Indeed, AGN are also categorised as Type 1 or Type 2 which is dependent on this viewing angle, and is an important consideration when analysing AGN and their host galaxy properties. Type 1 AGN are those which are viewed face on and so the nucleus is visible where both broad ($> 1000 \text{ km s}^{-1}$) and narrow emission line regions ($< 1000 \text{ km s}^{-1}$) are visible. The very broad lines observed imply that they are moving at high velocity around

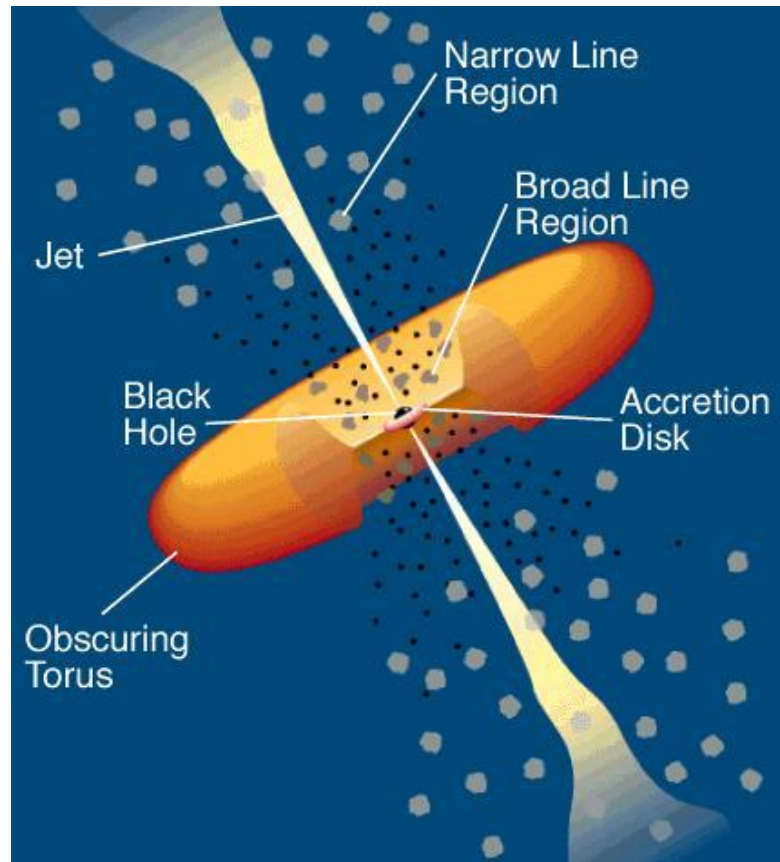


Figure 1.7: A schematic diagram showing the structure of AGN (adapted from [Urry & Padovani, 1995](#)). In the centre is the black hole surrounded by the accretion disk. Further out is the dusty torus, which obscures this centre. The broad line region and narrow line region are also labelled. Jets can also be present, being launched from the very central region, but are not universal in AGN. Credit: [Urry & Padovani \(1995\)](#).

the central supermassive black hole. These broad lines are also known to be forming in regions of high density located close to the central black hole, since we only observe the permitted line transitions, and not the forbidden lines (as discussed in Section 1.3).

On the other hand, Type 2 AGN are viewed edge on and so the broad line region is obscured by the dusty torus, therefore only narrow emission lines are visible. These narrow lines are formed in the low density clouds of gas outside of the nuclear region. Further, the stellar emission observed in Type 2 AGN is similar to normal star forming galaxies ([Bongiorno et al., 2010](#)).

This forms part of the AGN unified theory where AGN have the same structures but differences can arise in observations due to how they are observed and, in particular, the viewing angle.

AGN can be selected and identified in various ways. Perhaps the most unbiased way is through X-ray selection due to the emission being highly unlikely to be contaminated by host galaxy

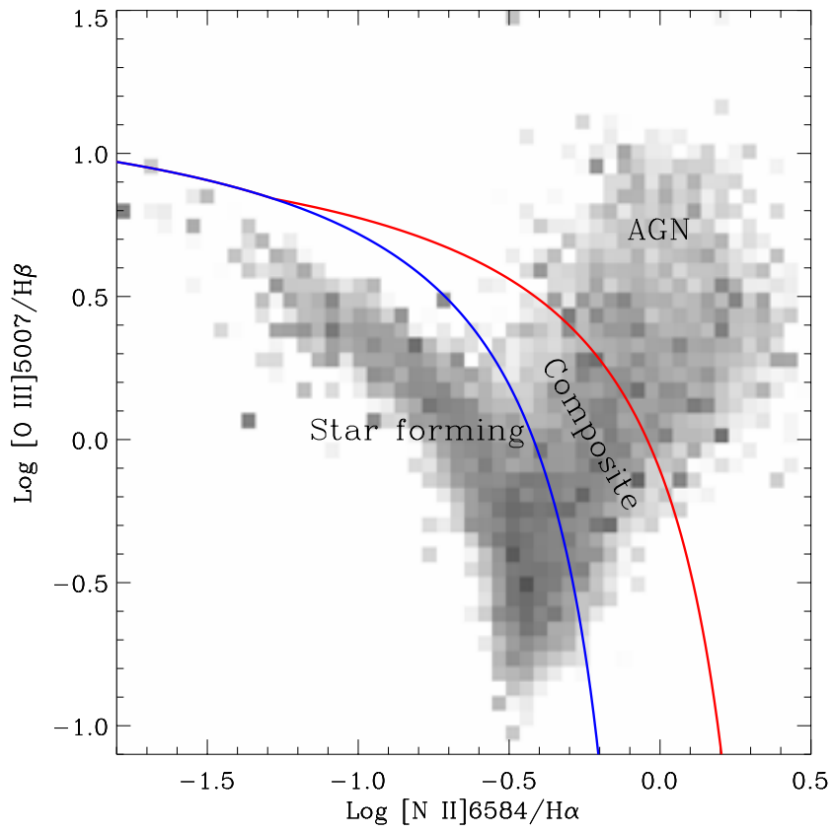


Figure 1.8: Example of a BPT diagram showing the excitation of gas and the parameter space in which different galaxies reside, with star forming and AGN forming the two main regions going from low to higher excitation, with a transition period in between labelled as composite. Credit: [Brinchmann et al. \(2004\)](#).

which emit at lower energies ([Brandt & Hasinger, 2005](#); [Brandt & Alexander, 2015](#)), although soft X-rays can be absorbed by high gas column-densities in highly-dust-obscured AGN. Being highly luminous in other parts of the electromagnetic spectrum can also be an identifier of AGN, e.g. [O III] or radio luminosity.

Another common method is to select AGN using optical data, looking at the excitation of gas/elements using a “Baldwin, Phillips & Terlevich” (BPT) diagram (see [Figure 1.8](#); [Brinchmann et al., 2004](#); [Kewley et al., 2006](#)). The BPT diagram for a classification between AGN and star forming galaxies (SFGs), due to the different ionising source responsible for their emission lines: whether from the AGN or by hot massive stars (for normal SFGs).

AGN play a key role in the evolution of galaxies as they co-evolve with their host galaxy. Cosmological models and simulations of galaxy evolution require some fraction of the released energy from AGN activity to couple to the surrounding interstellar medium (ISM) in order to reproduce the observed properties of massive galaxies and the surrounding intergalactic medium

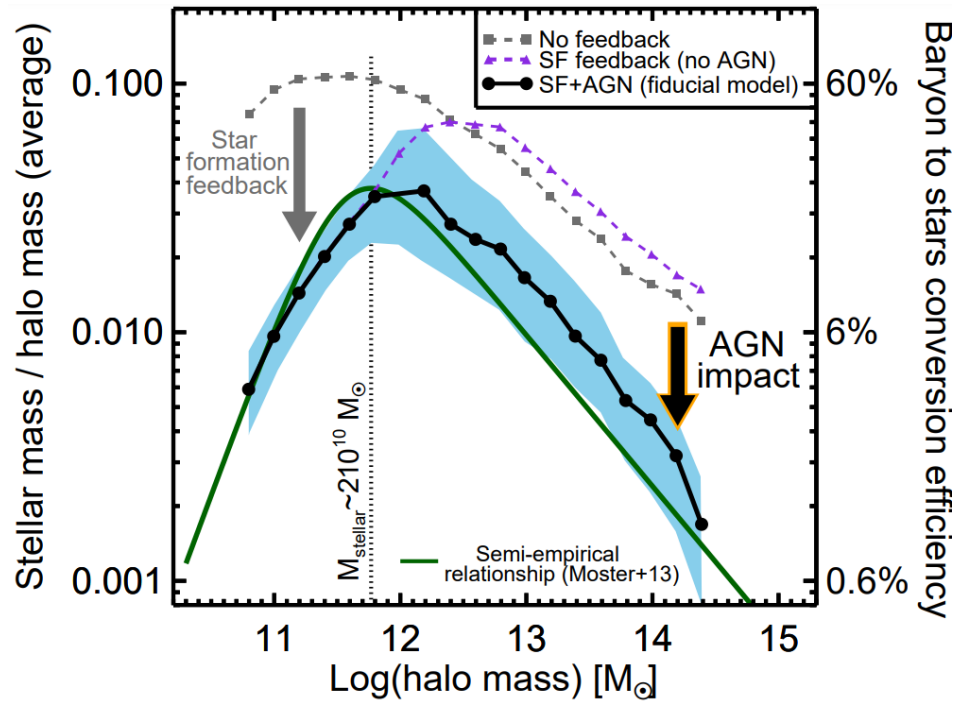


Figure 1.9: Plot to show halo mass versus stellar mass/ halo mass (tracing the fraction of baryons in the form of stars). This shows the semi-empirical relationship in green (Moster et al., 2013), then three models from simulations (Somerville et al., 2008) in grey (with no feedback included), purple (with just star formation feedback included) and black (with both star formation and AGN feedback). These models show the necessity to include AGN feedback to reproduce the observed galaxy populations. Credit: Harrison (2017).

(IGM, e.g. Bower et al., 2006; Vogelsberger et al., 2014; Hirschmann et al., 2014; Schaye et al., 2015; Crain et al., 2015; Beckmann et al., 2017; Choi et al., 2018, also see Figure 1.9).

Understanding the connection between galaxy growth and the growth of their central supermassive black holes remains one of the biggest outstanding problems of galaxy evolution research (Alexander & Hickox, 2012; Kormendy & Ho, 2013; Heckman & Best, 2014; King & Pounds, 2015; Harrison, 2017; Cresci & Maiolino, 2018). Analysis of wide samples of AGN, their feedback processes and their impact on the host galaxy are vital to address these outstanding questions.

1.4.2 AGN feedback

Galactic feedback processes are thought to regulate the observed co-evolution of accreting black holes and their host galaxy that is observed across cosmic time (e.g., Madau & Dickinson, 2014; Kormendy & Ho, 2013), but our understanding is still in its infancy.

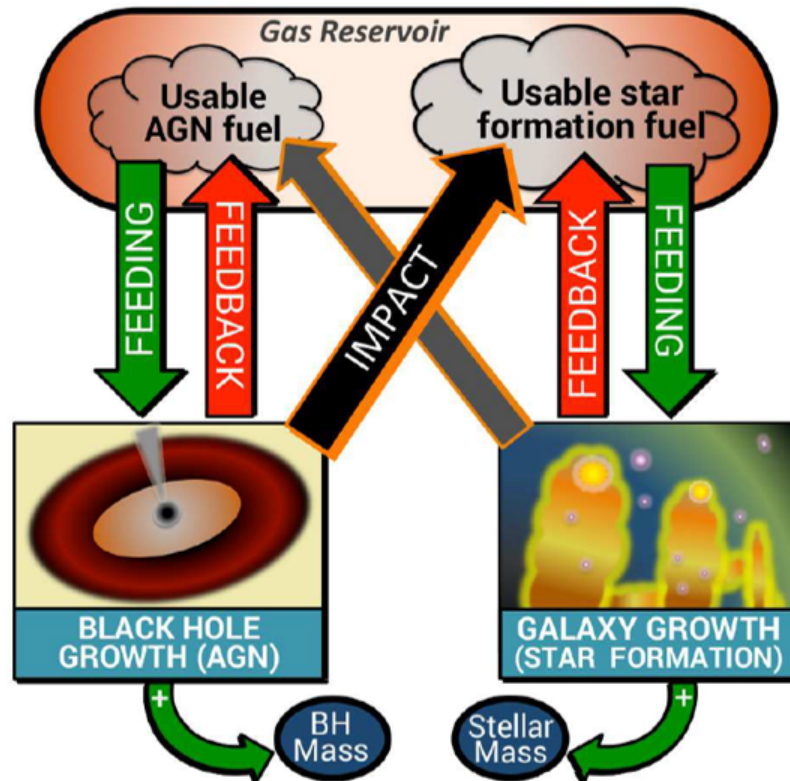


Figure 1.10: Figure to show the connection between galaxy evolution and supermassive black hole growth. Growing supermassive black holes at the centres of galaxies co-evolve with their host galaxy and are linked via feedback processes driven both by the AGN and by stars. These feedback processes impact on the gas reservoir which can be used to fuel star formation as well as the growth of the black hole via accretion. Credit: [Harrison \(2017\)](#).

Observational and theoretical studies have proposed both a suppression ([Silk & Rees, 1998](#); [Hopkins et al., 2006](#); [Booth & Schaye, 2010](#); [Feruglio et al., 2010](#); [Cicone et al., 2014](#); [King & Pounds, 2015](#); [Fiore et al., 2017](#); [Costa et al., 2018](#); [Ellison et al., 2021](#); [Bertemes et al., 2023](#)) and an enhancement of star formation in AGN host galaxies ([Ishibashi & Fabian, 2012](#); [Silk, 2013](#); [Zubovas et al., 2013](#); [Lacy et al., 2017](#); [Fragile et al., 2017](#); [Gallagher et al., 2019](#)). However, these interactions are still not fully understood and the diversity of results stress the need for multiwavelength, multi-tracer studies to characterise the interplay between the central supermassive black hole BH and the host galaxy. A schematic outline of this relationship can be seen in [Figure 1.10](#). The gas within the host galaxy can feed the black hole via accretion, whilst also being the fuel for star formation. Further, feedback processes, both stellar and AGN driven, can have an impact on the gas reservoir, therefore highlighting this link. Of particular interest in the gas reservoir is the molecular gas, as this is the fuel for star formation in these galaxies, and so analysing its relation to feedback properties is an important avenue of research.

In a simplified view, there are two major modes of AGN feedback processes that have been

identified. The first is ‘quasar or radiative mode’, associated with high black hole accretion rates, and the second is ‘radio or mechanical mode’, associated with low accretion rates typically exhibiting large radio jets. However, evidence now suggests these two modes might not be well separated and radio jets could also be an important feedback mechanism in radio-quiet quasars (Jarvis et al., 2019, 2021). See Section 1.4.3 for more on the role of radio emission in AGN feedback.

One observational strategy to uncover the connection between supermassive black hole growth and galaxy evolution is to identify, and to characterise, AGN-driven outflows in the multi-phase ISM (e.g. Veilleux et al., 2005; Morganti et al., 2005; Carniani et al., 2015; Perna et al., 2015; Brusa et al., 2015; Balmaverde et al., 2016; Rupke et al., 2017; Lansbury et al., 2018; Fluetsch et al., 2019; Ramos Almeida et al., 2019). These outflows are observed to be both multi-phase and multi-scale in nature, ranging from nuclear scales (< 1 pc) to the scales extending across the entire galaxy and beyond (> 10 kpc) (Cicone et al., 2018a).

Of most relevance for this thesis and the work presented in Chapter 3 is the presence of broad and-or asymmetrical [O III] λ 5007 emission-line profiles which have long been used to trace outflows of warm ($\approx 10^4$ K) ionised gas (Heckman et al., 1984; Whittle, 1985). This is a particularly useful outflow tracer because, through large optical spectroscopic surveys such as the Sloan Digital Sky Survey (SDSS; York et al., 2000), measurements on large samples of $z \lesssim 0.8$ AGN can be obtained (e.g., Mullaney et al., 2013; Zakamska & Greene, 2014; Zakamska et al., 2016; Balmaverde et al., 2016; Woo et al., 2016). Recent and on-going near-infrared spectroscopic surveys make it possible to obtain similar constraints on large samples of $z \approx 1 - 3$ galaxies (e.g., Harrison et al., 2016; Leung et al., 2017; Förster Schreiber et al., 2019a).

In high redshift studies, signs of extended [C II] emission (Matthee et al., 2019; Fujimoto, 2019; Carniani et al., 2020) as well as broad [O III] emission lines (Inoue et al., 2016) have been observed, both possibly related to galactic feedback processes. With the launch of JWST and the recent data for very high- z galaxies and AGN, the ability to perform these observations is enhanced (e.g. Maiolino et al., 2023). These observations, as well as current low and intermediate redshift studies, will enable the analysis and interpretation of AGN feedback across cosmic time. One particular process of interest which can be studied in detail in the local Universe is the role of radio jets in AGN feedback.

1.4.3 The role of radio jets in AGN and their effect on the interstellar medium

Traditionally AGN can be labelled as radio-loud or radio-quiet, where the radio loudness is defined as the ratio between the radio and the optical fluxes at 5GHz and 4400Å respectively. AGN are considered radio-loud if this ratio is greater than 10 and radio-quiet if less than 10 (Kellermann et al., 1989; Wilson & Colbert, 1995). With the advent of deeper radio data, increasing evidence is being found of potentially ubiquitous low-level radio emission in radio-quiet quasars (e.g. Jarvis et al., 2019, 2021; Macfarlane et al., 2021). However, despite a classification of radio-quiet, works have shown that they can still have a significant impact on their host galaxy (e.g. Jarvis et al., 2019; Girdhar et al., 2022).

In quasars that are radio-quiet, it is often assumed that the dominating radiative power of the central source drives the observed galactic outflows (e.g., Faucher-Giguère & Quataert, 2012; King & Pounds, 2015). However, studies highlighting an observed relation between outflows and radio emission opens up the possibility that the mechanical power of radio jets may be a crucial mechanism in driving the observed outflows (e.g., Mullaney et al., 2013).

Studies into AGN with radio jets (which is a form of mechanical feedback) have shown the interplay between radio activity and their host galaxies (e.g. Jarvis et al., 2019; Couto & Storchi-Bergmann, 2023). These radio jets are observed in both young and evolved stages but there are outstanding questions on how/when these jets can couple to the interstellar medium (ISM), and have a positive and/or negative impact on the star-forming molecular gas content (e.g. Silk, 2013; Gabor & Bournaud, 2014; Bieri et al., 2016; Costa et al., 2018). Further, recent work has shown the first direct evidence of a jet being physically linked to the central supermassive black hole (Lu et al., 2023).

As described above, ionised outflows are an indication of AGN feedback processes. These outflows can be observationally identified by a broadening of the spectral line. Previous studies have suggested a close relationship between the radio emission in AGN and the properties of the ionised phase of the ISM. It has been shown that AGN with higher radio luminosities are more likely to have larger $\text{FWHM}_{[\text{O III}]}$ (e.g. Mullaney et al., 2013; Villar Martín et al., 2014; Zakamska & Greene, 2014; Hwang et al., 2018), suggesting a relation between the radio emission and the kinematics of the ionised gas. One of these results is highlighted by Figure 1.11 taken from

Mullaney et al. (2013) and indicates a link between the radio properties and the ability to drive high velocity ionised outflows.

Indeed, from low-power AGN through to the most extreme sources, radio jets are seen to interact with the ISM (e.g., Whittle et al., 1986; Ferruit et al., 1998; Tadhunter et al., 2014; Riffel et al., 2014; Kharb et al., 2017; Nesvadba et al., 2017; Morganti et al., 2018; Jarvis et al., 2019; Morganti et al., 2021; Girdhar et al., 2022). Furthermore, the relationship between outflows and radio emission, may even be strongest for traditional “radio-quiet” AGN with moderate, $\log[L_{1.4\text{GHz}}/\text{W Hz}]^{-1} \approx 23 - 25$, radio luminosities (e.g., Mullaney et al., 2013; Zakamska et al., 2016; Jarvis et al., 2019). These observations suggest that radio jets are potentially an important feedback mechanism in radio-quiet quasars.

A natural assumption may be that the most powerful and luminous AGN and quasars will have the largest impact on their host galaxy. Indeed, studies suggest that they are able to drive kpc-scale outflows across the entire galaxy and disrupt the interstellar star-forming gas (e.g. Ciccone et al., 2012; Harrison et al., 2014; Feruglio et al., 2015; Circosta et al., 2018; Longinotti et al., 2023). However, studies at low redshift have also shown that AGN and quasars tend to live in gas-rich host galaxies and find no instantaneous depletion of the total gas content (Saintonge et al., 2017; Shangguan et al., 2020; Jarvis et al., 2020; Koss et al., 2021). These findings also agree with recent simulations (e.g. Piotrowska et al., 2022; Ward et al., 2022), supporting the idea that large gas reservoirs are needed to fuel the accreting supermassive black holes in quasar and AGN host galaxies.

On the other hand, star-formation driven outflows and quasar winds that shock the ISM provide alternative possibilities for producing the observed radio emission and correlation with outflow properties (e.g., Condon et al., 2013; Nims et al., 2015; Zakamska et al., 2016; Hwang et al., 2018; Panessa et al., 2019). In addition, other studies do not find such a relationship, but it should be noted that they can suffer from a relatively high radio detection limit; for example the study of Wang et al. (2018) is limited to radio luminosities of $\log[L_{1.4\text{GHz}}/\text{W Hz}]^{-1} \gtrsim 24$.

Aside from a kinematic impact on the ISM, radio jets can also have an impact on the gas excitation, with a focus on the molecular ISM. In simulations radio jet-ISM interactions have shown a *local* impact on the surrounding ISM even if global feedback signatures may not be clearly

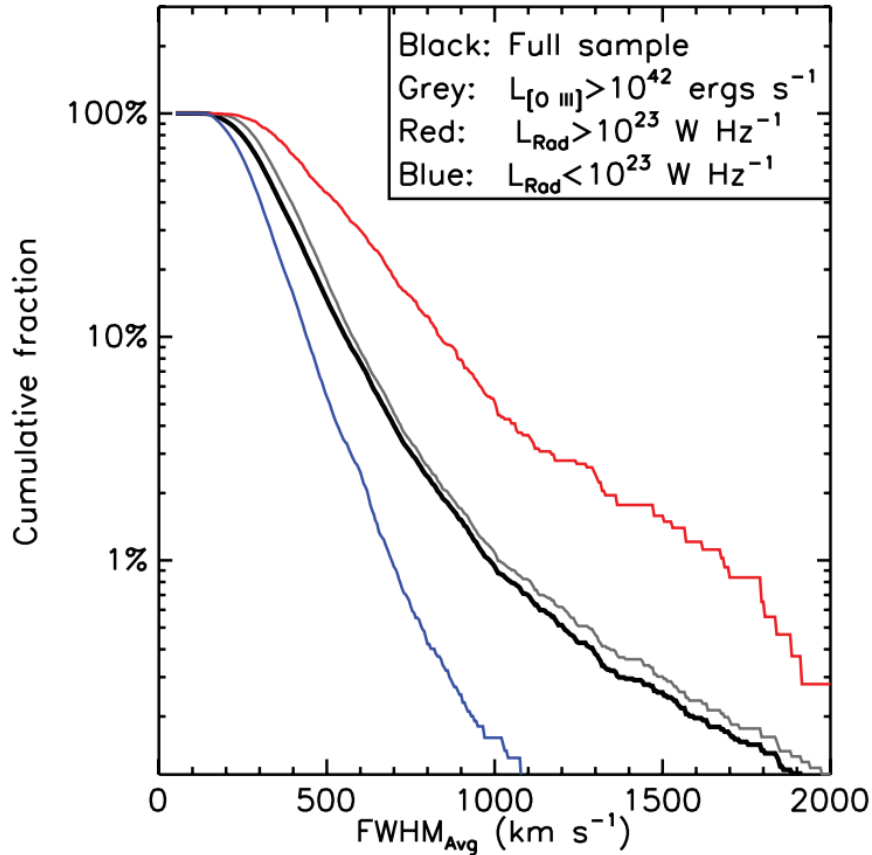


Figure 1.11: Figure to show the correlation between radio luminosity and FWHM of [O III]. Higher radio luminosities more likely to have broader [O III] lines, highlighted here by the difference between higher radio luminosities (shown in red) compared to the lower radio luminosities (shown in blue). Credit: [Mullaney et al. \(2013\)](#).

evident, especially in radio-quiet AGN ([Mukherjee et al., 2018b](#)). Observationally, no consensus has yet been reached on the impact of AGN on the overall molecular gas content in the ISM ([Kakkad et al., 2017](#); [Perna et al., 2018](#); [Kirkpatrick et al., 2019](#); [Rosario et al., 2019](#); [Circosta et al., 2021](#); [Morganti et al., 2021](#)). It may therefore be the case that in radio-quiet quasars the impact from feedback is limited to a more localised scale and the global properties of the ISM are left largely unaffected. There are recent works which support this and show the impact of AGN feedback on the excitation of the molecular gas content in central/localised part of the galaxy (e.g. [Oosterloo et al., 2017](#); [Audibert et al., 2023](#)). An example of enhanced excitation of carbon monoxide (CO) around radio jets is shown in [Figure 1.12](#) where it is clear there is a correlation between excitation and the location of the radio emission. There are however outstanding questions as to what is the range of this impact and whether excitation of CO is seen across the host galaxy.

An important consideration is also the time scales over which any impact of feedback may

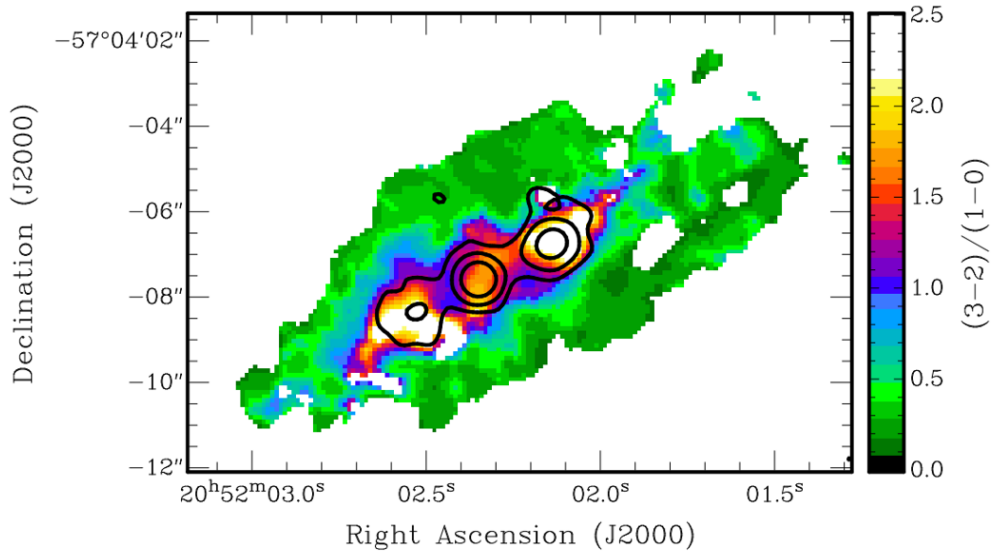


Figure 1.12: Example of enhanced CO excitation around radio jets in IC 5063. Black contours trace the radio jets in the central region of the galaxy. The CO excitation is traced by the line ratio of CO(3-2) and CO(1-0), which is concentrated around the radio jets and the extent is limited to these regions. Credit: [Oosterloo et al. \(2017\)](#).

take place ([King et al., 2011](#); [Mukherjee et al., 2018b](#); [Zubovas, 2018](#); [Ward et al., 2022](#)). For example, depletion times for outflows ([Cicone et al., 2014](#)) and cooling rates ([Costa et al., 2014](#)). Especially if these are young jets, it may take time for them to influence the wider ISM and hence why the impact observed is more local. Comparisons should therefore be made in sources with a range of radio sizes and jet structures. Comparisons to sources without radio jets should also be investigated as a control group to ensure that the observed excitation is indeed as a result of radio jet feedback and not other processes.

Models of CO excitation also suggest that AGN-related processes, such as X-ray emission ([Meijerink et al., 2007](#)) and shock heating induced by AGN jets and outflows ([Kamenetzky et al., 2016](#)), would mainly affect the molecular gas excitation at the higher CO transitions. It is therefore crucial to study both low and high CO transitions as the impact of feedback may only be present at higher CO excitation ($J_{up} > 5$). This is challenging at low redshifts ($z < 0.2$), where even using the maximum frequency limit of the ALMA bands, only $J_{up} \leq 8$ can be reached. Due to the observational difficulty of observing at higher frequencies, there are few examples of these critical higher CO transitions observed at low- z (e.g. [van der Werf et al., 2010](#); [Greve et al., 2014](#); [Rosenberg et al., 2015](#); [Liu et al., 2015](#); [Kamenetzky et al., 2016](#); [Yang et al., 2017](#)). Indeed, most $J_{up} > 7$ observations come from higher redshift ($z > 1$), highly luminous quasars, which are far more easily observed ([Carilli & Walter, 2013](#); [Wang et al., 2019](#); [Yang et al., 2019](#);

Li et al., 2020; Pensabene et al., 2021; Decarli et al., 2022), which in turn lack observations of low-J transitions, consequently lacking a complete characterisation of the molecular gas content and excitation.

Mapping CO transitions and analysing its relation to highly energetic and feedback processes, such as radio jets and outflows, is therefore an important avenue of research to understand these processes. To achieve these studies we require high quality observations from sub-mm observatories.

1.5 Sub-mm observatories

The work in this thesis has been done through multiwavelength observations across cosmic time. These have included those in the optical such as the Sloan Digital Sky Survey (SDSS [Abazajian et al., 2009](#)), the radio surveys FIRST ([Becker et al., 1995](#)) and NVSS ([Condon et al., 1998](#)) and further radio observations from the Very Large Array (see Chapter 3 for work including these studies). In addition however, a large part of this thesis has been done using observations in the sub-mm. Observations at sub-mm wavelengths can be a useful probe both in high-redshift observations and of more local objects. For this reason, here I will introduce the telescopes and types of observations that were performed as part of this thesis.

Observations at mm/sub-mm wavelengths require stable weather conditions and low water vapour, and so observatories at high altitudes in dry environments are most ideal. However, there are challenges of atmospheric transmission which restricts our ability to observe certain emission lines at certain redshifts if they fall into low transmission regions (see Figure 1.13, [Maiolino, 2008](#)).

As with all telescopes a large collecting area is desired, either by large aperture single dish telescopes, or by many smaller antennae working together as an interferometer. Both single dish telescopes and interferometers have benefits and drawbacks and so there is a necessity for both types of observatory to meet the variety of observational studies required by the astronomy community. Single dish telescopes are useful for blind studies, as well as studying diffuse,

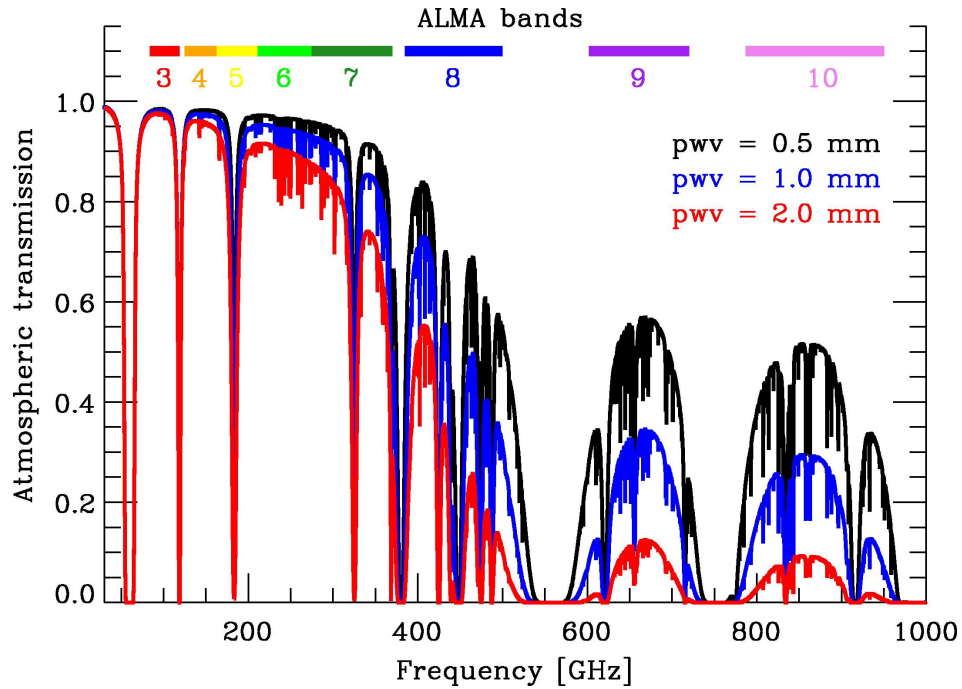


Figure 1.13: Atmospheric transmission across mm and sub-mm wavelengths (here shown by their frequencies instead of wavelength). The atmospheric transmission is also shown at different water vapour levels from 0.5 to 2 mm. Coverage of ALMA bands are also shown, highlighting the choice of ALMA to cover the frequencies which are most transmissible. Credit: [Maiolino \(2008\)](#).

low luminosity emission. On the other hand, interferometers are very powerful for follow up observations where high resolution and sensitivity is required.

As a result, in the work presented throughout this thesis both single dish and interferometers have been utilised, and therefore I introduce the facilities utilised in the following section.

1.5.1 APEX

The Atacama Pathfinder EXperiment telescope (APEX, see Figure 1.14) is a single dish, 12-metre diameter sub-mm telescope located on the Chajnantor plateau in the Atacama desert, Chile. It is currently fitted with several instruments covering frequency range 150 – 850 GHz enabling observations of the emission produced by the cold dust and gas both within the Milky Way and from extragalactic sources.

A single dish allows APEX to provide excellent observations of diffuse gas, and unresolved total gas observations of extragalactic sources. For example, performing studies of molecular

gas content in local targets (e.g. [Montoya Arroyave et al., 2023](#)) and studies of CO and [C II] in high- z AGN have been undertaken with APEX (e.g. [De Breuck et al., 2022](#)).



Figure 1.14: Atacama Pathfinder EXperiment telescope (APEX). Credit: S. J. Molyneux.

Observations from APEX were used for the work presented in Chapter 4, observing the total molecular gas content in quasar host galaxies.

1.5.2 ALMA

The Atacama Large Millimeter/submillimeter Array (ALMA, see Figure 1.15) is an interferometer array of 66 dishes located on the Chajnantor Plateau, in the Atacama desert, Chile. 54 of these dishes are 12 metre in diameter and 12 dishes are 7 metre in diameter. As a result of the number and size of these antennae, ALMA is the largest ground-based facility for observations in the millimeter/submillimeter regime.

The antennae can be moved around the plateau to change configurations for different types of observation. Depending on the configuration of the array and the observing frequency (ranging between 35 – 950 GHz), resolutions between a few milliarcseconds to 5 arcsec are possible.

This makes ALMA a versatile and incredibly useful tool for many scientific areas of research. In particular, ALMA has proved vital in spectroscopic redshift confirmation and observations of high redshift galaxies into the epoch of reionisation (e.g. [Hashimoto et al., 2018](#); [Smit et al., 2018](#); [Fujimoto, 2019](#); [Ginolfi et al., 2020a](#)). In the more local Universe, ALMA can also be used to resolve structures and kinematics of molecular gas.

As part of these configurations is a mostly fixed configuration of antennae known as the Atacama Compact Array (ACA). This consists of twelve 7 metre antennas and four 12 metre antennae. Due to being more compact than the total array, observations from the ACA are better suited to studying extended structures that are at risk of being over resolved by the full array. The ACA provided important observations for the work presented in Chapter 4.

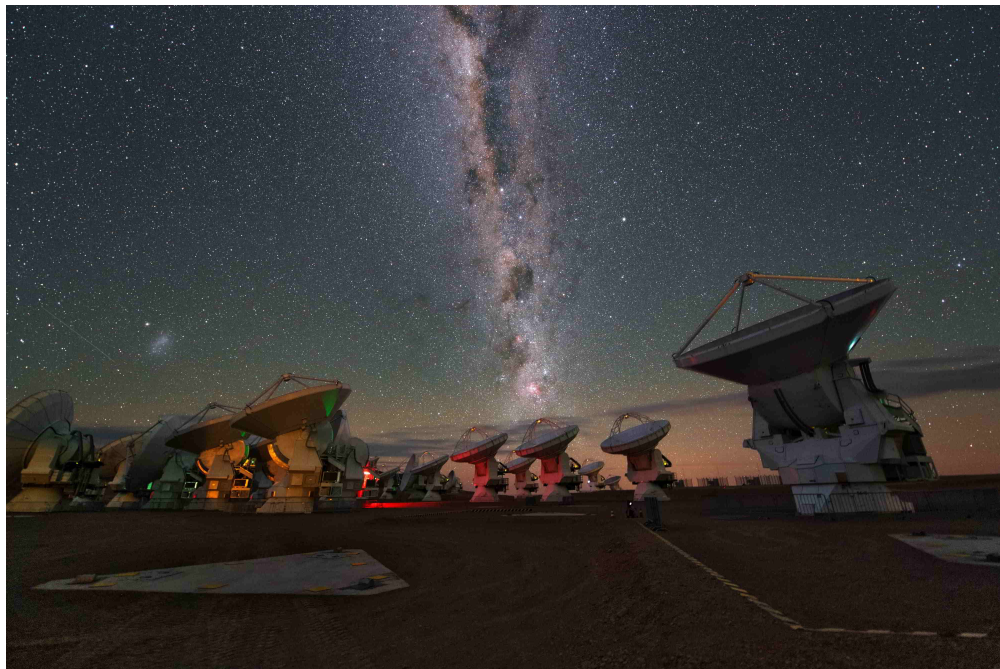


Figure 1.15: ALMA observatory. Credit: ESO/Y. Beletsky.

1.5.3 NOEMA

The Northern Extended Millimeter Array (NOEMA, see [Figure 1.16](#)) is an array of 12 dishes of 15 metre diameter each, located on the Plateau de Bure in the French Alps (NOEMA was formerly known as the Plateau de Bure Interferometer - PdBI).



Figure 1.16: The NOEMA interferometer. Credit: Jérémie Boissier/ IRAM.

It has recently been upgraded to increase the number of antennae from 6 to 12 providing more collecting power and therefore increased sensitivity to observe these fainter sources. A new correlator has also been installed (upgrading from Widex to PolyFix), which can cover a larger frequency range in one setup, meaning that improved line scans can be obtained that can cover a larger redshift range. These upgrades arguably make NOEMA the most powerful interferometer in the Northern Hemisphere.

As a result, NOEMA can play an important role in observing [C II] in faint galaxies at $z > 6$ and complementing ALMA to probe targets in the Northern hemisphere. This is because, despite the capability of ALMA to probe galaxies in the epoch of reionisation, it does not have full sky coverage in the Northern Hemisphere and so interesting targets in this region might be missed.

NOEMA can also play a critical role in analysing local galaxies with resolved studies of local galaxies, for example with studies of molecular gas outflows (e.g. [Herrera-Camus et al., 2020](#); [Lutz et al., 2020](#); [Longinotti et al., 2023](#)).

NOEMA provided the crucial data for the work presented in Chapter 2, confirming the spectroscopic redshift of a galaxy at $z > 6$.

1.6 Summary and thesis outline

I have so far given an overview of galaxy formation and evolution, starting with the first galaxies through the epoch of reionisation to the present day. I then introduced the interstellar medium and the main gas phases that will be discussed in the following chapters of this thesis, namely the ionised and molecular phase. Following this I introduced AGN and quasars as well as the current understanding of their importance in galaxy evolution and the mechanisms of AGN feedback that regulate the co-evolution of the central supermassive black holes and their host galaxies. Finally, I introduced the sub-mm facilities that have provided the key observational data that contributed to the work presented in the following thesis chapters.

- In Chapter 2, I present findings from a study of three galaxies at $z > 6$, confirming the spectroscopic redshift of one of these using observations from NOEMA. I also discuss the observed properties and how they compare to samples of both local and other high redshift galaxies.
- In Chapter 3, I present a study into 3000 optically selected AGN at $z < 0.2$ and establishing the relationship between the size of the observed radio emission and the prevalence of ionised outflows.
- In Chapter 4, I present the findings of a study into the excitation of the total molecular gas content traced by carbon monoxide lines, in a sample of 17 quasar host galaxies at $z < 0.2$.
- I present a short summary and conclusions from this thesis as well as an outlook for the future of the field and future projects for myself in Chapter 5.
- Finally in Chapter 6 I summarise the work of this thesis in a simplified way that is accessible for a general audience.

Context free quotes

“I ate a whole fish”

“My loyalties lie with alcohol”

“All you can eat shrimp for \$499”

“I welcome symmetric phone numbers”

“Do you have any idea how much technology goes into ham?”

“If you look long enough at the sun you will see the teletubbies baby”

“Free food occupies the first 10 places of my moral compass”

“I can take you to the valley and back”

“Look at the legs on that goose”

“You can join the llama group”

“This is a no hair zone”

Spec- z confirmation of Abell 1703-zD1 using NOEMA

In this chapter I present work confirming the spectroscopic redshift of a gravitationally lensed Lyman break galaxy in the Epoch of Reionisation, A1703-zD1, through the detection of [C II] $158\mu\text{m}$ at a redshift of $z = 6.8269 \pm 0.0004$. [C II] is reliably detected at 6.1σ co-spatial with the rest-frame UV counterpart, showing similar spatial extent. Correcting for the lensing magnification, the [C II] luminosity in A1703-zD1 is broadly consistent with the local $L_{[\text{CII}]} - \text{SFR}$ relation. We find a clear velocity gradient of $103 \pm 22 \text{ km s}^{-1}$ across the source which possibly indicates rotation or an ongoing merger. I further present spectral scans with no detected [C II] above 4.6σ in two unlensed Lyman break galaxies in the EGS-CANDELS field at $z \sim 6.6 - 6.9$. This is the first time that NOEMA has been successfully used to observe [C II] in a ‘normal’ star-forming galaxy at $z > 6$, and our results demonstrate its capability to complement ALMA in confirming galaxies in the Epoch of Reionisation. This chapter is based on the work published in [Molyneux et al. \(2022\)](#).

2.1 Introduction

In the past decade hundreds of galaxies have been identified in the Epoch of Reionisation (EoR), selected from their rest-frame UV light, using Hubble Space Telescope (*HST*) and ground-based

optical/NIR observatories (Stark, 2016, for a review and references therein). However, only a fraction of these sources have spectroscopic redshift determinations and we have a limited understanding of their physical properties. One reason for this is the difficulty in obtaining Lyman- α observations at such high redshifts, due to its absorption by neutral hydrogen in the intergalactic and interstellar medium (with detected Ly α emitters possibly residing in early ionised bubbles; e.g. Jung et al. 2020; Endsley et al. 2021).

In recent years ALMA has transformed this field by confirming the redshifts of galaxies out to redshift $z = 9$ (e.g., Smit et al., 2018; Hashimoto et al., 2018; Tamura et al., 2019; Hodge & da Cunha, 2020; Bouwens et al., 2021) and providing the first view of their dust obscured star-formation (e.g., Watson et al., 2015; Laporte et al., 2017; Bowler et al., 2018; Schouws et al., 2021), the kinematics of these sources (e.g., Smit et al., 2018; Hashimoto et al., 2019; Fujimoto, 2019; Ginolfi et al., 2020a), the cool gas traced by [C II] and highly ionised gas traced by [O III] (e.g., Maiolino et al., 2015; Inoue et al., 2016; Carniani et al., 2017; Laporte et al., 2017; Hashimoto et al., 2019; Tamura et al., 2019; Harikane et al., 2019; Bakx et al., 2020). Uncovering the physical properties of these primordial systems is fundamental to understanding the evolution of the first generation of galaxies and their role in Cosmic Reionisation.

In particular, ALMA has demonstrated its ability to detect [C II] in UV bright galaxies which are intrinsically bright ($\sim 2 - 3 \times L^*$ at $z = 7$) at $z \gtrsim 5$ (Capak et al., 2015; Willott et al., 2015; Smit et al., 2018; Matthee et al., 2019; Béthermin et al., 2020; Bouwens et al., 2021). However, much less is known about galaxies at these high redshifts which are more representative of the galaxy population as a whole ($L \leq L_{z=7}^*$). Our best insights into this fainter population are rare, apparently bright sources, which have been gravitationally lensed (Knudsen et al., 2016; Bradač et al., 2017; Fujimoto et al., 2021; Laporte et al., 2021). Despite the capability of ALMA to probe galaxies in the EoR, it has limited sky coverage in the Northern Hemisphere and so interesting targets might be missed.

Recently, the Plateau de Bure Interferometer (PdBI) has been upgraded to the Northern Extended Millimeter Array (NOEMA). The upgrades have increased the number of antennae from 6 to 10 (with 2 more planned to eventually increase the total number to 12) providing more collecting power and therefore increased sensitivity to observe these fainter sources. A new correlator has also been installed (upgrading from Widex to PolyFix Schuster et al. 2018), which can cover a larger frequency range in one setup, enabling faster line scans. These upgrades arguably make

NOEMA the most powerful interferometer in the Northern Hemisphere, and therefore might play an important role in observing [C II] in galaxies at $z > 6$.

Here we report on a line search for [C II]158 μ m with NOEMA, targeting 3 galaxies in the Northern Hemisphere at $z \sim 6.6 - 6.9$. The targets have been selected from a larger sample of Lyman Break Galaxies, with high-precision photometric redshifts (Smit et al., 2014, 2015). A1703-zD1 is the standout target of our sample, lying behind the strong lensing cluster Abell 1703, with a magnification of ~ 9 (Bradley et al., 2012). Due to its exceptional observed brightness, it has been targeted many times with previous observations attempting to observe Ly α , C IV and C III with the Keck Observatory (Schenker et al., 2012; Stark et al., 2015a; Mainali et al., 2018) and a previous attempt with PdBI (Schaerer et al., 2015) to observe [C II], however, these observations did not result in a significant detection.

In this chapter I present the successful spectroscopic confirmation of A1703-zD1 and constraints on the properties of two other sources based on their non-detections. In Section 2.2 I describe the sample selection and observations. In Section 2.2 I describe the sample selection and observations. In Section 2.3 I discuss the method for line scanning and the findings from the scans. In Section 2.4 I provide the properties of the sources and comparisons to the literature and in Section 2.5 I give the conclusions of this work. We adopt $H_0 = 70 \text{ km s}^{-1} \text{ Mpc}^{-1}$, $\Omega_M = 0.3$, and $\Omega_\Lambda = 0.7$ throughout. Magnitudes are quoted in the AB system (Oke & Gunn, 1983).

2.2 Sample selection and observations

Here I report on the line search for [C II]158 μ m with NOEMA, targeting 3 galaxies in the Northern Hemisphere at $z \sim 6.6 - 6.9$. The targets I will present here were selected from a larger sample of Lyman Break Galaxies, with high-precision photometric redshifts (Smit et al., 2014, 2015). A1703-zD1 is the standout target of the sample, lying behind the strong lensing cluster Abell 1703, with a magnification of $\sim 9\times$ (Bradley et al., 2012). Due to its exceptional observed brightness, it has been targeted many times with previous observations attempting to observe Ly α , C IV and C III with the Keck Observatory (Schenker et al., 2012; Stark et al., 2015a; Mainali et al., 2018) and a previous attempt with PdBI (Schaerer et al., 2015) to observe [C II], however, these observations did not result in a significant detection.

In this work I adopt a Kroupa IMF (Kroupa, 2001). We adopt $H_0 = 70 \text{ km s}^{-1} \text{ Mpc}^{-1}$, $\Omega_M = 0.3$, and $\Omega_\Lambda = 0.7$ throughout. Magnitudes are quoted in the AB system (Oke & Gunn, 1983).

2.2.1 Target selection and properties

We obtained NOEMA observations of three sources, A1703-zD1 (Bradley et al., 2012; Smit et al., 2014), EGS-5711424617 and EGS-1952445714 (hereafter EGS-5711 and EGS-1952 respectively; Smit et al., 2015). These galaxies were initially selected with the Lyman break technique as *HST*/F814W drop-out galaxies and subsequently identified as sources with blue *Spitzer*/IRAC [3.6]–[4.5] colours, implying high equivalent width [O III]+H β emission (Smit et al., 2014, 2015).

We selected these targets due to their observed brightness ($m_{UV} \sim 24 - 25$), but also as they are representative of ‘normal’ star-forming galaxies ($\text{SFR} < 100 M_\odot \text{ yr}^{-1}$) at $z \sim 7$, with intrinsic (corrected for lensing magnification, A1703-zD1 is magnified $\sim 9 \times$) UV SFRs of $5 - 38 M_\odot \text{ yr}^{-1}$. A list of some of the basic properties for all three galaxies are shown in Table 2.1. These same selection criteria were recently used to successfully confirm galaxies with ALMA at $z_{[\text{CII}]} = 6.808 - 6.854$ (Smit et al., 2018).

The inferred emission lines in the *Spitzer* observations reduce the probability range for the redshift such that observations can be carried out using one NOEMA setup. For both A1703-zD1 and EGS-1952 the photometric redshifts of $6.7_{-0.1}^{+0.2}$ and $6.75_{-0.10}^{+0.11}$, respectively, are within this range. However, we note that EGS-5711 has $z_{\text{phot}} = 6.47_{-0.10}^{+0.11}$, outside of the colour selection range due to a tentative detection in the *HST*/F814W band. For the extreme emission line sources from (Smit et al., 2015), systematic changes in the estimated photometric redshift ($\Delta z \sim 1$) are found when making changes to the input template set (in particular the strength of the emission line equivalent widths of the templates) used to fit the SEDs. As a result of these systematic uncertainties, we rely on the *Spitzer*/IRAC colour selection from Smit et al. (2015) to identify sources most likely in the redshift range $z \sim 6.6 - 6.9$, which includes some cases (like EGS-5711) where the z_{phot} is not within this range.

For A1703-zD1 we use a magnification value of $9.0_{-4.4}^{+0.9}$ taken from Bradley et al. (2012) calculated using the model described in Zitrin et al. 2010. The magnification error represents the

extreme value obtained from the minimum and maximum magnifications obtained within 0.5 arcsec of the target and assuming $\Delta z \pm 1.0$ for the source redshift. To obtain a better handle on the systematic uncertainties in the lensing magnification we ran two more trial models, one using a revised version of the Light Traces Mass (LTM) technique and one fully parametric model. These models suggest a magnification in agreement with that of [Bradley et al. \(2012\)](#) within the uncertainties, though towards the lower end ($\mu \sim 4 - 5$). Critically, the weight of the nearby cluster galaxy (seen in the bottom of Figure 2.4) is fixed according to the scaling relations, but in reality has a significant uncertainty that affects the magnification value. We therefore adopt the published magnification by [Bradley et al. \(2012\)](#) ($\mu = 9.0^{+0.9}_{-4.4}$), as the uncertainties are broad enough to include the new magnifications from the trial models.

Throughout this chapter, I report measured quantities (i.e. [C II] flux) as observed in the image plane, without a magnification correction, whereas derived physical quantities (i.e. $L_{[\text{CII}]}$, $\text{SFR}_{[\text{CII}]}$ and physical size) are corrected for the adopted lensing magnification.

2.2.2 NOEMA observations and data reduction

Recently, the Plateau de Bure Interferometer (PdBI) has been upgraded to the Northern Extended Millimeter Array (NOEMA). The upgrades have increased the number of antennae from 6 to 10 (with 2 more planned to eventually increase the total number to 12) providing more collecting power and therefore increased sensitivity to observe these fainter sources. A new correlator has also been installed (upgrading from Widex to PolyFix [Schuster et al. 2018](#)), which can cover a larger frequency range in one setup, enabling faster line scans. These upgrades arguably make NOEMA the most powerful interferometer in the Northern Hemisphere, and therefore might play an important role in observing [C II] in galaxies at $z > 6$.

We obtained 1.2 mm observations using NOEMA in its most compact 10D configuration, with a single setup for each of the three sources, A1703-zD1, EGS-5711 and EGS-1952, approved in program W18FC.

Observations of A1703-zD1 were taken on 21 March 2019, with 4.1 hours on source, and covering the frequency range 241.45 – 249.08 GHz (upper side band, USB) and 225.97 – 233.60

GHz (lower side band, LSB), corresponding to a redshift range 6.63 – 6.87 and 7.14 – 7.41 respectively. The USB frequency range partly overlaps with PdBI observations taken in 2013 by [Schaerer et al. \(2015\)](#) and we combine the NOEMA and PdBI data in the UV -plane to obtain maximum depth over the redshift range of 6.80 – 6.88.

Below in Figure 2.1 is the SED for A1703-zD1 alongside the photometric redshift probability distributions, redshift coverage of the observations and the measured $z_{[\text{CII}]}$ (see Section 2.3.1). The SED fitting was done using the software Easy and Accurate Zphot from Yale (EAZY; [Brammer et al., 2008](#)), see [Smit et al. \(2015\)](#) for a full description.

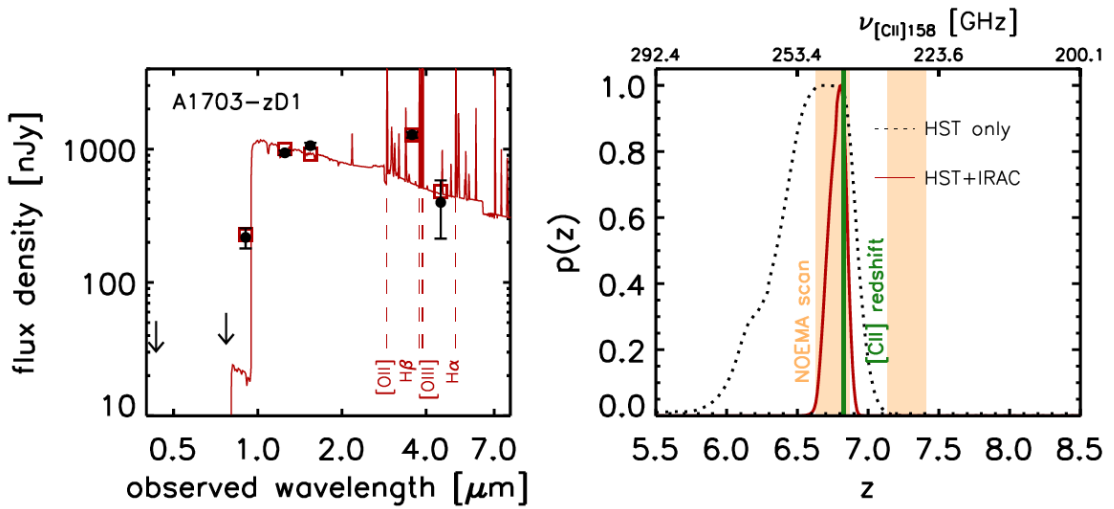


Figure 2.1: A1703-zD1 SED (**left panel**) and redshift probability distribution (**right panel**). Coverage by the NOEMA sidebands (USB and LSB) is indicated by the shaded orange region. The dotted black line and solid red line represent the probability for the target to be at a certain redshift based on HST only and HST+IRAC data, respectively. Here the USB was selected to cover the peak probability in the photometric redshift range, which is indeed where the detection of [C II] was made, indicated by the solid green line.

We observed EGS-5711 on 16 April, 30 April 2019 and 02 May with 7.1 hours on source in total. EGS-1952 was observed on 08 and 09 April 2019 as well as on 02 and 03 May 2019 with 8.7 hours on source in total. Observations for both of these targets covered the same frequency and redshift range. LSB coverage was 240.4 – 248.3 GHz, corresponding to redshift of 6.66 – 6.91 and USB coverage was 255.8 – 263.7 GHz, corresponding to redshift of 6.21 – 6.43. Below in Figures 2.2 and 2.3 are the redshift coverage of the observations alongside the SEDs and photometric redshift probability distributions for EGS-5711 and EGS-1952. The SED fitting was done using the software Easy and Accurate Zphot from Yale (EAZY; [Brammer et al., 2008](#)), see [Smit et al. \(2015\)](#) for a full description.

We note that for EGS-5711, NOEMA did not cover the central z_{phot} of $6.47^{+0.11}_{-0.10}$. The systematic uncertainties in estimating photometric redshifts in extreme emission line galaxies are discussed in section 2.1, which motivated a line search at $z \sim 6.6 - 6.9$ based on the [Smit et al. \(2015\)](#) colour selection.

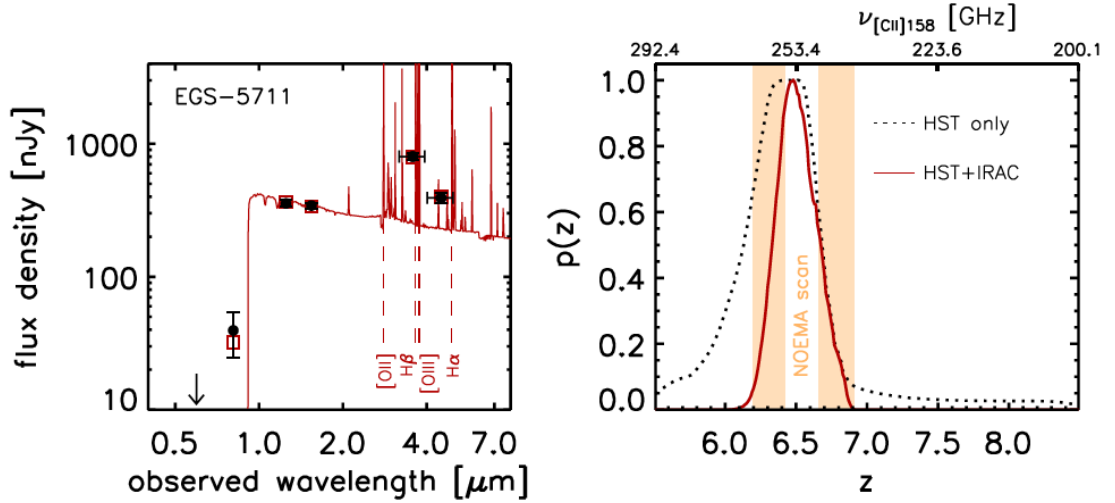


Figure 2.2: EGS-5711 SED (left panel) and redshift probability distribution (right panel). Coverage by the NOEMA sidebands (USB and LSB) is indicated by the shaded orange region. The dotted black line and solid red line represent the probability for the target to be at a certain redshift based on HST only and HST+IRAC data, respectively. This target was selected to be at $z \sim 6.6 - 6.9$ based on HST+IRAC data colour criteria ([Smit et al., 2015](#)), however, the peak of the $p(z)$ suggests a possible lower redshift. A broader and deeper line scan will be needed to establish the spectroscopic redshift of this source.

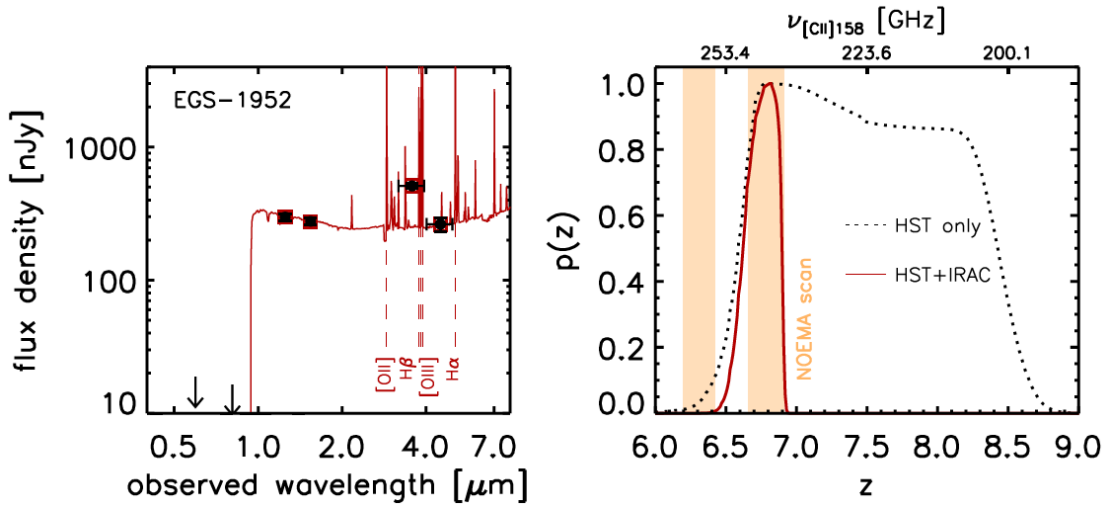


Figure 2.3: EGS-1952 SED (left panel) and redshift probability distribution (right panel). Coverage by the NOEMA sidebands (USB and LSB) is indicated by the shaded orange region. The dotted black line and solid red line represent the probability for the target to be at a certain redshift based on HST only and HST+IRAC data, respectively.

All of the data were reduced using the GILDAS software. From the NOEMA data of A1703-zD1 alone, we obtain a datacube with a median rms of 0.87 mJy in a 40 km s^{-1} channel, with a beam size of 1.52×1.28 arcsec. After merging with PdBI data (Schaerer et al., 2015) we obtain a datacube with a median rms of 0.83 mJy in a 40 km s^{-1} channel, with a beam size of 1.57×1.31 arcsec (~ 2 times lower sensitivity than ALMA observations in Smit et al. 2018). We then tapered the datacube for A1703-zD1 such that the beam size matched the spatial extent of the source in the HST imaging using a 50 metre taper at a 170 degree angle, in order to obtain a more accurate measurement of the total flux. We also cleaned the data with 100 iterations before imaging the datacube, including a threshold of 0.85 mJy ($2 \times \text{rms}$) to reduce the effects of contamination from a strong CO(3-2) emission line signal observed from a serendipitous source. This leads to a median rms in the datacube of 0.73 mJy in a 40 km s^{-1} channel, with a beam size of 2.88×1.48 arcsec.

We imaged the two EGS datacubes with natural weighting for optimal point source sensitivity, resulting in a beam size of 1.69×1.41 arcsec and 1.63×1.37 arcsec for EGS-5711 and EGS-1952 respectively. Our data reached a typical rms of 0.34 and 0.41 mJy in a 40 km s^{-1} channel respectively. We do not apply any tapering as our beam sizes are expected to cover any observable [C II] emission from these compact targets (Carniani et al., 2020).

We also produced continuum images using GILDAS for all three targets to provide constraints on the dust obscured star formation and on the dust content itself. For all three targets we merged the USB and LSB before making the continuum images. In the case of A1703-zD1 we removed the frequency range in which [C II] was detected in the corresponding side band. We find no continuum detections above 3σ within 1 arcsec of each source and therefore provide upper limits for the L_{IR} and SFR_{IR} , presented in Table 2.2. These upper limits are derived by taking $3 \times \text{rms}$ from the continuum image. Discussion about the significance of these continuum measurements can be found in Section 2.4.2.

We correct for any offset in the HST astrometry by identifying the closest star to the target galaxy in the Gaia Data Release 3 (DR3). For EGS-5711 and EGS-1952 the observations were taken ~ 4 years apart and we correct for the proper motion of the star during that timeframe, before shifting our HST image to the Gaia reference star. Unfortunately for A1703-zD1, none of the stars present in the HST image had proper motion data from Gaia DR3 as a result of being too faint (G magnitudes > 21). Given that the HST imaging for Abell 1703 was taken in

Target ID	A1703-zD1	EGS-5711424617	EGS-1952445714
RA	13:14:59.418	14:19:57.114	14:19:19.524
DEC	+51:50:00.84	+52:52:46.17	+52:44:57.14
z_{phot}	$6.7^{+0.2}_{-0.1}$ ^a	$6.47^{+0.11}_{-0.10}$ ^b	$6.75^{+0.11}_{-0.10}$ ^b
$m_{H_{160}}$	24.0 ± 0.1 ^a	25.1 ± 0.1 ^b	25.3 ± 0.1 ^b
M_{UV}	-20.6 ± 0.5 ^c	-21.77 ± 0.10	-21.64 ± 0.10
β_{UV}	-1.56 ± 0.32	-2.18 ± 0.36	-2.36 ± 0.43
μ	$9.0^{+0.9}_{-4.4}$ ^a	–	–

Table 2.1: Table of source properties based on previous observations. ^aValues from Bradley et al. (2012). ^bValues from Smit et al. (2015). ^cValues from Smit et al. (2014).

2004 (> 10 years apart from Gaia), and assuming a similar proper motion to the stars in the EGS field, we expect a ~ 0.3 arcsec offset from the reported Gaia DR3 position due to proper motion. This angular distance is similar to the typical spatial offset found for the stars in the Abell 1703 field between the HST imaging and Gaia DR3 catalogue. As a result, no improvement in the astrometry of A1703-zD1 could be obtained and we relied on the original HST imaging (see Bradley et al., 2012), but note that a maximum 0.3 arcsec astrometrical offset between the HST and NOEMA data is possible. However, we point out that the morphology and size of the [C II] emission for A1703-zD1 matches well to the HST image, as shown in Figure 2.4, so any real offset is perhaps likely to be small. Further, the detection of a serendipitous source with much higher S/N is also present and is seen to be co-spatial with the host galaxy as shown in Figure 2.7.

2.3 Line scans

Using the datacubes we obtain after processing, we scan for prominent lines by collapsing channels in the range of $80 - 400 \text{ km s}^{-1}$ (the range of expected [C II] line-widths). This optimises the width of the collapsed narrowband for which the strongest point-source signal within a 1 arcsec radius of the target source (identified in the *HST*-imaging) is found, if any. Scanning through the datacube also enables us to identify any lines present from serendipitous sources.

We replicate this scanning in the sign-inverse of the datacube, to check if any noise is comparable to the signal detected from the target source and assess the robustness of any tentative ($> 3\sigma$) line detections. We extract spectra from identified line candidates by summing all pixels detected at $\text{S/N} > 2$ in the collapsed narrowband.

2.3.1 A1703-zD1

Taking our NOEMA observations of A1703-zD1 in isolation we find a signal at 242.90 ± 0.01 GHz with $S/N = 4.6$, co-spatial with the lower bright clump and extended along the lensed arc, visible in *HST*-imaging (See Figure 2.4). From previous observations by [Schaerer et al. \(2015\)](#), we independently identified a tentative detection of [C II] with $S/N = 3.4$ at 242.853 ± 0.009 GHz. The top panel of Figure 2.4 presents the line detection after combining both data-sets (see Section 4.3), collapsed in a 120 km s^{-1} channel centered on 242.8 GHz, with a peak S/N of 5.5. To obtain an unresolved measurement of A1703-zD1 we taper the datacube to match the spatial extent of A1703-zD1 (described in Section 4.3). From this we find a detection at 242.82 ± 0.01 GHz with an increase in the peak S/N to 6.1, yielding a best-fit $z_{[\text{CII}]} = 6.8269 \pm 0.0004$ from the extracted spectrum (See Figure 2.5). This higher S/N when matching the spatial extent of the target (and alignment with the rest-frame UV emission) is a clear confirmation of the detection. We therefore use the tapered imaging for our final measurements. We collapse the datacube over the frequency range 242.72 – 242.92 GHz and measure the total flux using 2D gaussian fitting from the routine IMFIT in the Common Astronomy Software Application (CASA; [McMullin et al., 2007](#)).

We also note that within the same datacube, we identify a serendipitous line signal at 241.59 GHz with $S/N \sim 14$, (see spectra in Fig 2.6) ~ 8 arcsec offset to A1703-zD1. The signal is co-spatial with a foreground source (J131459.75+515008.6) which has $z_{\text{phot}} \sim 0.44 \pm 0.11$ (found in Sloan Digital Sky Survey DR12, [Alam et al., 2015](#)). We therefore identify the line as CO(3-2) (rest frame wavelength $867 \mu\text{m}$) at $z_{\text{spec}} = 0.43127 \pm 0.00003$, consistent with the z_{phot} . We also measure a $68 \mu\text{Jy}$ continuum flux from this source with S/N of 5.1.

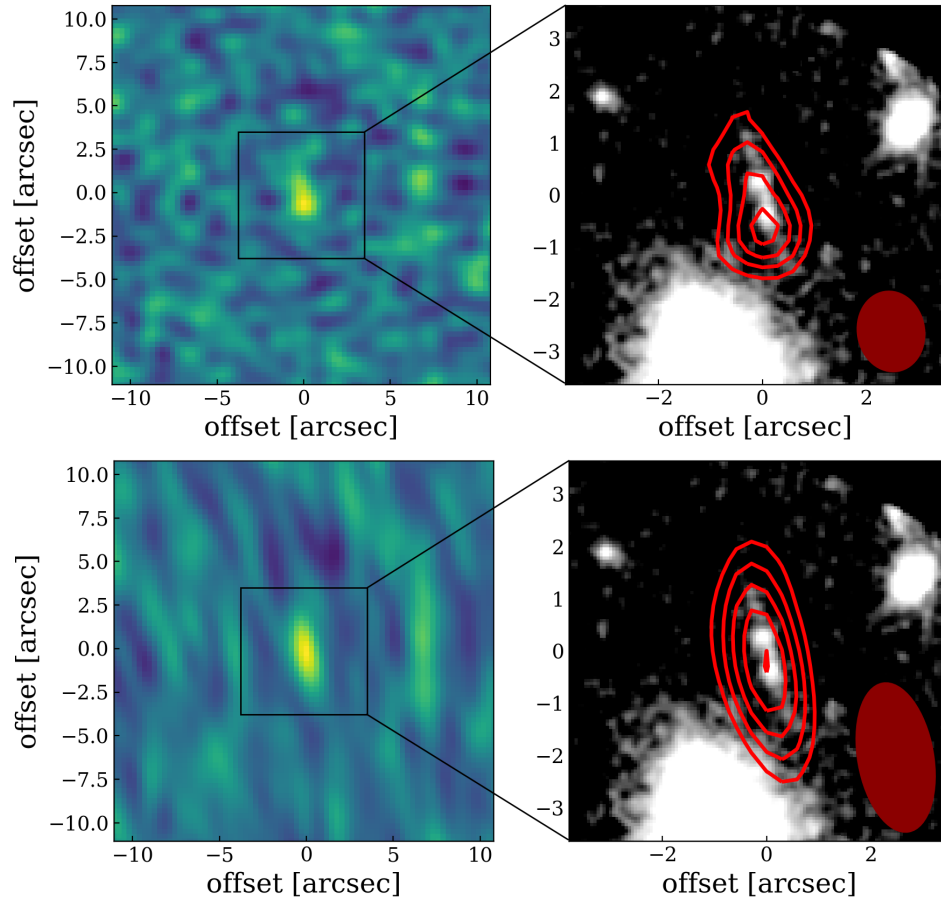


Figure 2.4: The detection of [C II] at $z = 6.827$ in A1703-zD1. The left panels show the NOEMA+PdBI data collapsed over the frequency range 242.76 – 242.86 GHz for the untapered (**top panels**) and tapered (**bottom panels**) imaging. The right panels show HST H_{160} imaging (grey-scale image) overlaid with the 2, 3, 4, 5 and 6 σ contours of the [C II] narrowband (red contours). The filled ellipses in the bottom right corner indicate the beam sizes (1.57×1.31 arcsec and 2.88×1.48 arcsec).

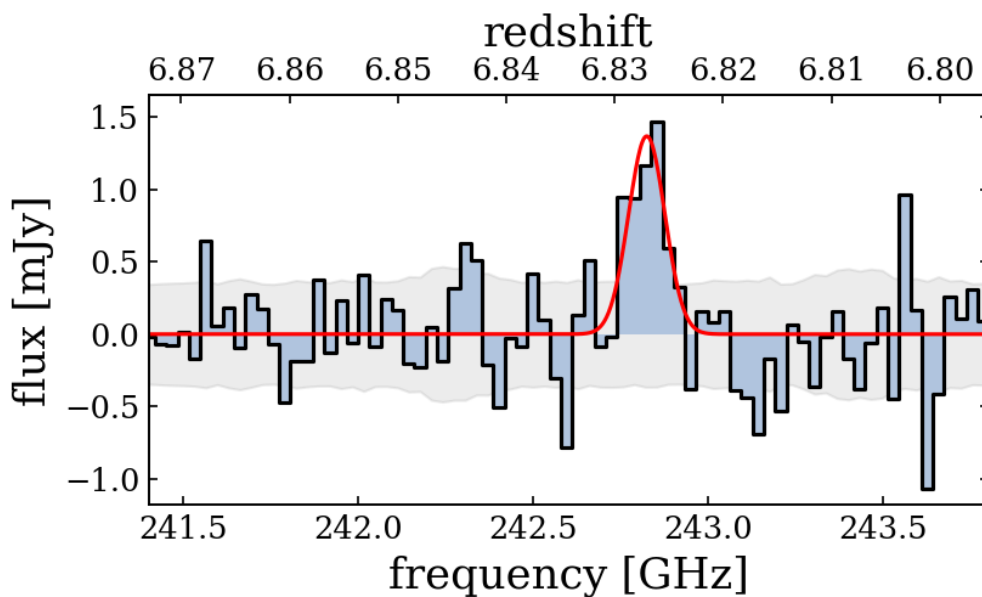


Figure 2.5: The spectrum of A1703-zD1 extracted by summing the flux over the source from all pixels with $S/N > 2$, using the tapered imaging. The red line shows the best fit Gaussian line profile. The grey shaded region gives the measured rms throughout the spectrum.

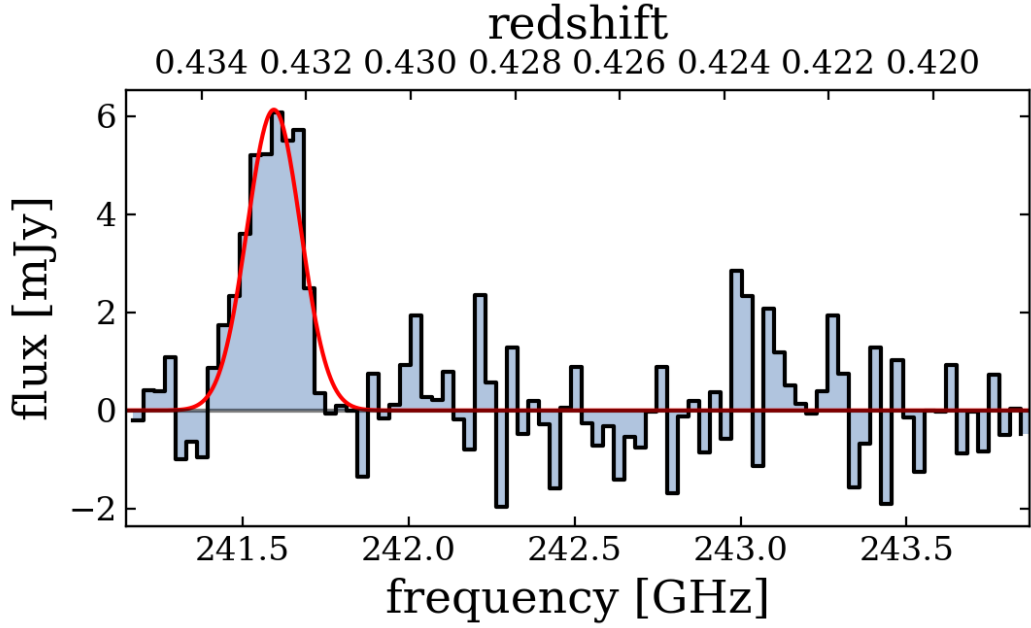


Figure 2.6: Spectrum of the serendipitous line identified in the datacube of A1703-zD1, with the best-fit Gaussian line profile in red. The redshifts plotted along the upper horizontal axis are based on the assumption the line detection is CO(3-2) for the source J131459.75+515008.6. The S/N of the line is 14.

2.3.2 Serendipitous source neighbouring A1703-zD1

Here we present a serendipitous 14σ detection in the datacube of A1703-zD1, with the spectra shown in 2.6 and the line contours overlaid on the HST imaging in 2.7. The spectral extraction is the same as described in Section 2.3. The detection is co-spatial with a foreground source (J131459.75+515008.6) which has $z_{\text{phot}} \sim 0.44 \pm 0.11$ (found in Sloan Digital Sky Survey DR12, Alam et al., 2015). We therefore attribute the line detection to CO(3-2) (rest frame wavelength $867\mu\text{m}$) putting the source at $z_{\text{spec}} = 0.43127 \pm 0.00003$, consistent with the z_{phot} .

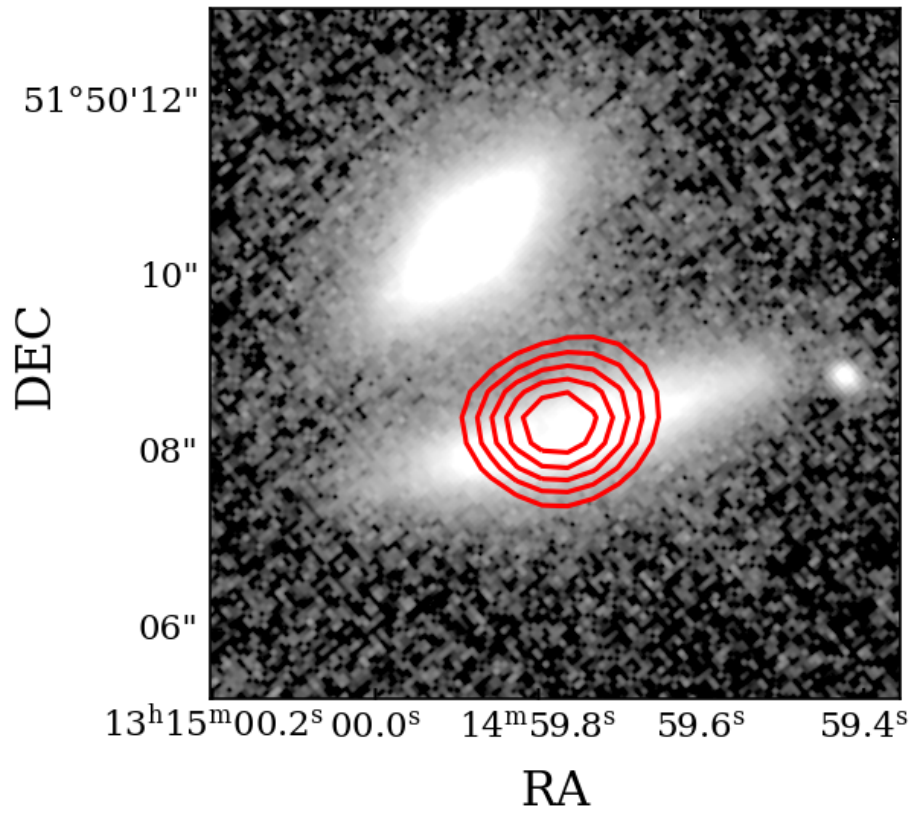


Figure 2.7: Serendipitous source (J131459.75+515008.6) with red contours overlaid corresponding to 4, 6, 8, 10 and 12 σ , identified as CO(3-2) emission. Background shows the HST z_{850} imaging of Abell 1703.

2.3.3 EGS-5711 & EGS-1952

When scanning for [C II] in EGS-5711 we find a tentative signal with $S/N = 4.6$ at 246.16 ± 0.02 GHz, 0.5 arcsec away from the centre of the target. This line, if real, would put the source at $z = 6.7263 \pm 0.0006$. A second signal at 242.10 ± 0.03 GHz with $S/N = 3.4$ is also found co-spatial with EGS-5711. The corresponding spectra and contour overlay plots for the $S/N = 4.6$ signal can be found in Figures 2.8 and 2.9. In Figure 2.10 we also present the spectra at the location of the source to illustrate the lack of detection there. Performing the same scan on the inverse datacube (searching within a radius of 15 arcsec), we find several signals with equivalent or higher S/N , the highest of which is $S/N = 5.3$. Given our 15 times larger search area, we expect ~ 1 spurious signal above 4.5σ within 1 arcsec radius of our target. More observations are therefore required to confirm any detection.

For EGS-1952 we find no evidence for [C II] with $S/N > 3$, co-spatial with the source. Spectra at the location of the source can be found in Figure 2.11. Further, we find no continuum signal for both EGS-5711 and EGS-1952 and as a result, we only provide upper limits for the continuum flux and an upper limit estimate for the [C II] line flux, based on the spectral line obtained for A1703-zD1, scaled to the median rms of the EGS-5711 and EGS-1952 datacubes.

We can either interpret these non-detections as faint [C II] lines due to the low dust content of these sources or alternatively it is possible that the limited frequency range that was scanned for each object missed the line emission entirely. Deeper and wider scans would be needed to distinguish between these two interpretations.

2.3.4 EGS-5711 tentative detection

Here we present a 4.6σ signal for EGS-5711, with the contours overlaid on the HST imaging in Figure 2.8 and the corresponding spectra in Figure 2.9. The spectral extraction is the same as described in Section 2.3. The weak signal is very narrow and clearly offset from the HST target, which likely makes this a spurious detection.

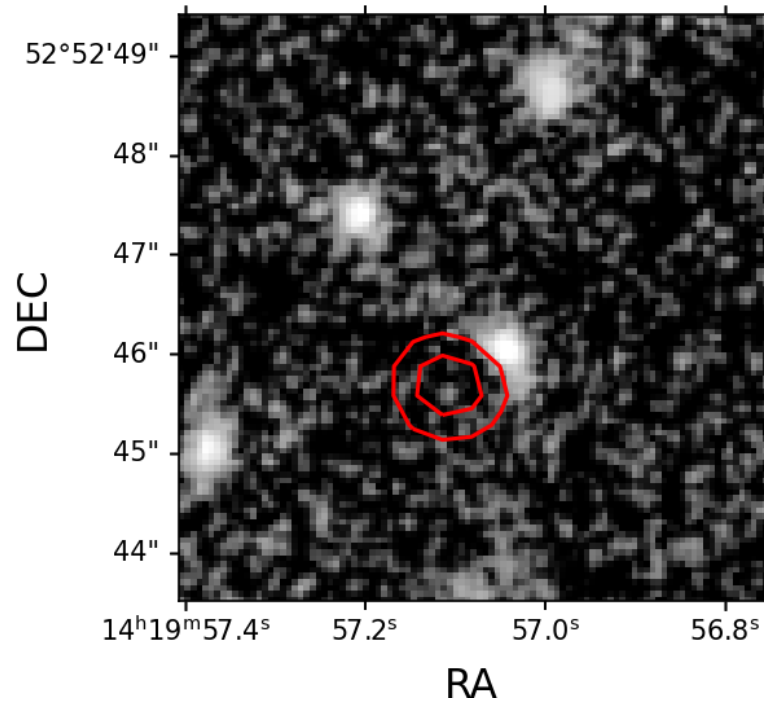


Figure 2.8: The $S/N = 4.6$ signal found for EGS-5711. Background shows the HST *H*-band image with red contours corresponding to 3 and 4σ [C II] emission. The extracted spectrum is also shown in Figure 2.9. This source would require further observations to confirm a robust detection.

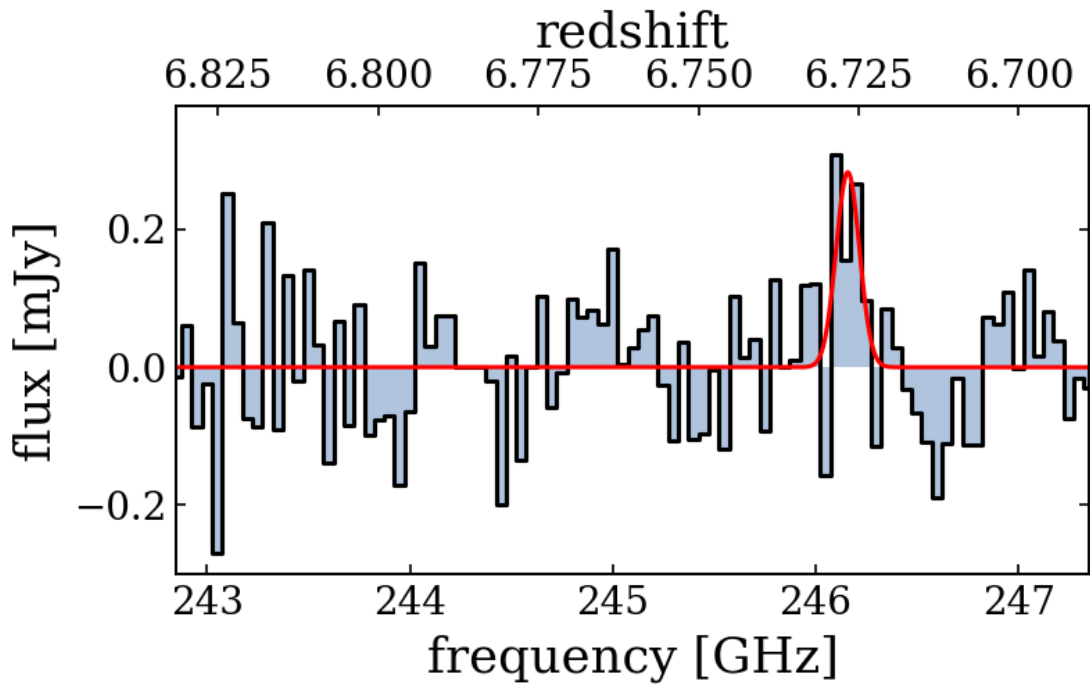


Figure 2.9: EGS-5711 spectrum of the $S/N = 4.6$ signal, extracted from the region of the contours shown in Figure 2.8, with the best-fit Gaussian line profile in red.

2.3.5 Empty scans

In Figures 2.10 and 2.11 we present the empty line scans in the LSB and USB for both EGS targets. The extractions were taken simply from the central pixel of the observations.

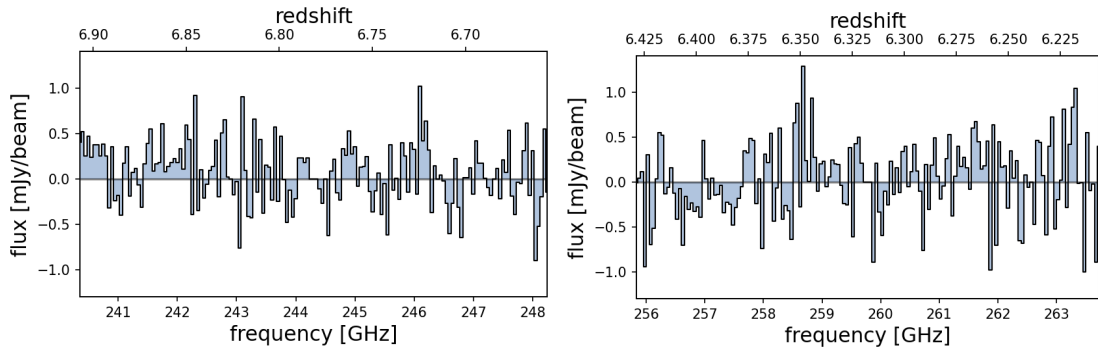


Figure 2.10: **Left:** LSB spectra taken at the location of EGS-5711. We find no robust detection and present upper limits in table 2.2. **Right:** USB spectra taken at the location of EGS-5711.

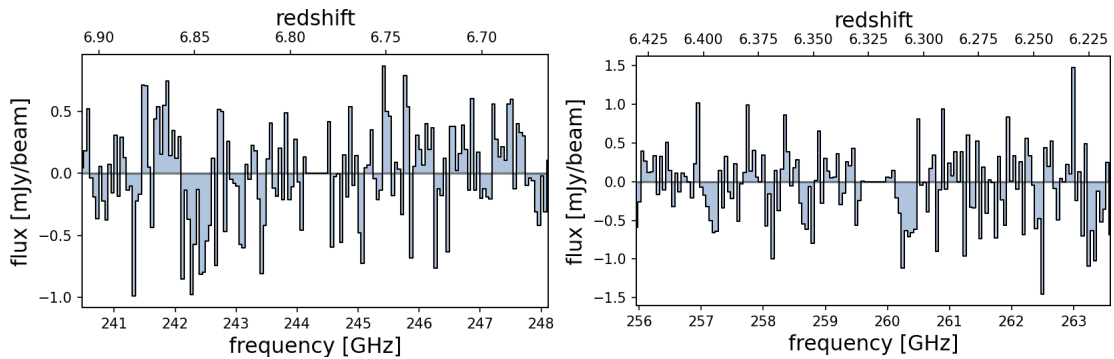


Figure 2.11: **Left:** LSB spectra taken at the location of EGS-1952. We find no detection and present upper limits in table 2.2. **Right:** USB spectra taken at the location of EGS-1952.

2.4 Source properties

Here we present the physical properties of our three targets derived from our observations and comparisons to the literature. A full table of galaxy properties is shown in Table 2.2.

Target ID	A1703-zD1	EGS-5711	EGS-1952
$z_{[\text{CII}]}$	6.8269 ± 0.0004	–	–
S/N	6.1	–	–
[C II] flux (Jy km s^{-1})	0.28 ± 0.06	$< 0.17^a$	$< 0.21^a$
$\text{FWHM}_{[\text{CII}]}$ (km s^{-1})	155 ± 31	–	–
Continuum flux (μJy)	$< 24.5^a$	$< 27.4^a$	$< 28.7^a$
$L_{[\text{CII}]}$ ($10^8 L_{\odot}$)	0.35 ± 0.07 ($_{-0.04}^{+0.29}$) ^c	$< 1.8^a$	$< 2.3^a$
$\text{SFR}_{[\text{CII}]}$ ($M_{\odot} \text{ yr}^{-1}$)	4.3 ± 0.9 ($_{-0.04}^{+0.29}$) ^c	$< 23.9^a$	$< 29.5^a$
L_{UV} ($10^{11} L_{\odot}$)	0.39 ± 0.04 ($_{-0.04}^{+0.41}$) ^c	1.2 ± 0.1	1.0 ± 0.1
SFR_{UV} ($M_{\odot} \text{ yr}^{-1}$)	6.7 ± 0.6 ($_{-0.61}^{+6.41}$) ^c	20.2 ± 1.9	17.9 ± 1.7
L_{IR} ($10^{11} L_{\odot}$)	< 0.35 (< 0.68) ^{a,b,c}	$< 3.6^{a,b}$	$< 3.9^{a,b}$
SFR_{IR} ($M_{\odot} \text{ yr}^{-1}$)	< 5.2 (< 10.1) ^{a,b,c}	$< 53.2^{a,b}$	$< 57.7^{a,b}$
$\log(\text{IRX})$	$< -0.05^a$	$< 0.48^a$	$< 0.57^a$

Table 2.2: Galaxy Properties ^a 3σ upper limits, ^bassuming a grey body approximation with $T = 50\text{K}$ and $\beta = 1.5$, ^ccorrected for a magnification of $\mu = 9.0$ (the uncertainty due to the lensing magnification are also shown in brackets). Observed quantities are uncorrected for magnification, while the derived physical properties use the magnification correction.

2.4.1 $L_{[\text{CII}]}$ vs SFR relation

In Figure 2.12 we present the measured [C II] luminosity as a function of SFR_{UV} and include sources from the literature for comparison (Matthee et al., 2019; Knudsen et al., 2016; Bradač et al., 2017; Fujimoto et al., 2021). The UV SFRs are calculated using the Kennicutt & Evans (2012) conversion and using a Kroupa IMF. EGS-5711 and EGS-1952 are given as 3σ upper limits.

In the local universe we see a tight $L_{[\text{CII}]} - \text{SFR}$ relationship as shown by the De Looze et al. 2014 relation ($\log \text{SFR} = -6.99 + 1.01 \times \log [\text{CII}]$) in Figure 2.12. Recent studies of ‘normal’ (i.e. main sequence) star-forming galaxies with redshifts at $4.4 < z < 5.9$ and galaxies at $z \sim 6.5$ with high $\text{Ly}\alpha$ luminosities have also shown consistency with the local relation when including the dust-obscured SFR (e.g., Matthee et al., 2019; Schaerer et al., 2020). In contrast, a few studies have found that lensed galaxies with a lower SFR are more likely to be below the locally observed relation (e.g., Knudsen et al., 2016; Bradač et al., 2017). In particular the strongest lensed object, MS0451-H (Knudsen et al., 2016), with the lowest intrinsic SFR shows the strongest deficit in $L_{[\text{CII}]}$. If confirmed, this could suggest differing ISM properties in faint, and possibly more metal-poor, high-redshift galaxies. A1703-zD1 is a strongly lensed galaxy with a modest intrinsic SFR_{UV} of $6.7 \pm 0.6 M_{\odot} \text{ yr}^{-1}$, but we find no evidence of a significant offset to the local relation, as A1703-zD1 lies slightly below, but still within 1σ of, the local $L_{[\text{CII}]} - \text{SFR}$ relation. We also note that including the magnification uncertainties in the

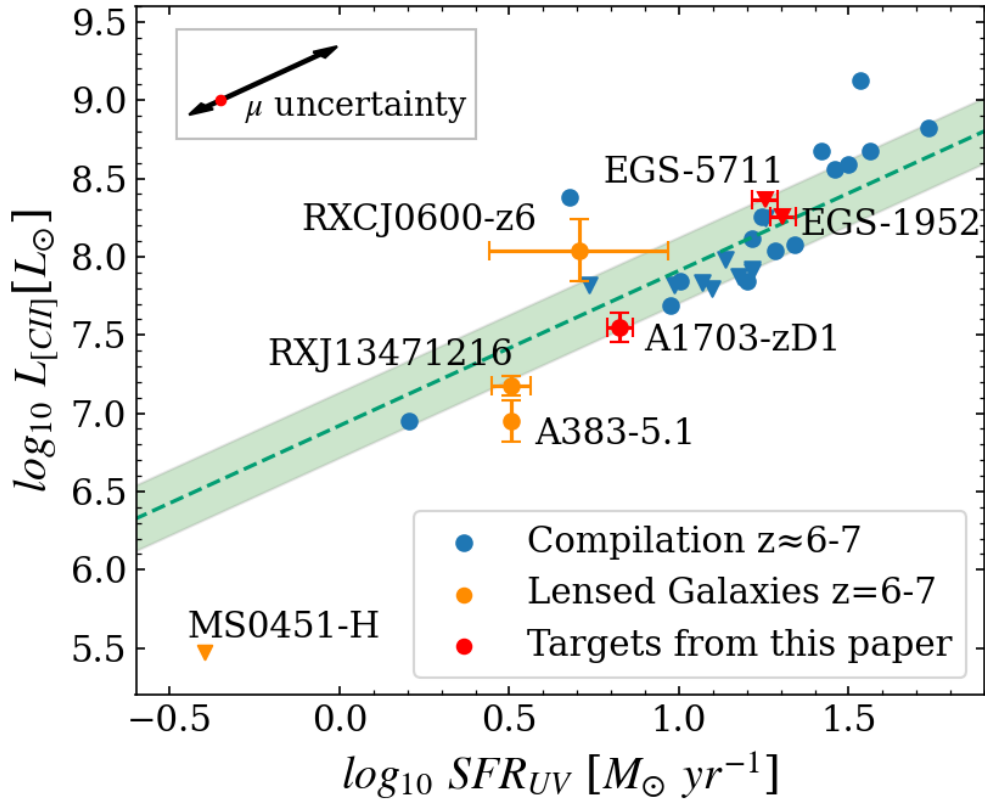


Figure 2.12: The [C II] line luminosity as a function of the star-formation rate, derived from the ultraviolet luminosity. The locally observed De Looze et al. 2014 relation is indicated by the dotted green line with the errors shown by the green shaded region. Sources with 3σ upper limits are shown by downward triangles. Our three targets are presented as red points. The black arrows in the top left indicate the magnification uncertainty for A1703-zD1. Changes in magnification affect both $L_{[\text{C II}]}$ and SFR_{UV} , such that A1703-zD1 moves along the local relation. We use a compilation of $z \approx 6 - 7$ sources for comparison (compiled from Matthee et al., 2019), shown in blue. In orange we highlight four lensed sources from the literature (Knudsen et al., 2016; Bradač et al., 2017; Fujimoto et al., 2021) for which three show an apparent offset from the local $L_{[\text{C II}]}$ – SFR relation, one of which shows a very clear offset (MS0451-H, discussed more in Section 2.4.1).

calculations of $L_{[\text{C II}]}$ and $\text{SFR}_{[\text{C II}]}$ has no impact on the offset to the local relation as indicated by the arrows in Figure 2.12. However, including the 3σ upper-limit on the SFR_{IR} would place A1703-zD1 below the local relation.

An important consideration in assessing a possible [C II] deficit is the potential for extended [C II] emission (e.g., Fujimoto, 2019; Fujimoto et al., 2020) compared to the rest-frame UV data, in particular for sources with smearing due to strong gravitational lensing. This effect was recently studied by Carniani et al. (2020), who find that [C II] emission can be two times more extended than [O III]. Specifically, Carniani et al. (2020) show that MS0451-H (Knudsen et al., 2016), nominally a 2.5σ deviation from the local De Looze relation (Figure 2.12), misses ~ 60

– 80 per cent of the [C II] emission if the effects of lensing are ignored. Taking into account possible extended [C II] moves MS0451-H to within 1σ of the local relation.

In A1703-zD1, we aim to account for lens smearing by tapering the datacube to match the spatial extent of A1703-zD1 in the *HST* imaging, allowing us to obtain a more accurate flux measurement. Without tapering and using the same routine as described in Section 2.3.1, we calculate a [C II] integrated flux value which is 51 per cent of our fiducial measurement. However, extended [C II] beyond the rest-frame UV could still be missed even with our current tapering strategy, consistent with Carniani et al. (2020).

2.4.2 L_{IR} and SFR_{IR} constraints

As discussed in Section 4.3, the continuum flux remains undetected for all our sources. We calculate upper limits for L_{IR} and SFR_{IR} by assuming an optically-thin grey-body infrared SED (Casey, 2012) using $T = 50\text{K}$ and $\beta = 1.5$, and present the results in Table 2.2. We estimate that these sources are likely below the classification of Luminous Infrared Galaxies (LIRG; $L_{\text{IR}} > 10^{11} L_{\odot}$). We furthermore find obscured SFR below $5\text{--}58 M_{\odot} \text{yr}^{-1}$ (3σ limits), which suggests less than 44 – 74% of star-formation comes out in the IR, consistent with recent studies (e.g., Bowler et al., 2018; Schouws et al., 2021).

We derive UV slopes (β) and upper limits on the Infrared Excess ($\text{IRX} = L_{\text{IR}}/L_{\text{UV}}$) for all our targets (see Tables 2.1 and 2.2) and find that the upper-limits for EGS-5711 and EGS-1952 are consistent with either the Meurer et al. (1999) relation or a SMC-like dust attenuation.

However, given a moderately red UV slope for A1703-zD1 of $\beta \sim -1.56$, we find this galaxy to be more consistent with an SMC like dust attenuation law, in agreement with stacking results of faint LBGs at $z \approx 2 - 10$ (Bouwens et al., 2016; Fudamoto et al., 2020, though see Schouws et al. 2021 for a discussion on the impact of the assumed dust temperature).

2.4.3 Velocity Structure of A1703-zD1

We use the spatial extent of the [C II] detection to investigate the velocity structure of A1703-zD1. We see a velocity gradient across A1703-zD1 shown in Figure 2.13. We find a maximum projected velocity difference over the galaxy (Δv_{obs}) of $103 \pm 22 \text{ km s}^{-1}$ from the first moment map. Such a velocity gradient could be the signature of a rotating disk, whilst another possibility is a merger of [C II] emitting galaxies. Similar velocity gradients are present in previous observations of high redshift galaxies (e.g., Smit et al., 2018; Hashimoto et al., 2019; Matthee et al., 2019; Fujimoto et al., 2021) as well as in simulations (Dekel & Burkert, 2014).

To determine the likelihood of a disk-like rotation we compare the projected velocity range of a galaxy with the velocity dispersion of the system using $\Delta v_{\text{obs}}/2\sigma_{\text{tot}}$, where a ratio of > 0.4 indicates a likely rotation dominated system (Förster Schreiber et al., 2009). We find $\Delta v_{\text{obs}}/2\sigma_{\text{tot}} = 0.79 \pm 0.23$ for A1703-zD1, which supports the interpretation of a possibly rotation dominated system. Bradley et al. (2012) find three distinct star-forming clumps with an extended linear morphology in the source-plane reconstruction of A1703-zD1. In Figure 2.13 we show the deflection due to the lensing magnification, using the LTM strong-lensing model published by Zitrin et al. (2010). This stretching of the source-plane leads to an effective increase in resolution of $3.5\times$, in the direction of the green arrow shown in Figure 2.13. The red and blue components identified in Figure 2.13 appear co-spatial with the two brightest clumps from Bradley et al. (2012). Clumps like this have been identified previously in high redshift galaxies and can be attributed to merging galaxies or large clumpy star formation due to the increased gas content in high-redshift galaxies. Higher resolution [C II] observations will be required to confirm a disk-like structure in A1703-zD1.

If we assume ordered circular rotation we can use the FWHM of [C II] to estimate the dynamical mass. We use $M_{\text{dyn}} = 1.16 \times 10^5 V_{\text{cir}}^2 D$ (Capak et al., 2015), where $V_{\text{cir}} = 1.763 \times \sigma_{[\text{CII}]} / \sin i$ in km s^{-1} , i is the disk inclination angle, and D is the disk diameter in kpc (we use $D = 4$ kpc found in Bradley et al. 2012; measured in the reconstructed sources-plane image). Assuming a viewing angle of 45 degrees we find $M_{\text{dyn}} = 12.1 \pm 4.8 \times 10^9 M_{\odot}$. The stellar mass of A1703-zD1 was estimated to be $0.7 \pm 0.1 \times 10^9 M_{\odot}$ (Bradley et al., 2012). This stellar mass is only ~ 6 per cent of the total dynamical mass that we measure. This is somewhat low compared to dynamical measurements from $\text{H}\alpha$ surveys at cosmic noon; for example, Stott et al. (2016) find a value of 22 ± 11 per cent in a sample of 584 $z \sim 1$ galaxies and Wuyts et al. (2016)

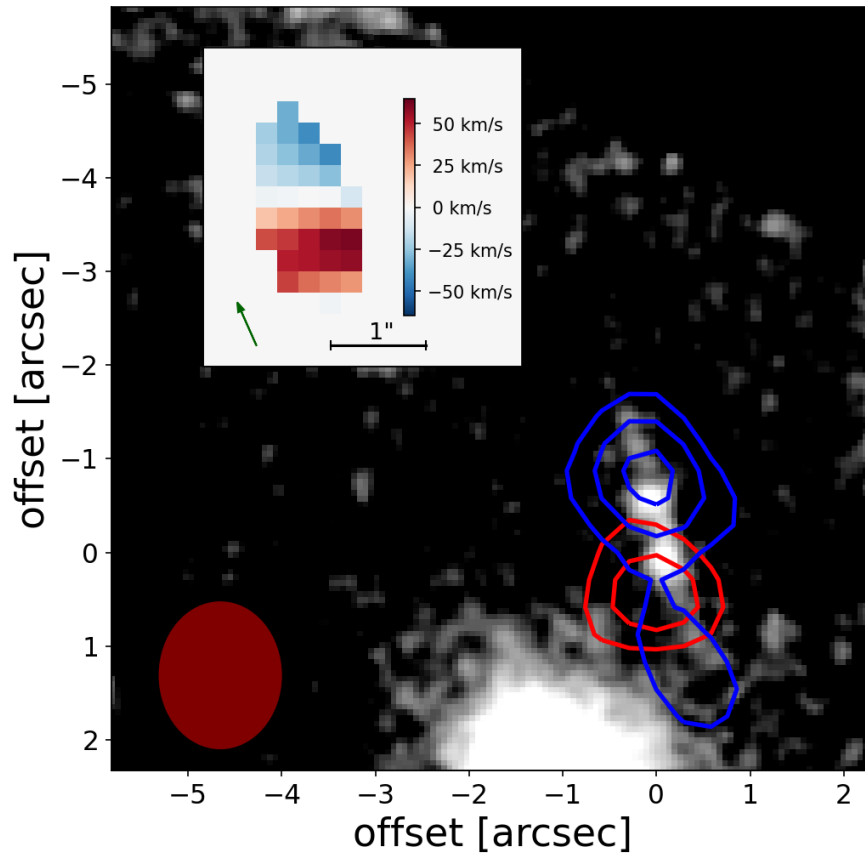


Figure 2.13: Main Panel: HST imaging overlaid with contours from the untapered datacube corresponding to 2, 3 and 4σ [C II] emission collapsed over channels redwards (red contours) and bluewards (blue contours) of the measured line centre, showing evidence for a velocity gradient. The observations are spatially resolved, as shown by the filled ellipse indicating the beam size (1.57×1.31 arcsec). **Inset Panel:** First moment map of the detected [C II] from A1703-zD1 (showing pixels above 2σ). We measure a velocity difference over the galaxy of 103 ± 22 km s $^{-1}$. We show the green arrow to illustrate the stretching of the arc in the image plane with respect to the source-plane image of this source.

find a value of 32_{-7}^{+8} per cent in star forming galaxies $0.6 < z < 2.6$. Larger and more detailed samples of dynamical measurements at $z \sim 7$ will be needed to establish evolutionary trends with redshift. We also note that there are large uncertainties on the dynamical mass, as there is a large dependency on the viewing angle (which is unknown). However, this low ratio does suggest that A1703-zD1 is a gas rich system, similar to typical star-forming galaxies 3 Gyr later in cosmic time.

2.5 Summary and conclusions

We have presented new NOEMA observations, scanning for the [C II]158 μ m line in three Lyman break galaxies with photometric redshifts at $z = 6.6 - 6.9$. Our main findings are as follows:

- We detect [C II] in one of our three sources, confirming the redshift at $z = 6.8269 \pm 0.0004$ for the strongly lensed galaxy A1703-zD1 (6.1σ). Our non-detections are consistent with these being dust-poor galaxies with low [C II] luminosity.
- We carefully account for any extended emission of [C II] due to lens smearing in A1703-zD1 and find the [C II] luminosity to be consistent with, but slightly below, the local $L_{[\text{C II}]} - \text{SFR}$ relation.
- No continuum emission is detected in any of the three targeted sources, suggesting less than 44 – 74% of star-formation comes out in the IR. For A1703-zD1, our results are most consistent with an SMC attenuation curve.
- We see a velocity gradient across A1703-zD1, with a kinematic ratio that suggests a possible rotation dominated system, though higher resolution [C II] observations will be needed to confirm this.

Over the last few years ALMA has demonstrated its role as a “redshift machine” in the Epoch of Reionisation by confirming galaxies out to redshift $z = 9$. In this paper we have demonstrated the ability of NOEMA to search for [C II] in ‘normal’ star-forming galaxies at $z > 6$, complementing ALMA by observing EoR galaxies in the Northern Hemisphere, with [C II] as a reliable spectroscopic tracer of these distant systems. With the launch of JWST this capability will be particularly useful for rare, lensed sources and intrinsically luminous objects that will be discovered far outside the limited JWST survey area using the next generation of large area surveys, such as the Euclid mission and the Rubin observatory.

Acknowledgements

We thank the anonymous referee for their constructive feedback and useful suggestions. RS acknowledges support from a STFC Ernest Rutherford Fellowship (ST/S004831/1). AZ acknowledges support by Grant No. 2020750 from the United States-Israel Binational Science Foundation (BSF) and Grant No. 2109066 from the United States National Science Foundation (NSF), and by the Ministry of Science & Technology, Israel. JH gratefully acknowledges support of the VIDI research program with project number 639.042.611, which is (partly) financed by the Netherlands Organisation for Scientific Research (NWO).

Context free quotes

“I need a horse”

“Don’t mix food with glue”

“When I’m drunk I lose gravity”

“One is an accident, two is statistics”

“My hands and legs are differently employed”

“It’s ridiculously large and I just rattle around in there”

“Let’s not talk about potatoes and we can still be friends”

“She just needs a human to spray her with water”

“Unless you only have a fork, soup is good”

“Now I know why he used Mickey Mouse”

“We don’t have pockets we have issues”

“Your feet are not as God intended”

“You’re a chakalaka girl”

Galactic ionised outflows are more common when the radio emission is compact in AGN host galaxies

In this chapter I present work exploring the relationship between radio size and the prevalence of ionised outflows, as traced using broad [O III] emission-line profiles in Sloan Digital Sky Survey (SDSS) spectra. The sample used in this study consists of 2922 $z < 0.2$, spectroscopically-identified Active Galactic Nuclei (AGN). In Section 3.2 I outline the sample selection, catalogues and the radio data used. In Section 3.3 I describe the analysis techniques used. In Section 3.4 I discuss the results and in Section 3.5 I give the conclusions of this work. This chapter is based on the work published in [Molyneux et al. \(2019\)](#).

Using a sample of 2922 $z < 0.2$, spectroscopically-identified Active Galactic Nuclei (AGN) we explore the relationship between radio size and the prevalence of extreme ionised outflows, as traced using broad [O III] emission-line profiles in Sloan Digital Sky Survey (SDSS) spectra. To classify radio sources as compact or extended, we combine a machine-learning technique of morphological classification with size measurements from two-dimensional Gaussian models to data from all-sky radio surveys. We find that the two populations have statistically different [O III] emission-line profiles, with the compact sources tending to have the most extreme gas kinematics. When the radio emission is confined within $3''$ (i.e., within the spectroscopic fibre or

$\lesssim 5$ kpc at the median redshift), there is twice the chance of observing broad [O III] emission-line components, indicative of very high velocity outflows, with $\text{FWHM} > 1000 \text{ km s}^{-1}$. This difference is most enhanced for the highest radio luminosity bin of $\log[L_{1.4\text{GHz}}/W \text{ Hz}^{-1}] = 23.5 - 24.5$ where the AGN dominate the radio emission; specifically, $> 1000 \text{ km s}^{-1}$ components are almost four-times as likely when the radio emission is compact in this subsample. Our follow-up $\approx 0.3'' - 1''$ resolution radio observations, for a subset of targets in this luminosity range, reveal that radio jets and lobes are prevalent, and suggest that compact jets might be responsible for the enhanced outflows in the wider sample. Our results are limited by the available, relatively shallow, all-sky radio surveys; however, forthcoming surveys will provide a more complete picture on the connection between radio emission and outflows. Overall, our results add to the growing body of evidence that there is a close connection between ionised outflows and compact radio emission in highly accreting ‘radiative’ AGN, possibly due to young or frustrated, lower-power radio jets.

3.1 Introduction

Understanding the physical processes that connect galaxy growth and the growth of their central supermassive black holes remains one of the biggest outstanding problems of galaxy evolution research (e.g., [Alexander & Hickox, 2012](#); [Kormendy & Ho, 2013](#); [Heckman & Best, 2014](#); [King & Pounds, 2015](#); [Harrison, 2017](#)). The sites of growing supermassive black holes are observationally identified as “Active Galactic Nuclei” due to the enormous amounts of energy that they release across the electromagnetic spectrum. Cosmological models and simulations of galaxy evolution require some fraction of this released energy to couple to the surrounding interstellar medium (ISM) in order to reproduce the observed properties of massive galaxies and the surrounding intergalactic medium (IGM; e.g., [Vogelsberger et al., 2014](#); [Hirschmann et al., 2014](#); [Crain et al., 2015](#); [Beckmann et al., 2017](#); [Choi et al., 2018](#)). However, the details of how this process works in the real Universe are not well established, particularly during periods of rapid black hole growth (e.g., [Harrison, 2017](#)).

One observational strategy to establish the connection between supermassive black hole growth and galaxy evolution is to identify, and to characterise, AGN-driven outflows in the multi-phase ISM (e.g. [Veilleux et al., 2005](#); [Morganti et al., 2005](#); [Carniani et al., 2015](#); [Perna et al., 2015](#);

Brusa et al., 2015; Balmaverde et al., 2016; Rupke et al., 2017; Lansbury et al., 2018; Fluetsch et al., 2019; Ramos Almeida et al., 2019). Of most relevance for this study, is the presence of broad and-or asymmetrical [O III] λ 5007 emission-line profiles which have long been used to trace outflows of warm ($\approx 10^4$ K) ionised gas in the narrow-line region of AGN (Heckman et al., 1984; Whittle, 1985). These outflows can be located on ≈ 10 pc – 10 kpc scales (Harrison et al., 2014; Husemann et al., 2016; Rupke et al., 2017; Villar-Martín et al., 2017; Finlez et al., 2018). This is a particularly useful outflow tracer because, through large optical spectroscopic surveys such as the Sloan Digital Sky Survey (SDSS; York et al., 2000), measurements on large samples of $z \lesssim 0.8$ AGN can be obtained (e.g., Mullaney et al., 2013; Woo et al., 2016; Zakamska & Greene, 2014; Zakamska et al., 2016; Balmaverde et al., 2016). Recent and on-going near-infrared spectroscopic surveys make it possible to obtain similar constraints on large samples of $z \approx 1 - 3$ galaxies (e.g., Harrison et al., 2016; Leung et al., 2017; Förster Schreiber et al., 2019a).

Here we are particularly interested in the observations showing that the prevalence and/or velocities of [O III] outflows is related to the radio luminosity (Mullaney et al., 2013; Villar Martín et al., 2014; Zakamska & Greene, 2014; Hwang et al., 2018); namely, that there is a higher prevalence of the most powerful outflows when the radio luminosity is higher. Although some work does not find such a relationship, they can suffer from a relatively high radio detection limit; for example the study of Wang et al. (2018) is limited to radio luminosities of $\log[L_{1.4\text{GHz}}/\text{W Hz}^{-1}] \gtrsim 24$. Indeed, the relationship between outflows and radio emission, may even be strongest for AGN with moderate to intermediate radio luminosities (i.e., $\log L_{1.4\text{GHz}}/\text{W Hz}^{-1} \approx 23 - 25$; see discussion in e.g., Mullaney et al., 2013; Zakamska et al., 2016; Jarvis et al., 2019).

For the most radiatively luminous AGN, sometimes called “quasars”, it is often assumed that the dominating radiative power of the central source drives the observed outflows (e.g., Faucher-Giguère & Quataert, 2012; King & Pounds, 2015). However, the observed relationship between outflows and radio emission, opens up the possibility that the mechanical power of radio jets may be a crucial outflow driving mechanism in these systems (e.g., Mullaney et al., 2013). Indeed, from low-power AGN through to the most extreme sources, radio jets are seen to interact with the ISM (e.g., Whittle et al., 1986; Ferruit et al., 1998; Tadhunter et al., 2014; Riffel et al., 2014; Kharb et al., 2017; Nesvadba et al., 2017; Finlez et al., 2018; Morganti et al., 2018; Jarvis et al., 2019). On the other hand, star-formation driven outflows and quasar winds that shock the ISM

provide alternative possibilities for producing the observed radio emission and correlation with outflow properties (e.g., Condon et al., 2013; Nims et al., 2015; Zakamska et al., 2016; Hwang et al., 2018; Panessa et al., 2019).

A tentative result that may shed more light on the outflow-radio connection is presented by Holt et al. (2008), who find that [O III] outflows are more extreme in *compact* radio galaxies (radio emission confined within $\lesssim 10$ kpc), compared to *extended* radio galaxies. The authors propose that radio jets, early in their evolution, are strongly interacting with the ISM in the nuclear regions (e.g., van Breugel et al., 1984; O’Dea et al., 1991; Bicknell et al., 2018; Mukherjee et al., 2018b). However, the primary sample of Holt et al. (2008) contains only 14 sources, all of which represent the most powerful - and rare - radio AGN ($\log[L_{5\text{GHz}}/\text{W Hz}^{-1}] > 26.4$) and, furthermore, the comparison samples are also small and inhomogeneous. It is therefore not clear how applicable this result is to the bulk of the AGN population. Here we test if this result holds for more typical AGN which do not have extreme radio luminosities using a sample of ≈ 3000 targets with both [O III] emission-line profile measurements and radio size measurements.

We adopt $H_0 = 70 \text{ km s}^{-1} \text{ Mpc}^{-1}$, $\Omega_M = 0.3$, and $\Omega_\Lambda = 0.7$ throughout, and assume a radio spectral index of $\alpha = 0.8$ when calculating the rest-frame 1.4 GHz radio luminosity, where $F_\nu \propto \nu^{-\alpha}$ (see Jarvis et al., 2019).

3.2 The Sample, Catalogues and Radio Data

We aim to explore the relationship between the size of radio emission and the presence of ionised outflows in AGN host galaxies. To do this we make use of the valued-added spectroscopic catalogue of $\approx 24,000$ AGN that were identified from the Sloan Digital Sky Survey (SDSS, Data Release 7; Abazajian et al. 2009) that is presented in Mullaney et al. (2013)¹ and is consequently cross-correlated with all-sky radio surveys.

¹<https://sites.google.com/site/sdssalpaka/downloads>

3.2.1 Catalogues and sample selection

The parent catalogue of [Mullaney et al. \(2013\)](#) contains 24624 sources that were identified as AGN from optical spectroscopy, using a combination of emission-line flux ratios (‘BPT’ diagnostics; [Baldwin et al. 1981](#); to identify ‘Type 2’ AGN) and the presence of broad $H\alpha$ emission-line components (to identify ‘Type 1’ AGN). For each AGN, the emission-lines, including the $[O\ III]\lambda 5007$ line, were fit with two Gaussian components in order to search for broad emission-line components indicative of ionised outflows. The final sample of AGN was cross-matched, by [Mullaney et al. \(2013\)](#), to the 1.4 GHz radio surveys of FIRST ([Becker et al. 1995](#)) and NVSS ([Condon et al. 1998](#)) largely following the procedure outlined in [Best et al. \(2005\)](#) but including sources down to signal-to-noise ratios > 3 in NVSS (i.e., 1.4 GHz flux densities of ≈ 2 mJy). Here, we make use of the matched catalogue as our ‘parent sample’; however, we update the FIRST radio measurements using the latest, and final, catalogue that is presented in [Helfand et al. \(2015\)](#) and contains radio sources with signal-to-noise ratios of ≥ 5 (detection limit ≈ 1 mJy).

As in [Mullaney et al. \(2013\)](#) we prefer to use the NVSS flux density measurements to infer the *total* radio luminosity densities ($L_{1.4\text{GHz}}$) because the larger beam (full-width-at-half-maximum [FWHM] ≈ 45 arcsec), compared to FIRST, reduces the chances of resolving away flux or missing extended radio structures. However, the FIRST data with a resolution of ≈ 5 arcsec is used for more accurate positional matching to the SDSS sources ([Mullaney et al. 2013](#)). Furthermore, we also make use of superior spatial resolution of the FIRST data for radio size measurements and morphological classifications (see Section 3.3.2).

Starting with the parent catalogue, we created the final sample to be used in this work by applying the following criteria:

1. We only consider AGN within a redshift range of $0.02 < z < 0.2$ (discussed in more detail below), leaving a sample of 16326 AGN.
2. We only consider AGN which have 1.4 GHz radio detections in the FIRST or NVSS catalogues (required to characterise the spatial extent of the radio emission), leaving a sample of 2948 AGN.

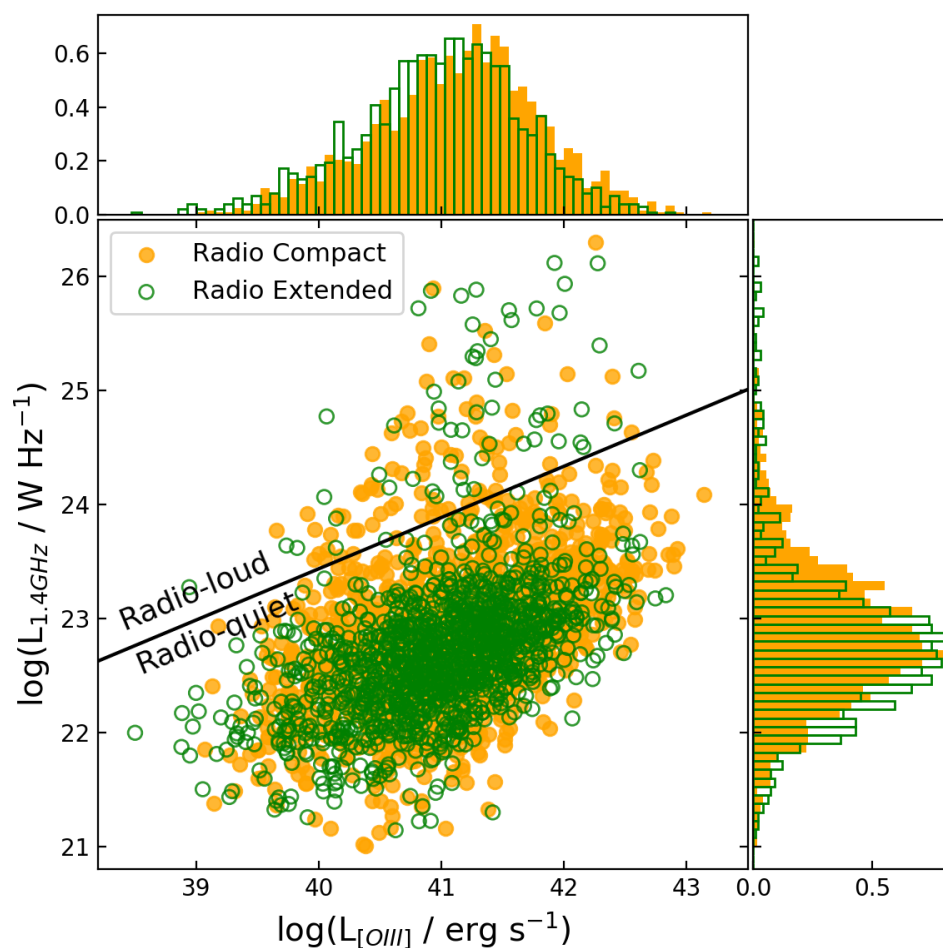


Figure 3.1: Radio luminosity (rest-frame 1.4 GHz) versus [O III] luminosity for our final sample of 2922 AGN. The line shows the division of ‘radio quiet’ and ‘radio loud’ AGN following [Xu et al. 1999](#). The sources classified as having extended radio emission are shown using green hollow symbols and those classified as radio compact are shown using filled orange symbols. The normalised histograms of luminosities for both populations are also shown as hollow and filled histograms, respectively. The radio and [O III] luminosities of the two samples are broadly similar; nonetheless, we take into account these small differences when comparing the two populations in Section 3.4.2.

3. We removed a small number of sources (only 0.9% of the sample) where, either: (a) the two-component fits to the [O III] emission-line profiles failed to converge in the [Mullaney et al. \(2013\)](#) catalogue (3 targets removed); or (b) the NVSS-only detections (i.e., those not in the FIRST catalogue) are not covered by FIRST imaging at all (which is required for our later analyses; Section 3.3.2) or that, by visual inspection, were associated with the wrong optical counterpart (usually mergers; 23 targets removed). This results in our final sample of 2922 AGN.

The upper bound of the redshift range in step (1) is a compromise between keeping a significant

number of luminous AGN in the sample, whilst having a reasonable detection limit on the radio (i.e., a limit of $\log[L_{1.4\text{GHz}}/\text{W Hz}^{-1}] \approx 22.8$ at the highest redshift of $z = 0.2$) and a reasonable physical resolution (1 arcsec corresponds to ≤ 3.3 kpc for $z \leq 0.2$). The lower bound of $z = 0.02$ is such that the 3 arcsec SDSS fibre still covers a reasonable fraction of the galaxy compared to the higher redshift sources (1 arcsec corresponds to 0.4 kpc at $z = 0.02$). We further consider the varying physical size scales covered by the SDSS spectroscopy during our results presented in Section 3.4.2.

The final sample used in this work consists of 2922 AGN. The distribution of rest-frame 1.4 GHz radio luminosities and the [O III] luminosities are presented in Figure 3.1. Overall the sample covers five orders of magnitude in radio luminosity, with a median of $\log[L_{1.4\text{GHz}}/\text{W Hz}^{-1}] = 22.8$, and four orders of magnitude in [O III] luminosity, with a median of $\log[L_{[\text{OIII}]}/\text{erg s}^{-1}] = 41.1$. The sample is dominated by “radio quiet” AGN (95 percent) following the criteria of Xu et al. 1999 (see dividing line in Figure 3.1).

3.2.2 Follow-up radio observations

To aid the interpretation of our results on this large sample of 2922 AGN, we also make use of follow-up radio observations that we have carried out with the Karl G. Jansky Very Large Array (VLA) that reach a higher spatial resolution than achieved by the FIRST and NVSS surveys. Example data are compared to the FIRST images in Figure 3.2. For our VLA observations we targeted a subset of the $z < 0.2$ AGN from Mullaney et al. 2013 to observe at 1.4 GHz (at ≈ 1 arcsec resolution) and 6 GHz (at ≈ 0.3 arcsecond resolution).² As in this work, the targets for these programmes were selected from Mullaney et al. (2013) to be radio detected in FIRST and/or NVSS but with an additional focus on AGN with $L_{[\text{OIII}]} > 10^{42}$ erg s⁻¹ (see discussion in Section 3.4.2). The radio images typically have root-mean-square (RMS) noise values of 10–50 μJy . The first 10 targets from these follow-up programmes were pre-selected to have ionised outflows and are presented in Jarvis et al. (2019). The wider sample of 42, with no pre-selection on outflows, is presented in Jarvis et al. (2021). In Figure 3.2, we include examples of our radio images from the full sample, with our 1.4 GHz images shown as green contours and our 6 GHz images inset with blue contours. The observing strategy and imaging techniques are described in Jarvis et al. 2019. In this work we make use of these images to qualitatively describe the radio

²The VLA programme IDs are: 13B–127; 16A–182 and 18A–300.

morphologies and to also give an indication as to what structures might be prevalent across the wider sample (e.g., radio jets; Section 3.3.2; Figure 3.2).

3.3 Analyses

In this work we are interested in: (1) searching for high-velocity ionised gas, indicative of outflows, by characterising the [O III] λ 5007 emission-line profiles and (2) relating the ionised gas kinematics to the spatial extent of the radio emission. In the following we describe how we characterise the [O III] emission-line profiles (Section 3.3.1) and constrain the spatial extent of the radio emission, defining each source as having either compact or extended radio emission (Section 3.3.2).

3.3.1 Characterising the emission-line profiles

The velocity widths of the [O III] emission-line profiles are good tracers of the ionised gas kinematics, and in particular, for identifying non-galactic motions associated with outflows (e.g., Mullaney et al., 2013; Liu et al., 2013). Here we make use of the two component fits to the [O III] emission-line profiles provided by Mullaney et al. (2013) and characterise the velocity widths in two different ways (we show two examples in Figure 3.3):

- The full-width-at-half-maximum of the second, broader, component (FWHM_B ; see bottom panel in Figure 3.3). For 2239 of the 2922 AGN in the parent sample, i.e., 77%, such a second component is required. We discuss the prevalence of high velocity (broad) components in Section 3.4.1.
- The flux-averaged FWHM of the two Gaussian components,

$$\text{FWHM}_{\text{Avg}} = \sqrt{(\text{FWHM}_A F_A)^2 + (\text{FWHM}_B F_B)^2},$$

where F_A and F_B are the fractional fluxes contained within the two fitted components, A and B. This definition has the advantage of considering lines that are fitted either with one or two Gaussians the same (e.g., sources may have broad emission-line profiles but are satisfactorily fitted with only a single Gaussian; Mullaney et al., 2013, see upper panel in Figure 3.3).

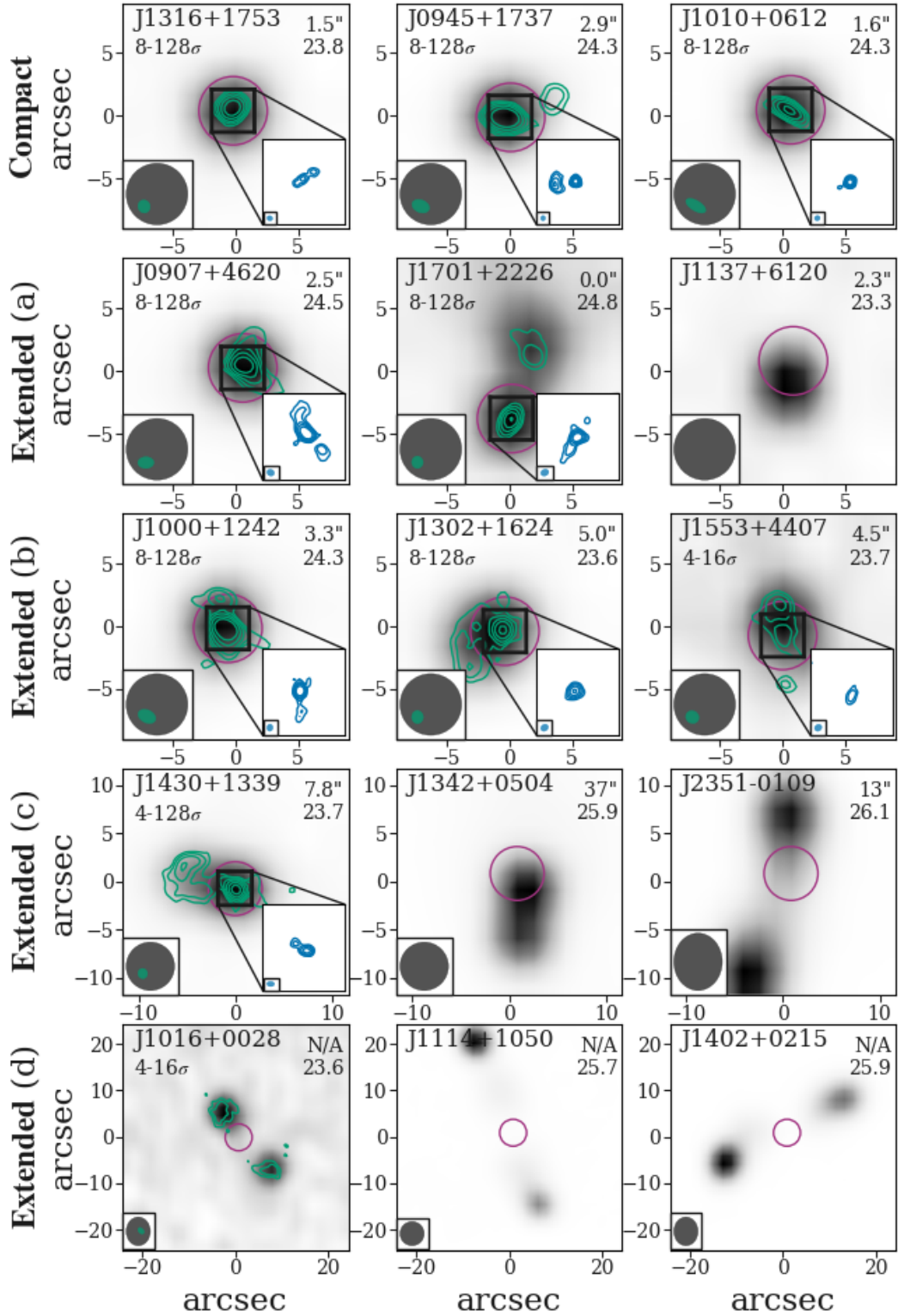


Figure 3.2: Example radio images to demonstrate our classification into compact and extended radio sources (Section 3.3.2). Grey-scale images show 1.4 GHz FIRST data (≈ 5 arcsec resolution). Where available, green contours are from our ~ 1 arcsec resolution 1.4 GHz images and the insets (**blue contours**) are from our ~ 0.3 arcsec resolution 6 GHz images (Section 3.2.2). Synthesised beam(s) are represented by appropriately coloured ellipses. Labels provide each galaxy’s name (Jarvis et al., 2019, 2021), minimum and maximum contour levels, radio sizes from FIRST (R_{Maj}) and radio luminosities (in $\log[W \text{ Hz}^{-1}]$). Magenta circles represent the SDSS fibre size. Compact radio sources (top row) are defined to have their radio emission dominated within the SDSS fibre, whilst extended sources (bottom four rows) show significant emission outside of the fibre extent.

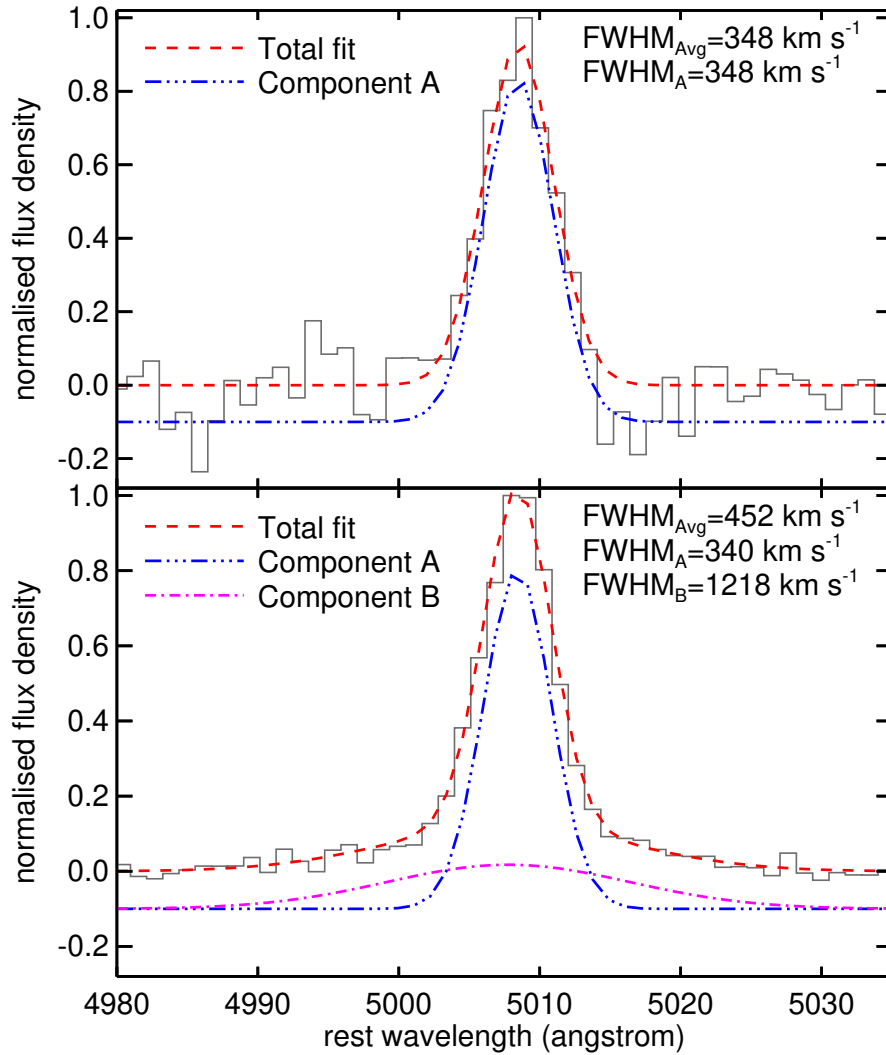


Figure 3.3: [O III] λ 5007 emission-line profiles (grey curves) and their fits (dashed curves) for an example with a single component (*Upper panel*) and an example with two components (*Lower panel*). The individual components “A” and “B” are shown as dot-dashed and three-dot-dashed curves, respectively, artificially offset by -0.1 in the y-axis. In this work we consider both the velocity widths of any identified broad components ($FWHM_B$) and the flux-weighted average line widths of all identified components ($FWHM_{Avg}$).

We take into account the corresponding uncertainties on each of these velocity width values [Mullaney et al. 2013](#), when presenting our results in Section 3.4.2.

3.3.2 Compact and extended radio emission

In order to make a direct connection to the [O III] emission-line profiles seen in the spectroscopy (see above), we determine which sources have their radio emission concentrated within, or outside of, the spatial extent of the SDSS fibre (i.e., 3 arcsec diameter). For the redshift range of

our sample ($z = 0.02 - 0.2$), 3 arcsec corresponds to 1.2 – 10 kpc; however, we note that our conclusions hold if we only consider sources $z = 0.1 - 0.2$, for which the physical size scale varies by less than a factor of two (Section 3.4.2).

To characterise the extent of the radio emission we combine two different approaches: (1) we use radio major axis sizes (R_{maj}) from simple elliptical Gaussian models (Section 3.3.3) and (2) we use an automated morphological classification scheme (Section 3.3.4). It was necessary to combine both of these approaches because whilst the former method has the advantage of providing a quantitative measure of the radio sizes, and corresponding uncertainties, it has the disadvantage of missing structures that are not well characterised by a single elliptical Gaussian model. For example, there are 89 sources in our sample which are detected by NVSS but are not in the FIRST catalogue at all, largely because the emission is located in large diffuse structures or off-nuclear lobes which are missed due to the relatively small beam of FIRST (e.g., see bottom row in Figure 3.2). Furthermore, in the FIRST catalogue, the fits to the images are dominated by central cores even if there is additional extended radio structures beyond the core (e.g., see rows 2 & 4 in Figure 3.2).

3.3.3 Basic radio size measurements

Helfand et al. (2015) fit an elliptical Gaussian model for each source detected in their FIRST catalogue. We make use of these major axis sizes (R_{Maj}) which have been deconvolved for the point-spread function (or ‘beam’), noting that 89 sources (3% of the sample) do not have any constraints on R_{Maj} because they only have radio detections in the NVSS catalogue (see above).³ The uncertainties in R_{Maj} depend on the signal-to-noise ratio (SNR), following approximately $\sigma(R_{\text{Maj}}) = 10 \times (1/\text{SNR} + 1/75)$ arcsec, where $\text{SNR} = (F_{\text{peak}} - 0.25)/\text{RMS}$, F_{peak} is the peak flux density and RMS is the root-mean-square noise of the image (Helfand et al. 2015). The signal-to-noise ratios are not simply $F_{\text{peak}}/\text{RMS}$, because of the applied CLEAN bias correction to the peak flux density. Importantly, as demonstrated by this equation, it is possible to obtain sizes with reasonable uncertainties well below the size of the nominal point-spread-function when the sources are detected with high signal-to-noise ratios. For example, a source

³Noise can cause the R_{Maj} sizes (before deconvolution) to be smaller than the beam (see Helfand et al. 2015). For the 618 cases in our sample the corresponding deconvolved sizes are assumed to be zero (example in second row of Figure 3.2).

with a $\text{SNR} = 10$ has a size uncertainty of ≈ 1 arcsec. We take into account the size uncertainties when presenting our results in Section 3.4.2. We plot the R_{Maj} values in Figure 3.4.

We can also define how extended a source is in the FIRST images based on the ratio of peak and integrated flux densities following $\theta = \sqrt{F_{\text{Int}}/F_{\text{Peak}}}$ (Kimball & Ivezić, 2008), where F_{Int} is the integrated flux from the elliptical Gaussian models (Helfand et al., 2015). These θ values describe how resolved a source is because the more extended it is, the larger the $F_{\text{Int}}/F_{\text{Peak}}$ ratio. A source in FIRST can typically be considered ‘extended’ if $\theta \geq 1.06$ (Kimball & Ivezić, 2008). We find that R_{Maj} and θ are well correlated for our sample, with a correlation coefficient value of 0.91, and the overall conclusions presented throughout this work are insensitive to the choice of setting $R > 3$ arcsec versus $\theta > 1.06$ to define a source as “radio extended”.

3.3.4 Morphological classification

As previously described, for a complete characterisation of which sources are compact or extended in the radio, it is important to apply a morphological classification in addition to simple sizes (e.g., to identify core-lobe structures). To do this we make use of the “FIRST Classifier”, presented in Alhassan et al. (2018), which is an automatic morphological classification tool applied to FIRST images that uses a trained, deep Convolutional Neural Network model. The code was “trained” using a set of radio sources with known classifications. Sources are classified as FRI, FRII (Fanaroff and Riley class I and II; Fanaroff & Riley 1974), Bent (determined to have a more complex, “bent” nature) or Compact. For the current study we are not interested in the individual classifications of FRI, FRII or Bent, just if the radio emission is extended or compact. The model achieves an overall accuracy of 97 per cent based on control samples (Alhassan et al., 2018).

We performed our own random visual inspection to verify that the morphological classifications returned by the FIRST Classifier were reliable. Furthermore, we could make use of the subset of our sample which are covered by our follow-up higher resolution radio observations (Section 3.2.2; Figure 3.2). Indeed, the FIRST Classifier is successful at identifying extended radio structures (e.g., those sources in the second and fourth row of Figure 3.2). Nonetheless, sources which are smoothly extended beyond $3''$ in FIRST, without clear distinct morphological structures can be miss-classified as compact by the FIRST Classifier (e.g., see third row of

Figure 3.2). Therefore, we found that a combination of using R_{Maj} and the results of the FIRST Classifier was required to robustly classify all of the sources in our sample as either “Radio Compact” or “Radio Extended”.

3.3.5 Final classification into compact and extended radio sources

As described above, we wish to define compact sources as those where the radio emission is dominated *within* the SDSS fibre (i.e., $\lesssim 3$ arcsec), and define sources as extended otherwise. Based on the measurements described in the previous two sub-sections, we apply the following criteria to separate the two populations:

- **Compact:** $R_{\text{Maj}} \leq 3$ arcsec and not identified as extended by the FIRST Classifier (1620 sources; i.e. see first row in Figure 3.2).
- **Extended (a):** Sources which have $R_{\text{Maj}} \leq 3$ arcsec but identified as extended by the FIRST Classifier (246 sources). Visual inspection shows that these targets typically have strong cores (which results in the small sizes from simple 2D-Gaussian fits) but with additional extended structures expanding beyond the core which are picked up the the FIRST Classifier (see second row in Figure 3.2).
- **Extended (b):** $R_{\text{Maj}} > 3$ arcsec but not classified as extended by the FIRST classifier (679 sources). Visual inspection reveals that these targets are large but do not have clear discernible features which would be picked up by the FIRST classifier (see third row in Figure 3.2).
- **Extended (c):** $R_{\text{Maj}} > 3$ arcsec and classified as extended by the FIRST Classifier. These sources are clearly extended with morphological structures on large scales (288 sources; see fourth row in Figure 3.2).
- **Extended (d):** Those not detected in the FIRST catalogue but are identified in NVSS (89 sources). Visual inspection verifies that these targets are large radio sources, which are usually dominated by symmetrical lobes (see bottom row of Figure 3.2).

Using these criteria 1302 sources are classified as extended and 1620 are classified as compact in the radio. A visual inspection of the FIRST images, in combination with our follow-up radio observations (Figure 3.2) provides verification that these criteria are effective at separating sources where the radio emission is dominated within 3 arcsec or extends beyond. Unsurprisingly there are a few ambiguous cases within the full sample of 2922. For example, from our follow-up radio observations, J0945+1737 in the top row of Figure 3.2 is known to have a weak radio structure beyond the central 3 arcsec; however, this constitutes only $\approx 9\%$ of the total radio emission and we see that the majority of the radio emission is due to a compact $\lesssim 2$ kpc central core and radio jet (Jarvis et al. 2019). Overall we feel confident that for this statistical study our classification into compact and extended radio sources is sufficient and is likely the best that can be achieved with the current radio surveys.

The radio and [O III] luminosities for the compact and extended samples are represented as solid and hollow symbols, respectively, in Figure 3.1. Their median radio luminosities are $\log[L_{1.4\text{GHz}}/\text{W Hz}^{-1}] = 22.81$ and 22.68 , respectively, with a standard deviation 0.7 dex in both cases. The median [O III] luminosities are $\log[L_{[\text{OIII}]}/\text{erg s}^{-1}] = 41.18$ and 41.03 , respectively, both with a standard deviation of 0.7 dex. Although there are only small, $\approx 40\%$, differences in the median radio and [O III] luminosities of the two populations, we note that we repeat all of our experiments using individual 1 dex bins of radio and [O III] luminosity to account for these differences, in Section 3.4.2.

With the final classifications of compact versus extended radio emission we can now explore the relationship between radio size and ionised gas kinematics.

3.4 Results and Discussion

To investigate the relationship between the prevalence of ionised outflows and the size of the radio emission in AGN host galaxies, we have constructed a sample of 2922 $z = 0.02 - 0.2$, spectroscopically-identified AGN which are detected in 1.4 GHz radio images (Section 3.2.1; Figure 3.1). Using a combination of direct size measurements and morphological classifications we have identified the sources which are “compact” versus “extended” in the radio, based upon

whether the radio emission is dominated within or outside of ≈ 3 arcsec (or ≈ 5 kpc at the average redshift; Section 3.3.2; Figure 3.2). Two Gaussian component fits to the [O III] emission-line profiles have been used to characterise the ionised gas velocities using: (1) the width of any identified broad emission-line components (FWHM_B) and (2) the flux-averaged width of the two components (FWHM_{Avg} ; Section 3.3.1; Figure 3.3). Here we present our results on the trend between radio size and ionised gas velocities (Section 3.4.1) and with the prevalence of ionised outflows (Section 3.4.2), before discussing the implication of our results in the context of AGN feedback and how galactic outflows are driven (Section 3.4.3). The quantitative results of our analyses are presented in Table 3.1.

z	$L_{1.4\text{GHz}}$ ($\log[\text{W/Hz}]$)	$L_{[\text{OIII}]}$ ($\log[\text{erg/s}]$)	$N_{\text{Comp.}}$	$N_{\text{Ext.}}$	p-value FWHM_{Avg}	p-value FWHM_B	Compact $\% > 1000 \text{ km/s}$	Extended $\% > 1000 \text{ km/s}$	Compact more outflows?
(1)	(2)	(3)	(4)	(5)	(6)	(7)	(8)	(9)	(10)
0.02–0.2	All	All	1620	1302	3.9×10^{-14} ($< 6.6 \times 10^{-9}$)	2.7×10^{-12} ($< 1.7 \times 10^{-6}$)	11 (< 13)	5.7 (< 8.5)	Y
0.1–0.2	All	All	813	584	2.6×10^{-8} ($< 4.1 \times 10^{-4}$)	6.4×10^{-5} ($< 1.6 \times 10^{-2}$)	15 (< 19)	9.1 (< 13)	Y
0.02–0.2	21.5–22.5	All	428	457	2.1×10^{-2} ($< 3.8 \times 10^{-1}$)	4.5×10^{-3} ($< 4.7 \times 10^{-1}$)	4.0 (< 7.5)	2.2 (< 6.0)	?
0.02–0.2	22.5–23.5	All	952	725	2.6×10^{-5} ($< 4.0 \times 10^{-3}$)	6.6×10^{-6} ($< 1.1 \times 10^{-2}$)	11 (< 14)	7.9 (< 11)	Y
0.02–0.2	23.5–24.5	All	188	61	2.7×10^{-4} ($< 2.2 \times 10^{-2}$)	3.1×10^{-3} ($< 5.5 \times 10^{-2}$)	27 (< 30)	6.6 (< 15)	Y
0.02–0.2	All	39.5–40.5	274	258	6.1×10^{-4} ($< 2.0 \times 10^{-1}$)	3.4×10^{-1} ($< 1.0 \times 10^0$)	1.1 (< 4.9)	0.0 (< 5.4)	?
0.02–0.2	All	40.5–41.5	869	741	4.4×10^{-5} ($< 3.0 \times 10^{-2}$)	9.6×10^{-6} ($< 3.8 \times 10^{-2}$)	7.8 (< 11)	5.1 (< 8.6)	?
0.02–0.2	All	41.5–42.5	440	264	5.2×10^{-6} ($< 7.4 \times 10^{-4}$)	6.1×10^{-5} ($< 1.3 \times 10^{-2}$)	22 (< 25)	13 (< 16)	Y

Table 3.1: Results of comparing the [O III] emission-line profiles for AGN with compact versus extended radio emission for various subsets of the sample. Column definitions are as follows: (1)–(3) ranges of redshift, radio luminosity and [O III] luminosity used in each subset; (4) & (5) number of AGN in the subset with compact and extended radio emission, respectively; (6) & (7) p-values from two-sided KS-tests for comparing the distributions of FWHM_{Avg} and FWHM_B (see Section 3.4.2), respectively, for the compact versus extended radio sources (p-values $< 5 \times 10^{-2}$ means statistically different distributions); (8) & (9) the percentage of compact and extended radio sources, respectively, with a broad [O III] emission-line component $\text{FWHM}_B > 1000 \text{ km s}^{-1}$ (see Section 3.4.1) (for columns (6)–(9) in brackets, with give the 99.7th percentile of the corresponding values from a 10^4 run Monte Carlo simulation where we randomly perturbed all relevant values by their uncertainties; see Section 3.4.2); (10) based on the 99.7th percentiles: ‘Y’ if it is confident that compact radio sources have a higher prevalence of $\text{FWHM}_B > 1000 \text{ km s}^{-1}$ components, otherwise ‘?’ is shown.

3.4.1 Trends between ionised gas velocities and radio sizes

In Figure 3.4 we plot the FWHM of the [O III] emission lines versus radio size (R_{Maj}) for the AGN in our sample. In the bottom panel, we show the same but using FWHM_{Avg} , which has the advantage of being defined for those targets with one or two Gaussian component fits to the [O III] profiles (see Section 3.3.1) and gives a sense of the flux-weighted average ionised gas velocities inside the galaxy (covered by the spectroscopic fibres). It can be seen that there is a general trend that the largest radio sources typically have lower ionised gas velocities: the average FWHM_{Avg} drops by $\approx 50\%$ from $R_{\text{Maj}} = 1$ arcsec to $R_{\text{Maj}} = 8$ arcsec. More easily interpreted is the top panel of Figure 3.4, where the number of targets which have a high-velocity component of $\text{FWHM}_B > 1000 \text{ km s}^{-1}$, indicative of extreme outflows, is higher for the smaller radio sources (see dashed line). Specifically, for targets with $R_{\text{Maj}} < 3$ arcsec, 10.7% exhibit [O III] emission-line components with $\text{FWHM}_B > 1000 \text{ km s}^{-1}$, whilst such features are half as common (5.3%) for targets with $R_{\text{Maj}} > 3$ arcsec.

One important limitation of using the radio size measurements, R_{Maj} , in Figure 3.4 is that it fails to properly capture sources with large extended radio structures, which is why sources classified as “extended” (green data points) can have apparently small sizes (see Section 3.3.2). Furthermore, until this point we have not considered the uncertainties on the size or velocity measurements. Therefore, in the following subsection we quantify the relationship between radio size and the prevalence of outflows further, using our careful classifications of compact versus extended radio emission (Section 3.3.2) and accounting for the uncertainties.

3.4.2 Outflows are more prevalent with compact radio emission

In the top two panels of Figure 3.5 we show the cumulative distribution of FWHM_{Avg} and FWHM_B for the full AGN sample of this work. Sources which are radio compact (orange curves) typically have higher ionised gas velocities than sources which are radio extended (green curves). A two-sided KS-test (Kolmogorov–Smirnov test) comparing the radio compact sources to the radio extended sources reveals that they have FWHM_{Avg} and FWHM_B distributions which are *not* consistent with each other, with p-values of 3.9×10^{-14} and 2.7×10^{-12} , respectively.⁴ Furthermore, we found that compact sources are twice as likely to have FWHM_B

⁴Where a p-value < 0.05 rejects the null hypothesis that the two samples are drawn from the same distribution.

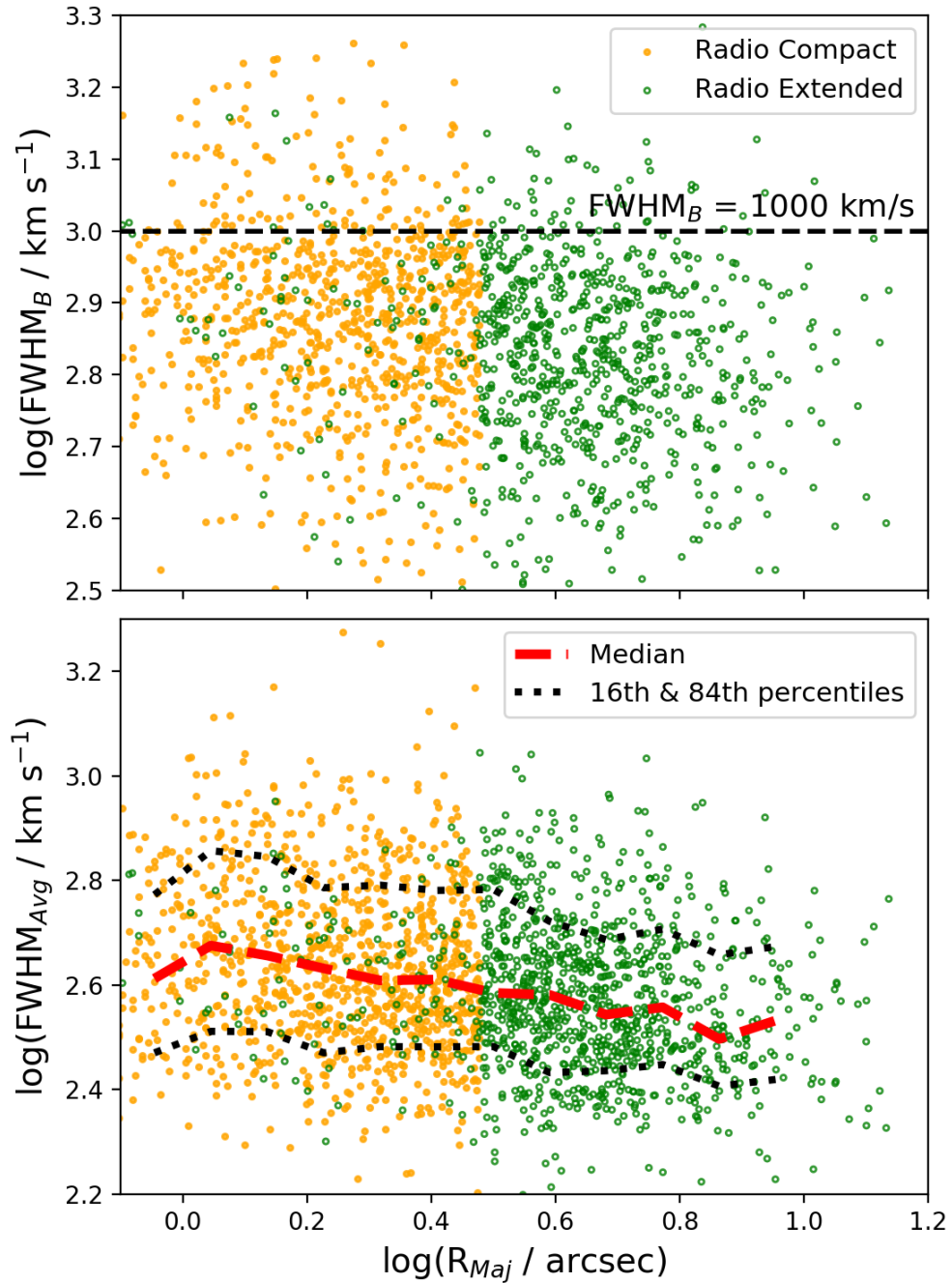


Figure 3.4: [O III] emission-line width versus radio size, using two definitions: (1) the velocity-width of the broadest [O III] emission-line component (FWHM_B ; top panel) and (2) the flux-weighted average velocity width of two emission-line components (bottom panel; FWHM_{Avg}). Symbols are colour-coded as in Figure 3.1 with the addition of the curve showing the running median (in 0.1 dex bins) and the corresponding 16th and 84th percentiles in the bottom panel (used to show the spread of one standard deviation). The small number of “Radio Extended” sources with apparently small sizes are due to extended radio structures beyond the core (see Section 3.3.2). We see a weak trend where the largest, ≈ 8 arcsec sources, have a 0.1–0.2 dex smaller velocity widths, on average, compared to the smaller ≈ 1 arcsec sources. Compact radio sources are more likely to have the broadest emission-line components (e.g., $\text{FWHM}_B > 1000 \text{ km s}^{-1}$; above dashed line; Section 3.4.1).

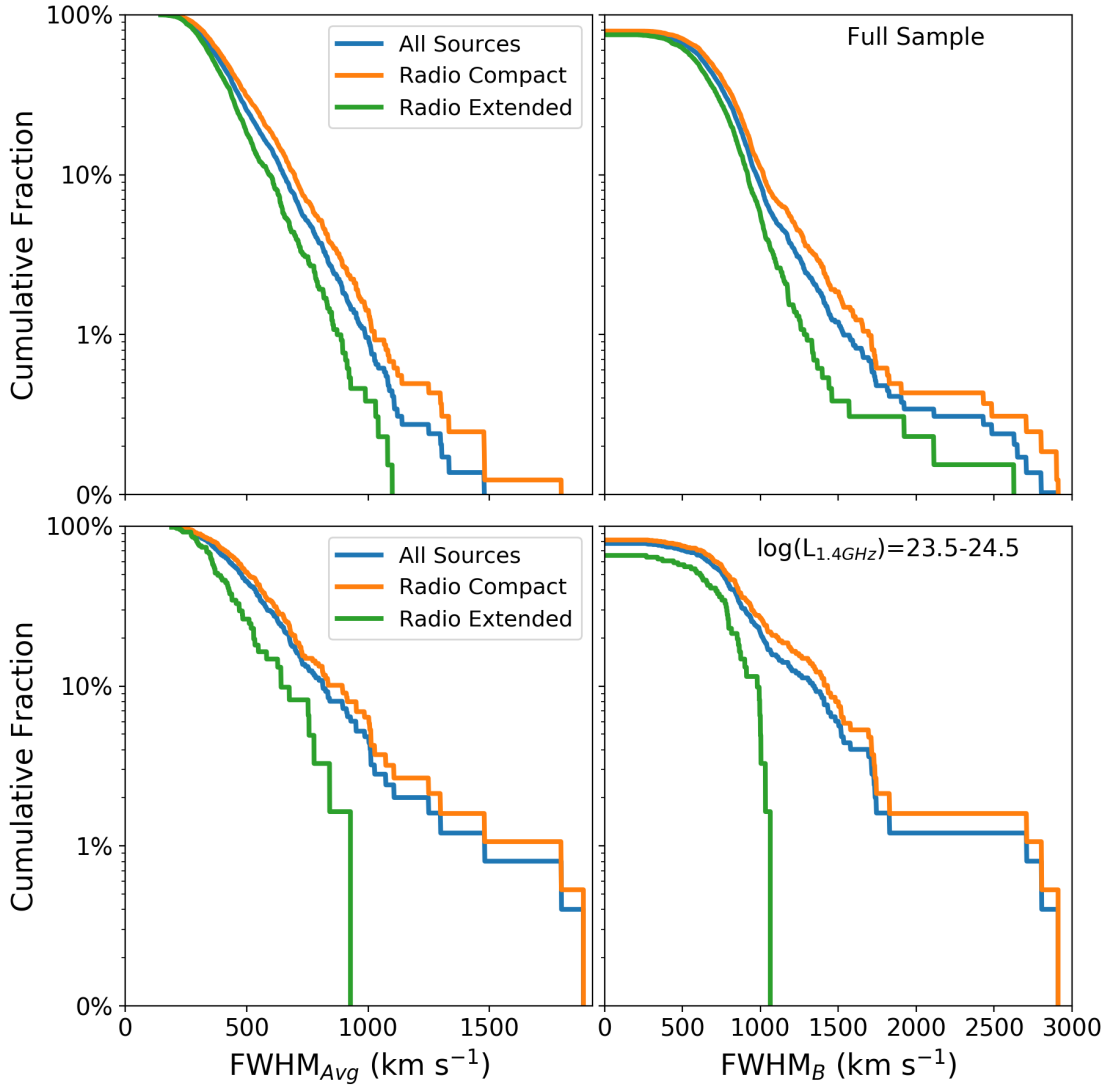


Figure 3.5: Fraction of AGN with [O III] FWHM greater than a given value, for both FWHM_{Avg} (left two panels) and FWHM_B (right two panels). The top two panels show the full sample of this work and the bottom two panels show the subset with radio luminosities of $\log[L_{1.4\text{GHz}}/\text{W Hz}^{-1}] = 23.5 - 24.5$. The cumulative distributions are shown for all the sources in each bin (blue curves) and split by compact and extended radio sources (orange and green curves, respectively). Extreme ionised gas velocities are more prevalent when the radio emission is compact; for example, components with $\text{FWHM}_B > 1000 \text{ km s}^{-1}$ are four times as likely in compact sources when considering the $\log[L_{1.4\text{GHz}}/\text{W Hz}^{-1}] = 23.5 - 24.5$ sample (bottom right panel).

$> 1000 \text{ km s}^{-1}$ emission-line components compared to extended radio sources, with 11% versus 5.7% exhibiting such components, respectively. Such differences between compact and extended radio sources also remains if we focus on a narrower redshift range of $z = 0.1 - 0.2$ so that there is only a factor of two variation in the physical size scale covered by the SDSS fibre. For a full breakdown of these results see the top two rows in Table 3.1.

As mentioned previously it is important for us to take into account the uncertainties on both the

radio size measurements and emission-line velocity width measurements. Therefore, we used a Monte Carlo approach to generate 10^4 sets of R_{Maj} , FWHM_B and FWHM_{Avg} values for the 2922 targets in our sample. To do this, we randomly perturbed the true values by their uncertainties using a normal distribution with a width equal to the measurement errors. For each of the 10^4 sets, we re-classified the full sample as “compact” or “extended”, following Section 3.3.2, and re-performed the two-sided KS-tests on the FWHM_B and FWHM_{Avg} distributions. From this exercise we found that the 99.73 percentiles of the p-values from the 10^4 Monte Carlo runs are 6.6×10^{-9} and 1.7×10^{-6} for FWHM_B and FWHM_{Avg} , respectively. This shows that when folding in the uncertainties the $\approx 3\sigma$ maximum p-values still reveal that the “compact” and “extended” radio sources have FWHM_{Avg} and FWHM_B distributions which are *not* consistent with each other. Furthermore, using these same Monte Carlo runs, at most, 8.5% of the compact radio sources have $\text{FWHM}_B > 1000 \text{ km s}^{-1}$ (again using the 99.73 percentile), which is still a smaller fraction than the 11% observed in the compact radio sources (see Table 3.1).

Another important consideration when interpreting our results is to confirm that the radio size/morphology is the driving physical parameter on the different prevalence of ionised outflows and that it is not driven by the underlying [O III] or radio luminosities (Figure 3.1, Mullaney et al., 2013). To test for this we repeat the above calculations and Monte Carlo simulations but we split the full sample into 1 dex bins of [O III] luminosity and radio luminosity. We only considered bins with > 50 sources, which meant we could explore the luminosity ranges of $\log[L_{1.4\text{GHz}}/\text{W Hz}^{-1}] = 21.5 - 24.5$ and $\log[L_{[\text{OIII}]}/\text{erg s}^{-1}] = 39.5 - 42.5$, split into three bins in both cases. The full results of these tests can be found in Table 3.1. We find that for all radio luminosity bins, except the lowest bin, we can be confident that the prevalence of outflows (i.e., components with $\text{FWHM}_B > 1000 \text{ km s}^{-1}$) is higher for the compact sources (even after accounting for the uncertainties; see Table 3.1). Furthermore, in nearly all luminosity bins the p-values consistently show that the compact and extended radio sources do not have the same distributions of FWHM_{Avg} or FWHM_B , even when considering the uncertainties during the Monte Carlo runs. The exceptions to this are the two lowest luminosity bins of $\log[L_{1.4\text{GHz}}/\text{W Hz}^{-1}] = 21.5 - 22.5$ and $\log[L_{[\text{OIII}]}/\text{erg s}^{-1}] = 39.5 - 40.5$, where the AGN are likely to be particularly weak and/or star-formation processes dominate the observed radio luminosities.

Exploring the effect of luminosity further we find that the difference in ionised gas velocities, between compact and extended radio sources, is most significant in our largest radio luminosity range considered of $\log[L_{1.4\text{GHz}}/\text{W Hz}^{-1}] = 23.5 - 24.5$. The FWHM cumulative distributions

for this sub-sample are shown in the bottom two panels of Figure 3.5. This result is quantified by the fact that the prevalence of $\text{FWHM}_B > 1000 \text{ km s}^{-1}$ components is *four times* higher in the compact versus extended radio sources, compared to a factor of two for the full population. In this radio luminosity range, AGN are generally accepted to dominate the radio emission at low redshift (e.g., Condon et al., 2013; Kimball & Ivezić, 2008). Following Kennicutt & Evans 2012, if we assumed the radio luminosities were all from star formation for the range $\log[L_{1.4\text{GHz}}/\text{W Hz}^{-1}] = 23.5 - 24.5$, this would correspond to star-formation rates of $\approx 200 - 2000 M_{\odot} \text{ yr}^{-1}$. At these redshifts, it would be extremely unlikely for more than one or two of the sources to have such high star-formation rates; for example, X-ray AGN have an average SFR of $\approx 1 - 8 M_{\odot} \text{ yr}^{-1}$ at $z \lesssim 0.5$ (Stanley et al., 2015; Shimizu et al., 2017). Even more importantly, follow-up observations of subsets of the sample in this luminosity range show that star-formation is very unlikely to dominate in most cases due to the observed collimated radio structures and very high radio excess (Figure 3.2; Jarvis et al. 2019). However, since these high-resolution radio observations (Section 3.2.2) only represent the [O III] and radio luminosity bins where the difference between compact and extended radio sources is strongest, further high-resolution radio observations are required to establish the origin of radio emission in all of the “radio quiet” population (also see Panessa et al., 2019).

Overall, we conclude that the prevalence of outflows is highest when the radio emission is compact and the AGN are clearly the dominating source of radio emission (i.e., $\log[L_{1.4\text{GHz}}/\text{W Hz}^{-1}] = 23.5 - 24.5$). Since we only have small numbers of sources at higher radio luminosities, we are unable to extend our results to $\log[L_{1.4\text{GHz}}/\text{W Hz}^{-1}] > 24.5$.

3.4.3 Implications of this result

We find that ionised outflows observed in SDSS spectroscopy for $z < 0.2$ AGN are more common when the radio emission is concentrated within the spatial extent of the spectroscopic fibre. This implies a strong relationship between the radio emission and the observed outflows. We suggest that this is not driven by star-formation processes because the result is strongest when AGN will be dominating the radio emission. Our result shows that the connection between outflows and compact radio emission for extremely radio bright AGN, found by Holt et al. (2008), is also found in the more representative “radio quiet” AGN population.

If the radio emission is tracing the extent of jets, our result could imply that we can see the effect of jet-ISM interactions from young radio sources or low-power frustrated jets that will never escape the host galaxy (e.g., [van Breugel et al., 1984](#); [O’Dea et al., 1991](#); [O’Dea, 1998](#); [Morganti, 2017](#); [Bicknell et al., 2018](#)). Where larger scale jets are depositing their energy outside of the region covered by the spectroscopic fibre, the spectroscopic measurements do not cover the physical region of jet-ISM interactions.

In favour of the jet scenario, we see collimated jet-like features (including hot spots and ‘bent’ jets) in our follow-up high resolution radio observations (Figure 3.2; [Jarvis et al., 2019](#)). Furthermore, spatially-resolved spectroscopic observations reveal jet-ISM interactions in sources with a range of jet powers, particularly on the scale of the galaxy bulges (i.e., a few kiloparsec; [Tadhunter, 2016](#); [Jarvis et al., 2019](#); [Husemann et al., 2019b,a](#)). Cutting-edge simulations show that compact jets interacting with a clumpy ISM may be a crucial aspect of ‘AGN feedback’ and possibly the most efficient mechanism for driving powerful outflows (e.g., [Wagner et al., 2012](#); [Mukherjee et al., 2016](#); [Bicknell et al., 2018](#); [Cielo et al., 2018](#)).

Alternatively, the increased prevalence of outflows for compact radio emission may be because quasar-driven winds drive the ionised outflows and simultaneously shock the ISM to produce radio emission in the same region of the galaxy ([Wagner et al., 2013](#); [Zakamska & Greene, 2014](#); [Nims et al., 2015](#); [Zakamska et al., 2016](#); [Wagner et al., 2016](#); [Hwang et al., 2018](#)). This scenario could become indistinguishable from those driven by jets, especially in the cases where the jets become disrupted and are more diffuse ([Wagner et al., 2013](#); [Alexandroff et al., 2016](#)). More theoretical and observational work on larger samples is required to distinguish between these two scenarios.

3.5 Conclusions

We have used a sample of 2922 $z = 0.02 - 0.2$ AGN, spectroscopically identified in SDSS, with a radio detection in FIRST and/or NVSS, to investigate the relationship between ionised outflows and the spatial extent of the radio emission. We made use of two component fits to the $[\text{O III}]\lambda 5007$ emission-line profiles to characterise the velocity widths, considering both the width of any identified broad components (FWHM_B) and the flux-weighted average width of

the two components (FWHM_{Avg} ; see Figure 3.3). To characterise the radio sizes we considered both major-axis sizes from two-dimensional Gaussian fits (deconvolved for the beam) and an automated morphological classification routine (see Figure 3.2). We find that:

- Except for the AGN with the lowest [O III] and radio luminosities (i.e., $\log[L_{[\text{OIII}]}/\text{erg s}^{-1}] < 40.5$; $\log[L_{1.4\text{GHz}}/\text{W Hz}^{-1}] < 22.5$) the radio compact and radio extended sources have statistically different distributions of ionised gas kinematics. Compact radio sources tend to have broader emission-line profiles on average (Section 3.4.1; Figure 3.4).
- When the radio emission is confined within $3''$ (i.e., within the SDSS fibre), equivalent to $\lesssim 5$ kpc at the median redshift, broad [O III] emission-line components with $\text{FWHM}_{\text{B}} > 1000 \text{ km s}^{-1}$, indicative of high-velocity outflows, are twice as prevalent (Figure 3.5).
- Extreme outflow components ($\text{FWHM}_{\text{B}} > 1000 \text{ km s}^{-1}$) are four-times more prevalent when only considering the sources with moderate radio luminosities (i.e., $\log[L_{1.4\text{GHz}}/\text{W Hz}^{-1}] = 23.5 - 24.5$), where AGN are most likely to be the dominant source of radio emission. Follow-up sub-kpc resolution radio observations of a subset of the sample, in this luminosity range, reveal a high prevalence of moderate power jets and lobes (Jarvis et al., 2019, Figure 3.2). We are too limited in source statistics to make strong conclusions about higher radio-luminosity AGN.

Our results add to the growing body of evidence that there is a strong connection between the presence of ionised outflows and the radio emission in AGN host galaxies (e.g. Mullaney et al., 2013; Villar Martín et al., 2014; Holt et al., 2008; Zakamska & Greene, 2014; Hwang et al., 2018; Jarvis et al., 2019). We find that outflows are more prevalent when the radio emission is compact for typical “radio quiet” AGN, as had previously been seen in the most powerful “radio loud” AGN (Holt et al., 2008). Follow-up high resolution observations of subsets of targets imply that compact, low-power radio jets, frustrated by interactions with the host galaxy ISM (Figure 3.2; Jarvis et al., 2019) may be responsible for the high-velocity ionised gas, inline with some recent model predictions (e.g. Mukherjee et al., 2018b). However, we can not rule out other possible processes, such as nuclear wide-angle winds, that contribute to producing the radio emission and outflows in the wider sample (e.g., see Zakamska et al., 2016). High-resolution observations of larger samples will help determine the relative contribution of these different processes.

This work was limited to AGN with detections in the radio surveys of NVSS and/or FIRST which are relatively shallow. On-going and future, deep and large-area multi-frequency radio surveys such as: VLASS ([Lacy et al., 2019](#)); those with LOFAR ([Smith et al., 2016](#); [Shimwell et al., 2017](#)) and eventually those with the SKA, that are combined with spectroscopic information will be crucial to unravelling a complete picture of the origin of radio emission in AGN and to further establish the physical processes behind AGN–host galaxy interactions.

Acknowledgements

S. J. M. acknowledges support from an internship provided by the European Southern Observatory’s Office for Science.

Context free quotes

“The finger is faster than the mind”

“I’m spending all my salary on shrimp”

“My mum forces me to wear red underwear”

“It’s the worst ball shaped thing I’ve ever eaten”

“Someone read my papers, my life is for something”

“The last time he played table tennis you weren’t born”

“The appearance of a powerful and mysterious otter”

“I seem to be reverberating all over the place”

“I should pass by your place to get crabs”

“You get to Paranal... taki taki rumba!!”

“The cats not just there for pleasure”

“Servus, no thanks I’m good”

“Tengo un sacapuntas”

“I’m not a spicy girl”

“I’ve seen cows”

Characterising CO excitation in quasar host galaxies

In this chapter I present a comprehensive study of the molecular gas properties of 17 Type 2 quasars at $z < 0.2$ from the Quasar Feedback Survey ($L_{[\text{O III}]}$ $> 10^{42.1}$ ergs $^{-1}$), selected by their extreme [O III] kinematics and displaying a large diversity of radio jet properties. With these data, we are able to investigate the impact of AGN feedback on the molecular interstellar medium. Using APEX and Atacama Compact Array observations, we measure the total molecular gas content using the CO(1-0) emission and homogeneously sample the CO spectral line energy distributions (SLEDs), observing CO transitions ($J_{up} = 1, 2, 3, 6, 7$). We observe high r_{21} ratios ($r_{21} = L'_{\text{CO}(2-1)}/L'_{\text{CO}(1-0)}$) with a median $r_{21} = 1.06$, similar to local (U)LIRGs (with $r_{21} \sim 1$) and higher than normal star-forming galaxies (with $r_{21} \sim 0.65$). This would suggest that the AGN feedback processes do not have a significant impact on these ratios on global scales. Despite the high r_{21} values, we find low excitation in CO(6-5) & CO(7-6) (r_{61} and $r_{62} < 0.6$ in all but one target), unlike high redshift quasars in the literature, which are far more luminous and show higher line ratios. The ionised gas traced by [O III] exhibit systematically higher velocities than the molecular gas traced by CO. We conclude that any effects of quasar feedback (e.g. via outflows and radio jets) do not have a significant impact on the global molecular gas content and excitation and we suggest that it only occurs on a more localised scales. This chapter is based on the work published in [Molyneux et al. \(2023\)](#).

4.1 Introduction

A fundamental outstanding question of galaxy evolution is what impact active galactic nuclei (AGN) have on the interstellar medium (ISM) and star formation in their host galaxies. AGN can release energy into their host galaxies via processes known as AGN feedback, which are required by our current models of galaxy evolution to regulate star formation (Bower et al., 2006; Schaye et al., 2015), and believed to be the mechanism that regulates the co-evolution of accreting black holes (BH) and their host galaxies that is observed across cosmic time (e.g. Madau & Dickinson, 2014; Kormendy & Ho, 2013; Cresci & Maiolino, 2018). Observational and theoretical studies have proposed both a suppression (Silk & Rees, 1998; Hopkins et al., 2006; Booth & Schaye, 2010; Feruglio et al., 2010; Cicone et al., 2014; King & Pounds, 2015; Fiore et al., 2017; Costa et al., 2018; Ellison et al., 2021; Bertemes et al., 2023) and an enhancement of star formation in AGN host galaxies (Ishibashi & Fabian, 2012; Silk, 2013; Zubovas et al., 2013; Lacy et al., 2017; Fragile et al., 2017; Gallagher et al., 2019). However, these interactions are still not fully understood and the diversity of results stress the need for multiwavelength, multi-tracer studies to characterise the interplay between the central supermassive black hole and the host galaxy.

A natural assumption may be that the most powerful and luminous AGN and quasars will have the largest impact on their host galaxy. Studies suggest that they might be able to drive kpc-scale outflows across the entire galaxy, expelling the interstellar star-forming gas (e.g. Cicone et al., 2012; Harrison et al., 2014; Feruglio et al., 2015; Circosta et al., 2018; Longinotti et al., 2023). However, studies at low redshift (z) have also shown that AGN and quasars tend to reside in gas rich, star-forming galaxies and find no instantaneous depletion of total gas content (Saintonge et al., 2017; Shangguan et al., 2020; Jarvis et al., 2020; Koss et al., 2021). These findings also agree with recent simulations (e.g. Piotrowska et al., 2022; Ward et al., 2022), therefore supporting the idea that large gas reservoirs are needed to fuel the accreting supermassive BHs in quasar and AGN hosts. It may therefore be the case that any impact from feedback is limited to a more localised scale and the global properties of the ISM are left largely unaffected. Indeed, there are works which show the possible impact of AGN feedback on the molecular gas content in central/localized part of the galaxy (e.g. Rosario et al., 2019; Feruglio et al., 2010; Ellison et al., 2021; Ramos Almeida et al., 2022; Audibert et al., 2023).

The molecular phase of the ISM, commonly traced by observing low transitions of carbon

monoxide (CO), plays a critical role in galaxy evolution as it is this gas which is redistributed to both promote star-formation activity and fuel BH growth (e.g. [McKee & Ostriker, 2007](#); [Carilli & Walter, 2013](#); [Vito et al., 2014](#); [Tacconi et al., 2020](#)). However, no consensus has yet been reached on the impact of AGN on the overall molecular gas content in the ISM ([Kakkad et al., 2017](#); [Perna et al., 2018](#); [Kirkpatrick et al., 2019](#); [Rosario et al., 2019](#); [Circosta et al., 2021](#); [Morganti et al., 2021](#)). One possible reason for this might be due to the time scales over which any impact may take place ([King et al., 2011](#); [Mukherjee et al., 2018b](#); [Zubovas, 2018](#); [Ward et al., 2022](#)). There are also complexities due to the resolution of observations, biases in the sample selection, what tracers of the gas are used, and the uniformity in the observations.

While most studies of the AGN impact on molecular gas have focused on the total gas content, much is still unknown about other molecular gas properties such as molecular gas excitation. Knowledge of the ground state CO(1-0) line is a crucial reference that is often used to not only compare to higher transitions and measure the excitation, but to also convert to the total molecular gas content of the galaxy. However, there is discussion in the community about how reliable the ground state is in doing these calculations for different objects (e.g. star forming galaxies (SFGs) or (ultra) luminous infrared galaxies (U)LIRGs, see [Leroy et al., 2022a](#); [Montoya Arroyave et al., 2023](#)). This therefore increases the importance in characterising the CO(1-0) across different samples.

Due to the expensive observations required to detect multiple emission lines for individual sources, most of our knowledge on molecular gas excitation is based on inhomogeneous coverage of few transitions, and limited to for the most luminous galaxies (e.g. [Kakkad et al., 2017](#); [Saintonge et al., 2017](#); [Lamperti et al., 2020](#); [Circosta et al., 2021](#); [Boogaard et al., 2021](#); [Valentino et al., 2021](#); [Harrington et al., 2021](#); [Leroy et al., 2022a](#)). Further, studies have investigated the driving mechanism for the excitation of the molecular gas (e.g. [Daddi et al., 2015](#); [Pozzi et al., 2017](#); [Mingozzi et al., 2018](#); [Leroy et al., 2022b](#); [Esposito et al., 2022](#)), suggesting photodissociation regions (PDRs) and X-ray dominated regions (XDRs), of diverse temperature and gas densities, are the key physical components driving CO excitation.

Models of CO excitation suggest that AGN-related processes, such as X-ray emission ([Meijerink et al., 2007](#)) and shock heating induced by AGN jets and outflows ([Kamenetzky et al., 2016](#)), would mainly affect the molecular gas excitation at the higher CO transitions. It is therefore crucial to study both low and high CO transitions as the impact of feedback may only be present

at higher CO excitations ($J_{up} > 5$), whereas the bulk of the molecular gas content is still traced by the ground transition. However, this is challenging at low redshifts ($z < 0.2$), where even using the maximum frequency limit of the ALMA bands, only $J_{up} \leq 8$ can be reached. Due to the observational difficulty of observing at higher frequencies, there are few examples of these critical higher CO transitions observed at low- z (e.g. [van der Werf et al., 2010](#); [Greve et al., 2014](#); [Rosenberg et al., 2015](#); [Liu et al., 2015](#); [Kamenetzky et al., 2016](#); [Yang et al., 2017](#)). Indeed, most $J_{up} > 7$ observations come from higher redshift ($z > 1$), highly luminous quasars, which are far more easily observed ([Carilli & Walter, 2013](#); [Wang et al., 2019](#); [Yang et al., 2019](#); [Li et al., 2020](#); [Pensabene et al., 2021](#); [Decarli et al., 2022](#)), and which in turn lack observations of low-J transitions, consequently lacking a complete characterisation of the molecular gas content and excitation.

Previous studies have suggested a close relationship between AGN feedback diagnostics and the properties of the ionised phase of the ISM. For example, a study of optically selected AGN from SDSS found that those with higher radio luminosities were more likely to have larger $\text{FWHM}_{[\text{O III}]}$ ([Mullaney et al., 2013](#)), suggesting a relation between the radio emission and the kinematics of the ionised gas. Further work on the same sample showed that the most extreme ionised outflows ($\text{FWHM}_{[\text{O III}]} > 1000 \text{ km s}^{-1}$) were found to be more common when the radio emission was compact ([Molyneux et al., 2019](#), see Chapter 3). With high resolution radio observations for a sample of 42 of these targets (presented in [Jarvis et al., 2019](#)) from the Karl G. Jansky Very Large Array (VLA), a prevalence of small scale radio jets (in the central few kpc) was found, leading to a suggestion that they could be the driver of these ionised outflows. Alternatively star formation driven outflows and quasar winds that shock the ISM may be responsible for producing the observed radio emission and correlation with outflow properties (e.g. [Condon et al., 2013](#); [Nims et al., 2015](#); [Zakamska et al., 2016](#); [Hwang et al., 2018](#); [Panessa et al., 2019](#)).

With the advent of deeper radio data, increasing evidence is being found of potentially ubiquitous low-level radio emission in radio-quiet quasars (e.g. [Jarvis et al., 2019, 2021](#); [Macfarlane et al., 2021](#)). These observations suggest that radio jets are potentially an important feedback mechanism in radio quiet quasars. Indeed radio jets have been found to have an impact on the surrounding multi-phase ISM (e.g. [Morganti et al., 2015](#); [Oosterloo et al., 2017](#); [Jarvis et al., 2019](#); [Morganti et al., 2021](#); [Girdhar et al., 2022](#)). However, an outstanding question is how and when these jets can couple to the ISM, and have a positive and/or negative impact on the star-forming molecular gas content (e.g. [Silk, 2013](#); [Gabor & Bournaud, 2014](#); [Bieri et al., 2016](#);

Costa et al., 2018). Studying the CO excitation of quasars with known outflows/jets is therefore key to solving these outstanding questions.

The Quasar Feedback Survey (QFeedS) is a multi-wavelength survey aiming to address these open questions in order to understand the co-evolution between quasars and their host galaxy, in particular in the context of ionised outflows and radio jets. These are luminous systems at $z < 0.2$ and so it is possible to study the impact that feedback (e.g. via radio jets) has on the multi-phase ISM on both resolved and global scales, whether it be driving outflows, disturbing the gas kinematics, affecting the molecular gas excitation, or impacting on star formation (Harrison et al., 2015; Lansbury et al., 2018; Jarvis et al., 2019, 2020, 2021; Girdhar et al., 2022; Silpa et al., 2022).

In this work we present a comprehensive study of the molecular gas properties of 17 quasars of the QFeedS sample which have multi-wavelength data. We characterise the molecular excitation in these sources, presenting CO(1-0), CO(2-1) and CO(3-2) results for the entire sample and also CO(6-5) or CO(7-6) results for 7 of the 17 targets. With the addition of ancillary multi-wavelength data, we will explore the impact of feedback, if any, on the total molecular gas content and molecular gas excitation within the quasar host galaxies.

In Section 4.2 I introduce the quasar sample presented in this work as part of the Quasar Feedback Survey. In Section 4.3 I describe the observations used and the data reduction. In Section 4.4 I describe the analysis techniques used to study our CO data, including making fits to the spectra, defining detections, and calculations made on the fluxes, line profiles and other properties of the gas. I also introduce the comparison samples from the literature that we utilise in our analysis. In Section 4.5 I present our results of the CO excitation, line profile properties and gas fractions, and at all times comparing to relevant samples from the literature. I then discuss our findings in the overall context of galaxy evolution and quasar feedback. Our final conclusions are presented in Section 4.6.

We adopt $H_0 = 70 \text{ km s}^{-1} \text{ Mpc}^{-1}$, $\Omega_M = 0.3$, and $\Omega_\Lambda = 0.7$ throughout.

4.2 Sample selection

QFeedS, presented in [Jarvis et al. \(2021\)](#), is a multi-wavelength study of 42 quasars at $z < 0.2$. This main sample was selected from a parent sample of 24264 optically selected AGN from SDSS at $z < 0.4$ from [Mullaney et al. \(2013\)](#). These 42 quasars were selected to have $L_{[\text{O III}]}$ $> 10^{42.1}$ ergs s^{-1} and to cover the full range of $\text{FWHM}_{\text{Avg}[\text{O III}]}$, (a flux weighted average of the FWHM of the two Gaussian components present in the spectra) with velocities in the range $= 339 - 1289$ km s^{-1} (see [Figure 4.1](#)).

Here we introduce a study as part of QFeedS to provide a detailed characterisation of molecular gas in 17 Type 2 quasars, studying properties such as molecular gas masses, gas fractions and CO excitation. The 17 targets were selected to be Type 2 quasars which are visible from the Very Large Telescope (VLT) and the Atacama Pathfinder EXperiment telescope (APEX) and that are representative of the parent population (see [Figure 4.1](#)). We selected Type 2 quasars in order to achieve a more robust characterisation of the host-galaxy stellar-emission properties ([Jarvis et al., 2019](#)). These 17 targets also have available optical (Multi Unit Spectroscopic Explorer, MUSE) and radio (VLA) data allowing us to perform a full multi-wavelength analysis of the quasar and host continuum emission, in addition to a multi-tracer characterisation of the ISM (these ancillary data are discussed further in [Section 4.3.5](#)). These 17 sources are representative of the survey sample as they cover the full range of QFeedS redshifts ($z \sim 0.1 - 0.2$) as well as [O III] and radio luminosities, $L_{[\text{O III}]} = 10^{42.1} - 10^{43.2}$ erg s^{-1} and $L_{1.4\text{GHz}} = 10^{23.5} - 10^{24.4}$ W Hz^{-1} .

Based on the criteria of [Xu et al. \(1999\)](#) using the [O III] and radio luminosity division all 17 of our sample are defined as ‘radio-quiet’ (see also [Jarvis et al., 2021](#)). From previous work ([Jarvis et al., 2019](#)), we also know that at least 8 of these 17 sample galaxies are consistent with being luminous infrared galaxies (LIRGs, $10^{11} L_{\odot} \lesssim L_{\text{IR,SF}} \lesssim 10^{12} L_{\odot}$, where $L_{\text{IR,SF}}$ is the far infrared luminosity associated with star formation). As only 9 of these targets have the required $L_{\text{IR,SF}}$ data then the number of sources consistent with being LIRGs is likely to be higher. This is an important consideration for when we make comparisons with samples in the literature.

The source selection for this study is shown in [Figure 4.1](#). The colours for the 17 targets in this sample (shown in the legend of [Figure 4.1](#)) are used in all further figures in this work. Further,

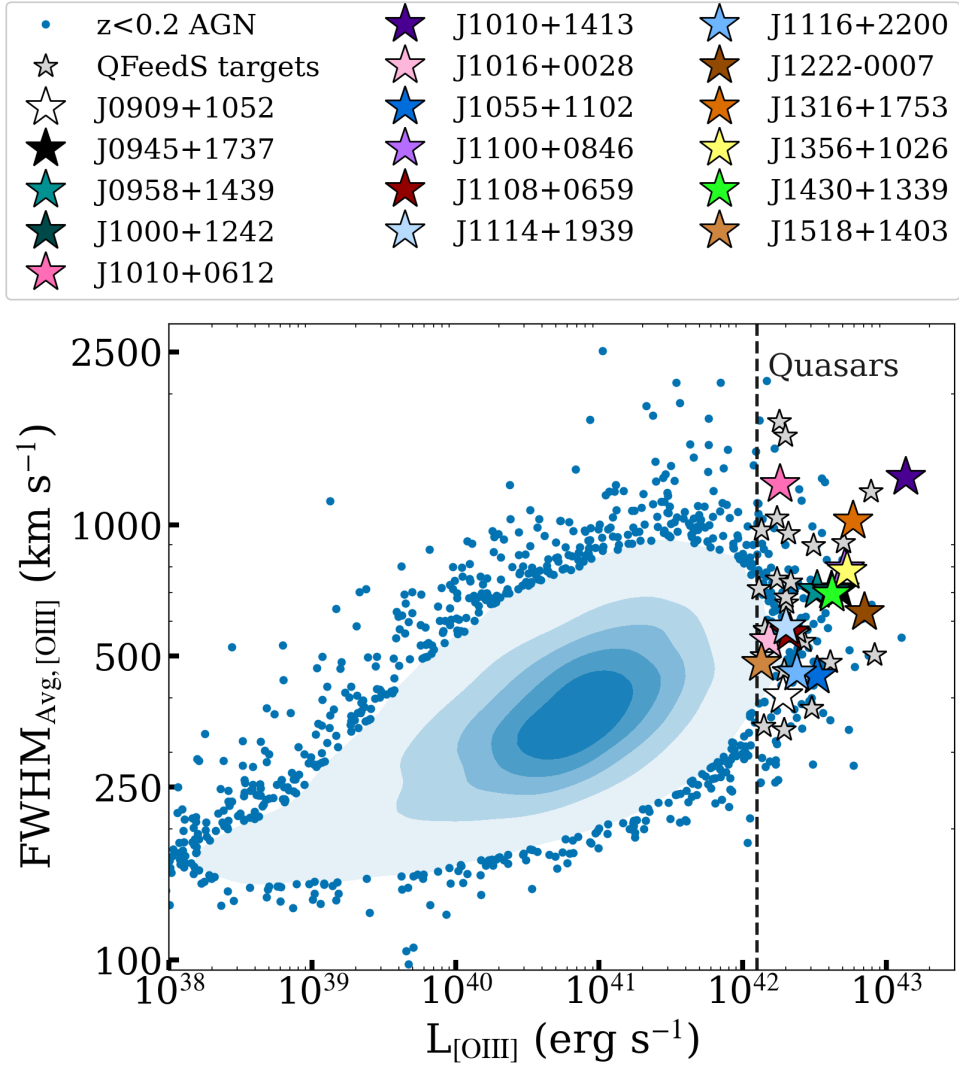


Figure 4.1: Sample Selection: [O III] luminosity versus emission line widths, demonstrating how the 42 quasars in the QFeedS sample (star symbols) are selected from $z < 0.2$ AGN sample (Mullaney et al., 2013, blue points and contours). The 17/42 selected for this work are highlighted by the larger coloured stars and the remaining 25/42 of the QFeedS sample are shown by small grey stars. The colours for the 17 targets in this sample (shown in the legend) are carried through in figures throughout the rest of this paper. The dashed line represents the selection criteria in QFeedS of $L_{[\text{O III}]} > 10^{42.1} \text{ erg s}^{-1}$.

basic properties of these sources can be found in Table 4.1.

Name (1)	RA (J2000) (2)	DEC (J2000) (3)	z (4)	$\log(L_{1.4\text{GHz}})$ (W Hz^{-1}) (5)	$S_{1.4\text{GHz}}$ (mJy) (6)	$\log(L_{[\text{O III}]})$ (erg s^{-1}) (7)	SDSS W_{80} (km s^{-1}) (8)
J0909+1052	09:09:35.49	+10:52:10.5	0.166	23.6	6.0 ± 0.5	42.28	399 ± 24
J0945+1737	09:45:21.33	+17:37:53.2	0.128	24.3	45.6 ± 1.4	42.67	799 ± 26
J0958+1439	09:58:16.88	+14:39:23.7	0.109	23.5	10.9 ± 0.5	42.52	786 ± 10
J1000+1242	10:00:13.14	+12:42:26.2	0.148	24.3	34.8 ± 1.1	42.62	813 ± 5
J1010+0612	10:10:43.36	+06:12:01.4	0.098	24.3	92.4 ± 3.3	42.26	1462 ± 8
J1010+1413	10:10:22.95	+14:13:00.9	0.199	24.1	11.1 ± 0.5	43.14	1426 ± 16
J1016+0028	10:16:53.82	+00:28:57.1	0.116	23.6	11.8 ± 0.9	42.18	596 ± 8
J1055+1102	10:55:55.34	+11:02:52.2	0.145	23.5	5.7 ± 0.4	42.52	478 ± 7
J1100+0846	11:00:12.38	+08:46:16.3	0.100	24.2	59.8 ± 1.8	42.71	883 ± 10
J1108+0659	11:08:51.03	+06:59:01.4	0.181	24.0	11.1 ± 0.5	42.32	660 ± 5
J1114+1939	11:14:23.81	+19:39:15.8	0.199	24.0	8.4 ± 0.5	42.30	650 ± 6
J1116+2200	11:16:25.34	+22:00:49.3	0.143	23.7	10.5 ± 0.5	42.38	465 ± 17
J1222-0007	12:22:17.85	-00:07:43.7	0.173	23.6	4.5 ± 0.4	42.85	839 ± 56
J1316+1753	13:16:42.90	+17:53:32.5	0.150	23.8	10.3 ± 0.5	42.77	1165 ± 8
J1356+1026	13:56:46.10	+10:26:09.0	0.123	24.4	62.9 ± 1.9	42.73	871 ± 72
J1430+1339	14:30:29.88	+13:39:12.0	0.085	23.7	26.5 ± 0.9	42.62	772 ± 9
J1518+1403	15:18:56.27	+14:03:19.0	0.139	23.6	8.6 ± 0.9	42.13	520 ± 28

Table 4.1: (1) Source name; (2)–(3) Optical RA and Dec positions from SDSS (DR7) in the format hh:mm:ss.ss for RA dd:mm:ss.s for Dec; (4) spectroscopic redshift of the source from SDSS DR7 (with an rms error on the redshift of 0.025, [Abazajian et al., 2009](#)); (5) Rest-frame 1.4 GHz radio luminosities from NVSS using a spectral index of $\alpha = -0.7$ and assuming ($S_\nu \propto \nu^\alpha$). The typical log errors are ~ 0.03 ; (6) 1.4 GHz flux density of the target from NVSS; (7) Total observed [O III] λ 5007 luminosity calculated using the fluxes from [Mullaney et al. \(2013\)](#), the typical log errors are ~ 0.01 ; (8) The line width (W_{80}) of the [O III] λ 5007 line measured from SDSS spectra.

4.3 Observations and data reduction

We use APEX and the Atacama Compact Array (ACA) to observe the carbon monoxide (CO) emission in the CO(1-0), CO(2-1), CO(3-2), CO(6-5) and CO(7-6) transitions for our sample of 17 Type 2 quasars (as detailed in Table 4.5 in the appendix and emission line properties are provided in Tables 4.6, 4.7, 4.8, 4.9, & 4.10). APEX is a single dish, 12 metre diameter telescope whereas the ACA is a subset of the Atacama Large Millimeter/submillimeter Array (ALMA) comprising of twelve 7 metre antennae. A description of all the observations used in this paper along with details of how the data was reduced is provided below.

4.3.1 CO(1-0) observations

Thirteen out of our 17 targets have CO(1-0) ACA observations [proposal ID: 2019.2.00194.S, PI: Calistro-Rivera], acquired between December 2019 and March 2020. Sources from this sample without CO(1-0) data are J1010+0612, J1010+1413, J1356+1026 and J1430+1339.

The required sensitivity for the ACA observations were estimated based on two different approaches. In the case of sources with archival infrared data around the dust SED peak, a conversion was made from total IR (L_{IR}) from SED-fitting to CO luminosities L'_{CO} . Otherwise, conversions were estimated based on the SED-inferred stellar mass and the average gas fraction value.

We image the CO(1-0) emission using the TCLEAN function in CASA and apply natural weighting with the Högbom deconvolver. Bin widths of 100 km s^{-1} were used for non-detections and 50 km s^{-1} bins were used if the S/N was high enough to see more structure in the line profile. In a few specific cases, slightly different bin sizes were used either to match to other available data or as a result of the data quality.

The beam size of the ACA observations ranged between 12 – 14 arcsec. However, to obtain the CO(1-0) spectra we take an aperture equivalent to the APEX beam size when observing CO(2-1), which is ~ 30 arcsec diameter at an observing frequency of ~ 200 GHz (observation frequency of CO(2-1) at the samples median redshift of 0.14). Using this aperture consistently

to extract the spectra allowed us to compare the fluxes obtained from the same regions, making calculations of line ratios and other properties more reliable. It further allowed us to investigate whether any extended diffuse gas was present, or at least detectable, when comparing to smaller apertures. The apertures used for the extraction and the contours of the CO(1-0) ACA data are shown in the Appendix (Figure 4.30 in the appendix), plotted over rgb images from the DESI Legacy Imaging Survey in the (z, r, g) bands. The 2 sigma contours in the highest S/N data show an extent of up to 27 arcsec (in J1108+0659). Further, those with low S/N (such as the cases of J0945+1737 and J1055+1102) show positional offsets extending out to the 30 arcsecond diameter aperture and slightly beyond. As positional uncertainty in the observations is proportional to $\frac{\text{beam size}}{S/N}$, using the 30 arcsecond aperture also allows us to account for these potential offsets and ensure we accurately measure the fluxes. From the CO(1-0) data there are no signs of any companions that are spatially and spectrally aligned with our targets, such that they would impact upon the measured flux values, aside from the apparent mergers occurring in J1222-0007 and J1518+1403 (which are both treated as single systems in this work). Companions that are visible in the background rgb images do not appear in the ACA data and so either are not emitting at those frequencies, or our observations are not deep enough to observe the emission from them. Therefore we can be confident of the fluxes measured in our ACA observations and that these also represent the total CO fluxes in these galaxies. Since this is the only aperture we have control over for the flux/spectra extraction, we choose to match this to the APEX CO(2-1) aperture of 30 arcsec to be as consistent as we can be in the region we are calculating fluxes.

Recent work in the literature has shown evidence for extended, low surface brightness emission in quasars, with CO emission detected out to 100s kpc.(e.g. [Cicone et al., 2021](#); [Li et al., 2021](#); [Scholtz et al., 2023](#)). This provides further support to the approach taken here, where we extract spectra with an aperture diameter of ~ 80 kpc at the median redshift.

To determine whether we obtain the total flux we plot the curves of growth of the ACA CO(1-0) (see Figure 4.2) where we indeed see that extracting the spectra at 30 arcsec is required to obtain a more accurate total flux value. Beyond 30 arcsec the flux density flattens off in almost all cases (note that in this figure we only plot those with an integrated signal-to-noise ratio (S/N) greater than 5). For a few sources we note that the curves of growth do continue to rise slightly after 30 arcsec, but by $< 10\%$ and within uncertainties. Given the larger uncertainties, we are still confident that we are consistent with obtaining the total flux. We also find that the curves of growth up to 30 arcsec follow the same trend and are consistent with each other so no

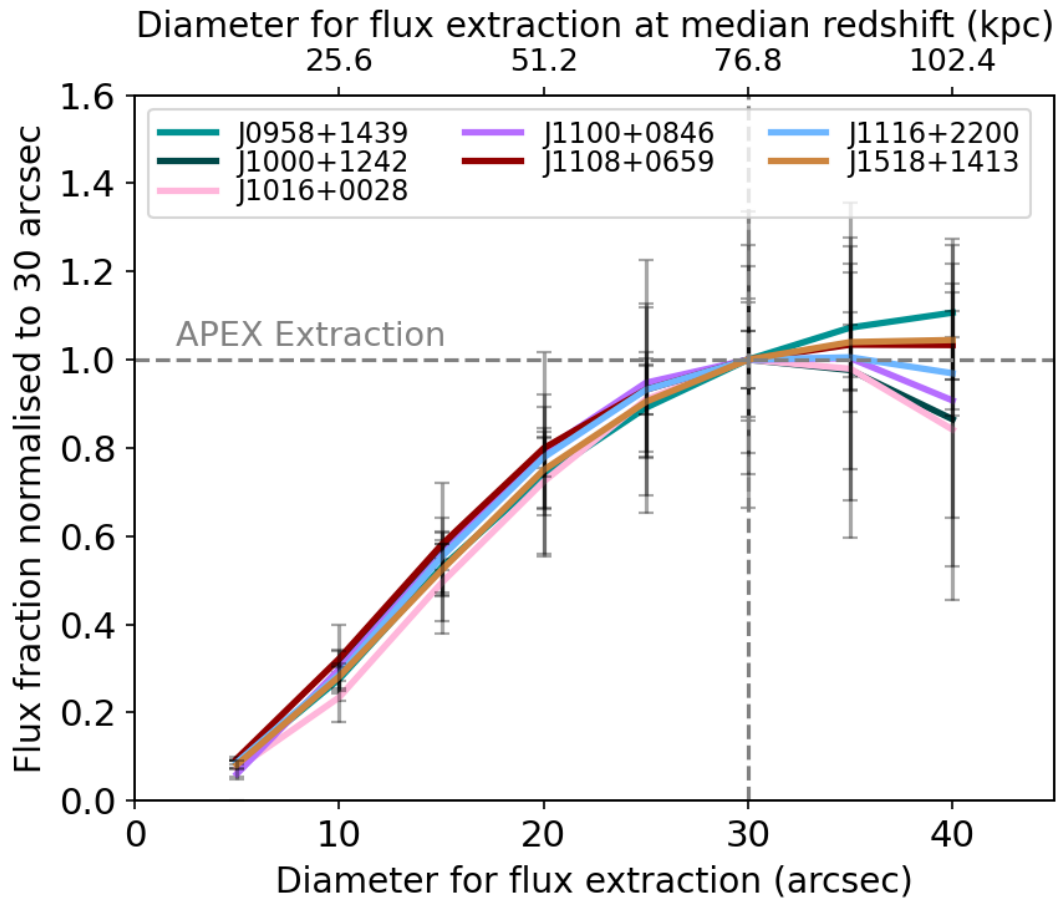


Figure 4.2: For the 7 targets with $S/N > 5$ in CO(1-0) we plot the flux extracted from various diameter apertures of the ACA data up to 40 arcsec. The flux presented here is normalised to 30 arcsec which is where we extract our flux to match with APEX data (dashed lines). Uncertainties on each flux estimate are presented with grey error bars.

conclusions can be drawn about any differences in morphology at these scales, with respect to galactic or feedback properties.

We note that if the CO(1-0) spectra were extracted using a 3σ minimum level, we would measure on average 60% less flux when compared to the extraction at 30 arcsec, and in one case almost 90% less flux (values range from 25 – 89%). Such differences would have a significant impact on the analysis of the excitation, stressing the importance of low-resolution data for a complete census of molecular gas content.

From available multi-wavelength data (Jarvis et al., 2021) we also note that J1518+1403 has a secondary source located 14.7 arcsec away to the north east and J1222-0007 has a secondary source 4.7 arcsec away which are both likely to be on-going mergers. Further, J1108+0659 and J1356+1026 show evidence of hosting two nuclei. In all these cases the flux from secondary

sources is likely to be included in the flux calculations for each. However, since they will also be covered by the CO(2-1) and CO(3-2) APEX observations then this is unavoidable in the analysis. No other sources have known companions that would affect the total fluxes measured.

4.3.2 CO(2-1) Observations

The CO(2-1) emission of 8/17 sources of the sample were observed with SEPIA180 on APEX between 09 December 2020 and 21 June 2021, (proposal ID: E-0105.B-0713A-2020 [PI: Calistro-Rivera]). The remaining 9 targets had equivalent APEX archival CO(2-1) observations presented as a pilot sample by [Jarvis et al. \(2020\)](#) (Proposal ID: E-0100.B-0166, [PI: Jarvis]). For this work we have re-analysed the raw archival data from [Jarvis et al. \(2020\)](#) using the new analysis techniques presented here for consistency, however we note that we find the same results reported by [Jarvis et al. \(2020\)](#) within uncertainties.

The data was reduced using the standard procedures in the Continuum and Line Analysis Single-dish Software (CLASS) ([Pety, 2005](#)). In all cases the reduction of the APEX data was done using a consistent strategy by modifying the template reduction script from APEX in CLASS. As with the CO(1-0) data we binned to 50 and 100 km s⁻¹ where appropriate. The observing frequency range of 192.3 – 212.5 GHz yields an APEX beam size in the range of 29 – 32 arcsec, corresponding to a physical size of 68 – 75 kpc at the median redshift of 0.14.

We fit Gaussians using standard procedures in python to obtain the integrated flux values and corresponding uncertainties for each target. We note that the results of fitting Gaussians in python match that of the Gaussian fits produced in CLASS. There is no spatial information for these data, however the beam size is large enough to cover the host galaxy, and so we are confident we measure the total flux, including any diffuse gas and do not over resolve.

Upper limits are calculated using line widths estimated from other CO transitions for the same targets where available. If none are available, the average CO W_{80} in that transition for all targets is used, for which these values are 397 km s⁻¹ for CO(1-0), 477 km s⁻¹ for CO(2-1) and 507 km s⁻¹ for CO(3-2). The flux upper limits are then the flux of a line with this width, with a peak at $3 \times$ the rms measured within the data. We note that this strategy is different from the calculations used by [Jarvis et al. \(2020\)](#), where upper limits were calculated by taking the maximum

CO line width from the sample in CO(2-1). The case by case approach based on information from the other CO lines for each target, and assuming we should see similar line widths between transitions, should therefore provide a more accurate and constraining upper limit. The two cases for which both methods have been applied are J0958+1439 and J1356+1026. For J0958+1439, the estimated CO(2-1) upper limit estimated with our method is 30 per cent of the value reported in [Jarvis et al. \(2020\)](#), whereas for J1356+1026 our estimate is 93 per cent of the value reported in [Jarvis et al. \(2020\)](#).

An important note to make is that during the period in which CO(2-1) and CO(3-2) observations were taken with APEX, the telescope was operating at significantly different efficiencies (at most by a factor of 40%). To account for this and to achieve accurate flux measurements, corrections have been made based on the following. Main beam characteristics have been determined from de-convolved continuum slews across Mars, Uranus and Jupiter. Using CO(3-2), this yielded a mean beam size $\theta_{mb} = 17.5 \pm 0.2$, which we confirmed to be consistent with data on the CO line pointing sources (which are standard AGB stars used for pointing and focus calibration during observations). To determine the main beam efficiency, we used cross scans¹ obtained between December 2020 and December 2021 and cross-checked the result against the CO(3-2) flux of 8 line intensity monitoring sources². This analysis yielded main beam efficiencies (at 345 GHz) that depended on periods $\eta_{mb} = 0.63 \pm 0.04$ (Dec 2020), 0.55 ± 0.04 (May – Jun 2020), and 0.67 ± 0.04 (Aug – Dec 2020) and an antenna gain factors of Jy/K = 45 ± 4 , 51 ± 4 , 42 ± 4 , respectively, which were converted to the science frequencies using the Ruze formula. In the observations we used the wobbler in symmetrical mode with an amplitude of 50 and frequency of 0.5 Hz. Pointing and focus were checked regularly against sources from the APEX line pointing catalog using the CO(3-2) emission line. We estimate the overall calibration uncertainty at 10% and that the pointing accuracy was typically within 2". Baselines were stable and we only had to fit a first order baseline to each scan before averaging them.

¹See <http://www.apex-telescope.org/telescope/efficiency/index.php>

²See <https://www.apex-telescope.org/ns/apex-data/>

4.3.3 CO(3-2) Observations

Of the 17 sources in our sample, 16 were observed in CO(3-2) with SEPIA345 between 09 December 2020 and 30 December 2021 (proposal ID: E-0105.B-0713B-2020 [PI: Calistro-Rivera]). The observing frequency range of 288.4 – 318.7 GHz yields an APEX beam size in the range of 19 – 22 arcsec, corresponding to a physical size of 44 – 51 kpc at the median redshift of 0.14. These data were reduced, and the flux densities were extracted in the same way as CO(2-1), as described in Section 4.3.2.

For the one remaining target, J1430+1339, we utilise archival CO(3-2) ACA observations (proposal ID: 2016.1.01535.S [PI: Lansbury]) taken on 03 November 2016. These data were available on the ALMA archive with bin widths of 27 km s^{-1} . The coverage in the velocity space is not as wide as that of the equivalent APEX observations. Caution should be taken in this case as the difference in spatial resolution (here a beam size of 4.3 arcsec and a maximal recoverable scale of 23 arcsec) means that there is a possibility it is slightly over resolved and perhaps missing flux, but even with these caveats it provides a useful data point.

4.3.4 CO(6-5) and CO(7-6) Observations

We observed 7 targets in either CO(6-5) or CO(7-6) using SEPIA660 on APEX, which were selected for observation based on their brightness in the lower CO transitions. CO(6-5) and CO(7-6) were chosen to give an indication of the excitation in these higher transitions, with CO(6-5) preferred, but if it was not observable (due to the frequency range offered by SEPIA660) then we chose CO(7-6) instead. We also note that [C I](2-1) are also covered by our CO(7-6) observations, however, since all three have non-detections and there are no signs of detection across the obtained spectra, we do not perform any further analysis.

All observations were taken between May – November 2022 (proposal ID: E-0109.B-0710 [PI: Molyneux]). Previous observations of 3 targets (J1010+0612, J1100+0846 & J1430+1339) are also utilised by combining this archival data to our own (proposal id. E-0104.B-0292 [PI: Harrison]). These data were reduced in the same way as CO(2-1) (see Section 4.3.2 for details).

From the range of frequencies 613 – 708 GHz, the corresponding beam size was 9 – 10 arcsec, which relates to a physical size of 21 – 23 kpc at the median redshift of 0.14. This beam size should still allow us to retrieve the full flux values for two reasons. Firstly, for targets in this sample that are observed at higher spatial resolution (0.2 arcsec) and presented by [Ramos Almeida et al. \(2022\)](#), the moment maps and position velocity diagrams show that the CO emission is confined within the APEX beam size. Furthermore, we would expect the CO(6-5) and CO(7-6) to be more compact than the emission of the lower transitions and we are therefore confident that we are measuring the total flux in these data. One caveat would be that if any extended, diffuse emission exists in these higher CO transitions we would potentially be resolving out some of the flux, but we consider this unlikely due to the reasons outlined above.

4.3.5 Ancillary Multiwavelength Data

To achieve a detailed characterisation of the AGN feedback processes in our sample, the 17 quasars studied in this work have ancillary radio and optical data from the VLA and MUSE on the VLT, respectively. Here we describe these data and all values used in this paper can be found in Table 4.1.

VLA radio data are available for all 17 quasars in the sample at 1–6 GHz and at a resolution of 0.3 – 1 arcsec. For a full review and analysis of the radio data see [Jarvis et al. \(2019, 2021\)](#). In this work we utilise knowledge of the 1.4 GHz radio data to aid in the interpretation of our findings. The quasars show a range of moderate radio luminosities of $\log(L_{1.4\text{ GHz}}/\text{WHz}^{-1}) = 23.5 - 24.4$. Crucially, although the quasars in our sample are ‘radio-quiet’, according to widely-used radio-loudness definitions ([Xu et al., 1999](#)), the bulk of them exhibit extended radio structures on 0.2 – 34 kpc scales, with evidence of jets and/or shocked winds being the dominant cause of the extended radio structures ([Jarvis et al., 2019, 2021](#)).

There is also strong evidence for these radio jets interacting with the ionised gas and driving outflows ([Jarvis et al., 2019](#); [Girdhar et al., 2022](#)). We therefore know that within this sample we are observing a diversity of radio AGN emission and ionised outflows in quasars. Further, from these ancillary data we know that this sample is dominated by AGN which are driving outflows, host jets/winds and show interactions with the ISM. The question remains however,

as to how these feedback mechanisms impact the molecular gas properties, which we aim to address in this work.

We have also obtained MUSE VLT observations for these 17 quasars (proposal ID: 0103.B-0071 [PI: Harrison]). In this work we use the MUSE data to extract spectra of the [O III] λ 5007 emission line where possible, and otherwise [O III] λ 4959 (1 case) or H β (2 cases) if no [O III] λ 5007 line were available. We use these lines as tracers of the ionised gas kinematics and to compare to the molecular CO gas presented here. The spectra were all extracted using the same aperture (diameter \sim 30 arcsec) as our APEX data (details in Section 4.3) to make a comparison of ionised gas on the same scales. Specifically we use the [O III] W_{80} and the properties of the line profile to analyse the differences between the impact of feedback on the ionised and molecular gas properties.

4.4 Analysis and results

In this section we present the main analysis and results of this work. Firstly, in Section 4.4.1 we introduce the comparison samples that are used to put our results into context of the overall population of both AGN and non-AGN. We then present the analysis undertaken of the observed CO transitions in Section 4.4.2. We present the calculations and results of the molecular gas masses and gas fractions in Section 4.4.3. Finally, we present our findings on the CO excitation via the use of CO Spectral Line Energy Distributions (CO SLEDs) and CO line ratios (Section 4.4.4). Further, an example of the spectra obtained can be found in Figure 4.3 and the remaining spectra, alongside tables of the line properties, are presented in the appendix.

4.4.1 Comparison samples

Throughout Section 4.4 we present comparison samples from the literature to put our work into context and aid in the interpretation of our analysis. These comparison samples are described below:

We first utilise non-AGN and AGN from [Tacconi et al. \(2018\)](#) to put the gas fractions of our sources in context and show that they are consistent with both AGN and non-AGN. The comparison sample is a compilation of data from xCOLD GASS ([Saintonge et al., 2017](#)), EGNOG ([Bauermeister et al., 2013](#)) and GOALS ([Armus et al., 2009](#)) surveys as well as from the sample presented in [Combes et al. \(2011\)](#). We matched this sample to be within $z \pm 0.05$ of the full range of redshifts spanned by our sample. AGN hosts for the sample were identified using BPT-based AGN classifications. The galaxies in this comparison sample also span the full range of stellar mass, sSFR, and ΔMS found for our sample (see Figure 6 in [Jarvis et al., 2020](#)) meaning that the dependency on the specific star-formation rate has been removed and we are focusing on any possible impact of having an active BH rather than the star-formation efficiency of the given galaxy. To ensure consistency in the comparison, the molecular gas masses presented for our sample are calculated using the same method as shown in [Tacconi et al. \(2018\)](#). This comparison is presented in Figure 4.4. For further information on this comparison sample also see [Jarvis et al. \(2020\)](#).

In our CO SLEDs (Section 4.4.4) we utilise the compilations by [Valentino et al. \(2021\)](#) and [Carilli & Walter \(2013\)](#) to compare to our CO SLEDs. From [Valentino et al. \(2020, 2021\)](#) we present the CO SLEDs (both Figures 4.5 and 4.6) of starburst and main sequence galaxies in the redshift range $z \sim 1 - 2$ with $L_{IR} > 10^{12} L_{\odot}$. These luminosities are similar to those in our sample (see Section 4.3.5) and therefore provide a useful comparison. From [Carilli & Walter \(2013\)](#) we utilise the compilation of high- z quasars ($z \sim 1 - 6$), shown as ‘‘C&W13’’ in Figures 4.5 and 4.6, to see how our low- z quasar sample compare to these more distant and more luminous objects ($L_{bol} > 10^{47} \text{ erg s}^{-1}$, compared to QFeedS with $L_{bol} < 10^{46.5} \text{ erg s}^{-1}$). We also show these high- z quasars in Figure 4.7 as individual points to show how they compare in the lower transitions to the range of line ratios in our sample and other comparison samples listed below. Finally, in Figure 4.8 we present the line ratios of our high J_{CO} transitions compared to the high- z quasar sample, as a function of bolometric luminosities.

As mentioned above, in Figure 4.7 we present the range of line ratios found in our sample compared to others in the literature in the form of violin plots. [Montoya Arroyave et al. \(2023\)](#) analysed a sample 40 local (U)LIRGs ($L_{IR,SF} \gtrsim 10^{12} L_{\odot}$) in the same redshift range as our sample ($z < 0.2$). The targets were selected based on OH absorption and not on the presence of radio jets, however this does not exclude radio jets being present. This sample also shows a range of AGN fractions, from 0 – 0.92, with 50% having an AGN fraction greater than 0.5. They

find no correlation between AGN fraction or AGN luminosity within the sample of (U)LIRGs. Since 8 sources out of 9 in the QFeedS sample with the required measurements are known to be LIRGs, [Montoya Arroyave et al. \(2023\)](#) provides a useful comparison to determine whether the presence of radio jets or shocked winds and ionised outflows found in our sample makes a significant difference to the observed line ratios.

In Figure 4.7 we also perform a similar comparison to a sample of (U)LIRGs at $z \leq 0.1$ from [Greve et al. \(2014\)](#). This sample of (U)LIRGs was selected against AGN, all with an AGN contribution of $\lesssim 0.3$. With this, alongside the sample in [Montoya Arroyave et al. \(2023\)](#), we have comparisons samples with similar IR luminosities and a range of AGN contribution. Since the QFeedS sample is compiled of quasars with LIRG-like infrared luminosities, but with additional known radio jets and ionised outflows, any differences in the excitation of CO could potentially be attributed to the jet and outflow properties of our sample.

In order to also investigate how local AGN (with a median $z \sim 0.05$) with lower luminosities (median $L_{\text{bol}} \sim 10^{44.8}$) compare with our sample, we utilise the sample by [Lamperti et al. \(2020\)](#). We can therefore test how our more luminous quasars are different in CO excitation. This comparison sample comprises of X-ray selected AGN, for which further information can also be found in [Ricci et al. \(2017\)](#); [Koss et al. \(2021\)](#). These data are also used in Figure 4.7. Finally, we also used a compilation of local star forming galaxies as a comparison [Leroy et al. \(2022a\)](#), which includes data from HERACLES ([Leroy et al., 2009](#)), the James Clerk Maxwell Telescope (JCMT) Nearby Galaxy Legacy Survey (NGLS [Wilson et al., 2012](#)), the CO Multiline Imaging of Nearby Galaxies (COMING) survey ([Sorai et al., 2019](#)), PHANGS ALMA ([Leroy et al., 2021](#)), IRAM 30m CO (2–1) observations, and Large APEX Sub-Millimetre Array (LASMA) CO (3–2) observations.

4.4.2 Spectral properties

We analyse the spectral properties across different CO transitions for all targets in our sample to investigate the integrated fluxes, line profiles, including line widths, velocity offsets and features within the lines (e.g. potential outflow components). These can then be compared to properties of the host galaxies and the line profiles of the ionised gas to search for any influence of AGN activity.

Spectra are mostly plotted for each target with the same bin widths across all transitions so that the line profiles of each transition can be easily compared (see Figure 4.3 and the remaining spectra in the appendix, Figures 4.13–4.29). In some exceptional cases, where we had enough S/N in some transitions to investigate the line profile in more detail, but not enough S/N in other transitions, we choose the bin widths accordingly. Central frequencies (where $v = 0 \text{ km s}^{-1}$) have been defined using the SDSS redshifts quoted in Table 4.1. We choose the SDSS redshifts as this has been used throughout the QFeedS survey work, and since we are only comparing CO and ionised gas lines within the same target, the specific reference velocity/redshift is not important. The aperture from which all the spectra are taken is consistent between CO(1-0) and CO(2-1) for each source, and for higher transitions will be slightly smaller due to the APEX beam size reducing as observing frequency increases (as mentioned in Section 4.3). However, our analysis is done in a way that is consistent between transitions and therefore any differences found are potential indications of the impact from feedback mechanisms being different on the different CO transitions.

As an example we present the spectra of all CO transitions (CO(1-0), CO(2-1), CO(3-2), and CO(6-5)) and the MUSE [O III] emission for one target in the main body of the paper (J1100+0846 shown in Figure 4.3) and all remaining spectra are then presented in the appendix. For all sources, [O III] line profiles are plotted in a separate panel below the CO spectra for comparison (in some cases the [O III] line was not available so the $H\beta$ emission line was used instead) extracted from MUSE data using the same aperture as that of the CO data. For some sources of our sample (J1010+0612, J1100+0846, J1356+1026 and J1430+1339), ALMA observations of the CO(2-1) at 0.2 arcsec resolution presented by Ramos Almeida et al. (2022) are available. We show these ALMA spectra plotted in orange over our APEX CO(2-1) spectra to compare. Making these comparisons required a velocity shift to the Ramos Almeida et al. (2022) data to match the zero velocity used here, which we determined using the SDSS redshift, as opposed to the approach taken in Ramos Almeida et al. (2022). Specifically, they used the SDSS redshift as the initial $v = 0 \text{ km s}^{-1}$ and then applied a small shift to make the peak (or centre of two peaks) at $v = 0 \text{ km s}^{-1}$. Despite this small difference, we find consistent flux values and line profiles within errors when comparing to Ramos Almeida et al. (2022). We also note the availability of CO(1-0) and CO(3-2) data for J1356+1026 from Sun et al. (2014), however due to the differences in resolution (at 1.3 and 0.6 arcsec for CO(1-0) and CO(3-2) respectively) and therefore high chance of over-resolving the total CO emission compared to the QFeedS observations, these are excluded from any analysis.

From a first look at our CO spectra it is immediately clear that there is a large variety of line profiles, luminosities and detections for the different transitions within our sample. We also find a large diversity of broad line profiles, double peaked profiles as well as a blue wing and offsets from $v = 0 \text{ km s}^{-1}$. A detailed comparison of the molecular and ionised gas line profiles is discussed in Section 4.5.3.

To analyse the line profiles of both the CO transitions and MUSE [O III] spectra, we fit either one, two, or three Gaussian components to the spectra where appropriate. In the CO data, since we have relatively low S/N, we find only two targets with more than one Gaussian component. However, in the MUSE data we see a wide range of line profiles, including many with multiple components. From the data we analyse the central velocity (V_{50}) and line width over which 80 percent of the flux is contained (W_{80}) which can either be done using the fits to the data or to the data itself. We choose to present the values calculated on the fits to the data for the following reasons.

There are 21 cases for which we are measuring V_{50} and W_{80} of spectra with $S/N > 5$ (used in future analysis) and of those 21, 17 of the W_{80} values from the data are within the uncertainties of the W_{80} from the fit, whilst 4 are outside the fit uncertainties. Three sources have higher S/N data published by [Ramos Almeida et al. \(2022\)](#); of these, two have line widths closer to the W_{80} values from the fit, while one is closer to the W_{80} of the data. Finally, of these 21 cases there are 16 where the W_{80} of the fit is larger, while there are five where the W_{80} of the data is larger. Given that both measures are mostly consistent with each other, that in two out of three cases the W_{80} of the fit is closer to higher S/N data in the literature and that in most cases W_{80} of the fit is larger, we decide that the W_{80} of the fits is more appropriate for this work. Since we are looking at relatively low S/N data across the sample, either measure used will give large uncertainties and so using the larger of the two means we are closer to the maximum value from the data, which is considered later in the analysis of the line profiles and further discussion in Section 4.5.3.

Therefore, in all cases we use the V_{50} and W_{80} of the fits to the data to analyse as the description of the line profiles. In the case of spectra which show a single Gaussian profile, the uncertainties on V_{50} and W_{80} are the errors on the fit. The uncertainties for the total flux is the uncertainty on the fit plus the uncertainty on the telescope efficiency. For those with multiple components, the uncertainty on V_{50} presented is the uncertainty on the narrowest components peak velocity. The

uncertainty on W_{80} is the uncertainty on the W_{80} of the broadest component. The uncertainty on the flux for those with multiple components is the uncertainties on each component added in quadrature plus the uncertainty on the telescope efficiencies ($\sim 5 - 10\%$ for all observations). The noise for each channel for APEX data was taken from the results of the CLASS reduction scripts. For ACA observations the rms was calculated by taking the median flux from the remaining spectrum, whilst masking the line (where present).

In order to determine which lines and fits are robust and can be used for further analysis we measure the data quality based on the S/N of the lines within our sample. We determine the integrated S/N using the following equation:

$$S/N = \frac{f_{\text{int}}}{(\text{rms}_{\text{chan}} / ((w)/v_{\text{res}})^{0.5} \times (w))} \quad (4.1)$$

where w is the full line width, v_{res} is velocity resolution, f_{int} is the integrated flux, rms_{chan} is the rms per channel.

We then define different levels of detection based on S/N calculations using equation 4.1. The three categories are “detections”, “low S/N detections” and “non-detections”. They are classified in the following way:

- “Detections” are defined as spectra which show lines with an integrated S/N ≥ 5 .
- “Low S/N detections” are defined as those lines with $3 \leq \text{integrated S/N} < 5$.
- Anything with no clear line or a line with an integrated S/N < 3 is defined as a “non-detection”.

When referring to “detections” from this point onward we refer to both “detections” and “low S/N detections” as defined here unless otherwise stated.

For those with low S/N detections we present the fits to the spectra with a dashed black line to differentiate from detections shown by solid black lines. The integrated S/N values are also shown in the tables presenting CO data. For a list of the classifications of all detections, low S/N detections and non-detections see Table 4.5 in the appendix.

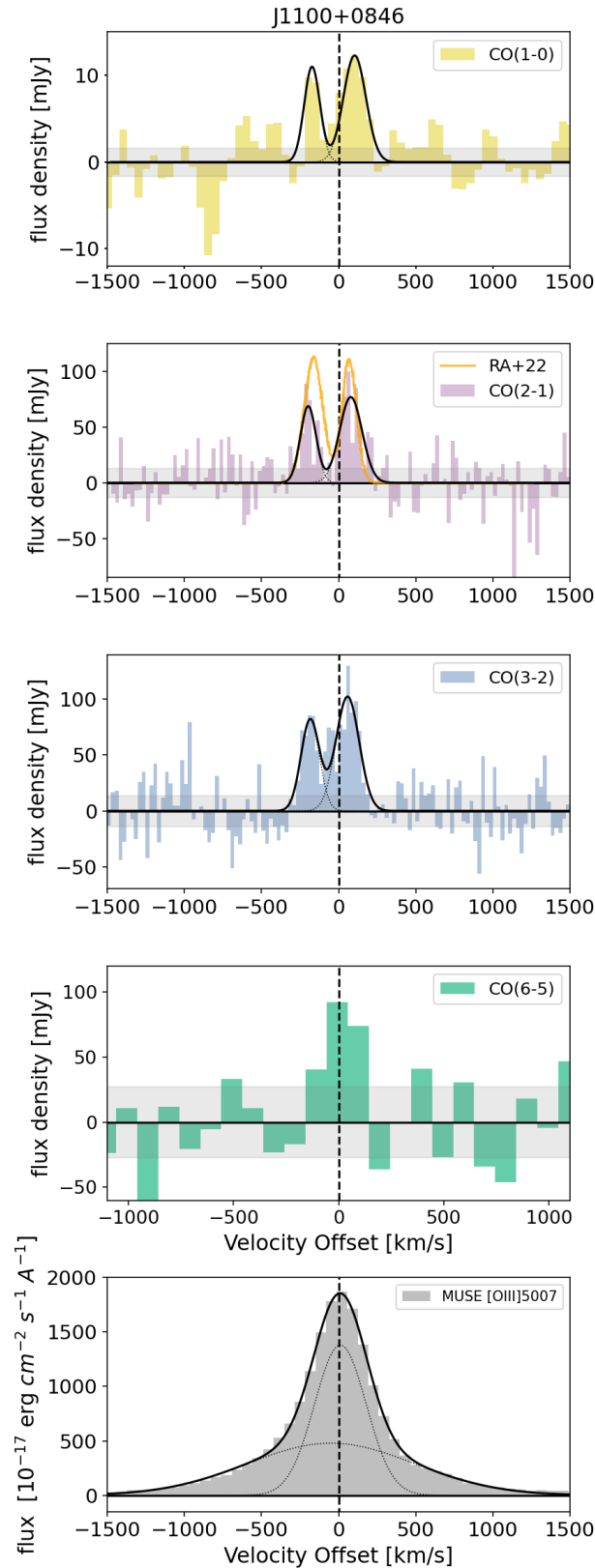


Figure 4.3: Example of multiple CO spectra and MUSE data obtained, here showing J1100+0846. Top panel: CO(1-0) from ACA. Second panel CO(2-1) from APEX (in this case the data was from [Jarvis et al., 2020](#)). Third panel: CO(3-2) data from APEX. Fourth panel: CO(6-5) data from APEX. Fifth panel: MUSE spectrum for the [O III] line extracted from a 30 arcsec diameter aperture. In all cases, solid black lines denote fits to the data. Here there are multiple components and as such, the dotted black lines denote the different components that make the total fit to the spectra. In the CO(2-1) spectrum we also show the fit from higher resolution ALMA observations (solid orange line labelled RA+22, [Ramos Almeida et al., 2022](#)). Shaded grey regions represent the 1 σ level. Spectra for all targets are shown in the appendix, using the same presentation methods.

There are three sources which show non-detections in all CO transitions which are J0909+1052, J1222-0007 and J1356+1026. However, we note that J1356+1026 does have a CO(2-1) detection in the deeper ALMA data from [Ramos Almeida et al. \(2022\)](#) which we utilise in later analysis. Several other targets also show non-detections in at least one transition. To test whether the non-detections might show any low-brightness signal when combined, we stack these data by bringing the observations from different targets to the same velocity reference. However, from stacking non-detections we don't find any underlying flux and thus we can make no more conclusions based on these data.

From these spectra we can calculate total fluxes, line widths (W_{80}), velocity offsets (V_{50}) and line luminosities (all data are presented in the appendix in Tables: [4.6](#), [4.7](#), [4.8](#), [4.9](#) & [4.10](#)) For those with non detections we choose to present the 3σ upper limits for CO flux and luminosity. Further observations would be required to confirm any of these detections. Line luminosities (L'_{CO}) are calculated using the following equation from [Solomon et al. \(1997\)](#) (also used in analysis in previous QFeedS work [Jarvis et al., 2020](#)):

$$L'_{CO}[\text{K km s}^{-1}\text{pc}^2] = \frac{3.25 \times 10^7}{\nu_{CO,\text{rest}}^2} \left(\frac{D_L^2}{1+z} \right) f \quad (4.2)$$

where $\nu_{CO,\text{rest}}$ is the rest frequency of the CO line, D_L is the luminosity distance, z is the redshift and f is the velocity integrated line flux density measured in Jy km s^{-1} .

4.4.3 Molecular gas masses

Studying the molecular gas masses in this sample will allow us to determine whether the presence of a quasar has an impact on the total gas fraction. We calculate the CO(1-0) molecular gas masses using the mass–metallicity relation used by [Tacconi et al. 2018](#) (see also [Genzel et al., 2015](#)), along with the following equations [4.4](#) and [4.5](#):

$$M_{CO} = \alpha_{CO} \times L'_{CO}(1-0) \quad (4.3)$$

where $L'_{CO}(1-0)$ is the CO(1-0) luminosity and α_{CO} is the conversion factor calculated as a function of metallicity (following the α_{CO} calculation from [Tacconi et al. 2018](#), taking the

geometric mean of the metallicity-dependent α_{CO} recipes of [Genzel et al. 2012](#) and [Bolatto et al. 2013](#)):

$$\alpha_{\text{CO}} = 4.36 \times \sqrt{\frac{0.67 \times \exp(0.36 \times 10^{-1 \times (12 + \log(O/H) - 8.67)})}{\times 10^{-1.27 \times (12 + \log(O/H) - 8.67)}}}, \quad (4.4)$$

where α_{CO} has units $M_{\odot} (\text{K km s}^{-1} \text{pc}^2)^{-1}$. Also following [Tacconi et al. \(2018\)](#) we use the following mass metallicity relation from [Genzel et al. \(2015\)](#):

$$12 + \log(O/H) = a - 0.087 \times (\log M_{\star} - b)^2 \quad (4.5)$$

where, $a = 8.74$, $b = 10.4 + 4.46 \times \log(1 + z) - 1.78 \times (\log(1 + z))^2$ and M_{\star} is the stellar mass obtained from SED fitting ([Jarvis et al., 2020](#)).

For those without CO(1-0) detections we use the CO(2-1) luminosity where possible and convert to CO(1-0). Conversions made from $L'_{\text{CO}}(2-1)$ use the median line ratios observed within this sample (presented in [Table 4.3](#)) as conversion factors (median line ratio of 1.06). Here the sources J1010+0612, J1010+1413, J1356+1753 and J1430+1339 are calculated using $L'_{\text{CO}}(2-1)$. For those with non-detections across all CO transitions we provide 3σ upper limits of M_{CO} based on the upper limits of the CO(1-0) flux.

The calculated values of α_{CO} from our sample are within the range 4.0 – 4.2 (shown in [Table 4.2](#)). These values are consistent with typical high redshift, high star-forming, quasar host galaxies ([Bolatto et al., 2013](#); [Carilli & Walter, 2013](#)). However, α_{CO} may also be significantly lower in LIRGs, submillimeter galaxies, mergers, starbursts and AGN, with values as low as $\sim 0.6 - 1$ (e.g., [Bolatto et al., 2013](#); [Sargent et al., 2014](#); [Calistro Rivera et al., 2018](#)). Therefore there are uncertainties that arise in these values and the calculated gas masses. There can also be dependencies on the metallicity and SFR (see e.g. [Bolatto et al., 2013](#); [Sandstrom et al., 2013](#), and references therein), but for most galaxies a value of ~ 4 is found, as is identified in our targets using the same method of calculation as the comparison sample in [Tacconi et al. \(2018\)](#) (which we follow for consistency).

The molecular gas masses in our sample range from $0.36 - 5.50 \times 10^{10} M_{\odot}$ and all molecular gas masses can be found in Table 4.2 along with stellar mass estimates obtained from SED fitting (see [Jarvis et al., 2020](#), for a description of these calculations). There are cases with large uncertainties which result from poor constraints on the SED fitting. These uncertainties also follow through into Figure 4.4 where we present the stellar and CO gas masses ([Jarvis et al., 2019](#), stellar masses calculated from SED fitting). Gas fractions are also presented in Table 4.2 calculated as M_{CO}/M_{\star} . We find values in the range 0.06 – 1.4. These are used in Figure 4.4 to compare to AGN and non-AGN from the literature ([Tacconi et al., 2018](#)). See section 4.4.1 for further information about this comparison sample. We find that our sources are consistent with the comparison sample of non-AGN and AGN. There are a few cases where we see higher gas fractions, in particular J0945+1737, J1108+0659 and J0958+1439 but these are still consistent with both AGN and non-AGN from the literature (see Figure 4.4). In fact, AGN have been found to have similar, or higher gas fractions than non-AGN (e.g. [Rosario et al., 2018](#); [Kirkpatrick et al., 2019](#); [Jarvis et al., 2020](#); [Shangguan et al., 2020](#); [Koss et al., 2021](#); [Zhuang et al., 2021](#); [Salvestrini et al., 2022](#)). Further, in AGN CO gas can also be detected in a warm phase (e.g. [Rosario et al., 2019](#)) so the molecular gas levels here could also be considered a lower limit of the total molecular gas content. However, it is important to note that even with the presence of high gas fractions, it does not exclude the possibility of AGN feedback (including cases with the presence of outflows) as shown in comparisons of simulations ([Ward et al., 2022](#)).

[Jarvis et al. \(2020\)](#) discuss gas fractions as well as analyse the star formation rate, specific star formation rate and distance from the main sequence for a subsample of these data. We note however, that there are differences in this work when comparing to the same targets in [Jarvis et al. \(2020\)](#), which used r_{21} of 0.8 to convert from CO(2-1) to CO(1-0). Given that we have the CO(1-0) measurements here we simply use those, and as discussed before we find higher values of r_{21} with a median of 1.06 within our sample. As such, the results of the total gas masses and gas fractions are also different here compared to [Jarvis et al. \(2020\)](#), with this work finding lower total gas masses, but within uncertainties and therefore still consistent.

4.4.4 CO excitation

To measure and analyse the excitation of the molecular gas we analyse both the observed shape of the CO SLEDs as well as the line ratios of the CO transitions. Studying the excitation of

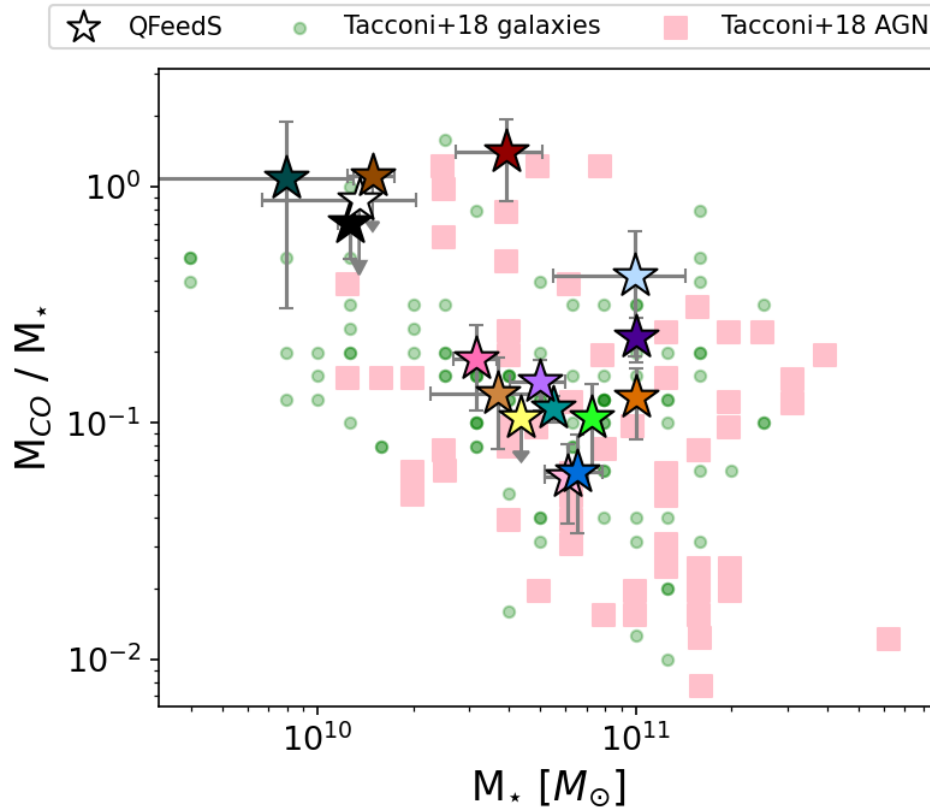


Figure 4.4: For all targets with data for both stellar mass (M_*) and CO gas masses (M_{CO}) we present the stellar mass versus the gas fraction (M_{CO}/M_*). Large coloured stars show targets from this work, with colours as in Figure 4.1. Background small green circles and pink squares show a compiled literature sample of AGN and non-AGN from Tacconi et al. 2018. Here 16/17 targets are presented, with J1116+2200 missing due to a lack of stellar mass information.

the gas and comparing to literature samples of both AGN and non-AGN will again allow us to determine whether the excitation in the quasar host galaxies is systematically different to that of other relevant galaxy samples.

CO SLEDs

We present the CO SLEDs of our sources in two different sets. Firstly, in Figure 4.5 we show CO SLEDs from the ground state up to CO(3-2), making comparisons to literature samples. We plot only those with detections in CO(1-0) (including low S/N detections), so that we have a reliable normalisation to the ground state. For those without a detection in CO(1-0) deeper observations would be required to provide a reliable CO SLED. The reference SLEDs shown here are the Milky Way and thermalised SLEDs, shown by dotted lines (Carilli & Walter, 2013). We further make comparison to starburst and main sequence galaxies at $z \sim 1 - 1.7$ taken from Valentino et al. (2021) (see Section 4.4.1 for further information on these comparison samples).

Name	α_{CO}	M_{CO} $M_{\odot} (\times 10^{10})$	M_{\star} $M_{\odot} (\times 10^{10})$	M_{CO}/M_{\star}
J0909+1052	4.28	$< 1.20^a$	1.35 ± 0.68	$< 0.88^a$
J0945+1737	4.24	0.89 ± 0.25^a	1.25 ± 0.10	0.71 ± 0.21^a
J0958+1439	4.24	0.64 ± 0.08^a	5.50 ± 0.10	0.12 ± 0.01^a
J1000+1242	4.34	0.87 ± 0.30^a	0.79 ± 0.50	1.09 ± 0.79^a
J1010+0612	4.20	0.59 ± 0.21^b	10.00 ± 0.50	0.19 ± 0.07^b
J1010+1413	4.18	2.30 ± 0.50^b	3.16 ± 0.10	0.23 ± 0.05^b
J1016+0028	4.05	0.36 ± 0.12^a	6.12 ± 0.95	0.06 ± 0.02^a
J1055+1102	4.05	0.40 ± 0.16^a	6.54 ± 1.35	0.06 ± 0.03^a
J1100+0846	4.16	0.75 ± 0.11^a	5.01 ± 1.00	0.15 ± 0.04^a
J1108+0659	4.10	5.50 ± 1.27^a	3.91 ± 1.18	1.41 ± 0.54^a
J1114+1939	4.05	4.17 ± 1.30^b	9.94 ± 4.43	0.42 ± 0.23^b
J1116+2200	4.19 ^c	3.07 ^c	–	–
J1222-0007	4.27	$< 1.65^a$	1.49 ± 0.25	$< 1.11^a$
J1316+1753	4.27	1.28 ± 0.42^b	10 ± 0.25	0.12 ± 0.04^b
J1356+1026	4.27	$< 0.46^b$	4.37 ± 0.10	$< 0.11^b$
J1430+1339	4.25	0.76 ± 0.30^b	0.79 ± 0.05	0.11 ± 0.04^b
J1518+1403	4.08	0.49 ± 0.08^a	3.68 ± 1.41	0.13 ± 0.06^a

Table 4.2: We present α_{CO} (calculated using equation 4.4), M_{CO} (calculated using equations 4.3, 4.4 and 4.5), M_{\star} and gas fractions (M_{CO}/M_{\star}) for each target in the sample. For J1116+2200 the stellar mass is unconstrained by the SED and so there is no value of M_{\star} (and therefore also α_{CO}). ^a Calculated from CO(1-0) line luminosity. ^b Converted to CO(1-0) from CO(2-1) using the median line ratio of those in the rest of the sample with detections. ^c Median α_{CO} value of 4.19, and M_{CO} calculated from this median.

We report that the CO SLEDs of 2 out of 9 sources are consistent with being above the thermalised relation at the CO(2-1) level (excluding the upper limit of J1055+1102) and 2 out of 9 at the CO(3-2) level (see Figure 4.5). However, including the uncertainties on the CO(1-0) fluxes in addition to the CO(2-1) or CO(3-2) they are all still consistent with being thermalised, with the exceptions of r_{21} for J1100+0846 and r_{32} for J1010+1413 (see Table 4.3 for individual values).

For sources within our sample with available observations in higher CO transitions ($J_{\text{up}} = 6, 7$) we plot the CO SLEDs extending to these higher transitions and normalise the SLED to CO(2-1) instead of CO(1-0) (see Figure 4.6). Normalisation to the CO(2-1) transition was done for two reasons. Firstly, two of our targets with high CO transition data have not been observed in CO(1-0) and so to make comparisons within our own sample the next transition available with detections for all targets was CO(2-1). Secondly, based on our observations of several super-thermal SLEDs at CO(2-1) and the ongoing discussion in the community about the optical thickness of CO(1-0) (see Section 4.5), we argue that CO(2-1) might be more reliable transition for normalisation. Again, in Figure 4.6 we make comparisons to other samples from

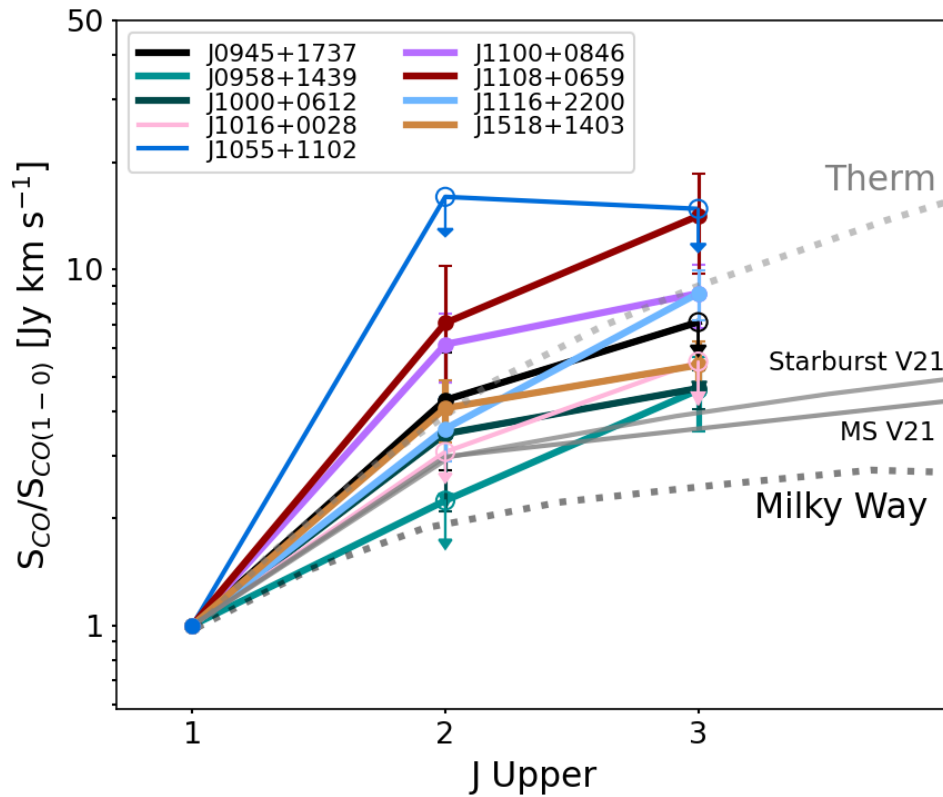


Figure 4.5: For the 9 targets which have detections in CO(1-0) we present the CO SLEDs, normalised to CO(1-0) with Milky Way and thermalised relations for comparison (Carilli & Walter, 2013). Also shown are $z = 1 - 2$ Starburst and main sequence (MS) CO SLEDs from Valentino et al. (2021) (V21). The CO SLEDs are colour coded by target (as in Figure 4.1). 3 sigma upper limits are indicated by empty circles with downward arrows. No uncertainties are shown for CO(1-0) as these are incorporated into the uncertainties on CO(2-1) and CO(3-2) to best represent the uncertainty on the excitation level.

the literature. In addition to the literature samples mentioned previously we also include high- z quasars ($z \sim 1 - 6$) compiled by Carilli & Walter (2013), to make comparisons to the low- z counterparts in our sample.

Out of the 7 sources observed, 6 show non-detections and only 1 source, J1430+1339, has a detection in either CO(6-5) or CO(7-6), based on the same criteria stated in Section 4.4.2. We find that this detection is relatively low in the CO SLED, suggesting that the peak of the SLED may be at $J_{CO} < 6$ (see Figure 4.6). It appears to be more similar to main sequence and starburst galaxies as opposed to high- z quasars (Carilli & Walter, 2013).

For the remaining CO SLEDs in Figure 4.6 we only have upper limits, however two of these are very constraining namely J1100+0846 and J1108+0659, which are at the same excitation level as the already detected J1430+1339). 5 targets are less excited than the high- z quasar CO

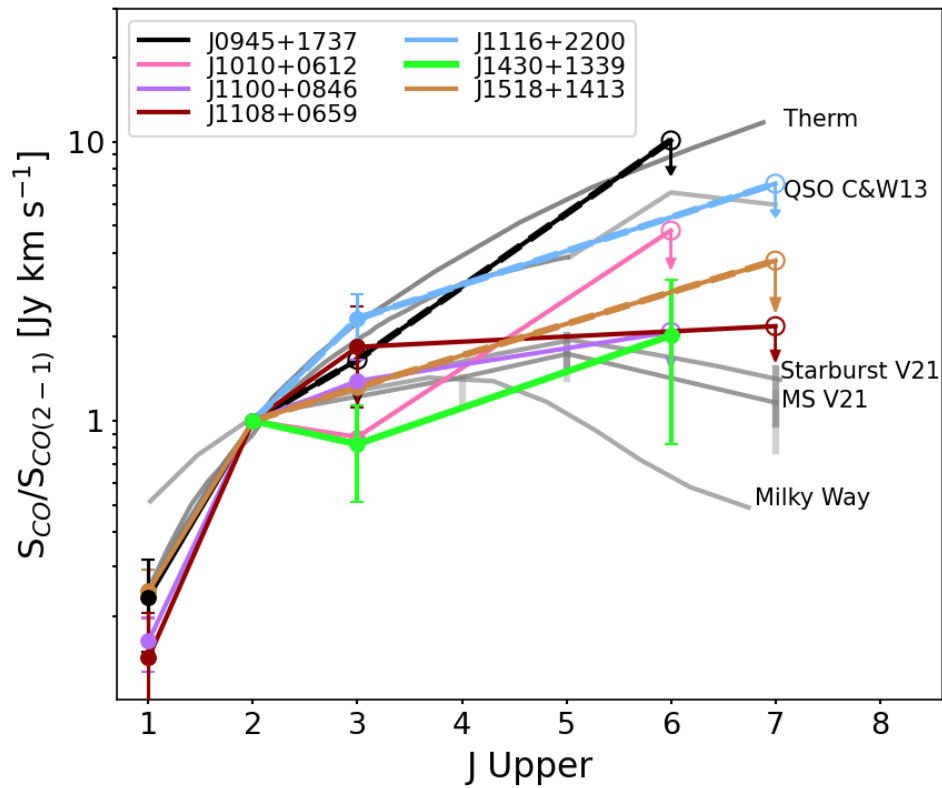


Figure 4.6: For the 7 targets which have either CO(6-5) or CO(7-6) data we present the CO SLEDs up to these higher transitions. Here we are normalising to the CO(2-1). Literature comparison data showing high- z quasars Carilli & Walter (2013) (C&W13) and $z = 1 - 2$ Starburst and main sequence (MS) Valentino et al. (2021) (V21). 3 sigma upper limits are indicated by empty circles with downward arrows. No uncertainties are shown for CO(2-1) as these are incorporated into the uncertainties on CO(1-0), CO(3-2) and CO(6-5) to best represent the uncertainty on the excitation level.

SLED, with 3 of these showing consistent excitation with starburst and main sequence galaxies. J1100+0846 shows signs of a detection, with a S/N of 2.2, but the 3σ upper limit is at a similar excitation to our detected J1430+1339. J1108+0659 shows no sign of any detection at a very constraining level in the CO SLED, placing it already at a similar excitation to starburst and main sequence galaxies. Likewise, J1518+1403 shows no signs of a detection but is between the excitation of the high- z and starburst CO SLED. J1010+0612 shows a very tentative signs of a line with a S/N of 1.1 at a higher excitation than starburst/MS galaxies, but still less than the high- z QSO CO SLED. Further observations would be required to confirm any detection and place a proper constraint on the excitation. The remaining two targets (J0945+1737, J1116+2200) can't be analysed in much detail since the upper limits are not very constraining. However, the fact that these upper limits are already at the level of the thermalised relation and that of the high- z quasars (see Figure 4.6 and Carilli & Walter, 2013) shows we are likely observing systems with

a significantly lower excitation. This along with the other targets clearly showing lower excitations shows a clear difference between our sample of quasars at $z < 0.2$ and those at $z \sim 1 - 6$.

Line Ratios

We can also investigate the excitation of the gas by calculating the ratios of line luminosities of different CO transitions. We calculate these via the following equation:

$$r_{xy} = \frac{L'_{\text{CO}(x-(x-1))}}{L'_{\text{CO}(y-(y-1))}}, \quad \text{e.g., } r_{21} = \frac{L'_{\text{CO}(2-1)}}{L'_{\text{CO}(1-0)}} \quad (4.6)$$

where L'_{CO} is the CO luminosity of a given CO transition line.

All measured line ratios for each individual target are shown in Table 4.3. We present the observed line ratios found in our sample of quasars and compare to literature values in Figure 4.7. In the lower panel of Figure 4.7 we present histograms of the line ratios from our sample, as well as violin plots for different reference samples in the upper panels. We choose violin plots as these show more information of the distribution of the data, with a wider section showing a larger number of data, as well as the maximum and minimum values in the range of the data plus a defined median and 16/84th quartiles. For targets within our sample which show multiple components in their CO spectra, we calculate the line ratios for these individual components and these are also presented in Table 4.3.

The overall line ratios observed in this sample (only including those targets with detections, and ignoring non-detections) are as follows:

For those in our sample with detections in both CO(1-0) and CO(2-1) (6 sources), we calculate the line ratios using equation 4.6 and find a median r_{21} of $1.06^{+0.53}_{-0.18}$, where the negative and positive uncertainties represent the 16th and 84th quartiles respectively. For r_{31} we find a median of $0.77^{+0.31}_{-0.20}$ from 6 sources with detections in both CO(3-2) and CO(1-0). We find a median r_{32} of $0.61^{+0.43}_{-0.21}$ from 8 sources with detections in both CO(3-2) and CO(2-1). We find that in those targets with multiple components, the excitation of the different, individual components and of the total emission across the entire spectral line from the galaxy are consistent (within uncertainties). Therefore, with the data we have available, we cannot measure any difference

between the excitation levels in these different components. The median line ratios in our sample along with literature comparisons can be found in Table [4.4](#).

Name	r_{21}	r_{31}	r_{32}	r_{61} (r_{71})	r_{62} (r_{72})	r_{63} (r_{73})
J0909+1052	—	—	—	—	—	—
J0945+1737	1.10 ± 0.40	< 0.80	< 0.73	< 1.20	< 1.10	—
J0958+1439	< 0.62	0.59 ± 0.14	> 0.96	—	—	—
J1000+1242	0.86 ± 0.34	0.51 ± 0.25	0.60 ± 0.24	—	—	—
J1010+0612	—	—	0.37 ± 0.18	—	< 0.50	< 1.40
J1010+1413	—	—	1.46 ± 0.33	—	—	—
J1016+0028	< 1.20	< 1.60	—	—	—	—
J1055+1102	< 4.20	< 1.70	—	—	—	—
J1100+0846	1.54 ± 0.34	0.95 ± 0.19	0.62 ± 0.12	< 0.43	< 0.28	< 0.45
J1100+0846 (red)	1.60 ± 0.40	0.96 ± 0.22	0.61 ± 0.14	—	—	—
J1100+0846 (blue)	1.60 ± 0.60	0.97 ± 0.31	0.62 ± 0.20	—	—	—
J1108+0659	1.80 ± 0.80	1.60 ± 0.50	0.89 ± 0.35	< 0.30	< 0.20	< 0.20
J1108+0659 (core)	1.60 ± 0.80	1.7 ± 0.60	1.10 ± 0.50	—	—	—
J1108+0659 (blue wing)	2.00 ± 1.20	1.40 ± 0.70	0.70 ± 0.40	—	—	—
J1114+1939	< 1.60	—	> 1.00	—	—	—
J1116+2200	0.89 ± 0.17	0.95 ± 0.15	1.06 ± 0.24	< 0.50	< 0.60	< 0.50
J1222-0007	—	—	—	—	—	—
J1316+1753	> 1.30	—	< 0.47	—	—	—
J1356+1026	—	—	—	—	—	—
J1430+1339	—	—	0.37 ± 0.14	—	0.22 ± 0.13	0.61 ± 0.27
J1518+1403	1.00 ± 0.20	0.60 ± 0.10	0.60 ± 0.20	< 0.43	< 0.42	< 0.71

Table 4.3: Table of line ratios along with uncertainties for all targets. Those with no data shown do not have the required data to present. Sources with multiple components are split into the line ratios for the individual components (components mentioned in brackets) as well as the total values.

Making comparisons to lower redshift, less luminous samples of AGN and star forming galaxies however, we find higher line ratios (see Figure 4.7). For example, [Lamperti et al. \(2020\)](#) present a study of 36 Hard X-ray selected AGN at $z = 0.002 - 0.04$, conducted as part of the BASS AGN sample. They present twelve targets with the requisite data to calculate the r_{21} values and find a median of $0.72^{+0.17}_{-0.17}$. These are lower than those measured in our sample. Further, the r_{32} of the same sample also shows lower excitation with a median of $0.50^{+0.20}_{-0.19}$.

As expected the line ratios of our sample are higher than for normal, star forming galaxies (e.g. [Saintonge et al., 2017](#); [Yajima et al., 2021](#); [den Brok et al., 2021](#); [Leroy et al., 2022a](#)). For example, a compilation of low- z samples found a median r_{21} of 0.65 [Leroy et al. \(2022a\)](#).

Further, we analyse the higher CO line ratios, which are mostly upper limits for our sample, and utilise data of high- z quasars which have CO line fluxes in at least one higher transition (taken from the compilation by [Carilli & Walter, 2013](#)) as well as corresponding bolometric luminosities (taken from [Trentham, 1995](#); [Lewis et al., 1998](#); [Lutz et al., 2007](#); [Aravena et al., 2008](#); [Bradford et al., 2009](#); [Wang et al., 2010](#)). We also note that in comparing bolometric luminosities we convert our [O III] luminosities to bolometric luminosities via the following equation: $L_{\text{bol}}/L_{[\text{O III}]} = 3500$ (from [Heckman et al., 2004](#)). We present these data in Figure 4.8 by also comparing the bolometric luminosities of the targets.

4.4.5 Gas temperature and density

We can utilise the measured line ratios to help understand the physical conditions of the molecular gas in individual targets. In particular, comparing the measured line ratios can give us an indication of the gas temperature and density within these quasar host galaxies ([Peñaloza et al., 2017](#); [Leroy et al., 2022a](#)). Specifically, the ratio of r_{32} with r_{21} gives hints as to these properties (see Figure 4.9). We present these data plotted over simulations of the expected parameter space covered for these line ratios based on variable temperature, densities and optical depths ([Leroy et al., 2022a](#)). Figure 4.9 shows this effect of temperature, density, and optical depth on the observed line ratios (grey points from [Leroy et al., 2022a](#)). The expected line ratios for starbursts and AGN would be close to 1 (e.g. [Mao et al., 2010](#); [Lamperti et al., 2020](#); [Yajima](#)

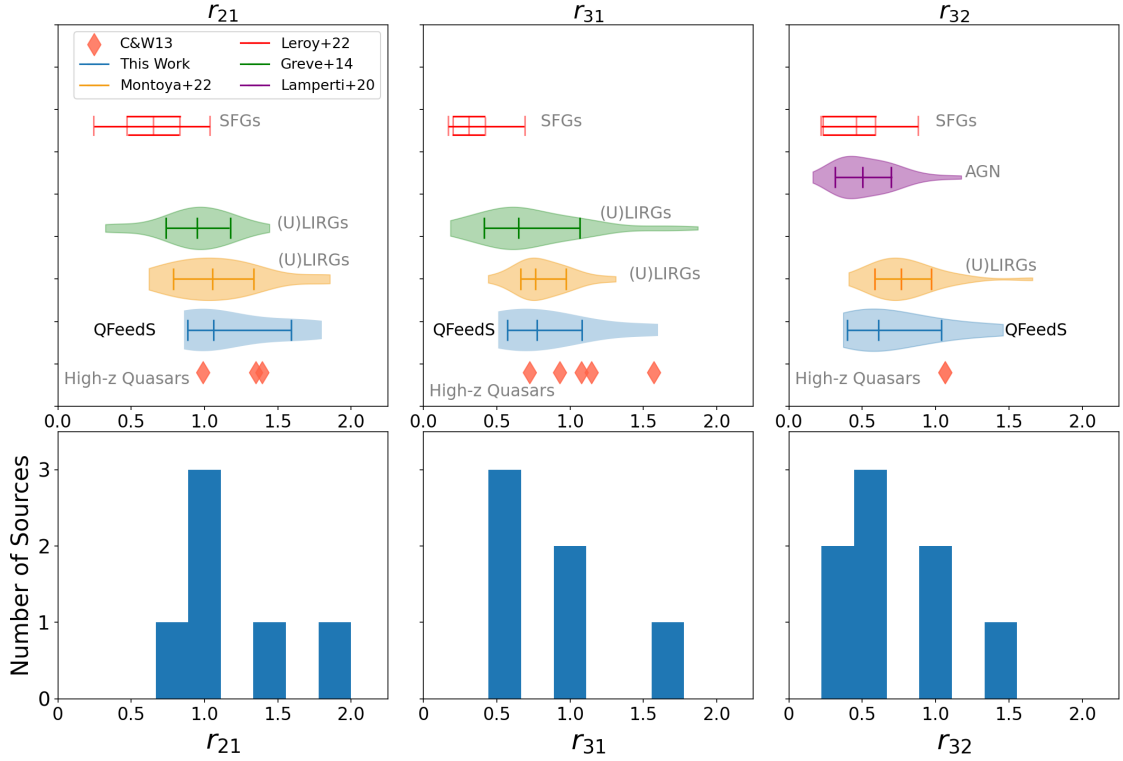


Figure 4.7: Bottom panels: Histograms to show the distribution of line ratios within our sample. Top panels: Violin plots showing the distribution of line ratio values from our sample and selected comparison samples including the median, 16th and 84th quartiles of data (ignoring upper limits). The violin plots shown in blue are those for our sample and are shown in the same colour in the corresponding histograms below. Individual high- z quasars from [Carilli & Walter 2013](#) are shown by red diamond markers. Other literature samples of SFGs and (U)LIRGs are also shown for comparison ([Greve et al., 2014](#); [Lamperti et al., 2020](#); [Leroy et al., 2022a](#); [Montoya Arroyave et al., 2023](#), more details of the selected literature comparisons can be found in section 4.4.4). Note these statistics do not include upper limits.

[et al., 2021](#)). These values are consistent with having both higher densities and hotter gas ([Leroy et al., 2022a](#)).

To further investigate the temperature and density of gas in these quasars we analysed the 5 targets with detections in all of the first three transitions (J1000+1242, J1100+0846, J1108+0659, J1116+2200 and J1518+1403), which provide best opportunity to test these properties. Using the Dense Gas Toolbox ([van der Tak et al., 2007](#); [Leroy et al., 2017](#); [Puschig, 2021](#)), the density of the gas and the dense gas fraction (fraction of gas with density $> 10^5 \text{ cm}^{-3}$) were calculated by fixing the temperatures in 5 degree increments in the range of 10 – 50 K. In 4 out of 5 sources (except J1000+1242) a temperature of less than 35K lead to the highest density provided in the model (10^5 cm^{-3}) and dense gas fractions greater than 90%. From 40K – 50K these four targets give densities in the range $10^5 - 5000 \text{ cm}^{-3}$. J1000+1242 is the only target showing different properties of the temperature and density. Only at 20K does the model give the highest density

Line Ratio/sample	z range	Median
r_{21}		
QFeedS (This work)	0.1 – 0.2	1.06 $^{+0.53}_{-0.18}$
High- z Quasars (C&W+13)	1 – 6	1.35
SFGs (Leroy+22)	0	0.65 $^{+0.18}_{-0.15}$
(U)LIRGs (Montoya+22)	< 0.2	1.05 $^{+0.32}_{-0.30}$
(U)LIRGs (Greve+14)		0.95 $^{+0.23}_{-0.21}$
r_{31}		
QFeedS (This work)	0.1 – 0.2	0.77 $^{+0.31}_{-0.20}$
High- z Quasars (C&W+13)	1 – 6	1.08
SFGs (Leroy+22)	0	0.31 $^{+0.11}_{-0.11}$
(U)LIRGs (Montoya+22)	< 0.2	0.76 $^{+0.22}_{-0.10}$
(U)LIRGs (Greve+14)		0.65 $^{+0.42}_{-0.23}$
r_{32}		
QFeedS (This work)	0.1 – 0.2	0.61 $^{+0.43}_{-0.21}$
High- z Quasars (C&W+13)	1 – 6	1.06
SFGs (Leroy+22)	0	0.46 $^{+0.13}_{-0.20}$
(U)LIRGs (Montoya+22)	< 0.2	0.76 $^{+0.23}_{-0.17}$
AGN (BASS, Lamperti+20)	median \sim 0.05	0.50 $^{+0.20}_{-0.19}$

Table 4.4: Table of median line ratios along with 16th and 84th quartiles (indicated by plus and minus values) for all targets and comparisons to the literature used in Figure 4.7 along with the z range for each sample. [Montoya Arroyave et al. 2023](#), [Leroy et al. 2022a](#), [Greve et al. 2014](#), [Lamperti et al. 2020](#), [Carilli & Walter 2013](#).

with a dense gas fraction greater than 90%. From 50 – 25K a gas density ranging between 600 – 4000 cm^{-3} was calculated. This is significant as J1000+1242 has the lowest line ratios amongst the 5 and is the only one with $r_{21} < 1$. This therefore shows that within our sample, those with high line ratios would require higher temperatures ($> 35\text{K}$) and densities. For those in this sample with lower line ratios, temperatures as low as 25K can still provide realistic scenarios.

From analysing the line ratios in Figure 4.9 we find that the molecular gas in J1116+2200 seems consistent with being optically thicker and J1100+0846 seems consistent with being optically thinner. J1000+1242 and J1518+1403 are most likely somewhere in the middle and J1108+0659 is more difficult to determine due to the larger uncertainties. Further studies with higher S/N observations across the entire sample would be required to make any further conclusions. However, from the large variety identified in these limited data we can say that there is not a particular tendency in optical depth valid for all our sources.

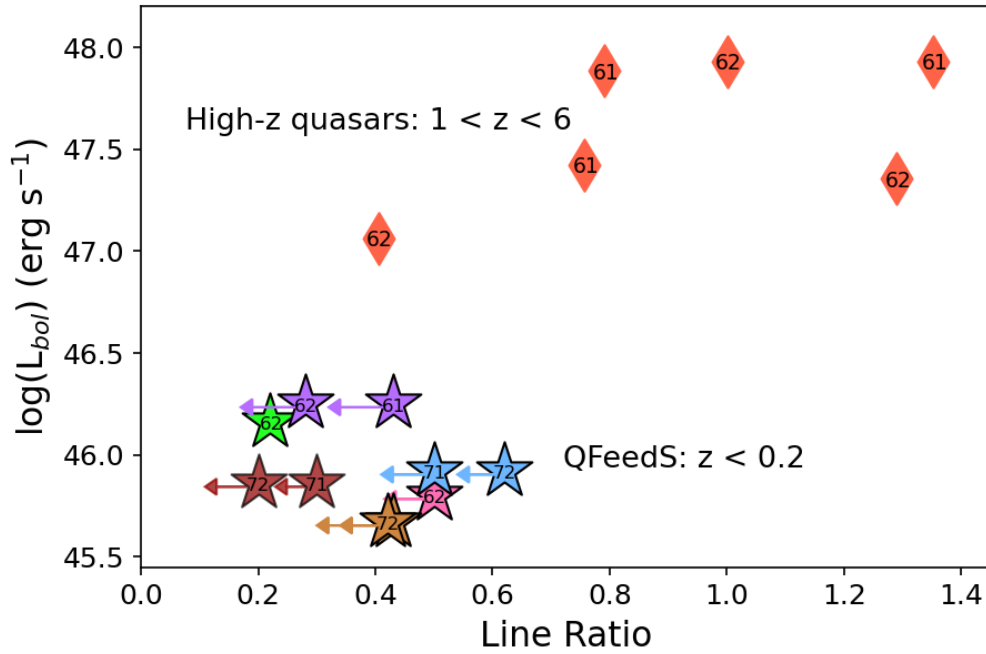


Figure 4.8: For the 7 targets which have either CO(6-5) or CO(7-6) data we compare the bolometric luminosity and line ratios of a sample of high- z quasars (from Carilli & Walter, 2013, shown by red diamond markers) to our sample of low- z quasars (shown by star markers and arrows indicating those that are upper limits). The numbers in each marker indicates the line ratio being plotted, e.g. “61” indicates r_{61} . Markers of the QFeedS targets are also coloured in the same way as in all previous plots (see Figure 4.1).

4.4.6 Comparing CO and ionised gas line profiles

To investigate any differences between the molecular and ionised phase of the ISM we analyse the CO and [O III] line profiles. We do this by comparing both the velocity offsets (V_{50}) and the line width (W_{80}) for the CO lines compared to MUSE observations of the ionised gas (in most cases traced by [O III] and for two cases $H\beta$, where the [O III] was not available). We present these results in Figure 4.10. We only perform this analysis on those with an integrated velocity integrated S/N greater than 5 so that the line profiles we compare are more reliable. This threshold will ensure that there is a lower uncertainty on the CO line profile, allowing us to make more reliable comparisons between the ionised and molecular phase. From these results, in all cases we observe consistent or broader [O III] line profiles than in the CO transitions (as measured by W_{80} , shown in Figure 4.10).

As well as the line widths, we can also analyse the velocity offsets of CO compared to [O III] (see Figure 4.10). From this we find that a number of targets are consistent in terms of the V_{50} measurements, whilst others do show significant differences, both positive and negative. While

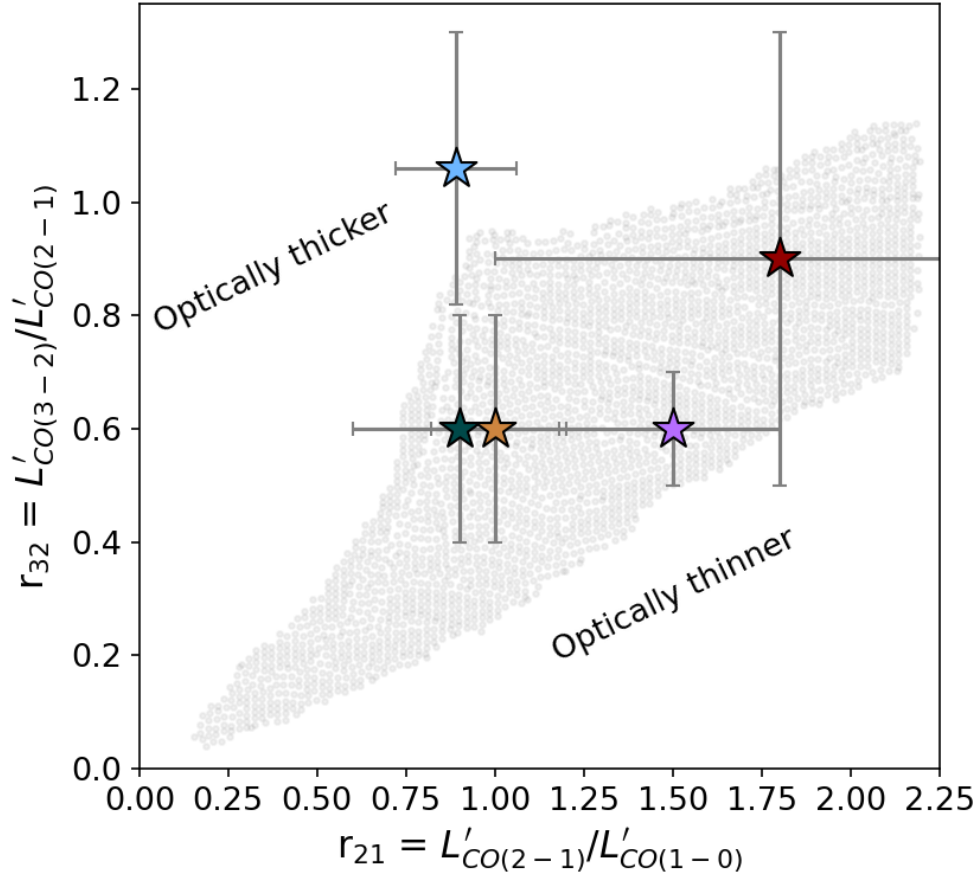


Figure 4.9: For the 5 targets which have detections in all three transitions r_{21} plotted vs r_{32} to give an indication of temperature, density and optical thickness. Background grey points taken from Leroy et al. 2022a, which show the parameter space of line ratios based on models which take into account different temperatures and densities.

sources which show more redshifted [O III] lines than CO also exhibit broader [O III] line widths, the few cases with more blueshifted [O III] lines present equivalent [O III] line widths to those observed in CO, which are among the most similar line profiles that we observe.

For our sample overall we also find more complex line profiles in the ionised gas than in the molecular phase. Specifically we identify 2 out of 17 sources with CO spectra that show multiple components in CO whereas in the MUSE ionised gas data we find 13 out of 17 sources with multiple components. This is limited by S/N in our CO data but interestingly, in the 2 cases where we find multiple components in the CO (J1100+0846 & J1108+0659) we identify the following:

J1100+0846 shows a clear double peaked line profile in the first three CO transitions, potentially due to disk rotation or outflows in opposite directions. This double peaked profile was also identified in Ramos Almeida et al. (2022) and we confirm the similarity by plotting them

together onto our CO(2-1) spectra. This double peak however is not present in the [O III] where instead a broad line is identified.

Another target within our sample (**J1010+0612**) also shows a double peak CO(2-1) profile (identified in higher resolution ALMA data by [Ramos Almeida et al., 2022](#)). In our APEX spectrum we also see tentative signs for a double peak profile in both our CO(2-1) and CO(3-2) data (see spectrum in Figure 4.17 in the appendix). However, like J1100+0846, J1010+0612 shows a broad line in the MUSE [O III] data, without signs of two narrower components as identified in CO.

J1108+0659 shows a prominent blue wing component, identified in the first three CO transitions. The spatial resolution in our CO(1-0) data is not enough to spatially locate where this potential outflow component is located. Interestingly, the $H\beta$ line profile also shows the same blue wing component, but with a more obviously present blue wing in $H\beta$ than the CO. The peaks of the two components are also at very similar velocities across the three CO transitions and the $H\beta$ data.

Looking at the ionised gas in isolation, we extracted [O III] spectra from the MUSE cubes at both 30 arcsec (to match our CO observations) as well as at 3 arcsec (to match the SDSS observations). We find that the observed [O III] line profiles in SDSS and extracted from 3 arcsec apertures from MUSE are consistent within uncertainties (Figure 4.11). However, we find a larger scatter when comparing SDSS line profiles to those extracted from 30 arcsec apertures in MUSE (Figure 4.12). There are 8 cases for which they are not consistent, 7 where the SDSS lines are broader, and 1 case where MUSE at 30 arcsec is broader. Cases where SDSS are broader suggest a larger impact on velocities of ionised gas close to the core but further work would be needed to confirm this. Interestingly, the only case which is broader in MUSE at 30 arcsec than SDSS is J1016+0028, with the largest radio size, known radio lobes extending to distances of ~ 15 arcsec, suggesting that impact on velocity of ionised gas is present out to these larger distances. There is no clear overall picture or trends from these results and so any differences likely depend on a case by case basis, but these observations do hint at potential differences in velocities of ionised gas in the halos, and that the integrated velocity is dominated by the kinematics in the core, since 7 out of 8 are broader at 3 arcsec. However, further and more focused studies, are needed to investigate these effects in more detail.

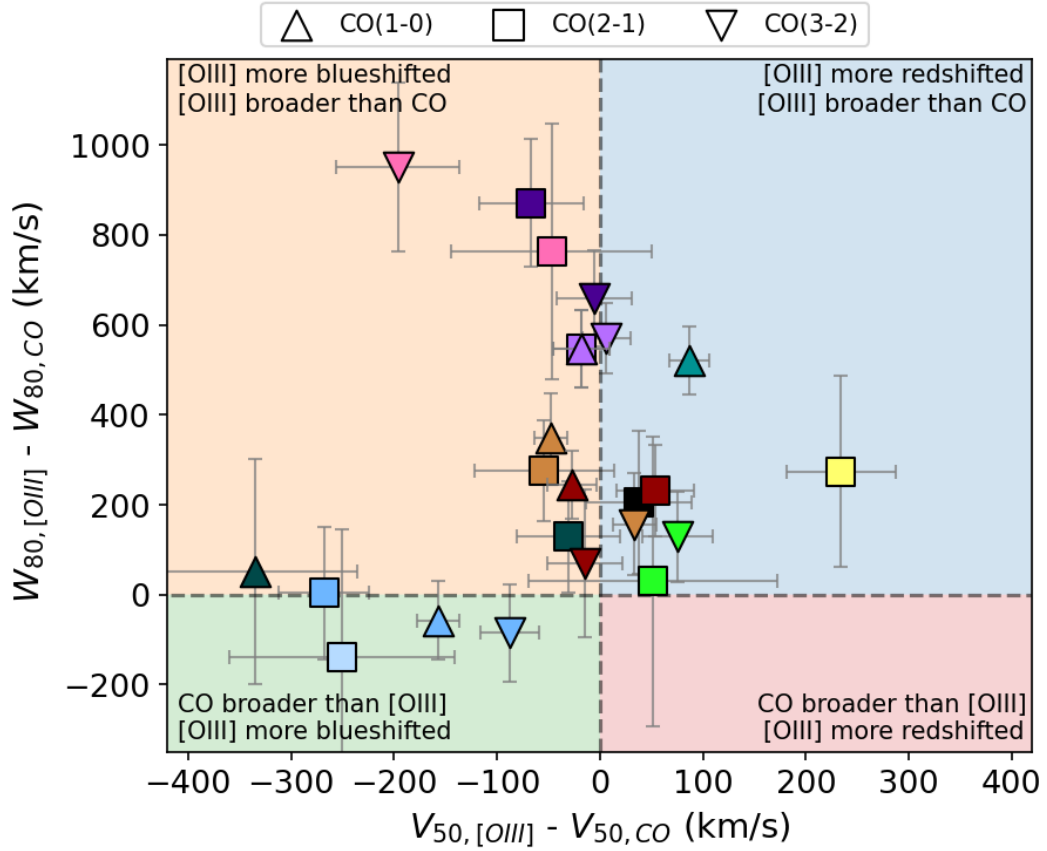


Figure 4.10: For the 11 targets which have lines with $S/N > 5$ we present an analysis of the velocity offsets (V_{50}) and line widths (W_{80}) of the CO and [O III] spectra. Colours of markers for the individual targets are the same as throughout this work (colours shown in the legend of Figure 4.1). Some targets have multiple transitions shown, which are differentiated by: Upward triangles indicate CO(1-0), squares are CO(2-1) and downward triangles are CO(3-2) data (see legend). Each region of the plot is shaded to highlight the corresponding properties and the differences between the [O III] and the CO. Note: J1108+0659 is $H\beta$ not [O III]. Also note that the CO data for J1356+1026 (yellow square) is taken from [Ramos Almeida et al. 2022](#).

4.5 Discussion

Here we discuss the findings and an interpretation of the results in relation to the literature. In Section 4.5.1 we discuss the observed CO excitation within our sample using CO SLEDs and line ratios, including comparisons to the literature. In Section 4.5.3 we discuss the differences in the line profiles seen in our CO data compared to ionised gas observations from MUSE. Finally, in section 4.4.5 we discuss the implications of our observed line ratios on the molecular gas temperature and density in our sources, based on theoretical models.

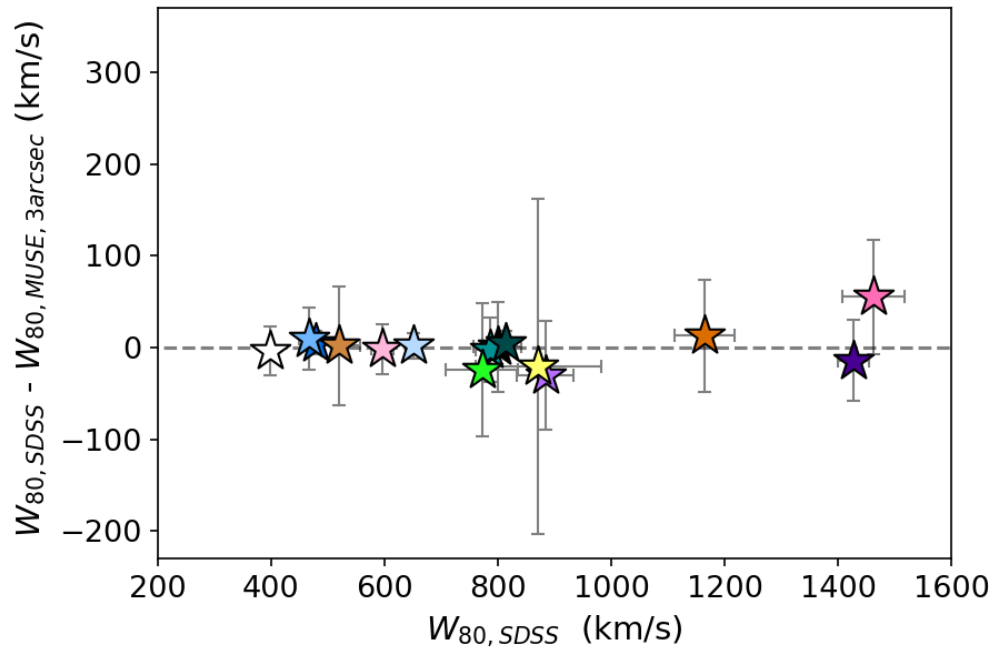


Figure 4.11: Difference between SDSS [O III] W_{80} and [O III] W_{80} extracted from MUSE at 3 arcsec, as a function of [O III] W_{80} from SDSS.

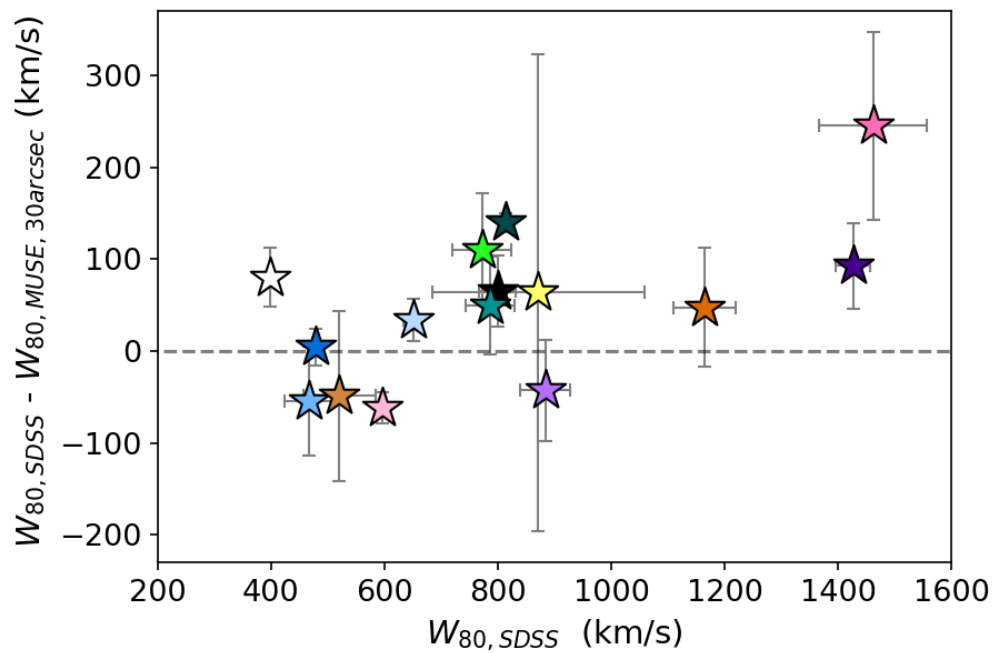


Figure 4.12: Difference between SDSS [O III] W_{80} and [O III] W_{80} extracted from MUSE at 30 arcsec, as a function of [O III] W_{80} from SDSS.

4.5.1 No observed impact on total CO excitation

Here we will discuss the findings of the CO excitation, in the context of the selected comparison samples from the literature (presented in Section 4.4.1). Overall, these sources which have evidence for AGN-driven ionised outflows and jets/winds do not have exceptional global CO content or excitation, beyond that seen in relevant comparison samples of (U)LIRGS and less luminous AGN. However, we discuss further that a local impact on CO excitation is still a possible scenario, and if present is likely to be driven by AGN feedback processes such as via radio jets.

Consistent CO excitation to local (U)LIRGs

Previous studies into the molecular excitation have found no consensus on whether AGN have systematically different r_{21} line ratios (see [Ocaña Flaquer et al., 2010](#); [Papadopoulos et al., 2012](#); [Xia et al., 2012](#); [Husemann et al., 2017](#); [Shangguan et al., 2020](#)), or the r_{31} line ratios ([Sharon et al., 2016](#)). With this work we looked for any correlations with these line ratios and AGN or galactic properties.

Our r_{21} values (median r_{21} of $1.06^{+0.53}_{-0.18}$) are consistent with those of recent studies of (U)LIRGs, e.g. [Greve et al. \(2014\)](#); [Montoya Arroyave et al. \(2023\)](#), with median values of 0.95 and 1.05 respectively. The r_{31} and r_{32} values are also found to be consistent with these (U)LIRG studies (as shown in Figure 4.7 and Table 4.4). As mentioned previously, 9 quasars in our sample of 17 have $L_{\text{IR,SF}}$ data, of which 8 are consistent with being LIRGs (see Section 4.2 and [Jarvis et al., 2019](#)). The ninth source, J1430+1339, is just below the threshold with $\log[L_{\text{IR,SF}}] = 44.32^{+0.06}_{-0.07}$ ergs^{-1} . The fact that we see similar line ratios to these studies of local (U)LIRGs is an indication that the presence of a quasar and the observed radio jets and ionised outflows has no significant impact on the excitation of the global molecular gas content at the mentioned transitions.

As mentioned above, we find slightly higher excitation in our sample than found in lower redshift AGN ([Lamperti et al., 2020](#)), with the distribution of QFeedS line ratios extending to higher values. These targets have a lower luminosity compared to our sample with a median $L_{\text{bol}} \sim 10^{44.8}$ which may explain the small differences observed in the CO excitation, despite the presence of AGN. However, it is important to note that the differences are not large (particularly when considering the smaller sample size in QFeedS) and so there is no clear impact from the presence of AGN-driven ionised outflows and jets/winds.

With the diversity of lines ratios observed for different populations, depending on the type of galaxy and properties, we note that extreme care should be taken when converting from higher J_{CO} lines to the ground state to make sure that correct line ratio is used based on these factors.

Optical depth effects

As presented in Section 4.4.4, we find cases where the CO SLEDs are above the thermalised relation in CO(2-1) and CO(3-2). The most straight-forward explanation might be that some of the CO(1-0) emission may be resolved out given the ACA spatial resolution, particularly if there is extended diffuse emission beyond the beam size of the observations, therefore obtaining a lower flux value than the true value. The larger uncertainties on the CO(1-0) flux values may also be a factor in this. Interestingly two out of the four non-detections in the ACA CO(1-0) data are known to be ongoing mergers/dual AGN (J1222-0007 and J1316+1753, see [Jarvis et al., 2021](#)). However, apart from this there are no special properties of these sources that would differentiate them from the rest of the sample, and as mentioned in Section 4.3.1, the sensitivity calculations for the observations were done using the same method across the sample.

For those that are above the thermalised level in the CO SLEDs, and assuming the thermalised level should be the maximum flux, then this would imply that between 7 and 50 per cent of the flux would be in extended emission at scales greater than 188kpc (median recoverable scale of the observations). Since this would be an unrealistic scenario, we favour a physical interpretation rather than an observational one. In addition, we can compare to [Montoya Arroyave et al. \(2023\)](#) which contains more nearby objects (at a median $z = 0.09$ compared to a median $z = 0.14$ for the QFeedS sample) and would therefore more subject to over-resolution effects with ACA CO(1-0). Despite this, they find very similar line ratios to ours (Figure 4.7), again lending credence to the interpretation that this is a physical and not an observational effect.

Although we cannot exclude the influence of the above mentioned observational effects we note that other investigations on ULIRG samples have reported similar trends, indicating that these super-thermal r_{21} ratios may have a physical explanation. For example, the high r_{21} values in our sample could be due to optical depth effects, with highly excited gas in combination with a low opacity in the CO(1-0) transition ([Zschaechner et al., 2018](#)). It has been argued that low opacities can be driven by large velocity gradients and would require the presence of turbulent or outflowing gas, perhaps also in a diffuse, warm phase ([Cicone et al., 2018b](#); [Montoya Arroyave et al., 2023](#)). In the case of our sample this could mean kinematic disturbances as a result of

quasar feedback (e.g. [Jarvis et al., 2019](#); [Ramos Almeida et al., 2022](#); [Girdhar et al., 2022](#)). However, in the data presented here we only see tentative indications of such outflows, but this may be the result of limited S/N and further studies with deeper observations at a higher spatial resolution are required to investigate this further.

It therefore may well be the case that the CO(2-1) is a more reliable line, especially when investigating the excitation through CO SLEDs. For example [Montoya Arroyave et al. \(2023\)](#) claimed that one cannot determine the CO excitation from the low-J CO lines, most likely because the optical depth effects add too much noise to the calculation. They also identified that weak correlations are found only from ratios involving the CO(1-0) line and L_{IR} and SFR. This therefore supports the idea that CO(1-0) is the only line affected by optical depth effects and not the CO(2-1) or CO(3-2).

Low excitation at CO $J_{\text{up}} = 6, 7$

As shown in Figure 4.6, we observe relatively low excitation in the CO(6-5) and CO(7-6) transitions, for at least 4 out of 7 targets with the appropriate data. We note that the differing beam sizes between the observations at CO(2-1) compared to CO(6-5) and CO(7-6) may play a role in the low excitation observed, especially if flux is resolved out in the smaller beam for observations in higher CO transitions. However, similarly low excitation is found when compared to the CO(1-0) ground state which has similar beam sizes to the higher CO transition APEX observation. From previous work into the CO(2-1) kinematics for some of these targets ([Ramos Almeida et al., 2022](#)) and the fact that higher CO transitions are expected to be more centrally located we argue that these line ratios are reliable and still very constraining.

One explanation (as discussed previously in relation to the r_{21} values) could be due to a difference in bolometric luminosity. The high- z quasars that show much higher line ratios do indeed have significantly higher bolometric luminosities (see Figure 4.8), with luminosities of $10^{47} - 10^{48} \text{ ergs}^{-1}$ compared to our sample which are all $L_{\text{bol}} < 10^{46.5} \text{ ergs}^{-1}$. The high excitation levels observed in quasar host galaxies with extreme luminosities, like those presented in [Carilli & Walter \(2013\)](#), and in particular unobscured sources ([Banerji et al., 2018](#); [Wang et al., 2019](#); [Li et al., 2020](#); [Bischetti et al., 2021](#)), can often be associated with depleted gas reservoirs (e.g. [Brusa et al., 2015](#); [Perna et al., 2018](#); [Förster Schreiber et al., 2019b](#); [Circosta et al., 2021](#)). These depleted gas reservoirs, potentially as a result of quasar activity, could therefore lead to lower observed CO fluxes at $J_{\text{CO}} < 3$, and consequently high excitation at $J_{\text{CO}} > 5$. Since

we observe gas-rich systems in our quasar host galaxies, the lower excitations that we measure might therefore be expected. Further studies of both low and high- z quasars covering much of the CO SLED are required to test this further (e.g. [Novak et al., 2019](#); [Pensabene et al., 2021](#)).

It is also possible that the effect of AGN may only be detected at $J_{\text{CO}} > 10$. CO is most commonly excited by photodissociation regions (PDRs) from the UV photons emitted from young stars. However, excitation at these higher CO transitions requires shocks and/or X-ray emission (through X-ray-dominated region models, XDR), both of which can be powered by AGN or jets ([Pereira-Santaella et al., 2013](#); [Carniani et al., 2019](#)). The effects of both XDR and PDR regions play an important role but observations with parsec scale resolution are required to disentangle and analyse these regions ([Wolfire et al., 2022](#)). Therefore, observations at even higher CO transitions and high resolution may be needed to detect the XDR-dominated CO lines and provide a more complete constraint on the influence of AGN (see e.g. [van der Werf et al., 2010](#); [Mashian et al., 2015](#); [Carniani et al., 2019](#)).

Differences in the overall star formation and ISM conditions at low and high redshifts could also contribute to the differences we observe in CO excitation between our sample and high- z quasars. Estimates of the cosmic molecular gas density indeed suggest that the molecular gas fractions peak at redshifts of $z = 1 - 3$ (see [Péroux & Howk, 2020](#), for a review), roughly mirroring the cosmic star formation rate density ([Madau & Dickinson, 2014](#)) and black hole accretion density (e.g., [Aird et al., 2015](#)). As a result, we might therefore expect higher gas temperatures and densities at nuclear scales in quasar host galaxies at redshifts 1 – 3 (higher than our sample), excited by stronger radiation fields from star formation and the AGN. However, there are cases where high- z quasars have also been found to have lower than expected CO excitation. For example, a recent study of nine $z \sim 3$ quasars ([Muñoz-Elgueta et al., 2022](#)) finds that their CO SLEDs peak in the range $J_{\text{up}} = 5 - 7$ compared to the expected $J_{\text{up}} > 6 - 8$. Further studies with coverage across a large range of the CO SLED is required for both low and high- z quasars to investigate these findings further.

Another factor could be the potential impact of obscuration and line-of-sight effects, when comparing Type 1, Type 2, and red quasars. For example, the CO emission in unobscured quasars might be dominated by gas within the ionising cone through which we observe Type 1 quasars (e.g. [Vayner et al., 2021](#); [Stacey et al., 2022](#)). Despite this, no significant differences in the molecular gas content and star formation efficiencies have been reported between obscured and

unobscured AGN in the context of AGN unification and line-of-sight effects (e.g. Perna et al., 2018). However, the increased incidence of high-velocity [O III] outflows and radio emission in red quasars has been associated with higher nuclear dust reddening at high redshifts (e.g., Perrotta et al., 2019; Klindt et al., 2019; Fawcett et al., 2020; Calistro Rivera et al., 2021; Andonie et al., 2022). This connection might suggest an increased amount of obscuring material (dust and gas) at nuclear scales for luminous quasars with ongoing outflows and jets or winds.

Line ratios as tracers of temperature and density

In Section 4.4.5 we presented the results of using the line ratios r_{21} and r_{32} to give an indication of the temperature and density of gas within the QFeedS sample. We are limited by the lack of detections across the CO SLED, with only 5 sources having detections in all of the first three J_{CO} transitions, and by the large uncertainties in the line ratios (see Figure 4.9). Further, the dynamic range of the line ratios observed in AGN, quasars, (U)LIRGs and star forming galaxies is not large and therefore, more accurate, high S/N observations are required to analyse these to a high degree (i.e. placing accurately on Figure 4.9).

Despite this, we can place constraints and upper/lower limits on the temperature and density as shown in Section 4.4.5. Indeed, we have shown a difference between those with line ratios ≥ 1 and those < 1 . The 4 out of 5 sources with higher line ratios ≥ 1 in our sample required temperatures $> 35\text{K}$ to show dense gas fractions less than 90%. On the other hand, for J1000+1242 with both r_{21} and $r_{32} < 1$, this was reduced to 25K.

Observations to constrain the CO properties of other targets in QFeedS would be an important next step, as well as observing other lines such as CI, HCN or HCO+ which would also help further constrain the the gas temperature and densities.

4.5.2 A localised impact on CO?

Although our sample consist of luminous quasars with known ionised outflows, radio jets and/or large radio structures, we report no signs of enhanced CO excitation on the global scales in which we are measuring when compared to local (U)LIRGs of similar luminosities.

There has previously been found a positive relation with L_{IR} and the line ratios r_{21} and r_{31} (Montoya Arroyave et al., 2023), as well as a positive relation between r_{31} and SFR. However, as mentioned in Section 4.5.1 they claim that one cannot determine the CO excitation from the low- J_{CO} lines because of optical depth effects.

We performed some basic analysis on the line ratios compared with galactic and AGN feedback diagnostics such as SFR, radio luminosities, $\text{FWHM}_{[\text{O III}]}$, finding no correlations within our sample. However, when working with such small sample (less than 10 sources for which we have the requisite data) and small parameter space, it is hard to take strong conclusions from these investigations.

Despite this, a lack of any correlation may not be surprising. For example, a study on local Seyferts found no clear evidence for a systematic reduction in the molecular gas reservoir at galactic scales with respect to SFGs (Salvestrini et al., 2022). Previous studies have also found weak or no correlation with properties such as stellar mass, AGN fraction and SFR offset to the main sequence (Liu et al., 2021). Recent work has also found no correlation between the cold molecular gas properties and AGN properties (Molina et al., 2023). Additionally, studies at both low and high redshifts have found no differences in low- J_{CO} excitation between samples of star forming galaxies (taken from the xCOLD GASS Survey Saintonge et al., 2011) and AGN host galaxies (Sharon et al., 2016; Lamperti et al., 2020). This finding again indicates a lack of influence from the AGN on the total molecular gas content. Further support for a lack of impact on global scales is the evidence of extended CO(1-0) emission as shown in Figure 4.30 in the appendix. These data may be an indication that for those with detections we still observe an extended molecular gas reservoir. On the other hand, those with non-detections may be an indication of disruption on these global scales, but with the data that is available we cannot make any conclusions about why a few of the targets have gone undetected in CO(1-0).

The typical theoretical prediction is that AGN outflows do not efficiently disrupt disc systems, because the outflow is deflected into the halo (Costa et al., 2020), therefore supporting the hypothesis of a lack of impact on the total molecular gas content. Some simulations predict that an outflow will carve out a small cavity (on scales of ~ 1 kpc) in the galactic nucleus. As we are far from resolving on these scales here then it is not surprising that we do not see a significant impact on galactic scales. This would also mean that any immediate impact on star formation is also likely to be modest (see also Gabor & Bournaud, 2014; Ward et al., 2022; Piotrowska et al.,

2022). However, this does not rule out any long-term impact through the effect of outflows on halo gas.

An explanation for our findings could therefore be that the impact of feedback and/or galactic properties on the excitation of the molecular gas may occur on a more localised scale, and once looking at the total molecular gas content, this effect is no longer observed. Indeed, higher spatial resolution studies have found differences in the excitation on scales < 1 kpc (e.g. [Dasyra et al., 2016](#); [Oosterloo et al., 2017](#); [Rosario et al., 2019](#); [Zhang et al., 2019](#); [Ellison et al., 2021](#); [Audibert et al., 2023](#)), in some cases also localised next to radio jets.

Further supporting this idea, two of this sample have been studied in a resolved way in which the CO velocity dispersion was observed to be effected perpendicular to radio jets (J1316+1737 [Girdhar et al., 2022](#)) and brightness temperature ratios were enhanced perpendicular to the radio jet (J1430+1339 [Audibert et al., 2023](#)). This provides further motivation for resolved studies of the CO excitation and kinematics around small scale radio-jets. One interesting scenario would also be to determine any dependence on the inclination of any radio jet with respect to galaxy plane ([Mukherjee et al., 2018b](#); [Venturi et al., 2021](#); [Girdhar et al., 2022](#); [Meenakshi et al., 2022](#); [Audibert et al., 2023](#)), something which needs to be studied further within this survey.

It therefore may be the case that any impact of AGN feedback on the excitation of the molecular ISM seems to only occur on localised scales ([Morganti et al., 2021](#)), but the impact does not take effect over the whole galaxy. Therefore, since we are observing the total molecular gas content in the host galaxies, these smaller scale effects are likely to be lost in the full picture.

One reason for this limited impact may be due to the power of the radio jets, being too weak to penetrate throughout the entire galaxy and they are deflected by interactions with the ISM and are contained within the central region of the galaxy. Another potential for these small scale jets is the potential time scales involved, and that what we observe are young jets which have not yet made their way to have an influence over the whole galaxy (e.g. [O’Dea et al., 1991](#); [Morganti, 2017](#); [Bicknell et al., 2018](#)). An alternative scenario may be quasar driven winds that drive ionised outflows and simultaneously shock the ISM to produce radio emission in the same region of the galaxy (e.g. [Wagner et al., 2013](#); [Zakamska & Greene, 2014](#); [Nims et al., 2015](#); [Zakamska et al., 2016](#); [Hwang et al., 2018](#)).

4.5.3 Comparing CO and ionised gas line profiles

Across our sample we see differences between the line profiles of the ionised gas and the CO (see individual spectrum in the appendix), suggesting potential differences in the impact of AGN feedback on the different gas phases.

As shown in Section 4.4.6 we identify broader [O III] line profiles than in the CO transitions indicating a larger impact from feedback (e.g. via known radio jets) on the ionised gas kinematics than in the molecular gas. As discussed in Section 4.4.2, the CO W_{80} measure based on the fit that can be considered as an upper limit as it is mostly higher than that measured on the data.

Despite this, we still see that the CO widths are less than, or consistent with, the [O III] line widths. This difference in molecular and ionised gas velocities could be attributed to the different densities, with the denser molecular gas being naturally more difficult to drive to higher velocities (Nayakshin & Zubovas, 2012; Mukherjee et al., 2016, 2018a; Girdhar et al., 2022).

The presence of double-peaked CO lines (e.g. in the case of J1100+0846 and J1010+0612) can be indicative of jet-gas interactions whereby jets are pushing the gas in opposite directions (Kharb et al., 2021). Alternatively, these profiles can indicate that the gas is in a disk, or that binary black holes with individual broad and narrow line regions are present. Binary black holes could have resulted from galaxy mergers.

However, as mentioned the lack of S/N in our CO data means that interpreting these multiple components is limited. On the other hand, we should nonetheless be sensitive to the overall gas kinematics, and so our finding of broader total [O III] line profiles compared to CO is reliable. It is worth mentioning that another explanation for this is that what we now observe as ionised gas was originally molecular gas that became ionised and heated in an outflow. In this case, the fact that [O III] is broader might reflect a shorter survival time of cold, dense gas in the outflow (see e.g. Costa et al., 2015, 2018), rather than the impact of AGN feedback.

Differences in the kinematics of CO compared to the ionised gas could also indicate that the molecular gas is not mixed in the outflowing ionised medium. This may be as a result of cold gas clouds being unable to survive in hot winds (e.g. Farber & Gronke, 2022).

4.6 Conclusions

We present a molecular gas excitation survey, observing a range of CO transitions ($J = 1, 2, 3, 6, 7$) for a sample of 17 quasars at $z < 0.2$. Our goal is to measure the molecular gas properties such as molecular gas masses, fractions, and CO excitation, as well as gas kinematics in order to identify any impact due to the presence of radio jets and ionised outflows on a global scale.

- From all the evidence presented here we suggest that the presence of ionised outflows and radio jets in these LIRG type systems does not significantly impact the CO excitation on a global scale, but that given evidence from the literature, localised effects are likely, and do not extend to the scales of the entire galaxy.

- We find no differences between the molecular gas fractions of our sample of quasars as compared to non-AGN in the literature (see Figure 4.4), in agreement with previous works.

- We observe median r_{21} , r_{31} and r_{32} ratios of $1.06^{+0.53}_{-0.18}$, $0.77^{+0.31}_{-0.20}$ and $0.61^{+0.43}_{-0.21}$ respectively, which are consistent with those reported for (U)LIRGs of similar redshift (see Figure 4.7).

- We suggest that optical depth effects may contribute to the high line ratios involving CO(1-0) that are observed, in agreement with previous studies.

- From analysing the CO SLEDs in 7 targets of our sample (see Figures 4.5 and 4.6), we observe lower excitation in CO(6-5) and CO(7-6) as compared to a sample of quasars at higher redshift ($z = 1 - 6$). We suggest this difference is due to higher bolometric luminosities in the higher redshift quasars (see Figure 4.8). We conclude that we detect no evidence of impact of AGN feedback on the CO SLEDs up to $J \leq 7$ for our quasar sample, despite the strong feedback signatures that characterise them (i.e., a sample with prevalent radio jets and/or shocked winds and ionised outflows).

- We observe differences between the CO and [O III] line profiles, both in the line widths and velocity offsets, finding systematically broader [O III] line profiles than CO. The median difference in W_{80} between [O III] and CO is $\sim 200 \text{ km s}^{-1}$, with a maximum difference of $\sim 650 \text{ km s}^{-1}$. This suggests a larger impact of feedback on the ionised gas than on the molecular

gas (see Figure 4.10). Alternatively this can indicate cold gas clouds are unable to survive in hot winds.

– We identify consistent [O III] line profiles in SDSS data compared to MUSE data extracted at a 3 arcsec aperture. However, differences in the line profiles are identified when extracted from MUSE data at a larger aperture of 30 arcsec. This suggests that the effects of feedback processes (such as outflows, radio jets or winds) are likely more dominant at smaller scales, closer to the central AGN/quasar (see Figures 4.11 and 4.12.

Overall we conclude that in these sample of quasars at $z < 0.2$ the impact of these quasars on the total molecular gas content, both in excitation and velocities, is likely to be minimal. On a global scale we see no real divergences from ULIRGs. This work therefore adds to the growing body of evidence that on global scales there is a minimal impact on CO excitation and total gas content, even in the extreme cases of luminous quasars with ionised outflows and extended radio structures. However, we note that on smaller scales an increased velocity dispersion (Girdhar et al., 2022) and increased line ratios (Audibert et al., 2023) for two targets in our sample plus displaced molecular gas in another two targets (Girdhar et al, submitted), have been previously identified with a spatial relation to the observed radio jets. The question remains as to whether this impact is seen across the entire sample and further resolved studies will shed light on the the impact on the multi-phase ISM, in particular further investigation into targets with well characterised radio emission.

4.7 Spectra and data tables

Appendix with the remaining spectra as well as all tables of data. We first present details of the CO observations including project id, beam sizes, rms and observation times in Table 4.5. We present all spectra for the targets in this paper including the multiple CO transition data and ionised gas observations from MUSE in Figures 4.13 – 4.29. For further information about what is presented in the spectra plots (e.g. lines, fits to the spectra etc.) see Figure 4.3. We present tables showing information about the spectra and line fits including the S/N of lines, integrated fluxes, line widths, velocity offsets and luminosities in Tables 4.6 – 4.10. Finally we present the line profile information from the fits to the ionised gas observations in Table 4.11.

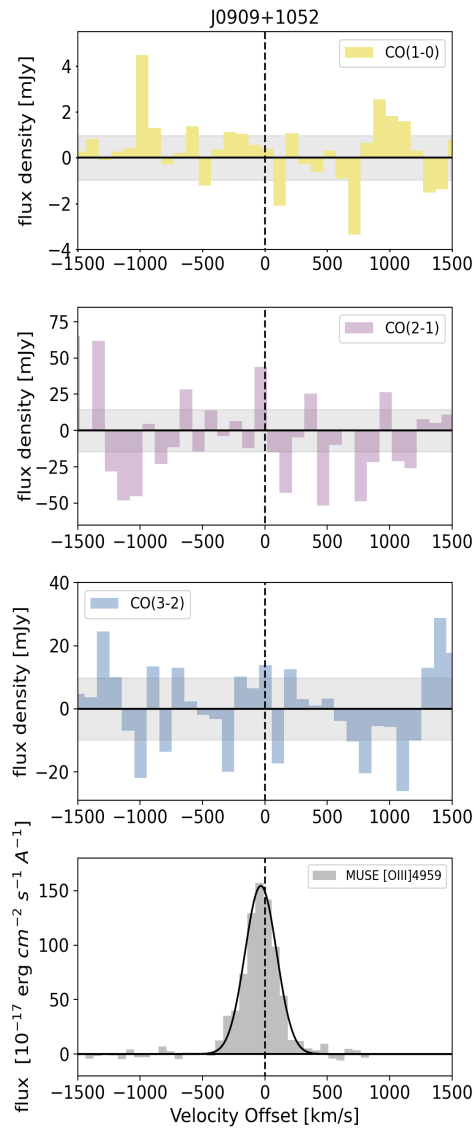


Figure 4.13: J0909+1052, non-detections across all three CO transitions. All shown with 100 km s^{-1} bins. MUSE [O III] observations show a single with Gaussian.

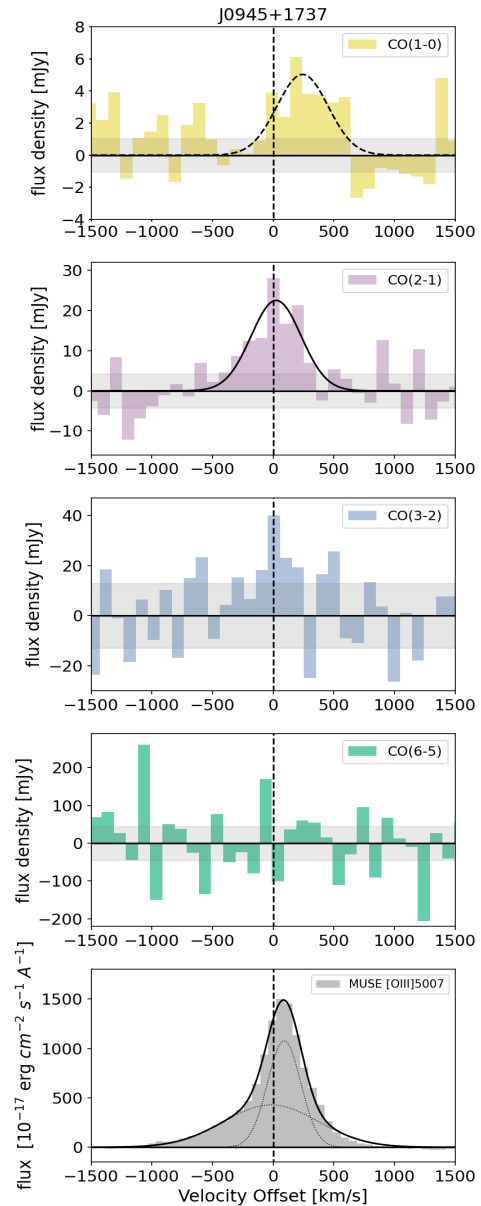


Figure 4.14: J0945+1737 spectra across four CO transitions. All with 100 km s^{-1} bins. Detection in CO(2-1) and low S/N detection in CO(1-0), non-detection in CO(3-2) (although tentative signs of a line at $S/N = 2.7$) or CO(6-5). MUSE [O III] observations show a two component fit with a narrow and broad component.

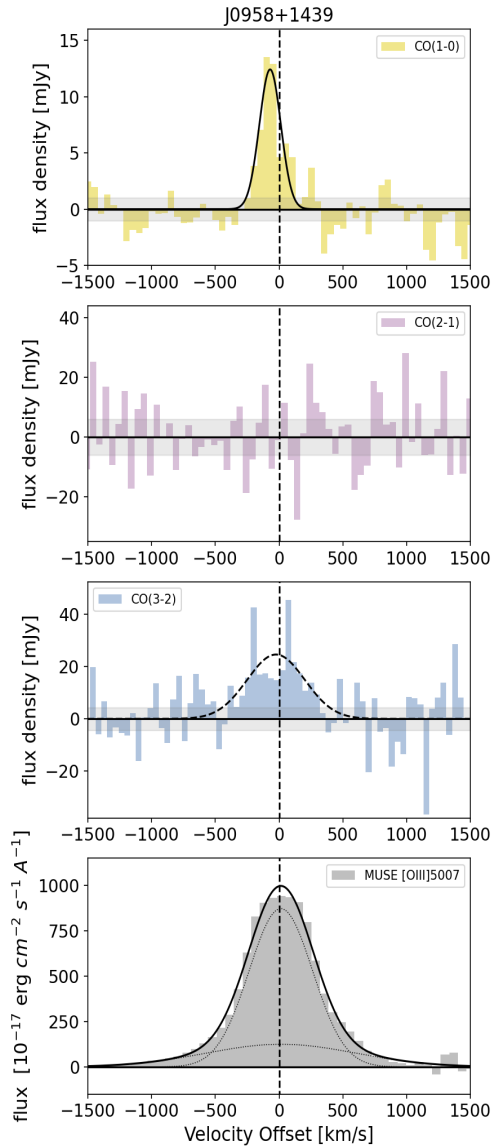


Figure 4.15: J0958+1439 detection in CO(1-0) and low S/N detection in CO(3-2). Non-detection in CO(2-1). MUSE [O III] observations show a two component fit with a narrow and broad component.

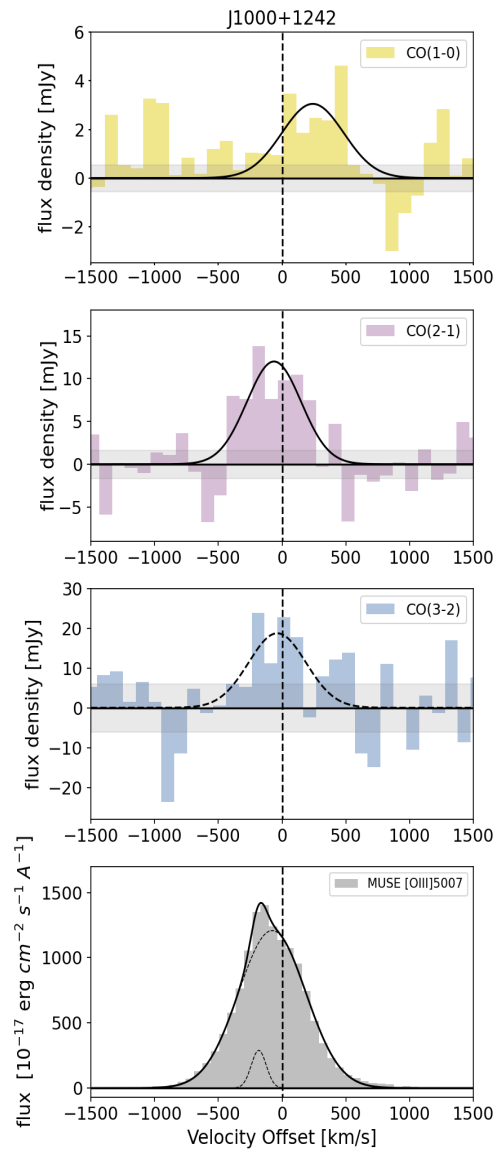


Figure 4.16: J1000+1242, detections in CO(1-0) and CO(2-1) with a low S/N detection in CO(3-2). MUSE [O III] observations show a broad single with Gaussian line profile.

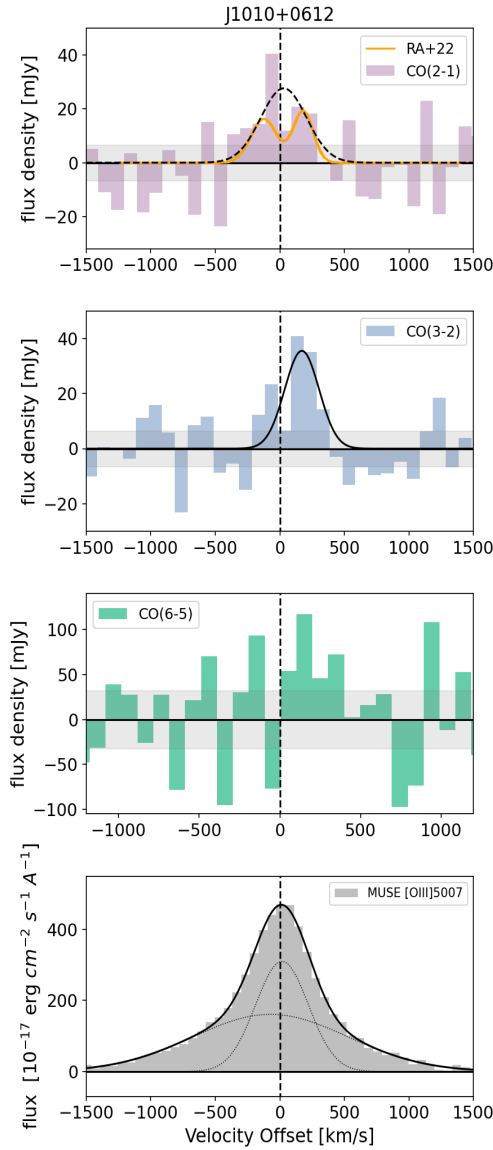


Figure 4.17: J1010+0612 spectra across three CO transitions, with no CO(1-0) observations available. All with 100 km s^{-1} bins. Detection in CO(3-2) and a low S/N detection in CO(2-1) which matches the two component line profile identified in Ramos Almeida et al. 2022 (spectrum shown in orange, labelled RA+22) for which we see tentative signs here. MUSE [O III] observations show a two component fit with a narrow and broad component.

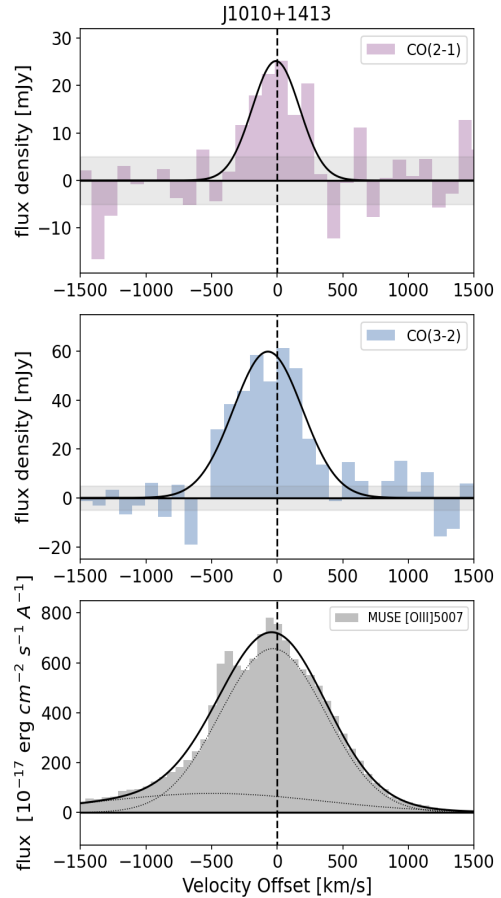


Figure 4.18: J1010+1413, detections in both CO(2-1) and CO(3-2). CO(1-0) not observed. MUSE [O III] observations show broad single with Gaussian line profile.

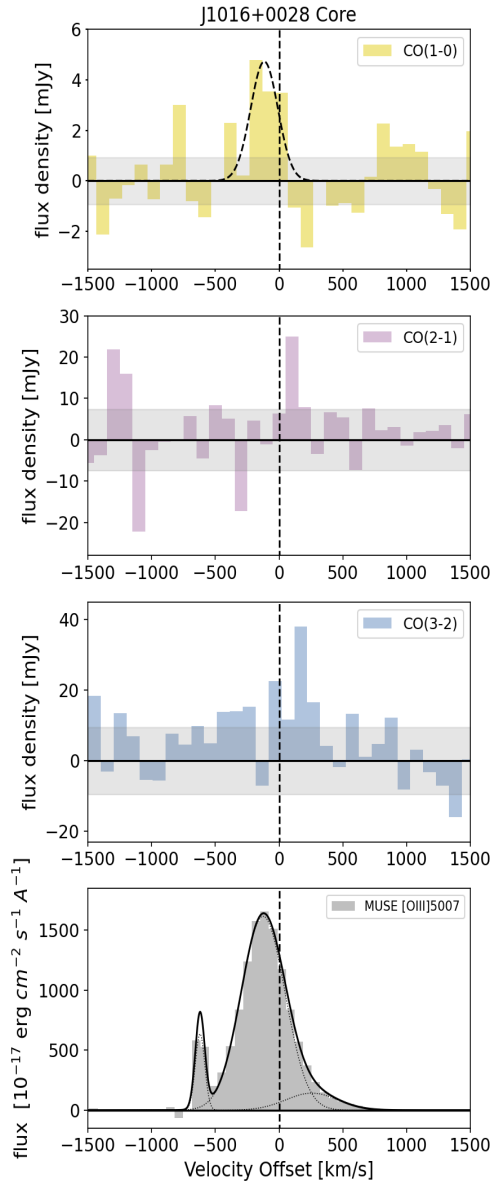


Figure 4.19: J1016+0028, low S/N detection in CO(1-0) and non detections in CO(2-1) and CO(3-2). MUSE [O III] observations show a two component line profile.

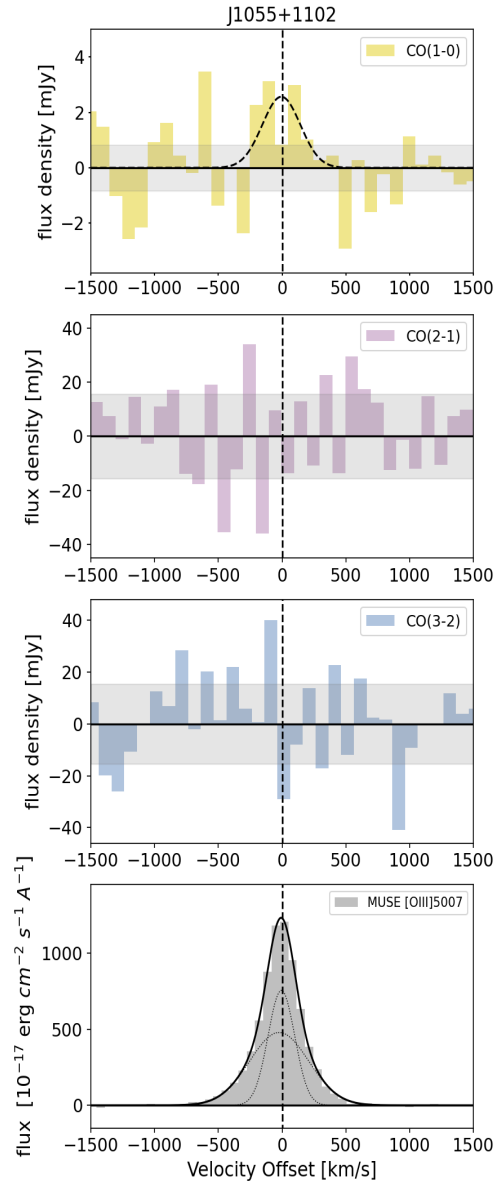


Figure 4.20: J1055+1102 only low S/N detection in CO(1-0), non detections in CO(2-1) and CO(3-2). MUSE [O III] observations show a two component fit with a narrow and broad component.

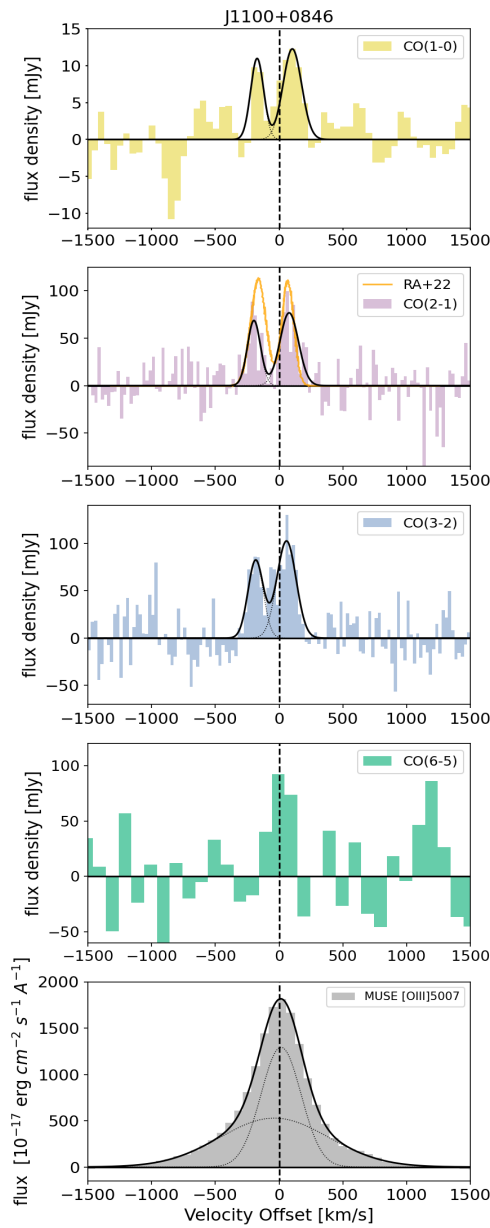


Figure 4.21: J1100+0846 spectra across four transitions. CO(1-0) with 50 km s^{-1} bins and CO(2-1) and CO(3-2) with 25 km s^{-1} bins. Detection in all four transitions, all with same double peak profile. The same double peaked profile was found by [Ramos Almeida et al. 2022](#) CO(2-1) observations (spectrum shown in orange, labelled RA+22). MUSE [O III] observations show a two component fit with a narrow and broad component.

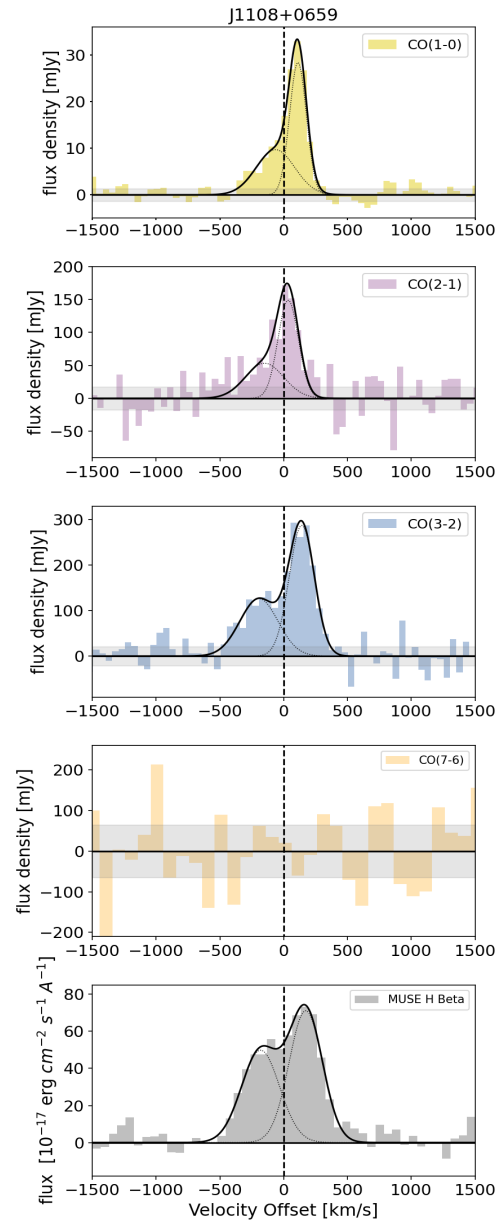


Figure 4.22: J1108+0659 spectra across four CO transitions. First three CO transitions plotted with 50 km s^{-1} bins and CO(7-6) plotted with 100 km s^{-1} bins due to a lack of detection. Blue wing in the first three CO transitions indicating a potential molecular outflow component. There is also potentially a small velocity shift in this outflow component across the first three CO transitions. We find a non-detection in CO(7-6). MUSE [O III] observations showing a similar blue wing to the CO data.

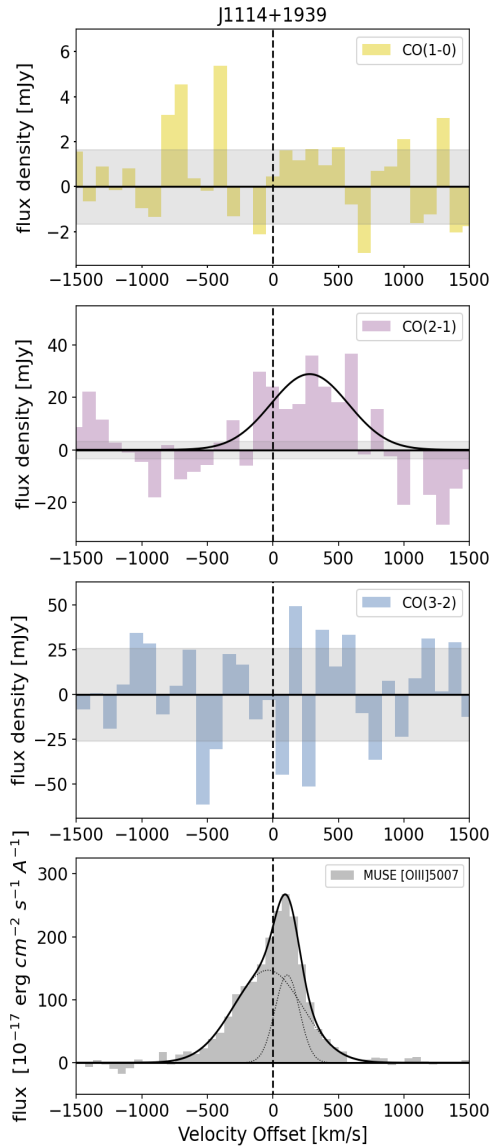


Figure 4.23: J1114+1939, only detection in CO(2-1). Non-detections in CO(1-0) and CO(3-2). MUSE [O III] observations show a two component fit with a narrow and broad component, with the broad component seemingly blueshifted potentially indicating an out-flow.

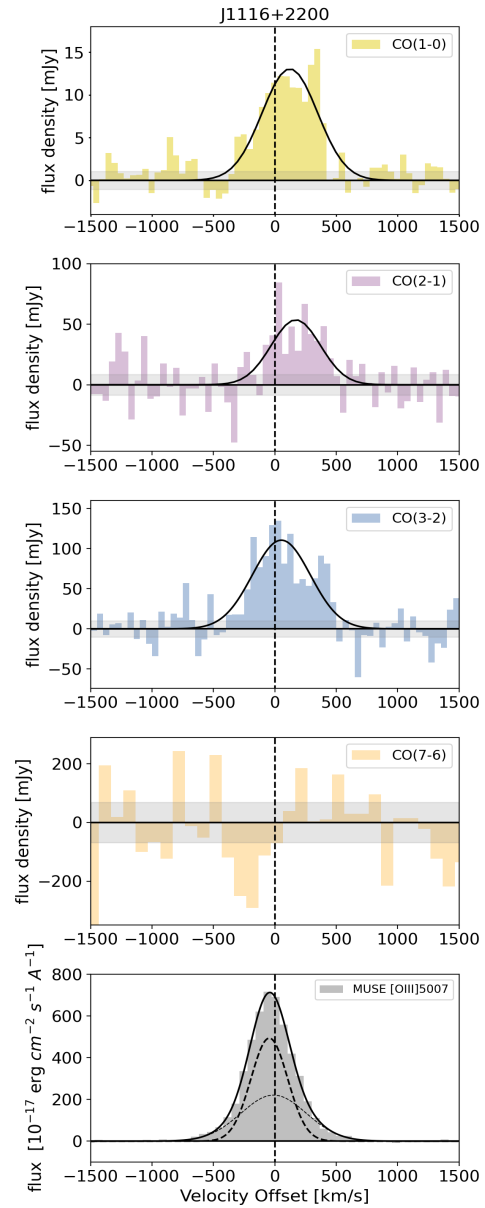


Figure 4.24: J1116+2200 spectra across four CO transitions. The first three transitions with 50 km s^{-1} bins and the CO(7-6) with 100 km s^{-1} bins. Detection of a broad line in the first three transitions. Non-detection in CO(7-6). MUSE [O III] observations show a single with Gaussian line profile.

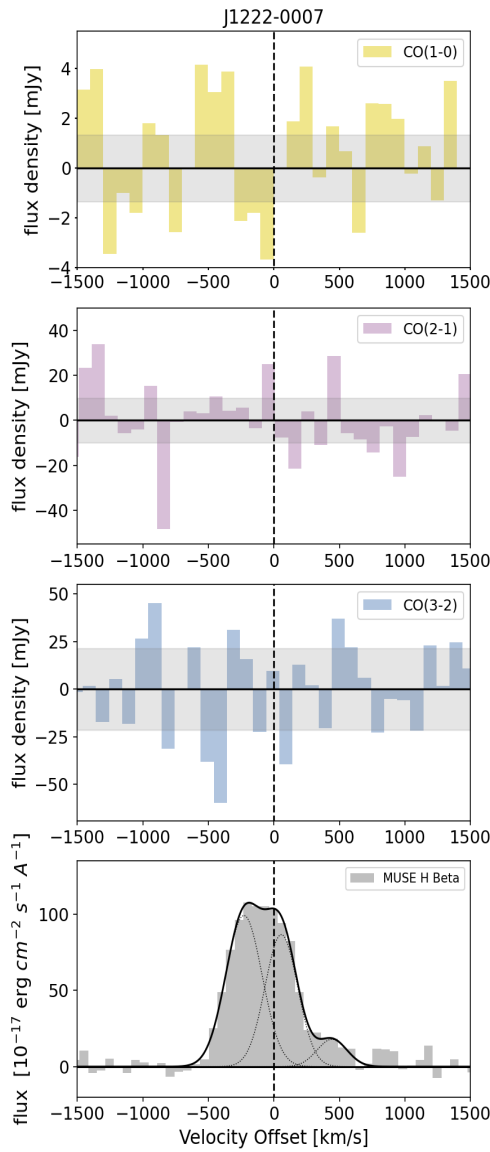


Figure 4.25: J1222-0007 non-detections in all three CO transitions. MUSE [O III] observations show a two component fit to the data.

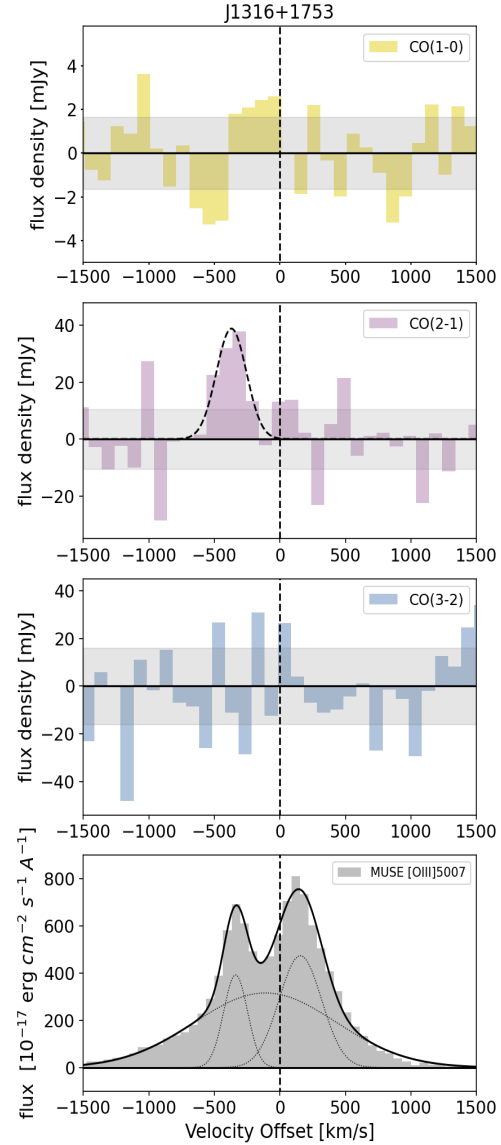


Figure 4.26: J1316+1753, low S/N detection in CO(2-1) and non-detection in CO(1-0) and CO(3-2). MUSE [O III] observations show a three component fit to the data. The low S/N detection in our CO(2-1) data seems to match the middle component present in the MUSE [O III] spectra.

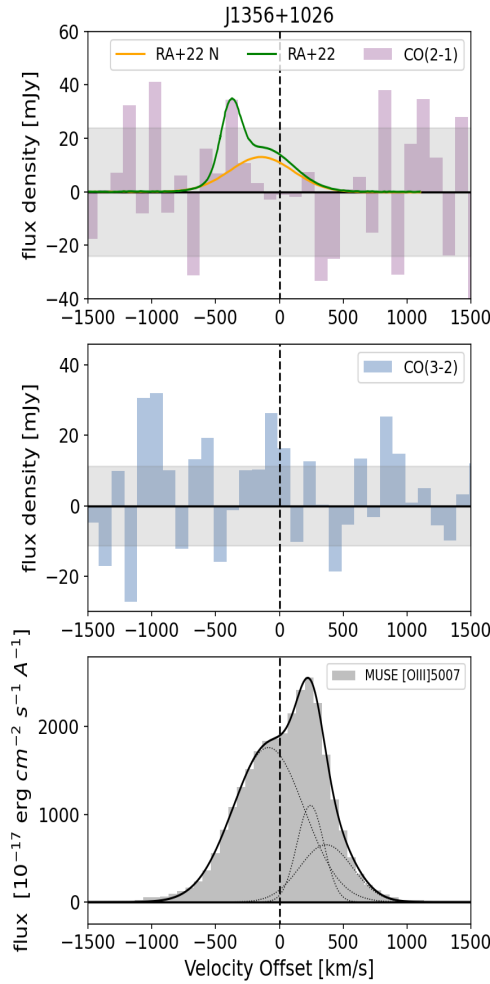


Figure 4.27: J1356+1026 spectra across two CO transitions with no CO(1-0) data available. All set to 100 km s^{-1} bin widths. Non-detection in both transitions. Also shown is the detection from Ramos Almeida et al. 2022 detection in CO(2-1) (labelled RA+22 in orange and RA+22 N in green). We use the RA+22 data in our analysis. MUSE [O III] observations showing a blue wing.

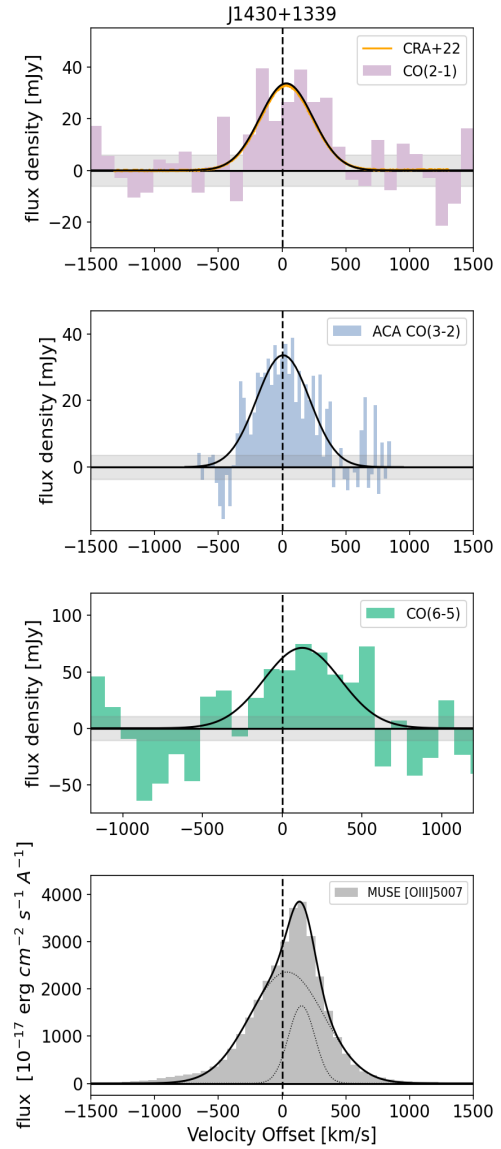


Figure 4.28: J1430+1339 spectra across three CO transitions, no observations in CO(1-0). CO(2-1) and CO(6-5) with 100 km s^{-1} bins, CO(3-2) with 26 km s^{-1} bins (ACA data). For CO(2-1) data from Ramos Almeida et al. 2022 was also available, shown here in orange (labelled RA+22) and showing an almost identical spectrum to our APEX data. Detections across all CO transitions observed. MUSE [O III] observations show a two component fit including a blue wing.

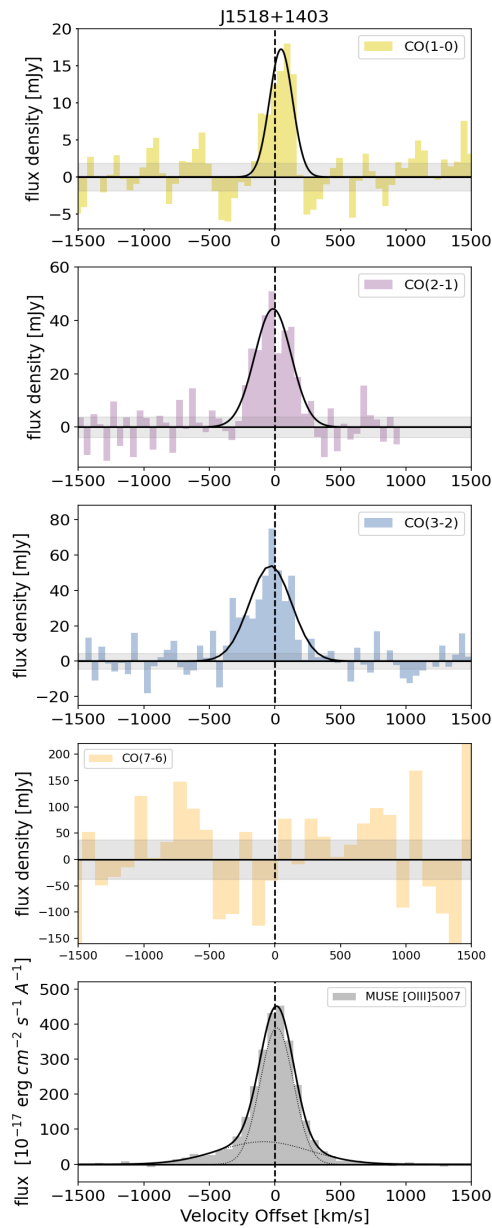


Figure 4.29: J1518+1403 spectra across four CO transitions. All with 50 km s^{-1} bins (except for CO(7-6) which is 100 km s^{-1} due to lack of a detection). Detections in both CO(1-0) and CO(3-2) and a low S/N detection in CO(2-1). MUSE [O III] observations show a two component fit with a narrow and broad component.

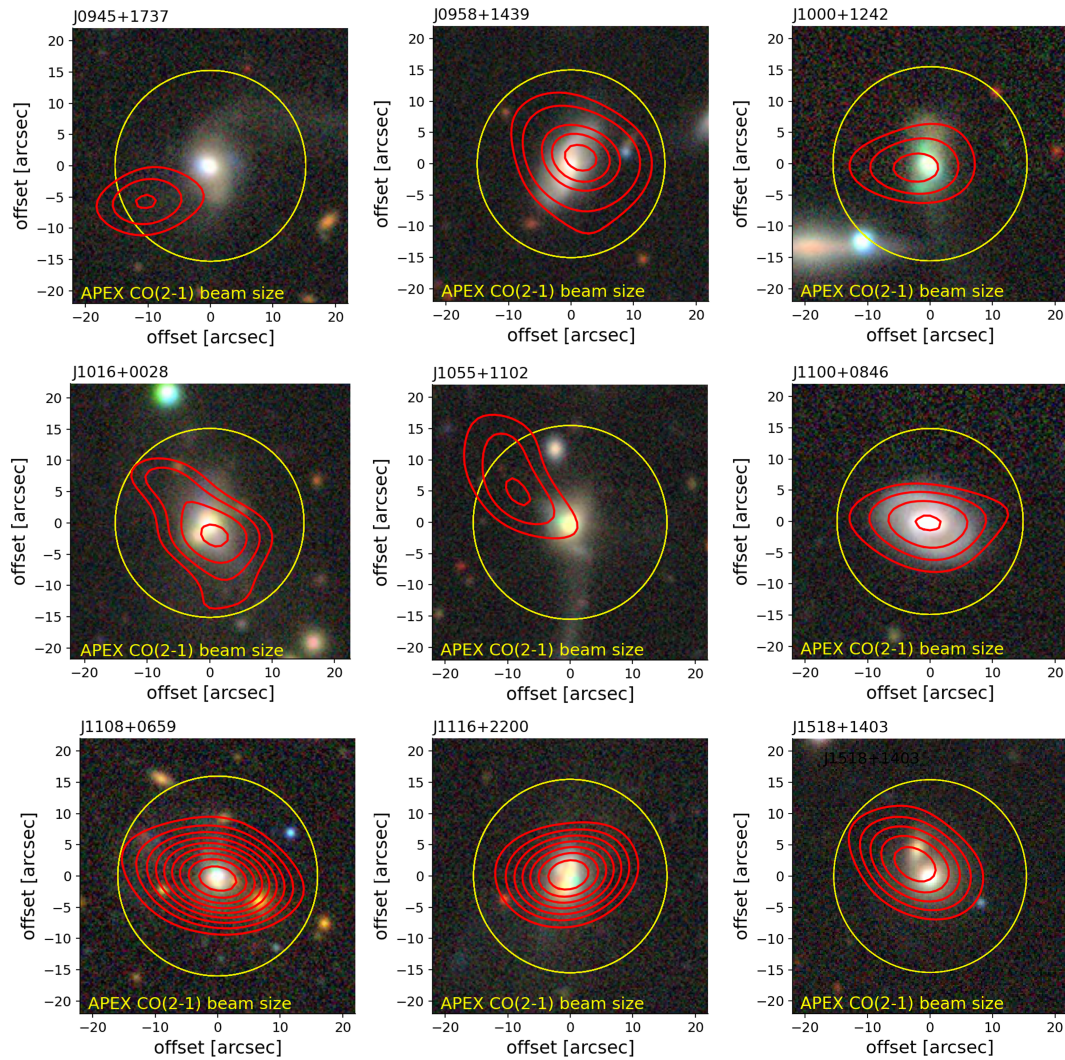


Figure 4.30: Contour plots for the 9 targets with an integrated $S/N > 3$ detection in the ACA CO(1-0) data, where red contours show the 2σ levels and upwards in integer values. The yellow circle denotes the beam size of the CO(2-1) observations, which is also the aperture used to extract the CO(1-0) spectra.

Line	Source Name	Beam Size (arcsec)	rms, $\Delta v = 100 \text{ km s}^{-1}$ (mJy)	t_{obs} (minutes)	Detection?
CO(1-0)	J0909+1052	12.7	1.8	43.8	N
	J0945+1737	11.9	1.7	31.2	L
	J0958+1439	12.7	1.1	85.7	D
	J1000+1242	12.8	1.3	92.7	D
	J1016+0028	12.2	1.2	42.3	L
	J1055+1102	11.7	1.1	44.3	L

Continued on next page

Table 4.5 – continued from previous page

	Name	Beam Size	rms $\Delta v = 100 \text{ km s}^{-1}$	t_{obs}	Detection?
	J1100+0846	12.3	2.5	10.2	D
	J1108+0659	12.8	1.1	35.3	D
	J1114+1939	14.1	1.7	63.5	N
	J1116+2200	13.1	1.7	51.4	D
	J1222-0007	12.7	1.3	30.2	N
	J1316+1753	12.9	1.6	21.2	N
	J1518+1403	12.5	1.9	12.1	D
CO(2-1)	J0909+1052	31.6	26.5	44.7	N
	J1016+0028	30.2	7.4	51.1	N
	J1055+1102	31.0	15.6	19.1	N
	J1108+0659	32.0	18.0	12.8	D
	J1114+1939	32.5	9.9	31.3	D
	J1116+2200	30.9	14.4	19.2	D
	J1222-0007	31.7	18.7	19.2	N
	J1430+1939	29.4	10.6	58.3	D
	J1518+1403	30.8	6.8	128.8	D
CO(2-1)	J0945+1737	30.5	7.6	42.0	D
	J0958+1439	30.0	6.0	71.9	N
	J1000+1242	31.1	3.2	239.1	D
	J1010+0612	29.8	12.0	23.0	D
	J1010+1413	32.4	6.8	60.0	D
	J1100+0846	29.8	18.9	27.5	D
	J1316+1753	31.2	11.0	49.6	L
	J1356+1026	30.4	24.0	35.8	N
CO(3-2)	J0909+1052	21.0	17.9	64.0	N
	J0945+1737	20.4	14.1	46.5	N
	J0958+1439	20.0	18.1	248.3	L
	J1000+1242	20.7	10.6	60.1	L
	J1010+0612	19.8	10.0	76.2	D
	J1010+1413	21.6	9.6	53.8	D

Continued on next page

Table 4.5 – continued from previous page

	Name	Beam Size	rms $\Delta v = 100 \text{ km s}^{-1}$	t_{obs}	Detection?
	J1016+0028	20.1	9.5	148.8	N
	J1055+1102	20.7	15.4	15.9	N
	J1100+0846	19.9	14.2	57.3	D
	J1108+0659	21.3	24.2	32.0	D
	J1114+1939	21.6	25.9	18.5	N
	J1116+2200	20.6	17.8	63.5	D
	J1222-0007	21.2	21.4	12.8	N
	J1316+1753	20.8	16.0	64.9	N
	J1356+1026	20.3	11.3	95.5	N
	J1518+1403	20.6	6.9	52.6	D
CO(3-2)	J1430+1339	4.3	10.3	26.2	D
CO(6-5)	J0945+1737	10.2	82.1	128.7	N
	J1010+0612	9.9	61.9	87.7	N
	J1100+0846	9.9	49.0	111.3	N
	J1430+1339	9.8	40.0	292.0	L
CO(7-6)	J1108+0659	9.1	118.0	96.4	N
	J1116+2200	8.8	124.9	87.5	N
	J1518+1403	8.8	68.3	245.2	N

Table 4.5: Details of the CO observations including the CO line, telescope used and project id, the source name, the beam size, the rms, observing times (t_{obs}) and whether we class a detection “D”, low S/N detection “L” or a non-detection “N” based on criteria stated in Section 4.4.2. ACA project id: 2019.2.00194.S. APEX id: CO(2-1) E-0105.B-0713A-2020, E-0100.B-0166B-2017, CO(3-2) E-0105.B-0713B-2020, CO(6-5) and CO(7-6) E-0109.B-0710A-2022, ALMA CO(3-2) project id: 2016.1.01535.S

Name	S/N	$S_{\text{CO}(1-0)}$ (Jy km s ⁻¹)	CO(1-0) V_{50} (km s ⁻¹)	CO(1-0) W_{80} (km s ⁻¹)	$L'_{\text{CO}(1-0)}$ ($1 \times 10^9 \times \text{K km s}^{-1} \text{pc}^2$)
J0909+1052	–	< 2.1	–	–	< 2.8
J0945+1737	4.8	2.7 ± 0.7	243 ± 65	539 ± 167	2.1 ± 0.6
J0958+1439	7.9	2.6 ± 0.3	-71 ± 13	215 ± 34	1.5 ± 0.2
J1000+1242	5.6	1.9 ± 0.6	259 ± 68	621 ± 246	1.8 ± 0.5
J1010+0612	–	–	–	–	–
J1010+1413	–	–	–	–	–
J1016+0028 (core)	4.6	1.3 ± 0.4	-116 ± 39	288 ± 101	0.8 ± 0.3
J1016+0028 North Lobe	–	0.6 ± 0.1	611 ± 68	116 ± 23	0.4 ± 0.1
J1016+0028 South Lobe	–	1.0 ± 0.2	-365 ± 16	126 ± 24	0.6 ± 0.1
J1055+1102	3.1	1.0 ± 0.4	-6 ± 74	381 ± 189	1.0 ± 0.4
J1100+0846 (Total)	7.6	3.7 ± 0.3	33 ± 42	378 ± 41	1.7 ± 0.3
J1100+0846 (red)	6.2	2.3 ± 0.4	79 ± 16	142 ± 41	1.1 ± 0.3
J1100+0846 (blue)	3.8	1.4 ± 0.4	-197 ± 15	204 ± 45	0.7 ± 0.2
J1108+0659 (Total)	32.2	8.4 ± 0.5	88 ± 5	354 ± 40	13.4 ± 3.1
J1108+0659 (core)	22.1	4.7 ± 1.3	112 ± 5	66 ± 8	7.5 ± 2.0
J1108+0659 (blue wing)	14.2	3.7 ± 1.4	-64 ± 68	151 ± 40	5.9 ± 2.3
J1114+1939	–	< 2.0	–	–	< 3.9
J1116+2200	12.4	7.4 ± 0.5	122 ± 17	578 ± 44	7.3 ± 0.5
J1222-0007	–	< 2.1	–	–	< 3.0
J1316+1753	–	< 1.8	–	–	< 2.4
J1356+1026	–	–	–	–	–
J1430+1339	–	–	–	–	–
J1518+1403	9.3	3.8 ± 0.5	47 ± 14	220 ± 36	1.2 ± 0.2

Table 4.6: Properties of the CO(1-0) line emission observed with the ALMA ACA. We present the peak S/N, the integrated flux from the single with Gaussian line fit, the velocity offset of the peak compared to $v = 0 \text{ km s}^{-1}$ (defined from the SDSS redshift), line width (W_{80}) and the line luminosity. Upper limits are 3σ upper limits based on the median rms in the spectra and using the average line profile from other transitions of the same target, or from others with CO(1-0) detections. Those with no data shown do not have the required data to present.

Name	S/N	$S_{\text{CO}(2-1)}$ (Jy km s ⁻¹)	CO(2-1) V_{50} (km s ⁻¹)	CO(2-1) W_{80} (km s ⁻¹)	$L'_{\text{CO}(2-1)}$ ($1 \times 10^9 \times \text{K km s}^{-1} \text{pc}^2$)
J0909+1052	–	< 34.1	–	–	< 12.6
J0945+1737	5.1	11.6 ± 2.4	25 ± 49	528 ± 125	2.3 ± 0.5
J0958+1439	–	< 6.5	–	–	< 1.0
J1000+1242	7.3	6.4 ± 1.2	-64 ± 47	544 ± 119	1.7 ± 0.3
J1010+0612	4.2	12.3 ± 4.5	30 ± 74	453 ± 190	1.4 ± 0.5
J1010+1413	5.0	11.4 ± 2.4	-10 ± 44	462 ± 112	5.5 ± 1.2
J1016+0028 (core)	1.9	< 6.6	–	–	< 1.1
J1055+1102	–	< 16.9	–	–	< 5.9
J1100+0846 (Total)	5.9	22.8 ± 3.4	-18 ± 39	378 ± 41	2.7 ± 0.4
J1100+0846 (red)	8.1	14.1 ± 2.6	79 ± 16	142 ± 41	1.7 ± 0.3
J1100+0846 (blue)	5.0	8.8 ± 2.2	-197 ± 15	204 ± 45	1.0 ± 0.3
J1108+0659 (Total)	10.0	59.4 ± 15.6	9 ± 19	366 ± 112	24.0 ± 9.0
J1108+0659 (core)	9.5	29.7 ± 13.2	35 ± 18	93 ± 26	24.0 ± 9.0
J1108+0659 (blue wing)	6.4	29.8 ± 17	-236 ± 185	277 ± 112	12.0 ± 7.0
J1114+1939	8.7	21.4 ± 6.6	280 ± 106	756 ± 270	10.3 ± 3.2
J1116+2200	6.3	26.4 ± 4.6	233 ± 41	517 ± 104	6.5 ± 1.1
J1222-0007	–	< 21.9	–	–	< 9.7
J1316+1753	3.7	11.1 ± 3.6	-370 ± 43	293 ± 110	3.0 ± 1.0
J1356+1026	–	< 30.9	–	–	< 5.8
J1430+1339	5.7	21.2 ± 7.9	31 ± 106	631 ± 271	1.8 ± 0.7
J1518+1403	11.5	15.5 ± 1.8	-14 ± 19	293 ± 49	3.6 ± 0.4

Table 4.7: Properties of the CO(2-1) line emission observed with APEX. We present the peak S/N, the integrated flux from the single with Gaussian line fit, the velocity offset of the peak compared to $v = 0 \text{ km s}^{-1}$ (defined from the SDSS redshift), line width (W_{80}) and the line luminosity. Upper limits are 3σ upper limits based on the median rms in the spectra and using the average line profile from other transitions of the same target, or from others with CO(2-1) detections. Those with no data shown do not have the required data to present.

Name	S/N	$S_{\text{CO}(3-2)}$ (Jy km s ⁻¹)	CO(3-2) V_{50} (km s ⁻¹)	CO(3-2) W_{80} (km s ⁻¹)	$L'_{\text{CO}(3-2)}$ ($1 \times 10^9 \times \text{K km s}^{-1} \text{ pc}^2$)
J0909+1052	–	< 22.5	–	–	< 3.3
J0945+1737	2.7	< 19.2	–	–	< 1.7
J0958+1439	4.3	13.3 ± 2.7	188 ± 59	578 ± 137	1.5 ± 0.4
J1000+1242	3.1	8.6 ± 3.0	-38 ± 81	576 ± 207	1.2 ± 0.4
J1010+0612	5.5	10.3 ± 3.1	179 ± 36.	264 ± 94	0.5 ± 0.2
J1010+1413	12.1	37.5 ± 3.4	-83 ± 30	673 ± 77	8.1 ± 0.7
J1016+0028 (core)	2.1	< 7.0	–	–	< 0.5
J1055+1102	–	< 14.8	–	–	< 1.7
J1100+0846 (Total)	7.4	31.7 ± 3.7	-21 ± 21	354 ± 36	1.7 ± 1.2
J1100+0846 (red)	–	19.4 ± 2.7	58 ± 12	210 ± 36	1.0 ± 0.1
J1100+0846 (blue)	–	12.3 ± 2.5	-184 ± 13	167 ± 39	0.7 ± 0.1
J1108+0659 (Total)	14.2	118.8 ± 20.5	55 ± 17	529 ± 141	21.0 ± 4.0
J1108+0659 (core)	14.7	71.3 ± 13.9	142 ± 17	276 ± 41	12.7 ± 2.5
J1108+0659 (blue wing)	8.3	47.6 ± 15.0	-194 ± 53	417 ± 141	8.5 ± 2.7
J1114+1939	–	< 48.9	–	–	< 6.9
J1116+2200	10.9	63.4 ± 5.7	53 ± 26	606 ± 65	6.7 ± 0.6
J1222-0007	–	< 26.7	–	–	< 4.2
J1316+1753	–	< 11.8	–	–	< 2.4
J1356+1026	–	< 14.5	–	–	< 0.5
J1430+1339	9.3	17.5 ± 1.4	33 ± 19	532 ± 49	0.7 ± 0.1
J1518+1403	12.2	20.5 ± 2.1	-34 ± 20	412 ± 50	2.1 ± 0.2

Table 4.8: Properties of the CO(3-2) line emission observed with APEX. We present the peak S/N, the integrated flux from the single with Gaussian line fit, the velocity offset of the peak compared to $v = 0 \text{ km s}^{-1}$ (defined from the SDSS redshift), line width (W_{80}) and the line luminosity. Upper limits are 3σ upper limits based on the median rms in the spectra and using the average line profile from other transitions of the same target, or from others with CO(3-2) detections. Those with no data shown do not have the required data to present.

Name	S/N	$S_{\text{CO}(6-5)}$ (Jy km s ⁻¹)	CO(6-5) V_{50} (km s ⁻¹)	CO(6-5) W_{80} (km s ⁻¹)	$L'_{\text{CO}(6-5)}$ ($1 \times 10^9 \times \text{K km s}^{-1} \text{ pc}^2$)
J0945+1737	–	< 117.4	–	–	< 2.6
J1010+0612	2.2	< 59.2	–	–	< 0.8
J1100+0846	1.1	< 47.5	–	–	< 0.8
J1430+1339	6.7	42.9 ± 18.7	126 ± 121	669 ± 337	0.4 ± 0.2

Table 4.9: Properties of the CO(6-5) line emission observed with APEX. We present the integrated flux from the single with Gaussian line fit, the velocity offset of the peak compared to $v = 0 \text{ km s}^{-1}$ (defined from the SDSS redshift), line width (W_{80}) and the line luminosity. Upper limits are 3σ upper limits based on the median rms in the spectra and using the average line profile from other transitions of the same target, or from others with CO(6-5) detections. Those with no data shown do not have the required data to present.

Name	S/N	$S_{\text{CO}(7-6)}$ (Jy km s ⁻¹)	CO(7-6) V_{50} (km s ⁻¹)	CO(7-6) W_{80} (km s ⁻¹)	$L'_{\text{CO}(7-6)}$ ($1 \times 10^9 \times \text{K km s}^{-1} \text{ pc}^2$)
J1108+0659	–	< 129.8	–	–	< 4.2
J1116+2200	–	< 187.1	–	–	< 3.8
J1518+1403	–	< 58.2	–	–	< 1.5

Table 4.10: Properties of the CO(7-6) line emission observed with APEX. We present the integrated flux from the single with Gaussian line fit, the velocity offset of the peak compared to $v = 0 \text{ km s}^{-1}$ (defined from the SDSS redshift), line width (W_{80}) and the line luminosity. Upper limits are 3σ upper limits based on the median rms in the spectra and using the average line profile from other transitions of the same target, or from others with or CO(7-6) detections. Those with no data shown do not have the required data to present.

Name	Emission Line	30'' V_{50} (km s ⁻¹)	30'' W_{80} (km s ⁻¹)	3'' V_{50} (km s ⁻¹)	3'' W_{80} (km s ⁻¹)	components
J0909+1052	[O III]4959	-34 ± 3	318 ± 8	-38 ± 1	402 ± 3	1
J0945+1737	[O III]5007	63 ± 2	734 ± 33	39 ± 1	798 ± 43	2
J0958+1439	[O III]5007	16 ± 7	736 ± 44	18 ± 4	788 ± 25	2
J1000+1242	[O III]5007	-95 ± 4	673 ± 5	-41 ± 6	808 ± 8	2
J1010+0612	[O III]5007	-17 ± 7	1216 ± 95	-28 ± 14	1406 ± 55	2
J1010+1413	[O III]5007	-76 ± 7	1333 ± 30	-14 ± 4	1440 ± 28	2
J1016+0028	[O III]5007	-130 ± 6	658 ± 8	-41 ± 4	598 ± 20	3
J1055+1102	[O III]5007	-12 ± 1	473 ± 13	-17 ± 1	473 ± 6	2
J1100+0846	[O III]5007	-5 ± 12	926 ± 45	0 ± 12	913 ± 49	2
J1108+0659	H β	40 ± 19	598 ± 36	-47 ± 5	653 ± 11	2
J1114+1939	[O III]5007	30 ± 4	616 ± 17	29 ± 2	648 ± 7	2
J1116+2200	[O III]5007	-35 ± 3	521 ± 43	-57 ± 1	456 ± 18	2
J1222-0007	H β	-79 ± 34	593 ± 51	-54 ± 3	831 ± 12	3
J1316+1753	[O III]5007	-27 ± 4	1117 ± 56	29 ± 30	1152 ± 52	3
J1356+1026	[O III]5007	75 ± 30	807 ± 188	-10 ± 33	891 ± 111	3
J1430+1339	[O III]5007	83 ± 15	661 ± 52	40 ± 14	796 ± 63	2
J1518+1403	[O III]5007	0 ± 2	569 ± 64	1 ± 1	518 ± 36	2

Table 4.11: Table presenting the MUSE line profile data used as a comparison to the molecular gas presented in this work. Here we show the emission line used as a tracer for the ionised gas, the velocity offset (V_{50}) and line width (W_{80}). Also shown is the number of components present in the line (and therefore how many Gaussian components we fit to analyse the line profile).

Context free quotes

“You put pisco sour in my kettle”

“For a big man you have a small bag”

“Valentine’s Day, brought to you by Shell”

“I don’t have any plans for my neck tonight”

“On a scale of 1 to Mr. Pancake how chaotic was it?”

“If it wouldn’t ruin my life I would have a really big parrot”

“You didn’t think the Easter bunny would be an old white man with no hair?”

“We’ve done some questionable things but we have some good hymns”

“I don’t have the power to put you in a room of wasps”

“You trust Google after it gave you butter goat?”

“He made me peel the egg without coffee”

“You forget that he’s 60kg on a good day”

“Hot pot is like Chinese fondue”

“I hunted eggs until I was 21”

Summary and Outlook

5.1 Summary of conclusions

Galaxies in epoch of reionisation

In Chapter 2 I presented the spectroscopic redshift confirmation of a galaxy in epoch of reionisation, Abell 1703-zD1 at $z = 6.8269 \pm 0.0004$, via the detection of the [C II] using NOEMA. Observations of these galaxies at $z > 6$ are important to gain insights into the properties of the first galaxies that form in the Universe, as well as the environment they live in. From these observations I identified a consistent, but slightly lower, $L_{[\text{C II}]} - \text{SFR}$ compared to the relation identified for local galaxies (De Looze et al., 2014). Previous studies have shown a slight deficit in $L_{[\text{C II}]}$, which seems to be exacerbated by gravitational lensing effects. We have accounted for the lensing effects by tapering the NOEMA data, and to obtain a more accurate flux measurement. In doing so, showing that missing fluxes in lensed sources may be a reason for some cases of galaxies with lower $L_{[\text{C II}]}$. Alternatively the differences could be attributed to differences in metallicity, where lower metallicities will cause a lower $L_{[\text{C II}]}$. More work is needed in this area to clarify whether these early galaxies are consistent with the local relation, whether there is more of a spread in the data, or whether the relation for high- z galaxies is in fact different.

In A1703-zD1, I also showed the presence of a velocity gradient across the galaxy, and even with the relatively low S/N data, basic analysis suggested a rotation dominated system rather than a

merger. This work has shown that NOEMA has the capability to observe “normal” galaxies at $z > 6$ since its upgrade, albeit with assistance from gravitational lens in this case. However, this is a useful exercise as now that JWST is identifying galaxies in large numbers at these high redshifts, it is crucial to know that we have coverage in the northern hemisphere for bright targets and follow up observations that might be out of the reach of ALMA.

It is also critical to obtain spectroscopic redshift confirmations of these galaxies, so that targeted follow up observations to study the galaxy properties in more detail can be pursued. For example, allowing for studies of fainter lines and detailed kinematics, such as signatures of outflows.

Investigating AGN and quasar feedback

In Chapter 3 I identified a relationship between radio emission and the presence of ionised outflows in AGN host galaxies. Specifically, that compact radio emission in AGN host galaxies are more likely to show extreme ionised outflows with velocities over 1000 km s^{-1} . High resolution VLA observations for a sample of the targets in this work showed the presence of small scale radio jets in those targets which were compact in radio emission, therefore suggesting that these radio jets are a driving mechanism for ionised outflows (Jarvis et al., 2019; Molyneux et al., 2019).

In Chapter 4 I presented work investigating the excitation of molecular gas in quasar host galaxies as part of quasar feedback survey. This was achieved by measuring multiple CO transitions in 17 quasar host galaxies, with multiwavelength data available. We find no significant impact on the *total* molecular gas excitation in these quasars which have known radio jets and ionised outflows. We also find a lower than expected excitation in CO(6-5) and CO(7-6) observations when compared to similar observations of quasars at high redshift, perhaps as a result of lower luminosities seen in the QFeedS sample.

Observations of resolved CO excitation for AGN with radio jets have shown both disturbed gas kinematics and increased CO excitation surrounding radio emission (e.g. Oosterloo et al., 2017; Girdhar et al., 2022; Audibert et al., 2023). These results combined with the findings of Chapter 4 (Molyneux et al., 2023) suggest that the impact of small scale radio jets, confined to

the central few kpc of galaxies do not have a wide ranging impact across the entire galaxy and that any impact is likely to be more localised. Further observations at higher spatial resolution and across multiple CO transitions are necessary to confirm this, especially covering a wide range of galactic and AGN properties to search for the causes and scenarios in which AGN feedback can excite CO and have a subsequent impact on galaxy evolution.

5.2 Where future observatories will take us

I wish to provide a brief outlook for some future planned observatories and discuss how they will provide significant advancements to fields of galaxy evolution/formation and AGN.

JWST: Despite JWST already launching and providing successful observations, it is still in its infancy. However, it has already demonstrated that it will indeed be revolutionary when it comes to observations of galaxies at $z > 6$. With the the NIRSpec instrument it has the capability to regularly confirm galaxies in large numbers, as well as pushing the boundaries in terms of redshift. JWST has already confirmed galaxies at $z > 10$ (e.g. [Curtis-Lake et al., 2023](#)) and with far greater ease than any previous telescope/instrument. Given the success of these observations already, it is clear that JWST will contribute to huge advancements in the coming decade and further our understanding of the very first galaxies and the early period of the Universe.

ELT: New ground based optical/infrared observatories like ESO's Extremely Large Telescope (ELT, see [Figure 5.1](#)) with a 39 metre diameter primary mirror will also further our understanding with detailed spectroscopic information of these high- z galaxies. Observations of extremely faint sources with the HARMONI and MOSAIC instruments on the ELT will further our understanding of the ionisation state of the Universe at redshifts from 5 to 13, adding to the work of JWST.

The HARMONI instrument on the ELT will also provide observations to estimate the properties of AGN/quasars and their host galaxy by, for example, further studies of outflows of gas and measuring black hole masses. Observations of stars orbiting the Galactic centre will also provide further insights into the black hole in the centre of the Milky Way and the physics at play in the

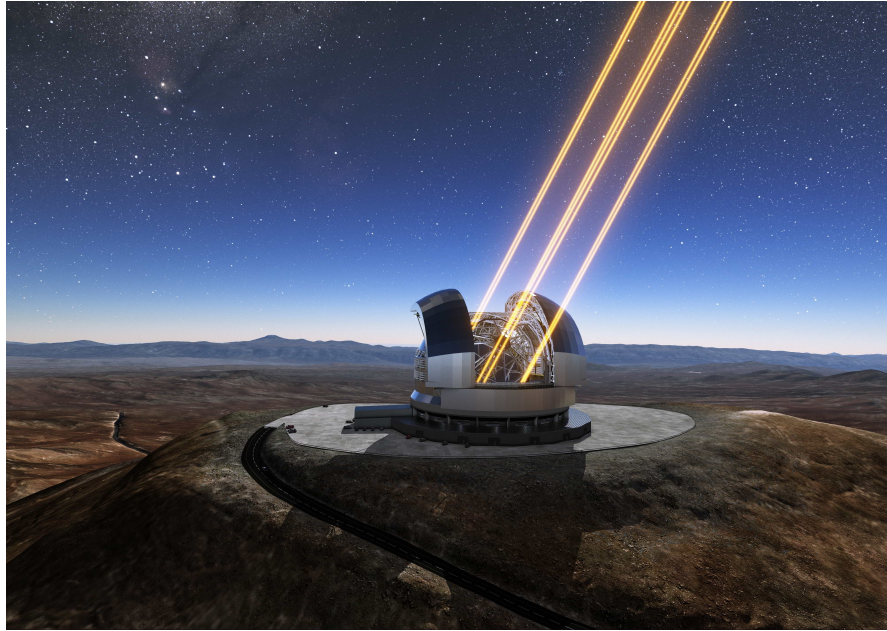


Figure 5.1: Artist's impression of ESO's Extremely Large Telescope, currently due to be completed in 2028. Credit: ESO/L. Calçada.

close proximity of supermassive black holes. All of which will add to studies of the role of black holes in galaxy formation and evolution.

AtLAST: The Atacama Large Aperture Submillimeter Telescope (AtLAST) is a planned 50 metre single dish sub-mm telescope on the Chajnantor plateau in Chile, close to APEX and ALMA telescopes in the Atacama desert. Due to the location it will benefit from the excellent weather conditions that these sub-mm telescopes require. This telescope will transform sub-mm observations and provide large surveys of the sky that will identify a huge amount of targets for follow up observations with ALMA.

AtLAST will be able to achieve an even broader range of science than APEX, which is already an excellent single dish facility. APEX currently performs observations on various scientific topics ranging from extragalactic to studies of the LMC/SMC, star forming regions, molecular clouds and observations of the galactic centre. AtLAST will be able to achieve all of this and more, with a higher sensitivity, $\sim 30 \times$ field of view, spectral bandwidth and spatial resolution which will also be very complementary to ALMA. All of which will make AtLAST very powerful and unique.

SKA: The Square Kilometer Array (SKA) will be the most powerful radio telescope in the world when completed. It will consist of telescopes in both South Africa and Australia and will be able

to study the first light in the Universe and probe reionisation by observing neutral hydrogen at $z > 6$.

The sensitivity and resolution of SKA will also be able to observe young, newly forming galaxies, again mapping the distribution of hydrogen.

SKA will also enable further advances in the role of radio emission in AGN and quasar host galaxies, strengthening our understanding of the link between growing supermassive black holes and the interstellar medium within their host galaxies. It will be able to perform studies of radio jets and lobes, much in the same way as the VLA has achieved in both young and evolved radio AGN, including radio quiet AGN and the mechanism of radio emission in these objects.

Finally, from these and other new and planned observatories, there will be the unexpected discoveries. New telescopes and instruments allow us to explore further into the unknown which can provide unexpected findings. It is therefore an exciting future with these upcoming telescopes, not just in the field of galaxy evolution but also for exoplanet studies, solar system science and cosmology.

5.3 Avenues of future work

Given the work presented in this thesis and the conclusions outlined above there are several avenues for further work which will expand on the findings.

The first of these would be for a resolved study of the molecular gas content, traced by CO, in the Quasar Feedback Survey sample. As presented in Chapter 2 the *total* molecular gas content has been traced by observations with APEX and ACA across multiple CO transitions. This has given insights into the total molecular gas content as well as the excitation of the molecular gas via CO SLEDs and the ratio between CO line luminosities. With resolved observations there are several ways in which this can be expanded upon, in particular establishing the level of CO excitation surrounding radio jets. In previous studies there has been evidence for an impact on a more localised scale impact around radio jets (Oosterloo et al., 2017, 2019; Audibert et al., 2023). This localised impact is also observed in simulations of these radio quiet systems (Mukherjee

et al., 2018b). Spatially resolved studies of the CO in the central few kpc surrounding radio jets will allow us to perform the same analysis in this sample of well observed quasars at $z < 0.2$.

Observations of resolved CO excitation are limited in number, and so expanding this to the full Quasar Feedback Survey sample where complementary multiwavelength data are available will allow for an in depth study of this. This can already be achieved with part of the sample which already have ALMA 12m array observations of CO(2-1) and CO(3-2).

In the literature these observations have been done at low J_{CO} transitions (at CO(3-2) as the maximum J_{CO} line), but this should also be expanded upon by extending this to higher J_{CO} transitions (at CO(6-5) and above). This would ensure any excitation observed is driven by AGN processes and not from other sources, since these transitions require higher temperatures and densities, more commonly associated with AGN processes (Bradford et al., 2003; Spinoglio et al., 2012; Meijerink et al., 2013; Gallerani et al., 2014). Resolved studies at both low and high J_{CO} transitions will also allow for comparisons to be made between these excitation levels and further, enable studies into the temperature and density conditions of the gas surrounding the observed radio jets.

Comparing the observations of the total gas content to resolved studies will also allow for calculations on the amount of gas in structures/outflows/filaments and how much is located in extended diffuse structures.

Another avenue is to explore the different line profiles observed in the CO spectra, shown in Chapter 4. For example a blue wing in J1108+0659 and double peaked profiles in J1100+0846 and J1010+0612. Investigating these velocity structures with resolved observations performed with ALMA could shed light on the kinematics of CO around the central AGN and across the wider galaxy. One expectation could be evidence for AGN driven outflows or a disruption in kinematics from the observed radio jets in the sample, as has been observed already in the ionised phase of the ISM. Indeed, work has already shown evidence for an impact on the molecular phase in a handful of targets, but with a smaller impact on velocities compared to the ionised phase (Ramos Almeida et al., 2022; Girdhar et al., 2022; Audibert et al., 2023).

From ACA observations, evidence was also found for CO(1-0) at the location of extended radio lobes at 7 and 10 kpc from the centre of the host galaxy J1016+0028. Confirmation of this by

resolved observations would show the ability of radio emission to lift the molecular gas out to these distances.

Resolved CO(1-0) observations of both J1108+0659 and J1016+0028 taken with NOEMA [PI: Molyneux] will be analysed to characterise the interesting kinematic and spatial features identified in lower resolution ACA CO(1-0) observations.

Finally, similar research to that presented in Chapter 3 will soon be possible with the upcoming WEAVE-LOFAR Survey, where optical spectroscopic observations from WEAVE will be matched with radio observations from LOFAR. This will provide for an exciting study into the link between radio properties and [O III] line widths in AGN. This will provide a statistical approach in the same way that was achieved in [Molyneux et al. \(2019\)](#).

With in-hand data available, some of this future work will be achievable in the coming years. In addition, with upcoming facilities and surveys there are also exciting prospects for the future, including new and exciting opportunities that we cannot yet comprehend or predict.

Context free quotes

“I say sozzalozz a lot”

“You have to live with your fries”

“I’ve lost everything... Happy Easter”

“He estimates magnitudes based off .jpegs”

“I think when I said hamster, I meant bear”

“It’s not doing too well in terms of being alive”

“I’m far too white to be a historically accurate Jesus”

“He died doing what he loved, snowboard base jumping”

“It’s against the ESO way but get the f*ck out”

“The dynamic Scandinavian duo strikes back”

“I’ll be a gentleman and use a bucket”

“Mammoths are not wheels”

“It’s an IKEA biergarten”

Chapter 6

A short summary for a general audience

Hello and welcome to this summary of my PhD work where I have tried to make it accessible for anyone of any level of expertise to understand. I hope you find this interesting and that it answers the questions of family and friends as to what I have been doing for the past few years. If you find yourself wanting to know more feel free to read the chapters of the main part of my thesis (with much more technical jargon). Or alternatively reach out to me with any questions! This chapter is far more informal and (hopefully) easier to read than the main chapters! I hope you enjoy!!

6.1 What are galaxies and how do we study them?

Galaxies are collections of millions or billions of stars and in between these stars is also dust and gas, all held together under gravity. We also believe that all galaxies have a supermassive black hole in the centre (more on this in Section 6.3). These components are the simple building blocks that make up a galaxy. You will most likely have seen pictures of galaxies which are incredibly beautiful, with nice spiral shaped arms and showing lots of detailed structures. However, not all galaxies look like this and they come in many different shapes and sizes, see Figure 6.1. They can also evolve throughout their lifetime, growing in size, evolving different structures, forming more or less stars, as well as merging with other galaxies. I won't go into detail about these processes here, but for simplicity, it's important to know that these changes take place.

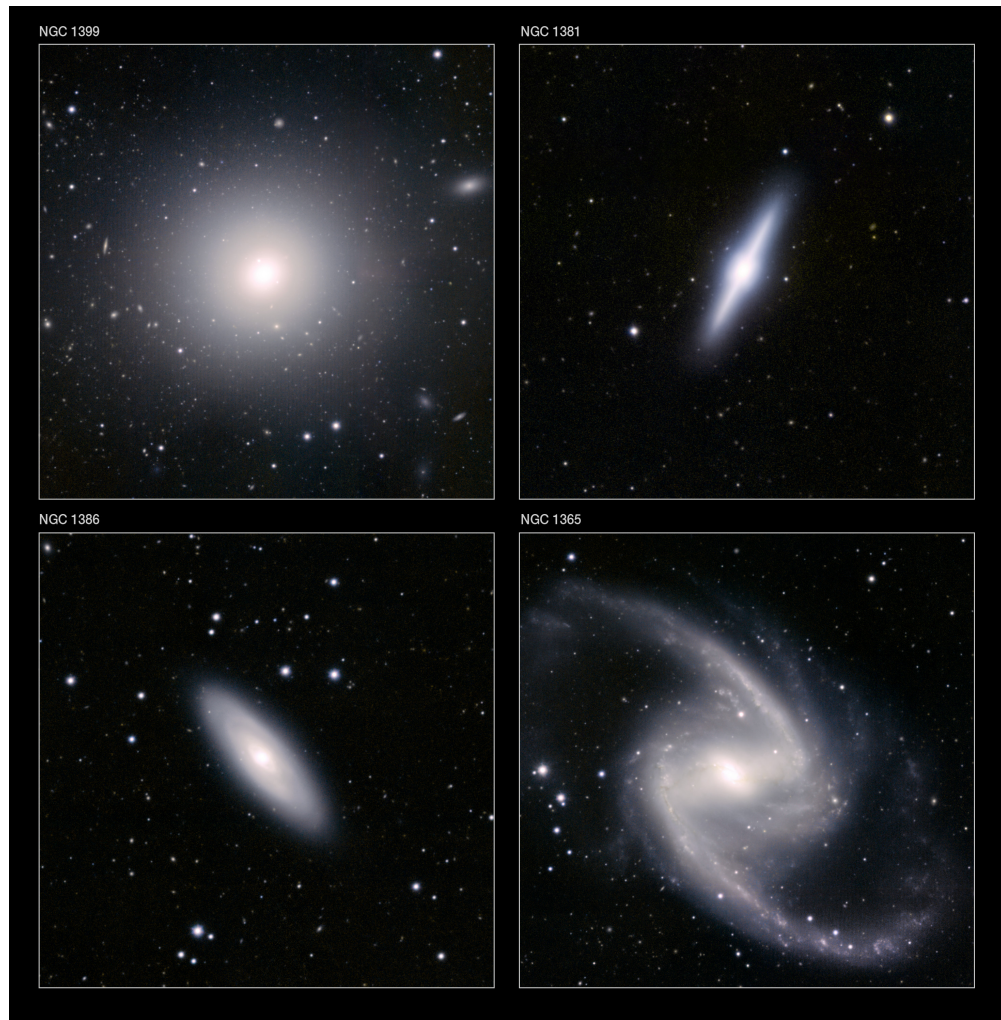


Figure 6.1: A compilation of galaxies to highlight some of the different types that are present in the Universe. **Top left:** Elliptical galaxy. **Top right:** Lenticular galaxy (halfway between elliptical and spiral). **Bottom left:** Spiral galaxy. **Bottom right:** Barred spiral galaxy. **Credit:** ESO/J. Emerson/VISTA. Acknowledgment: Cambridge Astronomical Survey Unit.

To observe and study these galaxies we need to use some of the most advanced telescopes, both on Earth and in space. However, not all galaxies are as easy to observe as each other. As we look to further and further distances, the galaxies of course look smaller and smaller, meaning that observing the most distant galaxies requires better telescopes and instruments. This is highlighted in the two images below, on the left is Andromeda, the nearest large galaxy to our own, the Milky Way, taken by an astrophotographer. The second, on the right, shows the most distant galaxy observed to date, using the James Webb Space Telescope, NASA's latest state of the art space telescope. Studying nearby galaxies is therefore far easier than studying these very distant galaxies.

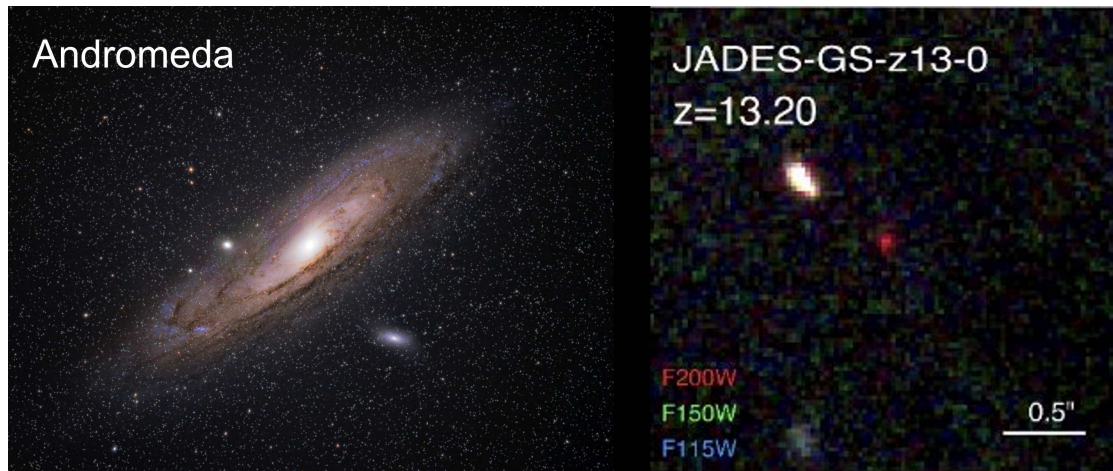


Figure 6.2: Two galaxies, one nearby and the most distant confirmed, sizes not to scale! **Left:** The Andromeda galaxy, one of galactic neighbours, taken with a publicly available digital camera. In dark skies away from light pollution it is actually visible with the naked eye. Amateur astronomer/astrophotographer can achieve this (as with this photo). Credit: Alyn Wallace. **Right:** The most distant galaxy observed to date. The small red smudge in the centre of the image is one of the first galaxies to form in the Universe. This image required observations from the James Webb Space Telescope, the most advanced and latest space telescope from NASA. Credit: [Curtis-Lake et al. \(2023\)](#).

Another important point about observing distant galaxies is that the further we look away in distance, the further back in time we are seeing. This is because of the time it takes for light to travel. In any normal situation you will encounter on Earth, it will seem as though light travels instantaneously. However, the speed of light has a finite limit. This means that across the vast distances in space this travel time has a noticeable effect. For example, light from the Sun takes 8 minutes to reach Earth. The next nearest star, Proxima Centauri, is 4.25 light years away (meaning that light takes 4.25 years to travel to us). The size of Milky Way is around 100 thousand light years across, and the nearest large galaxy to us, Andromeda (pictured above), is 2.5 million light years away... so we see that galaxy as it was 2.5 million years ago, when here on Earth it was the beginning of the ice ages. Therefore, because of the speed of light, we have a way to look back in time by simply looking to further distances.

As I mentioned earlier, galaxies can evolve over time and astronomers want to study this evolution of galaxies and analyse how they might be different at different stages of their life. However, we can't observe a single galaxy over its lifetime (to observe a galaxy for millions of years is not possible in the lifetime of a PhD student). Therefore, to understand the evolution of galaxies astronomers observe galaxies at different distances from Earth, which will correspond to different time periods of the Universe and therefore galaxies at different stages of their lifetime.

To observe the very first galaxies that form in the Universe, we need to observe light that has travelled 13 billion years from close to the beginning of the Universe. Studying these first galaxies allows us to understand how galaxies form and what the conditions were of the very early Universe.

6.2 Investigating the first galaxies in the Universe

One of the projects during my PhD was to study very distant galaxies that are some of the first to form in the Universe. The aim was to firstly confirm their distance, as well as understanding the basic properties of the galaxies such as the mass and velocities of gas in the galaxy, as well as the amount of star formation happening.

For the reasons outlined in Section 6.1, studying the first galaxies in the Universe can be very challenging. Therefore, one phenomenon we can use to assist us in observing these incredibly distant galaxies are gravitational lenses. This is a situation where a massive object, in our case a cluster of galaxies, bends and magnifies the light coming from objects behind it, thus making it easier to observe. If you imagine a giant magnifying glass in space, you will get the general idea of what's going on here. This was a tool used to aid our observations of a very distant galaxy in the work presented in Chapter 2.

With this work I identified the distance of a galaxy, called A1703-zD1, in the early period of the Universe. The light from this galaxy has been travelling for almost 13 billion years. Shown below in Figure 6.3 are data obtained with two different telescopes, on the left is the NOEMA observatory and data from this telescope, from which I calculated the distance. On the right is an image taken with the Hubble Space Telescope and the corresponding image of the galaxy from Hubble. These images also shows the differences of observing with an optical telescope such as the Hubble Space Telescope and observing with radio dishes like NOEMA.

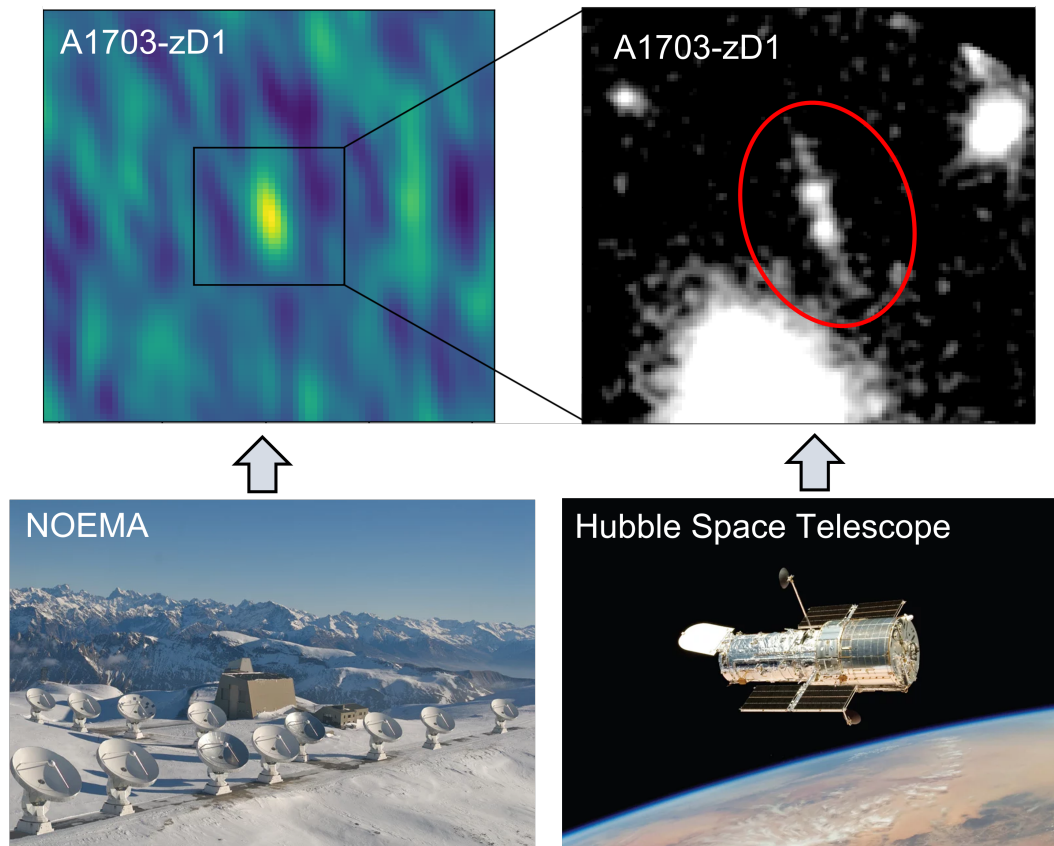


Figure 6.3: **Bottom left:** NOEMA interferometer telescope, used to observe the galaxy studied in Chapter 2, named A1703-zD1. Credit: IRAM/Rebus. **Top left:** Image obtained with NOEMA of the A1703-zD1, specifically looking at the cold gas. **Bottom right:** Hubble Space Telescope, used to image the galaxy studied in Chapter 2. Credit: Christine Klicka/NASA. **Top right:** Image of A1703-zD1 (circled in red) obtained with the Hubble Space Telescope.

This work was done under the supervision of Dr. Renske Smit at the Astrophysics Research Institute, Liverpool John Moores University.

6.3 Supermassive black holes at the centre of galaxies

At the centres of all galaxies are supermassive black holes. Black holes are incredibly dense objects which can result from the death of massive stars, whereby they collapse in on themselves. Supermassive black holes are the largest of these, residing at the centres of galaxies around which the rest of the galaxy orbits. Black holes are so dense and contain so much mass that not even light can escape their gravitational pull. For context, you would need to travel at 40,000 km per hour to escape the pull of Earth's gravity, but for black holes it is the speed of light (the



Figure 6.4: This image shows the array of telescopes that are positioned all of over the world and make up the Event Horizon Telescope (EHT). These telescopes combined create a telescope the size of the Earth, which is necessary to take the pictures of black holes in the centres of galaxies. The example shown in the top left is the supermassive black hole in M87, a galaxy located 53 million light years away, and was the first image of a black hole obtained from this array of telescopes. This figure is a compilation of an image adapted from NRAO Event Horizon telescopes and the EHT image of M87 also including images of APEX and ALMA. Credits NRAO:, EHT Collaboration, ALMA (ESO/NAOJ/NRAO), W. Garnier (ALMA) & S. J. Molyneux.

speed limit of the Universe), which is 1 billion km per hour or 300 million metres per second (this is roughly equivalent to the distance to the Moon in one second). To also contextualise the density and mass of black holes, a black hole is the equivalent of putting the mass of Earth into a the size of a marble.

Taking an image of black holes is also a huge challenge, in fact, the closest we can get is to observe the immediate surroundings of the black hole, since with the absence of light directly from the black hole it is impossible to see. To even observe the light that is just outside the grasp of the gravitational pull of the supermassive black hole in the centre of our own galaxy, we need to have incredibly high resolution that requires a telescope the size of the entire Earth! To achieve this, telescopes placed all around the world were combined, known collectively as the Event Horizon Telescope (EHT, see Figure 6.4). The resolution of these telescopes combined is 0.0000000056 degrees, a tiny fraction of 1 degree, and enough to cover the Moon 95 million times.

Despite the term “supermassive” and the fact that these supermassive black holes reside in the centres of galaxies about which everything else in the galaxy rotates, they still make up only a

few percent of the mass of the entire galaxy. However, they still play a significant role in how galaxies form and evolve.

6.4 Identifying a link between active galactic nuclei and the velocity of gas in the galaxy

Some of the supermassive black holes at the centres of galaxies are growing by feeding off the material (dust and gas) surrounding them. These growing supermassive black holes are known as active galactic nuclei (or AGN for short). As they grow they can release a huge amount of energy into the galaxy they live in (known as the host galaxy). This energy released can have an impact on the galaxy and is known as “AGN Feedback”. This feedback can disrupt the gas by transferring energy into the gas and changing its velocity or giving it higher excitation (meaning higher temperatures and densities of gas). This can also have an effect on the ability of stars to form, in both a positive and negative way.

One of the mechanisms of “feedback” is via radio jets. We observe these radio jets being ejected from centre of galaxy, thought to originate from the immediate surroundings of the AGN. Essentially, the radio jets can be driven by the AGN. One major impact these radio jets can have on the host galaxy is by interacting with gas in the galaxy. These jets can *push* the gas and cause it to change in velocity with respect to the host galaxy and can sometimes even expel gas from galaxy entirely.

These radio jets, and their interactions with the host galaxy are therefore important to study, as they show a link between the supermassive black hole and the host galaxy. From this we can learn more about the way galaxies and the central supermassive black holes evolve together.

In Chapter 3 I presented work in which I investigated the relationship between these radio jets and the gas in the host galaxy. Specifically I was looking at the velocities of the gas and whether there was any dependence on the properties of the radio emission. I studied a sample of ~ 3000 galaxies that are known to have an AGN and with such a large sample I could perform a statistical study to learn about the overall population.

From studying the radio emission and the velocities of the gas I found that those which had smaller radio sizes were more likely to have higher velocities of gas. Further to this, from studying the radio emission in a few of these targets, I found that those which had smaller radio sizes appeared to show evidence of small radio jets. This therefore supported the idea that radio jets were driving the change in velocity of the gas.

A simplified picture of what these outflows of gas driven by radio jets might look like can be seen in Figure 6.5.

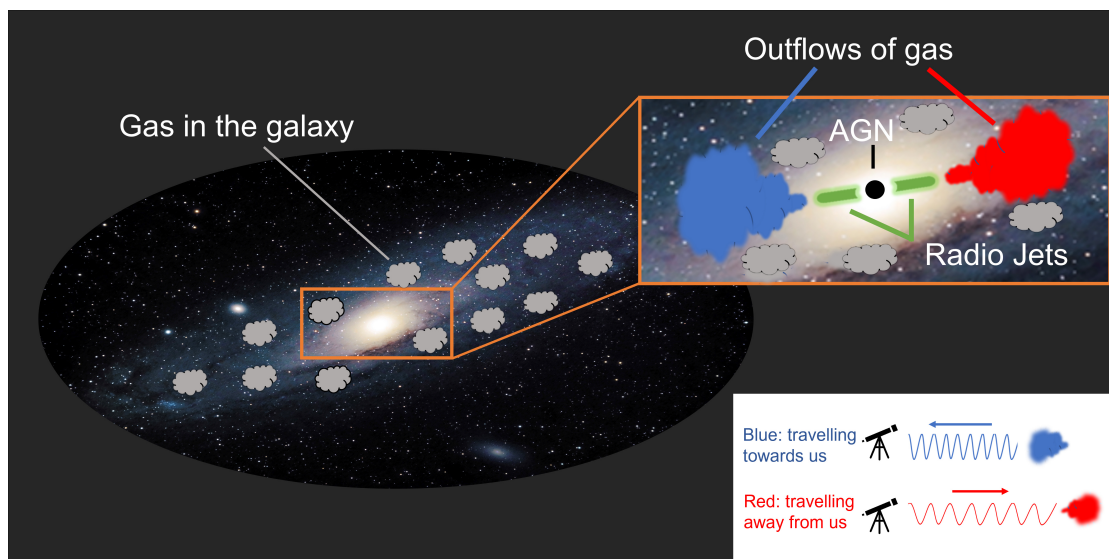


Figure 6.5: Schematic illustration of the process of radio jets in the centre of galaxies, which are driven by the AGN, having an influence on the gas surrounding them. The zoom in (shown in orange) highlights the central region of the galaxy surrounding the AGN and the radio jets (shown in green). The grey clouds indicate gas that is in the galaxy which is at rest velocity (i.e. moving normally within the galaxy). The red and blue clouds in the zoom in, and are at the location of the radio jets, indicate the gas that is being pushed by radio jets and changing the velocity of the gas with respect to the galaxy. The blue gas indicates a velocity towards us and the red gas indicates a velocity away from us.

This work was done under the supervision of Dr. Chris Harrison as part of an internship at the European Southern Observatory and a huge thank you to Chris for supporting me throughout this work and beyond.

6.5 A study of total molecular gas content in quasar host galaxies

From the 3000 galaxies talked about in the previous section, 17 were selected to be studied further in more detail, so not a statistical look but a more in-depth study for each target. These are being studied as part of a survey called the “Quasar Feedback Survey”, aiming to understand the impact of quasars (which are highly luminous AGN) on their host galaxy. From work already done, these targets have been found to have various radio jet properties, some being large and extended into the host galaxy, and some much smaller, close to the centre of the galaxy.

I have studied these 17 galaxies in detail, focusing on the total molecular gas content. The molecular gas is gas within the galaxy that will go onto form stars, and so is important to study to understand how any impact from AGN might influence a galaxies ability to form stars. In particular, I investigated the impact of the AGN feedback on the excitation of the total molecular gas content. A higher excitation needs higher temperatures and/or densities which can be caused as a result of the previously mentioned AGN feedback, injecting energy into the gas.

From this study I observed that there was no significant increase in the excitation of the *total* molecular gas content (when compared to what is expected for these galaxies). Therefore, this result indicates that the AGN feedback does not have a significant impact on the *total* molecular gas.

However, this does not rule out a more localised impact. In previous studies, increased excitation of gas has been observed very close to radio jets. This has so far only been done in a handful of cases, but the same effect might be expected in our galaxies. From our results, we can show that this impact, if present in our sample, does not have an impact across the entire galaxy. It therefore might still be the case that the localised impact is indeed occurring, which is something that I hope to test with future observations.

Below I have tried to illustrate what is happening in this scenario. The white ellipse covering the galaxy shows the normal excitation of gas in the galaxy. The red ellipse indicates more excited gas in the centre of the galaxy as a result of interactions with the radio jets (shown in green). This aims to illustrate the basic result from Chapter 4. In this work we observed the total molecular gas content, so in the diagram below this would be the white and the red part all together. If we observe everything together, then the highly excited gas in the centre is lost in

the full picture, shown by the sum of the red and white ellipse on the top row. Therefore, even if there is higher excitation in the centre, we would not be able to distinguish it. However, what we can do by observing the total molecular gas is to show that the gas across the whole galaxy does not have a higher excitation than expected. If the scenario of radio jets exciting the local gas surrounding it then if we observe just the centre in isolation, we would expect to see a higher excitation of gas than compared to the total. This is part of my future plans, to observe these central regions around radio jets in these galaxies and to test if there is enhanced excitation from the jets interacting with the gas.

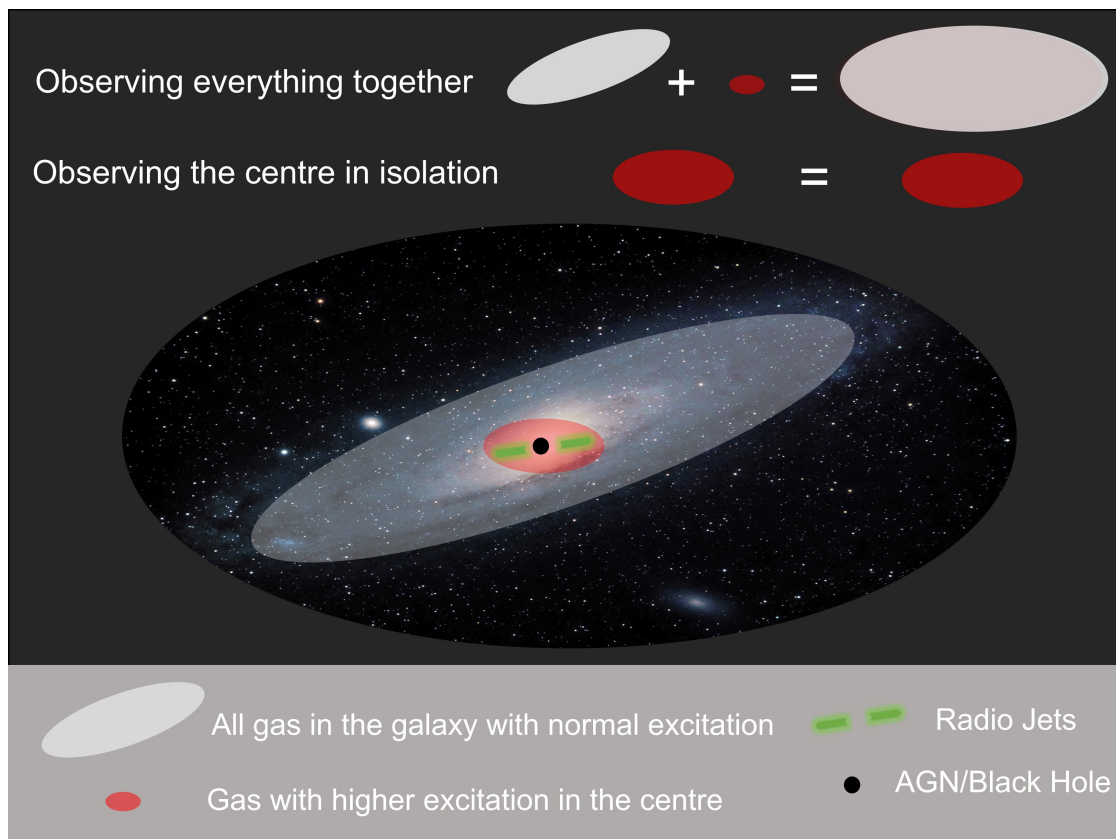


Figure 6.6: Schematic to illustrate observations of gas excitation in galaxies. In the centre of the galaxy are the AGN (in black) and the radio jets (in green). The white ellipse covering the galaxy denotes gas within the galaxy at a normal excitation. The red ellipse surrounding the black hole and the radio jets indicates higher excited gas. If we observe the total galaxy all together, the higher excited gas in the centre will be lost in the whole picture. However, if we focus observations just on the centre then we will be able to see the excited gas.

This work is presented in Chapter 4, which was work done under the supervision of Dr. Gabriela Calistro Rivera and Dr. Carlos De Breuck at the European Southern Observatory as well as important input from Dr. Chris Harrison and the rest of the Quasar Feedback Survey Team.

To finish, I would like to paraphrase Richard Ayoade:

“My modest aim for this thesis is that it delights, entertains and reconfigures the relationship between you and the Universe. I hope you have the humility to receive it.”

Bibliography

Abazajian K. N., et al., 2009, , 182, 543

Aird J., Coil A. L., Georgakakis A., Nandra K., Barro G., Pérez-González P. G., 2015, Monthly Notices of the Royal Astronomical Society, 451, 1892

Alam S., et al., 2015, ApJs, 219, 12

Alexander D. M., Hickox R. C., 2012, , 56, 93

Alexandroff R. M., Zakamska N. L., van Velzen S., Greene J. E., Strauss M. A., 2016, Monthly Notices of the Royal Astronomical Society, 463, 3056

Alhassan W., Taylor A. R., Vaccari M., 2018, Monthly Notices of the Royal Astronomical Society, 480, 2085

Andonie C., et al., 2022, Monthly Notices of the Royal Astronomical Society, 517, 2577

Aravena M., et al., 2008, Astronomy & Astrophysics, 491, 173

Armus L., et al., 2009, , 121, 559

Arrabal Haro P., et al., 2023, arXiv e-prints, p. arXiv:2303.15431

Audibert A., et al., 2023, arXiv e-prints, p. arXiv:2302.13884

Bait O., Barway S., Wadadekar Y., 2017, Monthly Notices of the Royal Astronomical Society, 471, 2687

Bakx T. J. L. C., et al., 2020, MNRAS, 493, 4294

Baldi R. D., et al., 2018, Monthly Notices of the Royal Astronomical Society, 476, 3478

Baldry I. K., Balogh M. L., Bower R., Glazebrook K., Nichol R. C., 2004, in Allen R. E., Nanopoulos D. V., Pope C. N., eds, American Institute of Physics Conference Series Vol. 743, The New Cosmology: Conference on Strings and Cosmology. pp 106–119 (arXiv:astro-ph/0410603), doi:10.1063/1.1848322

Baldwin J. A., Phillips M. M., Terlevich R., 1981, , 93, 5

Balmaverde B., Capetti A., 2015, *Astronomy & Astrophysics*, 581, A76

Balmaverde B., et al., 2016, *Astronomy & Astrophysics*, 585, A148

Banerji M., Jones G. C., Wagg J., Carilli C. L., Bisbas T. G., Hewett P. C., 2018, *Monthly Notices of the Royal Astronomical Society*, 479, 1154

Barkana R., 2006, *Science*, 313, 931

Bauermeister A., et al., 2013, *The Astrophysical Journal*, 768, 132

Becker R. H., White R. L., Helfand D. J., 1995, *The Astrophysical Journal*, 450, 559

Becker R. H., et al., 2001, , 122, 2850

Beckmann R. S., et al., 2017, preprint, (arXiv:1701.07838)

Beckwith S. V. W., et al., 2006, *The Astronomical Journal*, 132, 1729

Bennett C. L., et al., 1996, , 464, L1

Bertemes C., et al., 2023, *Monthly Notices of the Royal Astronomical Society*, 518, 5500

Best P. N., Kauffmann G., Heckman T. M., Ivezić Ž., 2005, *Monthly Notices of the Royal Astronomical Society*, 362, 9

Béthermin M., et al., 2020, *Astronomy & Astrophysics*, 643, A2

Bian F., Kewley L. J., Dopita M. A., Juneau S., 2016, *The Astrophysical Journal*, 822, 62

Bicknell G. V., Mukherjee D., Wagner A. e. Y., Sutherland R. S., Nesvadba N. P. H., 2018, *Monthly Notices of the Royal Astronomical Society*, 475, 3493

Bieri R., Dubois Y., Silk J., Mamon G. A., Gaibler V., 2016, *Monthly Notices of the Royal Astronomical Society*, 455, 4166

Bischetti M., et al., 2021, *Astronomy & Astrophysics*, 645, A33

Bolatto A. D., Wolfire M., Leroy A. K., 2013, , 51, 207

Bongiorno A., et al., 2010, *Astronomy & Astrophysics*, 510, A56

Boogaard L. A., et al., 2020, *The Astrophysical Journal*, 902, 109

Boogaard L. A., et al., 2021, *The Astrophysical Journal*, 916, 12

Booth C. M., Schaye J., 2010, *Monthly Notices of the Royal Astronomical Society*, 405, L1

Bouwens R. J., et al., 2011, *The Astrophysical Journal*, 737, 90

Bouwens R. J., et al., 2014, *ApJ*, 793, 115

Bouwens R. J., et al., 2016, *ApJ*, 833, 72

Bouwens R. J., et al., 2021, arXiv e-prints, p. arXiv:2106.13719

Bower R. G., Benson A. J., Malbon R., Helly J. C., Frenk C. S., Baugh C. M., Cole S., Lacey C. G., 2006, *Monthly Notices of the Royal Astronomical Society*, 370, 645

Bowler R. A. A., Dunlop J. S., McLure R. J., McLeod D. J., 2017, *MNRAS*, 466, 3612

Bowler R. A. A., Bourne N., Dunlop J. S., McLure R. J., McLeod D. J., 2018, *MNRAS*, 481, 1631

Bradač M., et al., 2017, *ApJl*, 836, L2

Bradford C. M., Nikola T., Stacey G. J., Bolatto A. D., Jackson J. M., Savage M. L., Davidson J. A., Higdon S. J., 2003, *The Astrophysical Journal*, 586, 891

Bradford C. M., et al., 2009, *The Astrophysical Journal*, 705, 112

Bradley L. D., et al., 2012, *The Astrophysical Journal*, 747, 3

Brammer G. B., van Dokkum P. G., Coppi P., 2008, *The Astrophysical Journal*, 686, 1503

Brandt W. N., Alexander D. M., 2015, , 23, 1

Brandt W. N., Hasinger G., 2005, , 43, 827

Bremer M. N., et al., 2018, *Monthly Notices of the Royal Astronomical Society*, 476, 12

Brinchmann J., Charlot S., White S. D. M., Tremonti C., Kauffmann G., Heckman T., Brinkmann J., 2004, *Monthly Notices of the Royal Astronomical Society*, 351, 1151

Brusa M., et al., 2015, *Monthly Notices of the Royal Astronomical Society*, 446, 2394

Buitrago F., Trujillo I., Conselice C. J., Bouwens R. J., Dickinson M., Yan H., 2008, , 687, L61

Bundy K., Ellis R. S., Conselice C. J., 2005, *The Astrophysical Journal*, 625, 621

Calistro Rivera G., et al., 2018, *The Astrophysical Journal*, 863, 56

Calistro Rivera G., et al., 2021, *Astronomy & Astrophysics*, 649, A102

Capak P. L., et al., 2015, *Nature*, 522, 455

Cardamone C., et al., 2009, *Monthly Notices of the Royal Astronomical Society*, 399, 1191

Carilli C. L., Walter F., 2013, *ARA&A*, 51, 105

Carniani S., et al., 2015, *Astronomy & Astrophysics*, 580, A102

Carniani S., et al., 2017, *A&A*, 605, A42

Carniani S., et al., 2019, *Monthly Notices of the Royal Astronomical Society*, 489, 3939

Carniani S., et al., 2020, arXiv e-prints, p. arXiv:2006.09402

Carroll S. M., 2001, *Living Reviews in Relativity*, 4, 1

Casey C. M., 2012, *Monthly Notices of the Royal Astronomical Society*, 425, 3094

Chevalier R. A., Fransson C., 1994, *The Astrophysical Journal*, 420, 268

Chevallard J., et al., 2019, *MNRAS*, 483, 2621

Choi E., Somerville R. S., Ostriker J. P., Naab T., Hirschmann M., 2018, *The Astrophysical Journal*, 866, 91

Cicone C., Feruglio C., Maiolino R., Fiore F., Piconcelli E., Menci N., Aussel H., Sturm E., 2012, *Astronomy & Astrophysics*, 543, A99

Cicone C., et al., 2014, *Astronomy & Astrophysics*, 562, A21

Cicone C., Brusa M., Ramos Almeida C., Cresci G., Husemann B., Mainieri V., 2018a, *Nature Astronomy*, 2, 176

Cicone C., et al., 2018b, *The Astrophysical Journal*, 863, 143

Cicone C., et al., 2021, *Astronomy & Astrophysics*, 654, L8

Cielo S., Bieri R., Volonteri M., Wagner A. Y., Dubois Y., 2018, *Monthly Notices of the Royal Astronomical Society*, 477, 1336

Circosta C., et al., 2018, *Astronomy & Astrophysics*, 620, A82

Circosta C., et al., 2021, *Astronomy & Astrophysics*, 646, A96

Cole S., Lacey C. G., Baugh C. M., Frenk C. S., 2000, *Monthly Notices of the Royal Astronomical Society*, 319, 168

Combes F., García-Burillo S., Braine J., Schinnerer E., Walter F., Colina L., 2011, *Astronomy & Astrophysics*, 528, A124

Condon J. J., Cotton W. D., Greisen E. W., Yin Q. F., Perley R. A., Taylor G. B., Broderick J. J., 1998, , 115, 1693

Condon J. J., Kellermann K. I., Kimball A. E., Ivezić Ž., Perley R. A., 2013, *The Astrophysical Journal*, 768, 37

Conselice C. J., 2014, , 52, 291

Costa T., Sijacki D., Haehnelt M. G., 2014, *Monthly Notices of the Royal Astronomical Society*, 444, 2355

Costa T., Sijacki D., Haehnelt M. G., 2015, *Monthly Notices of the Royal Astronomical Society*, 448, L30

Costa T., Rosdahl J., Sijacki D., Haehnelt M. G., 2018, *Monthly Notices of the Royal Astronomical Society*, 479, 2079

Costa T., Pakmor R., Springel V., 2020, *Monthly Notices of the Royal Astronomical Society*, 497, 5229

Couto G. S., Storchi-Bergmann T., 2023, *Galaxies*, 11, 47

Cox D. P., 2005, , 43, 337

Crain R. A., et al., 2015, *Monthly Notices of the Royal Astronomical Society*, 450, 1937

Cresci G., Maiolino R., 2018, *Nature Astronomy*, 2, 179

Croft S., et al., 2006, *The Astrophysical Journal*, 647, 1040

Curtis H. D., 1918, *Publications of Lick Observatory*, 13, 9

Curtis-Lake E., et al., 2023, *Nature Astronomy*,

Daddi E., et al., 2005, *The Astrophysical Journal*, 626, 680

Daddi E., et al., 2015, *Astronomy & Astrophysics*, 577, A46

Dalcanton J. J., Spergel D. N., Summers F. J., 1997, *The Astrophysical Journal*, 482, 659

Dasyra K. M., Combes F., Oosterloo T., Oonk J. B. R., Morganti R., Salomé P., Vlahakis N., 2016, *Astronomy & Astrophysics*, 595, L7

De Breuck C., Lundgren A., Emonts B., Kolwa S., Dannerbauer H., Lehnert M., 2022, *Astronomy & Astrophysics*, 658, L2

De Looze I., et al., 2014, *A&A*, 568, A62

Decarli R., et al., 2022, *Astronomy & Astrophysics*, 662, A60

Dekel A., Burkert A., 2014, *MNRAS*, 438, 1870

Dekel A., Sari R., Ceverino D., 2009, *The Astrophysical Journal*, 703, 785

Dey A., Spinrad H., Stern D., Graham J. R., Chaffee F. H., 1998, *ApJl*, 498, L93

Eckart A., Downes D., Genzel R., Harris A. I., Jaffe D. T., Wild W., 1990, *The Astrophysical Journal*, 348, 434

Eddington A. S., 1927, *Monthly Notices of the Royal Astronomical Society*, 88, 134

Eggen O. J., Lynden-Bell D., Sandage A. R., 1962, *The Astrophysical Journal*, 136, 748

Ellison S. L., Viswanathan A., Patton D. R., Bottrell C., McConnachie A. W., Gwyn S., Cuilandre J.-C., 2019, *Monthly Notices of the Royal Astronomical Society*, 487, 2491

Ellison S. L., et al., 2021, *Monthly Notices of the Royal Astronomical Society*, 505, L46

Endsley R., Stark D. P., Charlot S., et al., 2021, *Monthly Notices of the Royal Astronomical Society*, 502, 6044

Esposito F., Vallini L., Pozzi F., Casasola V., Mingozzi M., Vignali C., Gruppioni C., Salvestrini F., 2022, *Monthly Notices of the Royal Astronomical Society*, 512, 686

Event Horizon Telescope Collaboration et al., 2019, , 875, L1

Event Horizon Telescope Collaboration et al., 2022, , 930, L12

Fanaroff B. L., Riley J. M., 1974, *Monthly Notices of the Royal Astronomical Society*, 167, 31P

Farber R. J., Gronke M., 2022, arXiv e-prints, p. arXiv:2209.13622

Fath E. A., 1909, *Lick Observatory Bulletin*, 149, 71

Faucher-Giguère C.-A., Quataert E., 2012, *Monthly Notices of the Royal Astronomical Society*, 425, 605

Fawcett V. A., Alexander D. M., Rosario D. J., Klindt L., Fotopoulou S., Lusso E., Morabito L. K., Calistro Rivera G., 2020, *Monthly Notices of the Royal Astronomical Society*, 494, 4802

Ferruit P., Wilson A. S., Mulchaey J. S., 1998, *The Astrophysical Journal*, 509, 646

Feruglio C., Maiolino R., Piconcelli E., Menci N., Aussel H., Lamastra A., Fiore F., 2010, *Astronomy & Astrophysics*, 518, L155

Feruglio C., et al., 2015, *Astronomy & Astrophysics*, 583, A99

Finlez C., Nagar N. M., Storch-Bergmann T., Schnorr-Müller A., Riffel R. A., Lena D., Mundell C. G., Elvis M. S., 2018, *Monthly Notices of the Royal Astronomical Society*, 479, 3892

Fiore F., et al., 2017, *Astronomy & Astrophysics*, 601, A143

Fisher D. B., et al., 2014, , 505, 186

Fluetsch A., et al., 2019, *Monthly Notices of the Royal Astronomical Society*, 483, 4586

Fogasy J., Knudsen K. K., Drouart G., Lagos C. D. P., Fan L., 2020, *Monthly Notices of the Royal Astronomical Society*, 493, 3744

Förster Schreiber N. M., et al., 2009, *ApJ*, 706, 1364

Förster Schreiber N. M., et al., 2019b, *The Astrophysical Journal*, 875, 21

Förster Schreiber N. M., et al., 2019a, *The Astrophysical Journal*, 875, 21

Fragile P. C., Anninos P., Croft S., Lacy M., Witry J. W. L., 2017, *The Astrophysical Journal*, 850, 171

Fudamoto Y., et al., 2020, arXiv e-prints, p. arXiv:2004.10760

Fudamoto Y., et al., 2022, *The Astrophysical Journal*, 934, 144

Fujimoto S., 2019, in ALMA2019: Science Results and Cross-Facility Synergies. p. 63,
doi:10.5281/zenodo.3585292

Fujimoto S., et al., 2020, ApJ, 900, 1

Fujimoto S., et al., 2021, The Astrophysical Journal, 911, 99

GRAVITY Collaboration et al., 2018, Astronomy & Astrophysics, 615, L15

Gabor J. M., Bournaud F., 2014, Monthly Notices of the Royal Astronomical Society, 441, 1615

Gadotti D. A., 2009, Monthly Notices of the Royal Astronomical Society, 393, 1531

Gallagher R., Maiolino R., Belfiore F., Drory N., Riffel R., Riffel R. A., 2019, Monthly Notices of the Royal Astronomical Society, 485, 3409

Gallerani S., Ferrara A., Neri R., Maiolino R., 2014, Monthly Notices of the Royal Astronomical Society, 445, 2848

Gallimore J. F., Axon D. J., O’Dea C. P., Baum S. A., Pedlar A., 2006, , 132, 546

Genzel R., et al., 2012, The Astrophysical Journal, 746, 69

Genzel R., et al., 2015, The Astrophysical Journal, 800, 20

Ghez A. M., et al., 2008, The Astrophysical Journal, 689, 1044

Gillessen S., et al., 2017, The Astrophysical Journal, 837, 30

Ginolfi M., et al., 2020a, Astronomy & Astrophysics, 633, A90

Ginolfi M., et al., 2020b, A&A, 633, A90

Girdhar A., et al., 2022, Monthly Notices of the Royal Astronomical Society, 512, 1608

Gonçalves T. S., et al., 2010, The Astrophysical Journal, 724, 1373

Gonçalves T. S., Martin D. C., Menéndez-Delmestre K., Wyder T. K., Koekemoer A., 2012, The Astrophysical Journal, 759, 67

González-López J., et al., 2014, APJ, 784, 99

Greve T. R., et al., 2014, The Astrophysical Journal, 794, 142

Grogin N. A., et al., 2011, ApJs, 197, 35

Gunn J. E., Peterson B. A., 1965, *The Astrophysical Journal*, 142, 1633

Guo Y., et al., 2015, *ApJ*, 800, 39

Harikane Y., et al., 2019, *ApJ*, 883, 142

Harrington K. C., et al., 2021, *The Astrophysical Journal*, 908, 95

Harrison C. M., 2017, *Nature Astronomy*, 1, 0165

Harrison C. M., Alexander D. M., Mullaney J. R., Swinbank A. M., 2014, *Monthly Notices of the Royal Astronomical Society*, 441, 3306

Harrison C. M., Thomson A. P., Alexander D. M., Bauer F. E., Edge A. C., Hogan M. T., Mullaney J. R., Swinbank A. M., 2015, *The Astrophysical Journal*, 800, 45

Harrison C. M., et al., 2016, *Monthly Notices of the Royal Astronomical Society*, 456, 1195

Hashimoto T., Inoue A. K., Tamura Y., Matsuo H., Mawatari K., Yamaguchi Y., 2018, *arXiv e-prints*, p. arXiv:1811.00030

Hashimoto T., Inoue A. K., Tamura Y., Matsuo H., Mawatari K., Yamaguchi Y., 2019, *PASJ*, 71, 109

Heckman T. M., Best P. N., 2014, , 52, 589

Heckman T. M., Miley G. K., Green R. F., 1984, *The Astrophysical Journal*, 281, 525

Heckman T. M., Armus L., Miley G. K., 1990, , 74, 833

Heckman T. M., Kauffmann G., Brinchmann J., Charlot S., Tremonti C., White S. D. M., 2004, *The Astrophysical Journal*, 613, 109

Heckman T. M., et al., 2011, *The Astrophysical Journal*, 730, 5

Helfand D. J., White R. L., Becker R. H., 2015, *The Astrophysical Journal*, 801, 26

Herrera-Camus R., et al., 2020, *Astronomy & Astrophysics*, 635, A47

Hirschmann M., Dolag K., Saro A., Bachmann L., Borgani S., Burkert A., 2014, *Monthly Notices of the Royal Astronomical Society*, 442, 2304

Hoag A., et al., 2018, *The Astrophysical Journal*, 854, 39

Hoag A., et al., 2019, *APJ*, 878, 12

Hodge J. A., da Cunha E., 2020, *Royal Society Open Science*, 7, 200556

Holt J., Tadhunter C. N., Morganti R., 2008, *Monthly Notices of the Royal Astronomical Society*, 387, 639

Hopkins P. F., Hernquist L., Cox T. J., Di Matteo T., Robertson B., Springel V., 2006, , 163, 1

Horta D., et al., 2021, *Monthly Notices of the Royal Astronomical Society*, 500, 1385

Hubble E. P., 1927, *The Observatory*, 50, 276

Husemann B., Scharwächter J., Bennert V. N., Mainieri V., Woo J. H., Kakkad D., 2016, *Astronomy & Astrophysics*, 594, A44

Husemann B., Davis T. A., Jahnke K., Dannerbauer H., Urrutia T., Hodge J., 2017, *Monthly Notices of the Royal Astronomical Society*, 470, 1570

Husemann B., et al., 2019a, arXiv e-prints, p. arXiv:1905.10387

Husemann B., et al., 2019b, *Astronomy & Astrophysics*, 627, A53

Hwang H.-C., Zakamska N. L., Alexandroff R. M., Hamann F., Greene J. E., Perrotta S., Richards G. T., 2018, *Monthly Notices of the Royal Astronomical Society*, 477, 830

Hygate A. P. S., et al., 2023, arXiv e-prints, p. arXiv:2304.09206

Ibata R. A., Gilmore G., Irwin M. J., 1994, , 370, 194

Inoue A. K., et al., 2016, *Science*, 352, 1559

Ishibashi W., Fabian A. C., 2012, *Monthly Notices of the Royal Astronomical Society*, 427, 2998

Jarvis M. E., et al., 2019, *Monthly Notices of the Royal Astronomical Society*, 485, 2710

Jarvis M. E., et al., 2020, arXiv e-prints, p. arXiv:2007.10351

Jarvis M. E., et al., 2021, *Monthly Notices of the Royal Astronomical Society*, 503, 1780

Jung I., et al., 2020, *The Astrophysical Journal*, 904, 144

Kaasinen M., et al., 2023, *Astronomy & Astrophysics*, 671, A29

Kakkad D., et al., 2017, *Monthly Notices of the Royal Astronomical Society*, 468, 4205

Kamenetzky J., Rangwala N., Glenn J., Maloney P. R., Conley A., 2016, *The Astrophysical Journal*, 829, 93

Katz H., et al., 2019, *MNRAS*, 487, 5902

Kauffmann G., et al., 2003, *Monthly Notices of the Royal Astronomical Society*, 346, 1055

Kellermann K. I., Sramek R., Schmidt M., Shaffer D. B., Green R., 1989, , 98, 1195

Kennicutt Robert C. J., 1998, *ARA&A*, 36, 189

Kennicutt R. C., Evans N. J., 2012, *ARA&A*, 50, 531

Kewley L. J., Dopita M. A., Sutherland R. S., Heisler C. A., Trevena J., 2001, *The Astrophysical Journal*, 556, 121

Kewley L. J., Groves B., Kauffmann G., Heckman T., 2006, *Monthly Notices of the Royal Astronomical Society*, 372, 961

Kewley L. J., Maier C., Yabe K., Ohta K., Akiyama M., Dopita M. A., Yuan T., 2013, , 774, L10

Kharb P., Silpa S., 2023, *Galaxies*, 11, 27

Kharb P., O’Dea C. P., Baum S. A., Colbert E. J. M., Xu C., 2006, *The Astrophysical Journal*, 652, 177

Kharb P., Subramanian S., Vaddi S., Das M., Paragi Z., 2017, *The Astrophysical Journal*, 846, 12

Kharb P., Subramanian S., Das M., Vaddi S., Paragi Z., 2021, *The Astrophysical Journal*, 919, 108

Kim M., Ho L. C., Lonsdale C. J., Lacy M., Blain A. W., Kimball A. E., 2013, , 768, L9

Kimball A. E., Ivezić Ž., 2008, , 136, 684

Kimball A. E., Kellermann K. I., Condon J. J., Ivezić Ž., Perley R. A., 2011, , 739, L29

King A., Pounds K., 2015, , 53, 115

King A. R., Zubovas K., Power C., 2011, *Monthly Notices of the Royal Astronomical Society*, 415, L6

Kirkpatrick A., Sharon C., Keller E., Pope A., 2019, *The Astrophysical Journal*, 879, 41

Klindt L., Alexander D. M., Rosario D. J., Lusso E., Fotopoulou S., 2019, *Monthly Notices of the Royal Astronomical Society*, 488, 3109

Knudsen K. K., Richard J., Kneib J.-P., Jauzac M., Clément B., Drouart G., Egami E., Lindroos L., 2016, *MNRAS*, 462, L6

Kormendy J., Ho L. C., 2013, *ARA&A*, 51, 511

Koss M. J., et al., 2021, , 252, 29

Krolik J. H., Begelman M. C., 1988, *The Astrophysical Journal*, 329, 702

Kroupa P., 2001, *MNRAS*, 322, 231

Kruijssen J. M. D., Pfeffer J. L., Reina-Campos M., Crain R. A., Bastian N., 2019, *Monthly Notices of the Royal Astronomical Society*, 486, 3180

Labbé I., et al., 2013, , 777, L19

Lacy M., Croft S., Fragile C., Wood S., Nyland K., 2017, *The Astrophysical Journal*, 838, 146

Lacy M., et al., 2019, arXiv e-prints, p. arXiv:1907.01981

Lamperti I., et al., 2020, *The Astrophysical Journal*, 889, 103

Langan I., et al., 2023, *Monthly Notices of the Royal Astronomical Society*, 521, 546

Lansbury G. B., Jarvis M. E., Harrison C. M., Alexander D. M., Del Moro A., Edge A. C., Mullaney J. R., Thomson A. P., 2018, , 856, L1

Laporte N., Nakajima K., Ellis R. S., Zitrin A., Stark D. P., Mainali R., Roberts-Borsani G. W., 2017, *ApJ*, 851, 40

Laporte N., et al., 2021, *Monthly Notices of the Royal Astronomical Society*, 505, 4838

Lee B., et al., 2013, *The Astrophysical Journal*, 774, 47

Leroy A. K., et al., 2009, , 137, 4670

Leroy A. K., et al., 2017, *The Astrophysical Journal*, 835, 217

Leroy A. K., et al., 2021, , 257, 43

Leroy A. K., et al., 2022a, *The Astrophysical Journal*, 927, 149

Leroy A. K., et al., 2022b, *The Astrophysical Journal*, 927, 149

Leung G. C. K., et al., 2017, *The Astrophysical Journal*, 849, 48

Leung G. C. K., et al., 2019, arXiv:1905.13338, p. arXiv:1905.13338

Lewis G. F., Chapman S. C., Ibata R. A., Irwin M. J., Totten E. J., 1998, , 505, L1

Li J., et al., 2020, *The Astrophysical Journal*, 889, 162

Li J., et al., 2021, , 922, L29

Lilly S. J., Carollo C. M., Pipino A., Renzini A., Peng Y., 2013, *The Astrophysical Journal*, 772, 119

Liu G., Zakamska N. L., Greene J. E., Nesvadba N. P. H., Liu X., 2013, *Monthly Notices of the Royal Astronomical Society*, 436, 2576

Liu D., Gao Y., Isaak K., Daddi E., Yang C., Lu N., van der Werf P., 2015, , 810, L14

Liu D., et al., 2021, *The Astrophysical Journal*, 909, 56

Longinotti A. L., et al., 2023, *Monthly Notices of the Royal Astronomical Society*,

Lovell C. C., Vijayan A. P., Thomas P. A., Wilkins S. M., Barnes D. J., Irodotou D., Roper W., 2020, arXiv e-prints, p. arXiv:2004.07283

Lu R.-S., et al., 2023, arXiv e-prints, p. arXiv:2304.13252

Lutz D., et al., 2007, , 661, L25

Lutz D., et al., 2020, *Astronomy & Astrophysics*, 633, A134

Lynden-Bell D., 1969, , 223, 690

Lynden-Bell D., Rees M. J., 1971, *Monthly Notices of the Royal Astronomical Society*, 152, 461

Macfarlane C., et al., 2021, *Monthly Notices of the Royal Astronomical Society*, 506, 5888

Mackereth J. T., et al., 2019, *Monthly Notices of the Royal Astronomical Society*, 482, 3426

Madau P., Dickinson M., 2014, *ARA&A*, 52, 415

Mainali R., et al., 2018, *MNRAS*, 479, 1180

Maiolino R., 2008, , 52, 339

Maiolino R., et al., 2015, MNRAS, 452, 54

Maiolino R., et al., 2023, arXiv e-prints, p. arXiv:2305.12492

Malhotra S., Rhoads J. E., 2004, , 617, L5

Mao R.-Q., Schulz A., Henkel C., Mauersberger R., Muders D., Dinh-V-Trung 2010, The Astrophysical Journal, 724, 1336

Martin D. C., et al., 2007, , 173, 342

Mashian N., et al., 2015, The Astrophysical Journal, 802, 81

Mason C. A., Treu T., Dijkstra M., Mesinger A., Trenti M., Pentericci L., de Barros S., Vanzella E., 2018, APJ, 856, 2

Mason C. A., et al., 2019, MNRAS, 485, 3947

Matthee J., Sobral D., Santos S., Röttgering H., Darvish B., Mobasher B., 2015, MNRAS, 451, 400

Matthee J., et al., 2017, ApJ, 851, 145

Matthee J., et al., 2019, ApJ, 881, 124

McKee C. F., Ostriker J. P., 1977, The Astrophysical Journal, 218, 148

McKee C. F., Ostriker E. C., 2007, , 45, 565

McMullin J. P., Waters B., Schiebel D., Young W., Golap K., 2007, in Shaw R. A., Hill F., Bell D. J., eds, Astronomical Society of the Pacific Conference Series Vol. 376, Astronomical Data Analysis Software and Systems XVI. p. 127

Meenakshi M., Mukherjee D., Wagner A. Y., Nesvadba N. P. H., Morganti R., Janssen R. M. J., Bicknell G. V., 2022, Monthly Notices of the Royal Astronomical Society, 511, 1622

Meijerink R., Spaans M., Israel F. P., 2007, Astronomy & Astrophysics, 461, 793

Meijerink R., et al., 2013, , 762, L16

Meiksin A., Madau P., 1993, The Astrophysical Journal, 412, 34

Meurer G. R., Heckman T. M., Calzetti D., 1999, ApJ, 521, 64

Mifsud D. V., Hailey P. A., Traspas Muiña A., Auriacombe O., Mason N. J., Ioppolo S., 2021, *Frontiers in Astronomy and Space Sciences*, 8, 213

Mingozzi M., et al., 2018, *Monthly Notices of the Royal Astronomical Society*, 474, 3640

Molina J., Shangguan J., Wang R., Ho L. C., Bauer F. E., Treister E., 2023, arXiv e-prints, p. arXiv:2304.01017

Molyneux S. J., Harrison C. M., Jarvis M. E., 2019, *Astronomy & Astrophysics*, 631, A132

Molyneux S. J., et al., 2022, *Monthly Notices of the Royal Astronomical Society*, 512, 535

Molyneux S. J., et al., 2023, *Monthly Notices of the Royal Astronomical Society*,

Montoya Arroyave I., et al., 2023, arXiv e-prints, p. arXiv:2302.06629

Morgan W. W., 1958, , 70, 364

Morganti R., 2017, *Nature Astronomy*, 1, 596

Morganti R., Tadhunter C. N., Oosterloo T. A., 2005, *Astronomy & Astrophysics*, 444, L9

Morganti R., Oosterloo T., Oonk J. B. R., Frieswijk W., Tadhunter C., 2015, *Astronomy & Astrophysics*, 580, A1

Morganti R., Oosterloo T., Schulz R., Tadhunter C., Oonk J. B. R., 2018, arXiv e-prints, p. arXiv:1807.07245

Morganti R., Oosterloo T., Tadhunter C., Bernhard E. P., Raymond Oonk J. B., 2021, *Astronomy & Astrophysics*, 656, A55

Mortlock A., Conselice C. J., Bluck A. F. L., Bauer A. E., Grützbauch R., Buitrago F., Ownsworth J., 2011, *Monthly Notices of the Royal Astronomical Society*, 413, 2845

Moster B. P., Naab T., White S. D. M., 2013, *Monthly Notices of the Royal Astronomical Society*, 428, 3121

Muñoz-Elgueta N., Arrigoni Battaia F., Kauffmann G., De Breuck C., García-Vergara C., Zanella A., Farina E. P., Decarli R., 2022, *Monthly Notices of the Royal Astronomical Society*, 511, 1462

Mukherjee D., Bicknell G. V., Sutherland R., Wagner A., 2016, *Monthly Notices of the Royal Astronomical Society*, 461, 967

Mukherjee D., Wagner A. Y., Bicknell G. V., Morganti R., Oosterloo T., Nesvadba N., Sutherland R. S., 2018a, *Monthly Notices of the Royal Astronomical Society*, 476, 80

Mukherjee D., Bicknell G. V., Wagner A. e. Y., Sutherland R. S., Silk J., 2018b, *Monthly Notices of the Royal Astronomical Society*, 479, 5544

Mullaney J. R., Alexander D. M., Fine S., Goulding A. D., Harrison C. M., Hickox R. C., 2013, *Monthly Notices of the Royal Astronomical Society*, 433, 622

Naidu R. P., Tacchella S., Mason C. A., Bose S., Oesch P. A., Conroy C., 2020, *APJ*, 892, 109

Nakajima K., Ouchi M., 2014, *Monthly Notices of the Royal Astronomical Society*, 442, 900

Nayakshin S., Zubovas K., 2012, *Monthly Notices of the Royal Astronomical Society*, 427, 372

Nesvadba N. P. H., Drouart G., De Breuck C., Best P., Seymour N., Vernet J., 2017, *Astronomy & Astrophysics*, 600, A121

Nims J., Quataert E., Faucher-Giguère C.-A., 2015, *Monthly Notices of the Royal Astronomical Society*, 447, 3612

Novak M., et al., 2019, *The Astrophysical Journal*, 881, 63

O’Dea C. P., 1998, , 110, 493

O’Dea C. P., Baum S. A., Stanghellini C., 1991, *The Astrophysical Journal*, 380, 66

Ocaña Flaquer B., Leon S., Combes F., Lim J., 2010, *Astronomy & Astrophysics*, 518, A9

Oesch P. A., et al., 2015, *ApJl*, 804, L30

Oesch P. A., et al., 2016, *ApJ*, 819, 129

Oke J. B., Gunn J. E., 1983, *ApJ*, 266, 713

Oosterloo T., Raymond Oonk J. B., Morganti R., Combes F., Dasyra K., Salomé P., Vlahakis N., Tadhunter C., 2017, *Astronomy & Astrophysics*, 608, A38

Oosterloo T., Morganti R., Tadhunter C., Raymond Oonk J. B., Bignall H. E., Tzioumis T., Reynolds C., 2019, *Astronomy & Astrophysics*, 632, A66

Ouchi M., et al., 2018, , 70, S13

Overzier R. A., et al., 2008, *The Astrophysical Journal*, 677, 37

Overzier R. A., et al., 2009, *The Astrophysical Journal*, 706, 203

Padovani P., Bonzini M., Kellermann K. I., Miller N., Mainieri V., Tozzi P., 2015, *Monthly Notices of the Royal Astronomical Society*, 452, 1263

Pallottini A., Ferrara A., Gallerani S., Vallini L., Maiolino R., Salvadori S., 2017, *MNRAS*, 465, 2540

Pallottini A., et al., 2019, *MNRAS*, 487, 1689

Panessa F., Baldi R. D., Laor A., Padovani P., Behar E., McHardy I., 2019, *Nature Astronomy*, 3, 387

Papadopoulos P. P., van der Werf P. P., Xilouris E. M., Isaak K. G., Gao Y., Mühle S., 2012, *Monthly Notices of the Royal Astronomical Society*, 426, 2601

Pardo J. R., Cernicharo J., Serabyn E., 2001, *IEEE Transactions on Antennas and Propagation*, 49, 1683

Peñaloza C. H., Clark P. C., Glover S. C. O., Shetty R., Klessen R. S., 2017, *Monthly Notices of the Royal Astronomical Society*, 465, 2277

Peñaloza C. H., Clark P. C., Glover S. C. O., Klessen R. S., 2018, *MNRAS*, 475, 1508

Peebles P. J. E., 1984, *The Astrophysical Journal*, 284, 439

Peebles P. J., Ratra B., 2003, *Reviews of Modern Physics*, 75, 559

Peng Y.-j., et al., 2010, *The Astrophysical Journal*, 721, 193

Pensabene A., et al., 2021, *Astronomy & Astrophysics*, 652, A66

Pereira-Santaella M., et al., 2013, *The Astrophysical Journal*, 768, 55

Perna M., et al., 2015, *Astronomy & Astrophysics*, 583, A72

Perna M., et al., 2018, *Astronomy & Astrophysics*, 619, A90

Péroux C., Howk J. C., 2020, , 58, 363

Perrotta S., Hamann F., Zakamska N. L., Alexandroff R. M., Rupke D., Wylezalek D., 2019, *Monthly Notices of the Royal Astronomical Society*, 488, 4126

Peterson B. M., Wandel A., 1999, , 521, L95

Pety J., 2005, in Casoli F., Contini T., Hameury J. M., Pagani L., eds, SF2A-2005: Semaine de l'Astrophysique Francaise. p. 721

Pierce J. C. S., et al., 2023, Monthly Notices of the Royal Astronomical Society,

Pillepich A., et al., 2018, Monthly Notices of the Royal Astronomical Society, 473, 4077

Pillepich A., et al., 2019, Monthly Notices of the Royal Astronomical Society, 490, 3196

Piotrowska J. M., Bluck A. F. L., Maiolino R., Peng Y., 2022, Monthly Notices of the Royal Astronomical Society, 512, 1052

Posses A. C., et al., 2023, Astronomy & Astrophysics, 669, A46

Pozzi F., Vallini L., Vignali C., Talia M., Gruppioni C., Mingozi M., Massardi M., Andreani P., 2017, Monthly Notices of the Royal Astronomical Society, 470, L64

Press W. H., Schechter P., 1974, The Astrophysical Journal, 187, 425

Puschnig 2021, Dense Gas Toolbox, Zenodo, doi:10.5281/zenodo.3686329

Ramachandran V., et al., 2019, Astronomy & Astrophysics, 625, A104

Ramos Almeida C., Acosta-Pulido J. A., Tadhunter C. N., González-Fernández C., Cicone C., Fernández-Torreiro M., 2019, Monthly Notices of the Royal Astronomical Society, 487, L18

Ramos Almeida C., et al., 2022, Astronomy & Astrophysics, 658, A155

Ricci C., et al., 2017, , 233, 17

Ricotti M., Shull J. M., 2000, The Astrophysical Journal, 542, 548

Riffel R. A., Storchi-Bergmann T., Riffel R., 2014, , 780, L24

Rosario D. J., et al., 2018, Monthly Notices of the Royal Astronomical Society, 473, 5658

Rosario D. J., Togi A., Burtscher L., Davies R. I., Shimizu T. T., Lutz D., 2019, , 875, L8

Rosenberg M. J. F., et al., 2015, The Astrophysical Journal, 801, 72

Rupke D. S. N., Gültekin K., Veilleux S., 2017, The Astrophysical Journal, 850, 40

Saintonge A., et al., 2011, Monthly Notices of the Royal Astronomical Society, 415, 32

Saintonge A., et al., 2017, , 233, 22

Salim S., et al., 2007, , 173, 267

Salpeter E. E., 1964, *The Astrophysical Journal*, 140, 796

Salvestrini F., et al., 2022, *Astronomy & Astrophysics*, 663, A28

Sandage A., 1961, *The Hubble Atlas of Galaxies*

Sandstrom K. M., et al., 2013, *The Astrophysical Journal*, 777, 5

Sargent M. T., et al., 2014, *The Astrophysical Journal*, 793, 19

Schaerer D., Boone F., Zamojski M., Staguhn J., Dessauges-Zavadsky M., Finkelstein S., Combes F., 2015, *A&A*, 574, A19

Schaerer D., et al., 2020, arXiv e-prints, p. arXiv:2002.00979

Schawinski K., et al., 2014, *Monthly Notices of the Royal Astronomical Society*, 440, 889

Schaye J., et al., 2015, *Monthly Notices of the Royal Astronomical Society*, 446, 521

Schenker M. A., Stark D. P., Ellis R. S., et al., 2012, *The Astrophysical Journal*, 744, 179

Schlegel D. J., Finkbeiner D. P., Davis M., 1998, *The Astrophysical Journal*, 500, 525

Schmidt M., 1963, , 197, 1040

Schneider P., Ehlers J., Falco E. E., 1992, *Gravitational Lenses*, doi:10.1007/978-3-662-03758-4.

Schödel R., et al., 2002, , 419, 694

Scholtz J., et al., 2018, *Monthly Notices of the Royal Astronomical Society*, 475, 1288

Scholtz J., Maiolino R., Jones G. C., Carniani S., 2023, *Monthly Notices of the Royal Astronomical Society*, 519, 5246

Schouws S., et al., 2021, arXiv e-prints, p. arXiv:2105.12133

Schulz G. J., 1973, *Reviews of Modern Physics*, 45, 423

Schuster K. F., et al., 2018, in *Ground-based and Airborne Telescopes VII*. SPIE, <https://doi.org/10.1117/12.2313489>

Searle L., Zinn R., 1978, *The Astrophysical Journal*, 225, 357

Seyfert C. K., 1943, *The Astrophysical Journal*, 97, 28

Shakura N. I., Sunyaev R. A., 1973, *Astronomy & Astrophysics*, 24, 337

Shangguan J., Ho L. C., Bauer F. E., Wang R., Treister E., 2020, , 247, 15

Sharon C. E., Riechers D. A., Hodge J., Carilli C. L., Walter F., Weiß A., Knudsen K. K., Wagg J., 2016, *The Astrophysical Journal*, 827, 18

Shih H.-Y., Stockton A., Kewley L., 2013, *The Astrophysical Journal*, 772, 138

Shimizu T. T., Mushotzky R. F., Meléndez M., Koss M. J., Barger A. J., Cowie L. L., 2017, *Monthly Notices of the Royal Astronomical Society*, 466, 3161

Shimwell T. W., et al., 2017, *Astronomy & Astrophysics*, 598, A104

Shirazi M., Brinchmann J., Rahmati A., 2014, *The Astrophysical Journal*, 787, 120

Silk J., 2013, *The Astrophysical Journal*, 772, 112

Silk J., Rees M. J., 1998, *Astronomy & Astrophysics*, 331, L1

Silpa S., Kharb P., Harrison C. M., Girdhar A., Mukherjee D., Mainieri V., Jarvis M. E., 2022, *Monthly Notices of the Royal Astronomical Society*, 513, 4208

Skelton R. E., et al., 2014, *ApJs*, 214, 24

Smit R., et al., 2014, *APJ*, 784, 58

Smit R., et al., 2015, *ApJ*, 801, 122

Smit R., et al., 2018, *Nature*, 553, 178

Smith D. J. B., et al., 2016, in Reylé C., Richard J., Cambrésy L., Deleuil M., Pécontal E., Tresse L., Vauglin I., eds, *SF2A-2016: Proceedings of the Annual meeting of the French Society of Astronomy and Astrophysics*. pp 271–280 ([arXiv:1611.02706](https://arxiv.org/abs/1611.02706))

Solomon P. M., Downes D., Radford S. J. E., Barrett J. W., 1997, *The Astrophysical Journal*, 478, 144

Somerville R. S., Davé R., 2015, , 53, 51

Somerville R. S., Hopkins P. F., Cox T. J., Robertson B. E., Hernquist L., 2008, *Monthly Notices of the Royal Astronomical Society*, 391, 481

Sorai K., et al., 2019, , 71, S14

Spergel D. N., et al., 2003, , 148, 175

Spinoglio L., et al., 2012, *The Astrophysical Journal*, 758, 108

Springel V., et al., 2005, , 435, 629

Stacey H. R., Costa T., McKean J. P., Sharon C. E., Calistro Rivera G., Glikman E., van der Werf P. P., 2022, *Monthly Notices of the Royal Astronomical Society*, 517, 3377

Stanley F., Harrison C. M., Alexander D. M., Swinbank A. M., Aird J. A., Del Moro A., Hickox R. C., Mullaney J. R., 2015, *Monthly Notices of the Royal Astronomical Society*, 453, 591

Stark D. P., 2016, *ARA&A*, 54, 761

Stark D. P., et al., 2015a, *MNRAS*, 454, 1393

Stark D. P., et al., 2015b, *Monthly Notices of the Royal Astronomical Society*, 454, 1393

Stark D. P., et al., 2017, *MNRAS*, 464, 469

Steidel C. C., et al., 2014, *The Astrophysical Journal*, 795, 165

Steinhardt C. L., et al., 2020, *ApJs*, 247, 64

Stott J. P., et al., 2016, *Monthly Notices of the Royal Astronomical Society*, 457, 1888

Sun A.-L., Greene J. E., Zakamska N. L., Nesvadba N. P. H., 2014, *The Astrophysical Journal*, 790, 160

Szalay A. S., Connolly A. J., Szokoly G. P., 1999, , 117, 68

Tacconi L. J., et al., 2018, *The Astrophysical Journal*, 853, 179

Tacconi L. J., Genzel R., Sternberg A., 2020, , 58, 157

Tadhunter C., 2016, *Astronomische Nachrichten*, 337, 159

Tadhunter C., Morganti R., Rose M., Oonk J. B. R., Oosterloo T., 2014, , 511, 440

Tamura Y., et al., 2019, *ApJ*, 874, 27

Trentham N., 1995, *Monthly Notices of the Royal Astronomical Society*, 277, 616

Urry C. M., Padovani P., 1995, , 107, 803

Valentino F., et al., 2020, *Astronomy & Astrophysics*, 641, A155

Valentino F., et al., 2021, *Astronomy & Astrophysics*, 654, A165

Vayner A., et al., 2021, *The Astrophysical Journal*, 919, 122

Veilleux S., Cecil G., Bland-Hawthorn J., 2005, , 43, 769

Venturi G., et al., 2021, *Astronomy & Astrophysics*, 648, A17

Vijayan A. P., Lovell C. C., Wilkins S. M., Thomas P. A., Barnes D. J., Irodotou D., Kuusisto J., Roper W., 2020, arXiv e-prints, p. arXiv:2008.06057

Villar Martín M., Emonts B., Humphrey A., Cabrera Lavers A., Binette L., 2014, *Monthly Notices of the Royal Astronomical Society*, 440, 3202

Villar-Martín M., et al., 2017, *Monthly Notices of the Royal Astronomical Society*, 472, 4659

Vito F., et al., 2014, *Monthly Notices of the Royal Astronomical Society*, 441, 1059

Vogelsberger M., et al., 2014, *Monthly Notices of the Royal Astronomical Society*, 444, 1518

Wagner A. Y., Bicknell G. V., Umemura M., 2012, *The Astrophysical Journal*, 757, 136

Wagner A. Y., Umemura M., Bicknell G. V., 2013, , 763, L18

Wagner A. Y., Bicknell G. V., Umemura M., Sutherland R. S., Silk J., 2016, *Astronomische Nachrichten*, 337, 167

Walter F., et al., 2012, *The Astrophysical Journal*, 752, 93

Wang R., et al., 2010, *The Astrophysical Journal*, 714, 699

Wang J., Xu D. W., Wei J. Y., 2018, *The Astrophysical Journal*, 852, 26

Wang F., Wang R., Fan X., Wu X.-B., Yang J., Neri R., Yue M., 2019, *The Astrophysical Journal*, 880, 2

Ward S. R., Harrison C. M., Costa T., Mainieri V., 2022, *Monthly Notices of the Royal Astronomical Society*, 514, 2936

Watson D., Christensen L., Knudsen K. K., Richard J., Gallazzi A., Michałowski M. J., 2015, *Nature*, 519, 327

White S. D. M., Rees M. J., 1978, *Monthly Notices of the Royal Astronomical Society*, 183, 341

Whittle M., 1985, *Monthly Notices of the Royal Astronomical Society*, 213, 1

Whittle M., Haniff C. A., Ward M. J., Meurs E. J. A., Pedlar A., Unger S. W., Axon D. J., Harrison B. A., 1986, *Monthly Notices of the Royal Astronomical Society*, 222, 189

Wilkins S. M., Bunker A. J., Stanway E., Lorenzoni S., Caruana J., 2011, *MNRAS*, 417, 717

Williams C. C., et al., 2014, *The Astrophysical Journal*, 780, 1

Willott C. J., Carilli C. L., Wagg J., Wang R., 2015, *ApJ*, 807, 180

Wilson A. S., Colbert E. J. M., 1995, *The Astrophysical Journal*, 438, 62

Wilson C. D., et al., 2012, *Monthly Notices of the Royal Astronomical Society*, 424, 3050

Windhorst R. A., Cohen S. H., Jansen R. A., Conselice C., Yan H., 2006, *New Astronomy Reviews*, 50, 113

Wolfire M. G., Vallini L., Chevance M., 2022, , 60, 247

Woo J.-H., Bae H.-J., Son D., Karouzos M., 2016, *The Astrophysical Journal*, 817, 108

Wuyts S., et al., 2016, *The Astrophysical Journal*, 831, 149

Wyder T. K., et al., 2007, , 173, 293

Xia X. Y., et al., 2012, *The Astrophysical Journal*, 750, 92

Xu C., Livio M., Baum S., 1999, , 118, 1169

Yajima Y., et al., 2021, , 73, 257

Yang C., et al., 2017, *Astronomy & Astrophysics*, 608, A144

Yang J., et al., 2019, *The Astrophysical Journal*, 880, 153

York D. G., et al., 2000, , 120, 1579

Yung L. Y. A., Somerville R. S., Finkelstein S. L., Popping G., Davé R., Venkatesan A., Behroozi P., Ferguson H. C., 2020, *MNRAS*, 496, 4574

Zakamska N. L., Greene J. E., 2014, *Monthly Notices of the Royal Astronomical Society*, 442, 784

Zakamska N. L., Strauss M. A., Heckman T. M., Ivezić Ž., Krolik J. H., 2004, , 128, 1002

Zakamska N. L., et al., 2016, Monthly Notices of the Royal Astronomical Society, 455, 4191

Zhang C.-P., Li G.-X., Zhou C., Yuan L., Zhu M., 2019, Astronomy & Astrophysics, 631, A110

Zhuang M.-Y., Ho L. C., Shangguan J., 2021, The Astrophysical Journal, 906, 38

Zitrin A., et al., 2010, Monthly Notices of the Royal Astronomical Society, 408, 1916

Zitrin A., et al., 2015, , 810, L12

Zschaechner L. K., et al., 2018, The Astrophysical Journal, 867, 111

Zubovas K., 2018, Monthly Notices of the Royal Astronomical Society, 473, 3525

Zubovas K., Nayakshin S., King A., Wilkinson M., 2013, Monthly Notices of the Royal Astronomical Society, 433, 3079

de Sá-Freitas C., et al., 2022, Monthly Notices of the Royal Astronomical Society, 509, 3889

de Sá-Freitas C., et al., 2023, Astronomy & Astrophysics, 671, A8

den Brok J. S., et al., 2021, Monthly Notices of the Royal Astronomical Society, 504, 3221

van Breugel W., Miley G., Heckman T., 1984, , 89, 5

van den Bergh S., 1960, The Astrophysical Journal, 131, 558

van den Bergh S., 1976, The Astrophysical Journal, 206, 883

van der Tak F. F. S., Black J. H., Schöier F. L., Jansen D. J., van Dishoeck E. F., 2007, Astronomy & Astrophysics, 468, 627

van der Werf P. P., et al., 2010, Astronomy & Astrophysics, 518, L42